AD-A128 815 RESEARCH INVESTIGATION DIRECTED TOWARD EXTENDING THE USEFUL RANGE OF THE ELECTROMAGNETIC SPECTRUM(U) COLUMBIA RADIATION LAB NEW YORK G W FLYNN 31 MAR 83 1/3

UNCLASSIFIED DAAG29-82-K-0080 F/G 20/3 NL

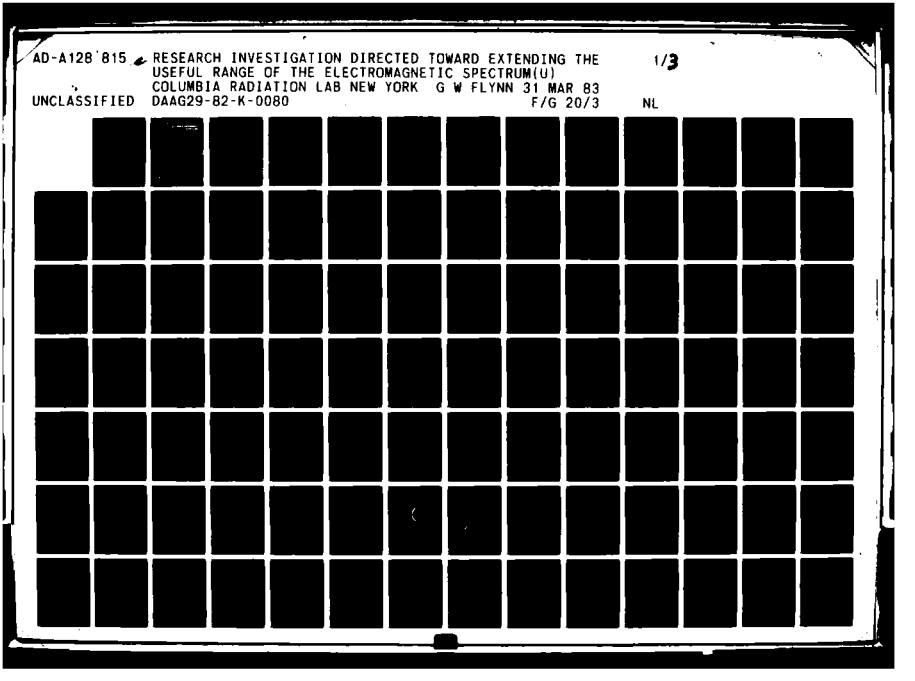

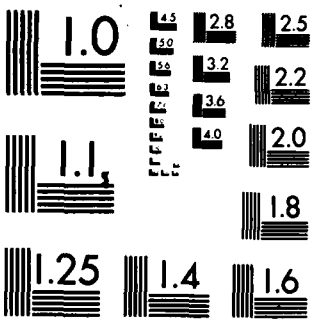

MICROCOPY RESOLUTION TEST CHART
NATIONAL BUREAU OF STANDARDS-1963-A

CRL **COLUMBIA UNIVERSITY**

DEPARTMENTS OF PHYSICS, CHEMISTRY, ELECTRICAL ENGINEERING

PROGRESS REPORT NO. 33

April 1, 1982 - March 31, 1983

CONTRACT DAAG29-82-K-0080

APPROVED FOR PUBLIC RELEASE: DISTRIBUTION UNLIMITED

TO:

THE JOINT SERVICES TECHNICAL ADVISORY COMMITTEE

REPRESENTING: THE U.S. ARMY ELECTRONICS COMMAND
THE U.S. ARMY RESEARCH OFFICE
THE OFFICE OF NAVAL RESEARCH
THE AIR FORCE OFFICE OF SCIENTIFIC RESEARCH

COLUMBIA RADIATION LABORATORY, NEW YORK, NEW YORK 10027

March 31, 1983

COLUMBIA RADIATION LABORATORY

RESEARCH INVESTIGATION DIRECTED TOWARD EXTENDING THE USEFUL RANGE OF THE ELECTROMAGNETIC SPECTRUM

Progress Report No. 33

April 1, 1982 through March 31, 1983

Contract DAAG29-82-K-0080

Object of the Research:

Basic research in the fields of quantum electronics; electromagnetic propagation, detection and sensing; and solid state electronics.

The research reported in this document was made possible through support extended the Columbia Radiation Laboratory, Columbia University, by the Joint Services Electronics Program (U.S. Army Electronics Command and U.S. Army Research Office, Office of Naval Research, and the Air Force Office of Scientific Research) under Contract DAAG29-82-K-0080.

Submitted by: G. W. Flynn, Director

Coordinated by: Vicki J. Zell, Administrative Assistant

COLUMBIA UNIVERSITY

Division of Government-Aided Research

New York, New York 10027

March 31, 1983

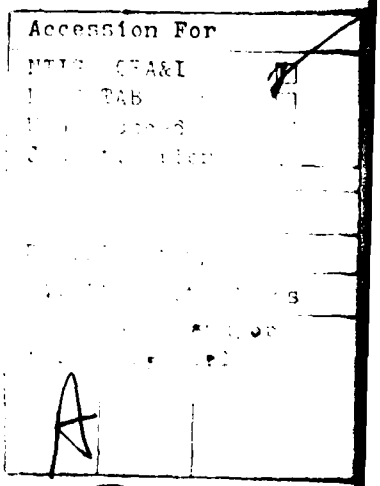

The research reported in this document was made possible through support extended to the Columbia Radiation Laboratory, Columbia University by the Joint Services Electronics Program (U.S. Army Electronics Command and U.S. Army Research Office, Office of Naval Research, and the Air Force Office of Scientific Research) under Contract DAAG29-82-K-0080.

Portions of this work were also supported by:

Air Force Office of Scientific Research

AFOSR-81-0009-A
AFOSR-81-0009-C

AFOSR/DARPA

F-49620-82-K-0008

Army Research Office

Contract DAAG29-82-K-0089

National Science Foundation

Grant NSF-ENG 78-26498
Grant NSF-ECS 80-06881
Grant NSF-DMR 80-06966
Grant NSF-CHE 80-23747
Grant NSF-BNS 80-21140
Grant NSF-ECS 81-16163
Grant NSF-ECS 82-07610
Grant NSF-ECS 82-09218
Grant NSF-ECS 82-17677

Office of Naval Research

Contract N00014-78-C-0517

Department of Energy

Contract DE-AC02-78-ER-S-04940
Contract DOE/SERI xz-ϕ-9226
Contract DOE/SERI xB-2-02185-1

National Institutes of Health

NIH-2-R01-NS503654

The support of these agencies is acknowledged in footnotes in the text.

Unclassified

SECURITY CLASSIFICATION OF THIS PAGE (When Data Entered)

REPORT DOCUMENTATION PAGE		READ INSTRUCTIONS BEFORE COMPLETING FORM
1. REPORT NUMBER Progress Report No. 33	2. GOVT ACCESSION NO. AD-A128 815	3. RECIPIENT'S CATALOG NUMBER
4. TITLE (and Subtitle) RESEARCH INVESTIGATION DIRECTED TOWARD EXTENDING THE USEFUL RANGE OF THE ELECTROMAGNETIC SPECTRUM		5. TYPE OF REPORT & PERIOD COVERED 1 April 1982 - 31 March 1983 6. PERFORMING ORG. REPORT NUMBER 33
7. AUTHOR(s) George W. Flynn		8. CONTRACT OR GRANT NUMBER(s) DAAG29-82-K-0080
9. PERFORMING ORGANIZATION NAME AND ADDRESS Columbia Radiation Laboratory Columbia University New York, New York 10027		10. PROGRAM ELEMENT, PROJECT, TASK AREA & WORK UNIT NUMBERS
11. CONTROLLING OFFICE NAME AND ADDRESS Department of the Army U. S. Army Research Office Research Triangle Park, NC 27709		12. REPORT DATE 31 March 1983 13. NUMBER OF PAGES 214
14. MONITORING AGENCY NAME & ADDRESS(if different from Controlling Office)		15. SECURITY CLASS. (of this report) Unclassified 15a. DECLASSIFICATION/DOWNGRADING SCHEDULE

16. DISTRIBUTION STATEMENT (of this Report)

Approved for public release; distribution unlimited

17. DISTRIBUTION STATEMENT (of the abstract entered in Block 20, if different from Report)

18. SUPPLEMENTARY NOTES

Portions of this work were also supported by the Air Force Office of Scientific Research, the Army Research Office, the National Science Foundation, the Office of Naval Research, the Department of Energy, AFOSR/DARPA, and NIH.

19. KEY WORDS (Continue on reverse side if necessary and identify by block number)

Light generation
Light detection
Coherence
Photon statistics (continued)

20. ABSTRACT (Continue on reverse side if necessary and identify by block number)

Substantial progress has been made in understanding the generation and detection of light from an unified statistical point of view. To this end, the coherence properties and photon statistics of stationary light obtained by the superposition of nonstationary emissions occurring at random times, in accordance with a homogeneous Poisson point process has been investigated.

DD FORM 1 JAN 73 1473 EDITION OF 1 NOV 65 IS OBSOLETE

Unclassified

SECURITY CLASSIFICATION OF THIS PAGE (When Data Entered)

The individual emissions were assumed to be in a coherent, chaotic, or n state. The statistical nature of the emission times results in fluctuations of the relative contributions of different emissions at a given time. In the limit when the emissions overlap strongly, the field exhibits the correlation properties of chaotic light, regardless of the statistics of the individual emissions. This is an important result. The effect of Bernoulli random deletion and additive independent Poisson noise on photon-counting statistics has been examined. Under the action of such deletion and/or noise, both super-Poissonian and sub-Poissonian distributions move toward the Poisson distribution but never convert from one form to the other. We also studied the counting statistics for stationary and nonstationary cascaded Poisson processes, obtaining a simple equation for the variance-to-mean ratio (noisiness) in the limit of long counting times. These results will be important for understanding light detectors, such as avalanche photodiodes.

Signal-dependent noise is manifested in many physical processes and often represents a fundamental limitation to the minimum uncertainty in the magnitude of a physical quantity. When this quantity is the number of photons incident on a photodetector, the uncertainty in the number of photons is proportional to the total energy received. This signal-dependent photon noise places a limit on the minimum light energy that can be received with a given reliability. When the quantity of interest is the number of impurities implanted in a semiconductor material, the uncertainty in the number of impurities is proportional to their average number. This signal-dependent "impurity-noise" places a limit, in certain circumstances, on the minimum device dimensions in a VLSI system that will function with a given reliability.

Substantial progress has been made in understanding the role of signal-dependent noise in the performance of source modulation formats in fiber optic communications and on the performance of VLSI systems containing ion-implanted bipolar transistors.

The recombination of excess minority carriers at grain boundaries, or other interfaces with space-charge regions, has been treated theoretically for general energy distributions of interface states (recombination centers). The distinction is made between minority carrier recombination velocity at the

(grain-boundary) interface itself, and the effective recombination velocity for the collection of these carriers by the adjacent space-charge region. Calculations of the effective recombination velocity have been made as a function of the excess minority-carrier concentration at the edge of the space-charge region since this is the quantity of most convenience for device modelling.

Results of theoretical and experimental investigations of the effects of high temperature (27°C to 300°C) on N and P channel MOS transistors have been obtained. At the device level, the temperature dependences of the electrical parameters are characterized individually; they include the threshold voltage, the surface mobility, and the junction leakage currents. Current-voltage characteristics were obtained for the subthreshold, nonsaturation, and saturation regions of operation. Transistor performance limitations were determined from the observed degradation mechanisms. The conventional large and small signal models of the MOSFET were modified so as to embody the effects of high temperature. The static and switching high temperature performances of a CMOS inverter, a basic logic cell, were also obtained. Some implications of the experimental result on high temperature analog circuit design are discussed.

A general theory of phonon-assisted transition of majority carriers across a grain boundary (GB) has been formulated with the GB angle as a variable. The bulk relaxation time in the crystalline region and the transition time at the GB have been found to be the important parameters that determine the transmission coefficient of carriers across the GB. Using the proposed model, an n-type polycrystalline silicon is employed as an example in a numerical calculation.

Using the classical diffusion equation for an amorphous (a)-Si-Al-Si sandwich structure, the diffusivity of a-Si in Al between 470-570°C has been measured and the mass-transfer coefficient under the equilibrium solid-phase epitaxial growth condition has been derived. Our data can be used to explain recent results of junction formation by solid-phase epitaxy. The activation energy of this process is found to be 0.80 eV.

Block 20 continued - Abstract

Thin films have been grown on <111> germanium by thermal nitridation. The surface morphology, composition, thickness, and refractive index of the films have been investigated. Compositional analysis was performed by electron beam x-ray microanalysis which indicates that the films contain oxygen as well as nitrogen and have a nitrogen to oxygen ratio on the order of 2.5:1. Film thickness and refractive index were determined by ellipsometry. The thicknesses ranged from 60 to 150 Å, and the refractive indices ranged from 1.5 to 2.3 depending on growth parameters. A universal chart for evaluating the thickness and refractive index of dielectric films on germanium from the ellipsometric parameters ψ and Δ is also presented.

An experimental technique has been developed to study the electrical properties of semiconductor grain boundaries (GB's) by a focused laser beam. The laser beam is trained on a GB while the photoconductivity of the sample is measured. This technique allows a localized region of an individual GB in semiconductors with multiple grains to be examined. The measurement of the steady state and transient signals as a function of temperature determines the grain boundary barrier height, trap energy, and capture cross section.

A study of the UV photochemistry of organometallic molecules in the vapor and adsorbed phases has been made. The gas-phase spectra is interpreted on the basis of molecular-orbital theory and experimental data. The absorption spectra of the surface adlayers are determined by computer subtraction of the gas-phase spectra and an interpretation is provided.

Submicrometer gratings have been etched in GaAs and CdS crystals which have been immersed in an oxidizing etch and illuminated with interfering laser beams. A resolution of 130 nm was obtained. The use of in-situ optical measurements of grating parameters allows ready optimization of the grating fabrication process.

Both pulsed excimer lasers and focused cw ion lasers have been used to form SiO_2 patterns from spun-on silicates on silicon substrates. The patterns formed using the Ar^+ laser have ~1-2 μm resolution. This resolution allows direct patterning of SiO_2 on various substrates for both microelectronics and integrated optics.

Block 20 continued - Abstract

The deposition of thin films with UV laser light and the physical processes which contribute to the deposit microstructure are being investigated. TEM studies of the early stages of film growth show the importance of the light interaction with the deposit nuclei.

Observation of the laser enhancement of the etching rate in a planar plasma etcher has been made. The enhancement has been measured as a function of laser intensity.

Photon-assisted dry etching of GaAs has been achieved. The process is based on photodissociation of halogen-containing organic molecules, using UV laser radiation.

The characteristics of the capillaritron, a high intensity source of ions and radicals, are being investigated. Mass spectrometry and optical detection suggest that many species are present in the beam. Time of flight studies indicate that while the ions exhibit a wide spread in velocity, the neutral species have a much narrower distribution.

Work has been completed on the study of the photophysics of I_2 isolated in rare gas matrices. Following excitation with a dye laser, emission was seen from the three low lying electronic states: B $^3\pi O_u^+$, A $^3\pi_{1u}$, and A' $^3\pi_{2u}$. The last state emits only when the host matrix is Xe. The results are discussed in terms of the importance of the solvent cage effect and potential implication for the development of Iodine atom chemical lasers.

Low temperature matrices of I_2 in CCl_4 have been studied. Iodine was photodissociated by excitation with a dye laser at 500-540 nm.; the fluorescence obtained subsequently was characterized temporally as well as spectrally. Spectral resolution of the fast component of emission was achieved, but its origin could not be determined. Comparison with the absorption spectrum of iodine in liquid CCl_4 is being sought to elucidate the nature of the emitting species.

The rates of intermolecular vibrational energy transfer among the ν_2 bending fundamental, the $2\nu_2$ overtones, and the ν_1 symmetric stretch fundamental of CO_2 have been measured. The system was treated as a 4-level system and the 3 measured eigenvalues were:

Block 20 continued - Abstract

$$390 \pm 80 \text{ msec}^{-1}\text{torr}^{-1}$$
$$1000 \pm 300 \text{ msec}^{-1}\text{torr}^{-1}$$
$$2000 \pm 500 \text{ msec}^{-1}\text{torr}^{-1}$$

The ladder climbing rate for the ν_2 mode corresponded to the first measured eigenvalue of 390 ± 80 msec^{-1}torr^{-1}, in good agreement with previously measured values. The ν_2 fundamental appears to couple directly to the (02^20) level and only indirectly to the Fermi coupled lower laser levels, the (10^00) and (02^00) states. Work is in progress to establish the remaining two eigenvalues to better accuracy and to establish the kinetic rates constants derived from these eigenvalues.

T-V excitation transfer by hot atoms has been studied in the HBr-N_2O and HCl-CH_4 systems where channels for both inelastic and reactive scattering are available. In the HBr-N_2O system at least, both kinds of scattering are observed. Also, mode-specific excitation of N_2O by hot hydrogen atoms appears to be a distinct possibility.

Emission from the ν_3 vibrational mode of the ground electronic state of SO_2 has been observed after excitation to low-lying singlet electronic states. Preliminary results indicate that the ν_1 mode is initially excited, followed by equilibration with the ν_3 mode.

Collision induced multiple-photon absorption by SF_6 of cw CO_2 laser radiation has been carried out inside a transparent, capillary nozzle beam source. Resonant laser excitation of the gas just upstream of the nozzle exit enhances the internal energy by 0.38 eV molec^{-1} over its value at T_{nz} = 290K. In comparison, simple thermal heating of the nozzle to 544K, which provides a velocity distribution in the beam similar to that found with laser excitation, produces a beam enhanced in internal energy by only 0.03 eV molec^{-1}. A relative (laser on/laser off) cross section has been determined for crossed-beam reactions of SF_6 with K_2. This chemi-ionization cross section, σ_{rel}, decreases with vibrational excitation.

Block 20 continued - Abstact

The dominant pathway in the photodissociation of an anthracene endoperoxide yielding excited singlet oxygen plus an aromatic fragment has been found to involve an intermediate chemical structure. The decay time (45 ps) of the intermediate, believed to be either a Dewar like isomer or an excited biradical, was observed by a picosecond laser induced fluorescence method.

The dynamics of generation of diphenylcarbene from a diphenyldiazomethane precursor and energy relaxation in the diphenylcarbene fragment was carried out using picosecond fluorescence methods. Information on the dynamics of singlet-triplet interconversion, of key importance in the chemistry of carbenes, and the energy separation between these states was obtained from these studies.

The stabilization of a twisted internal charge transfer state in the molecule p-dimethylamino benzonitrile, which is responsible for a dual fluorescence, was discovered to be due to a local interaction with polar solvent molecules. The dynamics of the twisting process were not found to correlate with the dielectric relaxation times of the solvent as had been proposed by various research groups.

The Billiard Ball Echo Model was extended to include the effects of using sub-Doppler-linewidth lasers in photon echo experiments. The resulting Elliptical Billiard Ball Echo Model develops the theory in a more rigorous manner and explains such echo phenomena in gases as echo duration and degradations of echo intensity with excitation beam angling. Photon echo experiments are described supporting the Elliptical Billiard Ball Model. These experiments have detected echoes over a dynamic range exceeding 10^{10} produced by atoms excited as much as 15 lifetimes earlier.

Two-photon tri-level echoes have been generated which enable the measurement of collisional relaxation of D-P superposition atom states. Tri-level echo studies of S-S and S-D superposition state relaxation in Li vapor has begun. A search for the first detection of tri-level echoes in solids is underway.

Block 19 continued - Key Words

Random deletion
Cascaded processes
Avalanche photodiodes
Signal-dependent noise
Frequency-shift keying
Optical fibers
VLSI
Reliability
GaAs
Direct-writing
Microelectronics
Surface chemistry
Laser photochemistry
SiO_2
Dry processing
Dry etching
Surface spectroscopy
Physisorbed layers
Submicrometer fabrication
CdS
Polycrystalline silicon
Grain boundary
Interface states
Laser-spot photoconductivity
Germanium nitride
Solid-phase epitaxy
Carrier Recombination
Grain boundaries and effective recombination velocity
MOSFETs
High-temperature electronics
CMOS
Multi-photon
CO_2 laser
SF_6
Photofragmentation
Hot atoms
Matrix
Electronic relaxation
Iodine chemical laser
Capillaritron
Ion beam
CO_2 relaxation
Picosecond lasers
Photodissociation
Singlet oxygen
Diphenylcarbene
Energy relaxation
Singlet-triplet spin re ion
Twisted internal
Charge transfer
Aromatic endoperoxide
Rapid molecular phenomena
Charge hopping
Short-lived chemical intermediates
Divalent carbon fragments
Materials
"Frozen"
Rapid evolution
Carbenes
Degradation
Raman
Absorption
Resolution
Billiard Ball Echo Model
Photon echoes
Large dynamic range
Multi-lifetime excitations
Two-photon tri-level echo
Super radiant enhancement

TABLE OF CONTENTS

PUBLICATIONS AND REPORTS

Publications

M. C. Teich, P. R. Prucnal, G. Vannucci, M. E. Breton, and W. J. McGill, "Multiplication Noise in the Human Visual System at Threshold: 1. Quantum Fluctuations and Minimum Detectable Energy," J. Opt. Soc. Am. 72, 419 (1982). (NIH and NSF)

P. R. Prucnal and M. C. Teich, "Multiplication Noise in the Human Visual System at Threshold: 2. Probit Estimation of Parameters," Biol. Cybern. 43, 87 (1982). (NIH and NSF)

M. C. Teich, P. R. Prucnal, G. Vannucci, M. E. Breton, and W. J. McGill, "Multiplication Noise in the Human Visual System at Threshold: 3. The Role of non-Poisson Quantum Fluctuations," Biol. Cybern. 44, 157 (1982). (NIH and NSF)

M. C. Teich and S. M. Khanna, "Pulse-number Distribution for the Neural Discharge in the Cat's Auditory Nerve," J. Acoust. Soc. Am. 71, S17 (1982). (NIH)

G. Lachs, R. A. Saia, and M. C. Teich, "A Neural-Counting Model Incorporating Refractoriness and Spread of Excitation: Extension of the Model to Include Receptor Saturation and Spontaneous Neural Activity," J. Acoust. Soc. Am. 71, S18 (1982). (NSF)

M. C. Teich, G. Lachs, and R. A. Saia, "A Neural Counting Model Incorporating Refractoriness and Spread of Excitation: Role of the Peripheral Auditory System in Intensity Discrimination," J. Acoust. Soc. Am. 71, S18 (1982) (NSF)

M. C. Teich, "Cascaded Poisson Processes in Optical Communications," in Prof. NSF Grantee-User Meeting, edited by J. Whinnery (University of California, Berkeley, 1982), Optical Communication Systems, p. 62. (NSF)

M. C. Teich, "Neural Counting Statistics in Sensory Communications," in Proc. 35th Annual Conf. on Eng. in Medicine and Biology, 24, 29 (1982). (NIH and NSF)

M. C. Teich and B. E. A. Saleh, "Effects of Random Deletion and Additive Noise on Bunched and Antibunched Photon-Counting Statistics," Opt. Lett. 7, 365 (1982). (JSEP and NSF)

K. Matsuo, B. E. A. Saleh, and M. C. Teich, "Cascaded Poisson Processes," J. Math. Phys. 23, 2353 (1982). (JSEP and NSF)

P. R. Prucnal and H. C. Card, "Effects on VLSI Yield of Doubly-Stochastic Impurity Distributions," IEEE Trans. Reliability, R31, 185 (1982). (JSEP)

P. R. Prucnal, "Experiments in Digital Signal Processing," IEEE Trans. Educ. E-25, 91 (1982).

P. R. Prucnal and B. E. A. Saleh, "Evaluation of Fiber-Optic Error Rates Using a Normalizing Transform," J. Opt. Soc. Am. 72, 1171 (1982). (NSF and JSEP)

P. Panayotatos, E. S. Yang, and W. Hwang, "Determination of the Grain Boundary Recombination Velocity in Polycrystalline Silicon as a Function of Illumination from Photoconductance Measurements," Solid State Electronics 25, 417 (1982). (JSEP and DOE/SERI)

E. Poon and W. Hwang, "Phenomenological Model of Grain Boundary Trapping States in Polycrystalline Silicon under Optical Illumination," Solid State Electronics 25, 699 (1982). (JSEP and DOE/SERI)

G. F. Fulop, P. V. Meyers, C. H. Liu, S. M. So, W. Hwang, and E. S. Yang, "Electrical Characterization of Electrodeposited CdTe Solar Cells," Proceedings 16th IEEE Photovoltaic Specialists Conference, San Diego, Calif. 917-921, 1982. (DOE/SERI and AMETEK)

E. Poon, H. L. Evans, W. Hwang, R. M. Osgood, Jr., and E. S. Yang, "Measurement of Grain Boundary Parameters by Laser-Spot Photoconductivity," MRS Meeting Boston, November 1982. (accepted for publication). (JSEP and DOE/SERI)

E. S. Yang, "Structures and Performance of Polycrystalline Thin-Film Solar Cells," Thin Solid-Films 93, 287 (1982). (DOE/SERI)

C. M. Wu and E. S. Yang, "Phonon-assisted Carrier Transport Across a Grain Boundary," IEEE Trans. Electron Devices, ED-29, 1598 (1982). (DOE/SERI and JSEP)

Q. Hua, E. S. Yang, and H. Izmirliyan, "Diffusivity and Growth Rate of Silicon in Solid-phase Epitaxy," Solid-State Electronics, 25, 1187 (1982). (JSEP and DOE/SERI)

Q. Hua, S. Rosenberg, J. Ye, and E. S. Yang, "Thin Germanium Nitride Films Grown by Thermal Reaction Process," J. Appl. Phys. 53, 8969 (1982). (JSEP and NSF)

V. Daneu, D. J. Ehrlich, and R. M. Osgood, Jr., "Reflectometric Spectroscopy of Adsorbed Molecular Layers," Opt. Lett. 8, 151 (1982). (ARO)

D. J. Ehrlich and R. M. Osgood, Jr., "Laser Microchemistry, Local Nucleation Mechanisms for Photodeposition," Thin Solid Films, 90, 287 (1982). (DARPA and AFOSR)

M. Mandich, P. Beeken, and G. W. Flynn, "Emission Spectra and Relaxation Dynamics of Excited $^{79}Br_2$ in Ar and Kr Matrices," J. Chem. Phys. 77, 702 (1982). (DOE, NSF, and JSEP)

P. Beeken, M. L. Mandich, and G. W. Flynn, "Photochemical Dynamics of $^{79}Br_2$ in Xe Matrices," J. Chem. Phys. 76, 5995 (1982). (DOE, NSF, and JSEP)

T. Allik and G. W. Flynn, "Laser Excited Infrared Fluorescence in Oxalyl Fluoride: Rapid Intermode Equilibration," J. Phys. Chem. 86, 3673 (1982). (DOE, NSF, and JSEP)

Carol Wood, George Flynn, and Ralph E. Weston, Jr., "Evidence for High Rotational Excitation in CO Produced by Collisons with Hot H Atoms Formed in the Photodissociation of HBr," J. Chem. Phys. 77, 4776 (1982). (DOE, NSF, and JSEP)

Y. Wang, E. V. Sitzmann, F. Novak, C. Dupuy, and K. B. Eisenthal, "Reactions of Excited Triplet Diphenylcarbene Studied with Picosecond Lasers," J. of Am. Chem. Soc. 104, 3238 (1982). (AFOSR, NSF and JSEP)

Ying Wang and K. B. Eisenthal, "Picosecond Laser Studies of Ultrafast Processes in Chemistry," J. of Chem. Ed. 59, 482 (1982). (AFOSR, NSF and JSEP)

E. V. Sitzmann, C. Dupuy, Y. Wang, and K. B. Eisenthal, "Studies of the Generation and Energy Relaxation in Chemical Intermediates-Divalent Carbon Molecules and Singlet Oxygen," in Picosecond Phenomena (Proceedings of the Third Topical Meeting on Picosecond Phenomena, Garmisch-Partenkirchen, West Germany), R. Hochstrasser, W. Kaiser and C. V. Shank, eds., Springer-Verlag, New York, New York: 1982. (AFOSR, NSF and JSEP)

Ying Wang and K. B. Eisenthal, "Picosecond Dynamics of Twisted Internal Charge Transfer Phenomena. The Role of the Solvent," J. of Chem. Phys. 77, 12, 6076 (1982). (AFOSR, NSF and JSEP)

Ying Wang, M. C. Crawford, and K. B. Eisenthal, "Picosecond Laser Studies of Intramolecular Excited-State Charge-Transfer Dynamics and Small-Chain Relaxation," J. of Am. Chem. Soc. 104, 5874 (1982). (AFOSR, NSF and JSEP)

P. R. Berman, T. W. Mossberg, and S. R. Hartmann, "Collision Kernels and Laser Spectroscopy," Phys. Rev. A 25, 2550 (1982). (ONR and JSEP)

E. A. Whittaker and S. R. Hartmann, "Hyperfine Structure of the $^1D_2$-$^3H_4$ Levels of Pr^{3+}:LaF_3 with the use of Photon Echo Modulation Spectroscopy," Phys. Rev. B. 26, 3617 (1982). (NSF and JSEP)

K. P. Leung, T.W. Mossberg, and S. R. Hartmann, "Observation and Density Dependence of the Raman Echo in Atomic Thallium Vapor," Opt. Comm. 43, 145 (1982). (JSEP)

K. P. Leung, T. W. Mossberg, and S. R. Hartmann, "Raman Echo in Atomic Thallium Vapor," Opt. Comm. 43, 145 (1982). (JSEP)

B. E. A. Saleh, D. Stoler, and M. C. Teich, "Coherence and Photon Statistics for Optical Fields Generated by Poisson Random Emissions," Phys. Rev. A27, 360 (1983). (JSEP and NSF)

D. Charlton and P. R. Prucnal, "The Mixed Blessings of High-Technology Gifts," Eng. Ed. 73, 346 (1983).

P. R. Prucnal, "Wideband FSK Fiber-Optic Communication Experiment, " J. Opt. Comm. in press. (NSF and JSEP)

P. R. Prucnal and M. C. Teich, "Refractory Effects in Neural Counting Processes with Exponentially Decaying Rates," IEEE Trans. on Sys., Man, and Cybern., in press. (NSF)

W. Hwang, E. Poon, and H. C. Card, "Carrier Recombination at Grain Boundaries and Effective Recombination Velocity," Solid State Electronics, 26, 599 (1983). (JSEP and DOE/SERI)

W. Hwang, E. Poon, E. S. Yang, H. L. Evans, J. S. Song, and R. M. Osgood, Jr., "Electrical Characterization of Grain Boundary Parameters by Laser-Spot Photoconductivity Techniques," 1983 Symposium on VLSI Technology, Systems and Applications, 275-278, 1983. (JSEP and DOE/SERI)

F. Shoucair, W. Hwang, and P. Jain, "Electrical Characteristics of Large Scale Integration (LSI) MOSFETs at Very High Temperatures: Part I - Theory," (submitted for publication).

F. Shoucair, W. Hwang, and P. Jain, "Electrical Characteristics of Large Scale Integration (LSI) MOSFETs at Very High Temperatures: Part II - Experiment," (submitted for publication).

F. Shoucair, W. Hwang, and P. Jain, "Electrical Characteristics of Large Scale Integration (LSI) MOSFETs at Very High Temperatures: Part III - Modeling and Circuit Behavior," (submitted for publication).

E. Poon, E. S. Yang, H. L. Evans, W. Hwang, and R. M. Osgood, Jr., "Determination of Grain Boundary Barrier Height and Interface States by a Focused Laser Beam," Appl. Phys. Lett. 42, 285 (1983). (JSEP and DOE/SERI)

E. S. Yang, E. Poon, H. L. Evans, W. Hwang, J. S. Song, and C. M. Wu, "Electronic Properties of Grain Boundaries in Polycrystalline Silicon," SPIE Symposium Proc. Jan. 1983. (accepted for publication). (JSEP and DOE/SERI)

C. J. Chen and R. M. Osgood, Jr., "Surface Enhancement of Interface Photochemical Reactions," to be published in J. Applied Phys. (JSEP)

R. M. Osgood, D. J. Ehrlich, T. F. Deutsch, D. J. Silversmith, and A. Sanchez, "Direct-Write Laser Fabrication: Customization, Correction, and Repair," to be published in Microelectronics-Structures and Complexity.

A. M. Hawryluk, H. I. Smith, R. M. Osgood, and D. J. Ehrlich, "Deep UV Spatial Period Division Using Excimer Laser Sources," to be published in Opt. Lett. (ARO and JSEP)

C. J. Chen and R. M. Osgood, "Ultraviolet Absorption Spectra of Physisorbed Molecules," Chem. Phys. Lett. Spring 1983.

D. Podlesnik, H. H. Gilgen, R. M. Osgood, A. Sanchez, V. Daneu, "High Resolution Etching of GaAs and CdS Crystals," Published in Laser Diagnostics and Photochemical Processing for Semiconductor Devices, Elsevier, New York, NY. (DARPA and AFOSR)

C. J. Chen and R. M. Osgood, "Spectroscopy and Photoreactions of Organometallic Molecules on Surfaces," Published in Laser Diagnostics and Photochemical Processing for Semiconductor Devices, Elsevier, New York, NY. (ARO)

R. M. Osgood, S. R. J. Brueck, and H. Schlossberg, Laser Diagnostics and Photochemical Processing for Semiconductor Devices, Elsevier, New York, NY. (AFOSR)

C. J. Chen and R. M. Osgood, "Direct Observation of the Local-Field-Enhanced Surface Photochemical Reactions," to be published in Phys. Rev. Letts. (ARO and JSEP)

C. J. Chen and R. M. Osgood, "Surface-Catlyzed Photochemical Readings of Physisorbed Molecules," to be published in Appl. Phys. (ARO and JSEP)

R. M. Osgood, "Excimer Laser Interface Chemistry for Microelectronic Processing," to be published in Excimer Lasers (AIP, NY). (JSEP)

Jack Chu, George W. Flynn, and Ralph E. Weston, Jr., "Spectral Distribution of CO_2 Vibrational States Produced by Collisions with Fast Hydrogen Atoms from Laser Photolysis of HBr," J. Chem. Phys. 78, 2990 (1983). (DOE, NSF, and JSEP)

J. L. Ahl, and G. W. Flynn, "Temperature Dependent Studies of Vibrational Energy Transfer in $S^{18}O_2$ and $S^{18}O_2$ Rare Gas Matrices," to be published in J. Chem. Phys., May 1983. (DOE, NSF, and JSEP)

J. L. Ahl, R. H. Bohn, K. H. Casleton, Y. V. C. Rao, and G. W. Flynn, "A Complete Energy Transfer Map for COF_2," J. Chem. Phys. 78, 3899 1983. (DOE, NSF, and JSEP)

Paul B. Beeken, Eric A. Hanson, and George W. Flynn, "Spectroscopy and Energy Transfer in Electronically Excited States of I_2 Trapped in a Rare Gas Matrix Cage," to be published in J. Chem. Phys., May 1983. (DOE, NSF, and JSEP)

R. Beach, B. Brody, and S. R. Hartmann, "Photon Echoes Made Simple," International Conf. on Photochemistry and Photobiology, Alexandria, Egypt Jan. 1983. (ONR and JSEP)

R. Beach, B. Brody, and S. R. Hartmann, "Photon Echoes in Lithium Vapor using Angled Excitation Beams," to be published in Phys. Rev. Lett. (ONR and JSEP)

R. Beach, B. Brody, and S. R. Hartmann, "Elliptical Billiard-ball Echo Model," Phys. Rev. A 27, 2537 (1983). (ONR and JSEP)

Lectures and Presentations

M. C. Teich, "Neural Counting Statistics in Sensory Communications", Plenary Session Lecture, 35th Annual Conference on Engineering in Medicine and Biology, Philadelphia, Pennsylvania, September 1982.

M. C. Teich, "Neural Coding in Audition and Vision", IBM Thomas J. Watson Research Center, Yorktown Heights, New York, March 1983.

E. S. Yang, "Investigation of Grain Boundary in Poly-Si by a Focused Laser Beam," IBM Research Center, Yorktown Heights, NY, October 1982.

R. M. Osgood, "Laser Microetching of Semiconductors," IBM Watson Research Center, Yorktown, NY, January 1982.

R. M. Osgood, "Microelectronics Processing at Columbia," Columbia-T.J. Watson Lab. Joint Seminar, New York, NY, July 1982.

R. M. Osgood, "Laser Processing," IBM-East Fishkill Facility, East Fishkill, NY, November 1982.

T. Allik, "Relaxation Dynamics in Small Molecules", Center for Naval Analysis, Alexandria, Virginia, April 1982.

T. Allik, "Relaxation Dynamics in Small Molecules", B. F. Goodrich, Inc. Breaksville, Ohio, February 1983.

P. Beeken, "Photophysics of Iodine and Bromine Isolated in Rare Gas Matrices", University of Colorado, Boulder, CO, November 1982.

P. Beeken, "Photophysics of Iodine and Bromine Isolated in Rare Gas Matrices", University of Berkeley, CA, November 1982.

P. Beeken, "Photophysics of Iodine and Bromine Isolated in Rare Gas Matrices", Bringham Young University, Provo, UT, November 1982.

P. Beeken, "Photophysics of Iodine and Bromine Isolated in Rare Gas Matrices", California Institute of Technology, Pasadena, CA, April 1983.

G. W. Flynn, "Photofragmentation and Energy Transfer in Low Pressure Gases and Low Temperature Matrices," Frontiers in Chemistry Series, Case-Western Reserve University, Cleveland, Ohio, April 1982.

G. W. Flynn, "Hot Atom Excitation of Small Molecules in Gases and the Photophysics of Br_2 and I_2 in Rare Gas Matrices," Columbia College Deans's Day, Columbia University, New York, NY, April 1982.

G. W. Flynn, "Photofragmentation and Energy Transfer in Low Pressure Gases and Low Temperature Matrices," Gordon Conference on Atomic and Molecular Interactions, Wolfeboro, NH, July 1982.

G. W. Flynn, "Hot Atom Excitation of Small Molecules in Gases and the Photophysics of Br_2 and I_2 in Rare Gas Matrices," Rowland Institute of Science, Cambridge, MA, August 1982.

G. W. Flynn, "Photofragmentation and Energy Transfer in Low Pressure Gases and Low Temperature Matrices," William Pyle Phillips Lecturer, Haverford College, Haverford, PA, October 1982.

G. W. Flynn, "Photofragmentation and Energy Transfer in Low Pressure Gases and Low Temperature Matrices," Am. Chem. Soc., Brooklyn College, Brooklyn, NY, October 1982.

G. W. Flynn, "Hot Atom Excitation of Small Molecules in Gases and the Photophysics of Br_2 and I_2 in Rare Gas Matrices," Brandeis University, Waltham, MA, February 1983.

G. W. Flynn, "Hot Atom Excitation of Small Molecules in Gases and the Photophysics of Br_2 and I_2 in Rare Gas Matrices," Indiana University, Bloomington, Indiana, March 1983.

G. W. Flynn, "Hot Atom Excitation of Small Molecules in Gases and the Photophysics of Br_2 and I_2 in Rare Gas Matrices," Yale University, New Haven, Connecticut, March 1983.

G. W. Flynn, "Photofragmentation and Energy Transfer in Low Pressure Gases and Low Temperature Matrices," Nobel Laureate Signature Award Symposium, Am. Chem. Soc. Meeting, Seattle, Washington, March 1983.

K. Eisenthal, "Picosecond Studies of Electron Transfer and Photofragmentation in Molecules", University of Texas at Austin, Austin, Texas, November 1982.

K. Eisenthal, "Picosecond Laser Studies in Chemistry", Western Spectroscopy Association, 29th Annual Conference, Asilomar, California, January 1982.

K. Eisenthal, "Picosecond Chemistry", IBM Colloquium, IBM, Yorktown Heights, NY, April 1982.

K. Eisenthal, "Studies of Ultra Fast Phenomena in Chemistry with Picosecond Lasers", Wesleyan University, Middletown, CT, April 1982.

K. Eisenthal, "Picosecond Laser Studies of Intramolecular Charge-Transfer Phenomena", Gordon Conference on Electron Donor-Acceptor Interactions, Wolfeboro, New Hampshire, August 1982.

K. Eisenthal, "Studies of the Generation and Energy Relaxation in Chemical Intermediates -- Divalent Carbon Molecules and Singlet Oxygen", Third Topical Meeting on Picosecond Phenomena, Garmisch-Partenkirchen, West Germany, June 1982.

K. Eisenthal, "Picosecond Chemistry", Joint Stanford-Berkeley Colloquium, Palo Alto, CA, October 1982.

K. Eisenthal, "Excited State Proton Transfer", University of Paris, Paris, France, June 1982.

K. Eisenthal, "Twisted Internal Charge Transfer Phenomena", University of Paris, Paris, France, June 1982.

K. Eisenthal, "Electron Solvation", University of Paris, Paris, France, June 1982.

K. Eisenthal, "Chemical Intermediates", University of Paris, Paris, France, June 1982.

S. R. Hartmann, "Elliptical Billiard Ball Theory," New York University, New York, NY, November 1982.

Resonance Seminars

Meetings are held periodically at Columbia University, New York, New York during the academic year and are open to all members of the New York scientific community. Guest speakers are invited to discuss work in the general area of the research in the Columbia Radiation Laboratory.

Paul Beeken, Columbia University, "Photophysics of Iodine Isolated in a Matrix," August 5, 1982.

Christos Flytzanis, "Nonlinear Optical Properties of Conjugated Polymer Crystals in their Topochemical Polymerization," September 17, 1982.

Robert Hellworth, University of Southern California, "Optical Beam Phase Conjugation," November 22, 1982.

Daniel Grischkowsky, IBM Research Laboratory, "Nonlinear Pulse Propagation in Optical Fibers-Generation of Femtosecond Laser Pulses," March 11, 1983.

Phaedon Avouris, IBM, Thomas J. Watson Research Center, "Electron Scattering Spectroscopy of Molecular and Atomic Adsorbates on Metal Surfaces," April 6, 1983.*

Emil Wolf, University of Rochester, "Wavefront Correction by Phase Conjugation," April 8, 1983.

Chung Tang, Cornell University, "Femtosecond Optics and Time Resolved Studies of Molecular Rotation in Liquids," April 14, 1983.

Michael Salour, MIT, "Picosecond Optics with Excited Semiconductor Crystals," April 27, 1983.*

Thomas Deutch, MIT-Lincoln Laboratory, "Excimer Lasers for Semiconductor Processing," May 4, 1983.*

*Seminars which were part of a special series entitled "CRL Series on Pure and Applied Science".

I. QUANTUM DETECTION AND SENSING OF RADIATION

A. NOISE IN THE GENERATION, PARTITION, AND DETECTION OF LIGHT*

(B.E.A. Saleh, D. Stoler, P.R. Prucnal, K. Matsuo, M.C. Teich)
(JSEP work unit 1, 1982-1985)
(Principal Investigator: M. C. Teich (212) 280-3117)

1. Noise in the generation of light

Since 1956, when Hanbury-Brown and Twiss observed correlation in the fluctuations of two photoelectric currents induced by thermal light[1] and by starlight,[2] the coherence properties of optical fields have been studied intensively, from both a theoretical and an experimental point of view.[3]-[6] The usual kinds of light that have been investigated are chaotic (thermal) light, coherent (laser) light, and mixtures of both.[4]-[6] More recently, the fluctuation properties of antibunched light have received considerable attention.[7]-[9]

Fluctuations in the overall number of active radiators in a source of light can be an important determinant of its coherence properties, as pointed out by Forrester,[10a] and discussed by Loudon.[10b] This effect is of central importance for scattered light, where the number of active radiators is a stochastic quantity.[11] Such fluctuations also play a role in the generation of antibunched resonance fluorescence, as discussed by Carmichael et al.,[12],[13] Jakeman et al.,[14] and Mandel et al.[9],[15]

We have examined the coherence and fluctuation properties of optical fields when the times of emission of the individual radiators are describable by a homogeneous Poisson process.[16] In particular, we obtained the first- and second-order field correlation functions for such light in the framework of semiclassical theory and quantum electrodynamics. The mean and variance of the photon count were also obtained. In certain limits, expressions for the

photon-counting distributions were derived. We considered in detail a number of special cases, including individual atomic emissions modeled by coherent, chaotic, and number-state descriptions.

Our model is expected to play an important role in a number of diverse applications. Consider, for example, the light emitted when a stream of energetic electrons impinges on a betaluminescent material. If the times at which the electrons strike the material occur in accordance with the Poisson process, this randomness will be imparted to the emitted optical field. This effect will be particularly evident when the electron current is low (its fluctuations are then the largest). These fluctuations are in addition to those intrinsic to the optical field.[12]

In previous work,[17] we presented a semiclassical analysis of phenomena similar to those described above, under the assumption that the irradiance could be modeled as shot noise. We have now provided a more complete analysis of this class of processes when the optical field, rather than the irradiance, is modeled as a shot-noise process. Thus, intrinsic field as well as intensity fluctuations are incorporated into our model.

Our results indicate[16] that the underlying Poisson randomness of the emission times imparts additional fluctuations to the radiated field. When the optical field at a given time is a result of contributions from a large average number of radiators, the light becomes chaotic, whether the individual emissions are themselves coherent or chaotic. This is a consequence of the central limit theorem. When the average number of radiators contributing to the optical field at a certain time is not large, the deviations from chaotic behavior have been calculated. These deviations are characterized by an increase in the normalized second-order correlation function, which corresponds to an increase in the variance of the number of photons counted in

a fixed time interval, and to additional photon bunching.

The excess variance is proportional to the mean number of photons, indicating that these excess fluctuations are particle-like in nature. Furthermore, we have shown that the corresponding excess fluctuations of the number of photons in a given time interval are enhanced by an increase of the time interval. This is unlike the excess noise due to wave fluctuations, which are known to be averaged by an increase in the counting time.

It has also been shown that, when the lifetime of the individual emissions is so short, or when their rate is so low, that overlap is unlikely, no interemission interference takes place, and the light intensity is described by a shot-noise stochastic process. The photons are then described by the shot-noise-driven doubly stochastic Poisson point process, which also exhibits excess bunching of a particle-like nature. If counted over a counting time longer than the lifetime of a single emission, the excess fluctuations due to random emission times exhibit themselves fully. In this case, when each single emission is coherent, and when it is chaotic, the photons are described by the Neyman type-A and the generalized Polya-Aeppli counting distributions, respectively.

We have also formulated a general quantum-electrodynamic model for an optical field generated by a sequence of emissions at random times.[16] This enabled us to examine the effect of random emission times in cases when the emissions cannot be described classically. For example, when the individual emissions are in the highly antibunched Fock state, we find that the randomness of the emission times results in particle-like bunching which quickly overpowers the inherent quantum-mechanical antibunching, as the rate of emissions increases and the emissions overlap. In the limit of a large number of overlapping emissions, the second-order correlation function

eventually exhibits the usual (bunched) chaotic behavior. The important role played by the randomness in the number of radiators for the observation of antibunched light in resonance fluorescence is well recognized.[14]

While the analysis we carried out has been limited to the more common statistical models which individual emissions may satisfy (coherent, chaotic, coherent-chaotic mixture), other statistical models may be analyzed through the use of the same methods.

Spatial effects have also not yet been considered. These effects may be included by assigning positions to the radiators, and by making the radiated field a function of position as well as time. By assuming that the positions of the radiators in the source volume, and their emission times, are random points in four-dimensional time-position space, in accordance with a 4D Poisson point process, we may proceed to determine the temporal and spatial coherence properties of the radiated field through generalizations of the methods we employed.

2. Noise in the partition of light

Point processes often undergo random deletion or partition. An obvious example of importance in optics is the usual case of photodetection, in which the quantum efficiency is invariably less than unity. Another case in point is optical absorption. It has long been known that the Poisson process, which is probably the most ubiquitous of all point processes, remains Poisson under the action of such Bernoulli selection.[18]

We have explicitly considered the effects of random deletion on the photon-counting statistics for a number of cases that appear repeatedly in optics.[19] The doubly stochastic Poisson point process (DSPP),[20] which always gives rise to a super-Poissonian counting distribution (count variance

greater than count mean)[21] has been treated in detail. The results for thermal light[22] and multiplied-Poisson light[17] are special examples. Since antibunched light[3],[4],[23],[24] appears to be playing an ever-increasingly important role in optics, we also treated several cases in which the count variance is less than the count mean. Finally we studied the combined effects of random deletion and additive independent Poisson-noise counts.

Consider a random number n of events, and let each event be multiplied by a discrete multiplication or reduction factor $x_k = 0,1,2,\ldots$ for $k = 1,2,\ldots,n$. Then the total number of multiplied events is

$$m = \sum_{k=1}^{n} x_k. \tag{1}$$

If the multiplication factors $\{x_k\}$ are statistically independent, then the random variable m has a moment-generating function (mgf) $Q_m(s) = \langle \exp(-sm) \rangle$, which is related to the mgf's of n and x by[18]

$$Q_m(s) = Q_n(-\ln Q_x(s)). \tag{2}$$

The means and variances are related by

$$\langle m \rangle = \langle n \rangle \langle x \rangle \tag{3}$$

and

$$\mathrm{Var}(m) = \langle x \rangle^2 \mathrm{Var}(n) + \langle n \rangle \mathrm{Var}(x). \tag{4}$$

Equation (4) is known as the Burgess variance theorem.[25],[26] When the multiplication factors $\{x_k\}$ are Bernoulli distributed, i.e., $x_k = \{1,0\}$ with probabilities $\{\eta, 1 - \eta\}$,

$$Q_x(s) = 1 - \eta + \eta e^{-s},$$
$$\langle x \rangle = \eta, \qquad \mathrm{Var}(x) = \eta(1 - \eta). \tag{5}$$

Substituting Eqs. (5) into Eqs. (2)-(4), we obtain

$$Q_m(s) = Q_n(-\ln(1 - \eta + \eta e^{-s})),$$
$$\langle m \rangle = \eta \langle n \rangle,$$
$$\mathrm{Var}(m) = \eta^2 \mathrm{Var}(n) + \eta(1 - \eta)\langle n \rangle. \tag{6}$$

Equations (6) relate the properties of the number of counts after Bernoulli deletion to those before Bernoulli deletion, in terms of the deletion parameter η.

By repeated use of Eqs. (6), it can be easily shown that successive random deletions, with deletion parameters $\eta_1, \eta_2, \ldots$, are equivalent to a single process of random deletion with parameter $\eta = \eta_1 \eta_2 \ldots$

We consider the effect of random deletion on a representative sub-Poissonian distribution.[19] Consider the counting distribution

$$p(n) = \begin{cases} 1, & n = N \\ 0, & n \neq N \end{cases} \tag{7}$$

associated with the number state (Fock state) $|N\rangle$. This corresponds to

$$Q_n(s) = \exp(-sN),$$

$$\langle n \rangle = N, \quad \mathrm{Var}(n) = 0. \tag{8}$$

Using Eqs. (6), we obtain

$$\begin{aligned} Q_m(s) &= (1 - \eta + \eta e^{-s})^N, \\ \langle m \rangle &= \eta N, \\ \mathrm{Var}(m) &= \eta(1 - \eta)N = \langle m \rangle (1 - \eta), \end{aligned} \tag{9}$$

so that the randomly deleted number-state counting distribution is binomial.[6] It is clear from Eqs. (8) and (9) that both the number state and the binomial distributions are sub-Poissonian.

Note that, if a binomial distribution of parameters (η, N) is further Bernoulli selected with a deletion paramter η', the resultant distribution remains binomial, with paramters $(\eta\eta', N)$.

We have also shown[19] that neither additive independent Poisson noise events, nor Bernoulli random deletion, alters the sub- or super-Poissonian nature of the light. Indeed, both effects are quite similar; increasing the amount of either drives the counting distribution toward Poisson. A moment's thought provides the reason: The deletion serves to reduce correlated (or anticorrelated) event occurrences, thereby bringing the distributions close to the zero-memory Poisson distribution.

The result is of particular importance in the current effort to produce sub-Poissonian light. It shows that although loss (e.g., low quantum efficiency) and additive Poisson noise serve to reduce the observability of the sub-Poissonian character of the light, they do not destroy it.

3. Noise in the detection of light

Optical detectors often operate by random multiplication to increase the responsivity. Well known examples are the photomultiplier tube and the avalanche photodiode. In the process of multiplying the signal, the detectors introduce noise. The purpose of the study described here[27] is to investigate this noise.

Multiplication, reduction, and branching processes have been examined in a broad variety of contexts.[28]-[33] Applications range from astrophysics to biological information transmission. In the majority of mathematical treatments, the multiplication or branching is treated as an instantaneous effect. However, in many physical systems, a random time delay (or spatial dispersion) is inherent in the multiplication process. We have carried out an analysis of a cascade of Poisson multiplications that includes such time effects.[27] Our results reduce to previously known descriptions, in the limit of instantaneous multiplication.

We developed the statistics of a point process generated by a cascade of independent Poisson processes, and found the moment generating function, as well as the counting and time statistics when dynamics are included. Both the stationary and nonstationary cases were considered. A simple expression for the variance-to-mean ratio at the mth stage has been obtained. We have carried out a parametric study of the counting distributions, by employing the DEC PDP 11/60 and IBM 4341 computers.

In some of the aforementioned applications of cascaded Poisson processes, a statistically independent additive Poisson point process may also be present, representing for example, broadband background light and/or thermionic emission in a photomultiplier tube. The counting statistics for the superposition process can be simply determined by the rise of numerical

discrete convolution. We are in the process of considering related branching processes, in which all initiating events are included in the final point process. In the future, this work will be applied to the noise properties of real detection devices.

*This research was also supported by the National Science Foundation under Grant NSF-ENG78-26498.

(1) R. Hanbury Brown and R. Q. Twiss, Nature (London) 177, 27 (1956).

(2) R. Hanbury Brown and R. Q. Twiss, Nature (London) 178, 1046 (1956).

(3) R. J. Glauber, Phys. Rev. 130, 2529 (1963).

(4) R. J. Glauber, Phys. Rev. 131, 2766 (1963)

(5) L. Mandel and E. Wolf, Rev. Mod. Phys. 37, 231 (1965).

(6) J. Perina, Coherence of Light (Van Nostrand-Reinhold, London, 1972).

(7) D. Stoler, Phys. Rev. Lett. 33, 1397 (1974).

(8) H. J. Kimble, M. Dagenais, and L. Mandel, Phys. Rev. lett. 39, 691 (1977).

(9) M. Dagenais and L. Mandel, Phys. Rev. 18, 2217 (1978).

(10) (a) A. T. Forrester, J. Opt. Soc. Am. 62, 654 (1972); (b) R. L. Loudon, Rep. Prog. Phys. 43, 913 (1980).

(11) D. W. Schaefer and P. N. Pusey, Phys. Rev. Lett. 29, 843 (1972).

(12) H. J. Carmichael and D. F. Walls, J. Phys. B 9, L43 (1976); 9, 1199 (1976).

(13) H. J. Carmichael, P. Drummond, P. Meystre, and D. F. Walls, J. Phys. A 11, L121 (1978).

(14) E. Jakeman, E. R. Pike, P. N. Pusey, and J. M. Vaughan, J. Phys. A 10. L257 (1977).

(15) H. J. Kimble, M. Dagenais, and L. Mandel, Phys. Rev. 18, 201 (1978).

(16) B. E. A. Saleh, D. Stoler, and M. C. Teich, Phys. Rev. A 27, 360 (1983).

(17) M. C. Teich and B. E. A. Saleh, Phys. Rev. A 24, 1651 (1981); B. E. A. Saleh and M. C. Teich, Proc. IEEE 70, 229 (1982).

(18) E. Parzen, Stochastic Processes (Holden-Day, San Francisco, 1962).

(19) M. C. Teich and B. E. A. Saleh, Opt. Lett. 7, 365 (1982).

(20) D. R. Cox, J. R. Stat. Soc. B17, 129 (1955).

(21) B. E. A. Saleh, Photoelectron Statistics (Springer-Verlag, New York, 1978).

(22) L. Mandel, Proc. Phys. Soc. 74, 233 (1959).

(23) H. Paul, Rev. Mod. Physics. 54, 1061 (1982)

(24) L. Mandel, Opt. Lett. 4, 205 (1979).

(25) R. E. Burgess, Discuss. Faraday Soc. 28, 151 (1959).

(26) L. Mandel, Brit. J. Appl. Phys. 10, 233 (1959).

(27) K. Matsuo, B. E. A. Saleh, and M. C. Teich, J. Math. Phys. 23, 2353 (1982).

(28) T. E. Harris, The Theory of Branching Processes (Springer-Verlag, New York, 1963).

(29) S. Karlin, A First Course in Stochastic Processes (Academic, New York, 1966).

(30) D. R. Cox and P. A. W. Lewis, The Statistical Analysis of Series of Events (Methuen, London, 1966).

(31) W. Feller, An Introduction to Probability Theory and its Applications (Wiley, New York, 1968).

(32) R. A. Howard, Dynamic Probabilistic Systems (Wiley, New York, 1971).

(33) K. M. van Vliet and L. M. Rucker, Physica 95A, 117 (1979).

B. SIGNAL-DEPENDENT NOISE*

(P. R. Prucnal, M. C. Teich)
(JSEP work units 1 and 4, 1982-1985)
(Principal Investigators: M. C. Teich (212) 280-3117,
E. S. Yang (212) 280-3120,
W. Hwang (212) 280-3115)

Signal-dependent noise is manifested in many physical processes and often represents a fundamental limitation to the minimum uncertainty in the magnitude of a physical quantity. When this quantity is the number of photons incident on a photodetector, the uncertainty in the number of photons is proportional to the total energy received. This signal-dependent photon noise places a limit on the minimum light energy that can be received with a given reliability. When the quantity of interest is the number of impurities implanted in a semiconductor material, the uncertainty in the number of impurities is proportional to their average number. This signal-dependent "impurity-noise" places a limit, in certain circumstances, on the minimum device dimensions in a VLSI system that will function with a given reliability.

Substantial progress has been made in understanding the role of signal-dependent noise in each of these situations: the performance of source modulation formats in fiber optic communications; the performance of VLSI systems containing ion-implanted bipolar transistors. These results are summarized below and reported in detail in the literature.[1],[2]

1. Effect of signal-dependent noise on VLSI yield

An expression was derived for the doubly-stochastic distribution of the number of impurities in the base region of a bipolar transistor; the distribution results from signal-dependent uncertainty in ion implantation parameters. Expressions were derived for device yield, and VLSI (very large scale integration) chip yield with an N-bit parity check. These derivations

can be extended to other devices in a straightforward manner.

The following notation was used:

L	emitter dimension, defined as the fundamental dimension in the technology
$C_{d1}(x)$	emitter donor impurity concentration
A_1, r_1, s_1	amplitude, range, and straggle of $C_{d1}(x)$
$C_{a2}(x)$	base acceptor impurity concentration
A_2, r_2, s_2	amplitude, range, and straggle of $C_{a2}(x)$
A_3	amplitude of collector donor impurity concentration
G_b, G_e	base, emitter Gummel number
k	scaling factor
n	number of base impurities
μ_n	average number of base impurities
β	current gain
D_{nb}, D_{pe}	diffusion coefficient; electrons in base, holes in emitter
λ	tolerable fractional range of variation of β about $E\{\beta\}$
N_{chip}	number of devices per chip
R	number of s-dependent devices in a given region of chip
N	number of bits per word
$Y_{1,D}$	device yield
$Y_{chip,D}$	chip yield, no parity check
$Y_{D;N}$	yield of N-bit word with parity check
$Y_{chip,D;N}$	chip yield, N-bit parity check
binm (), poim ()	pmf of binomial and Poisson distributions

The following assumptions were made:

1. The device structure is typical of recent 1 μm bipolar technology. See Fig. 1, for details.

2. The collector region has uniform (substrate) doping concentration. In a real device this doping is not uniform but increases proceeding deeper into the substrate (away from the base) due to the presence of a buried N^+ layer. The collector doping, is, however, constant over the region of interest here.

3. The base region is formed by implanting acceptor (boron) impurities. The emitter region is formed by implanting donor (phosphorous or arsenic) impurities.

4. The impurity concentrations are Gaussian in shape. The effects of channeling on the distribution (which modify the Gaussian shape) are minimized by implanting off-axis of the crystal.

5. The doping is uniform in the plane parallel to the silicon surface.

6. For the narrow base regions considered, the base transport factor is unity.

7. $\beta \gg 1$.

8. The n is a (signal-dependent) Poisson r.v., provided the impurities are s-independent, that is, the presence of an impurity does not influence the presence of an adjacent impurity.

9. Any of the parameters r_1, r_2, s_1, s_2 may be stochastic. The Gaussian distribution is used as an example, although another distribution, such as the uniform, could be used as easily. For a 1 μm structure $E\{r_1\} = 0$, $E\{r_2\} = 0.05$ μm $E\{s_1\} = E\{s_2\} = 0.02$ μm, $A_1 = 10^{20}cm^{-3}$, $A_2 = 10^{18}cm^{-3}$, $A_3 = 10^{16}cm^{-3}$.

Calculations have been performed using specific parameters, which have led to the following observations: (see Figs. 1 to 9 for details)

1. The doubly stochastic effect is most sensitive to uncertainty in the straggle (standard deviation) of the emitter impurity distribution.

2. Uncertainty of the order of 5% in an implantation parameter causes substantial broadening of the distribution of impurities, for the case

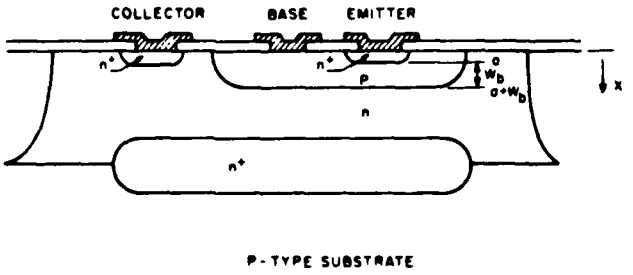

Fig. 1 Ion-implanted bipolar transistor structure.

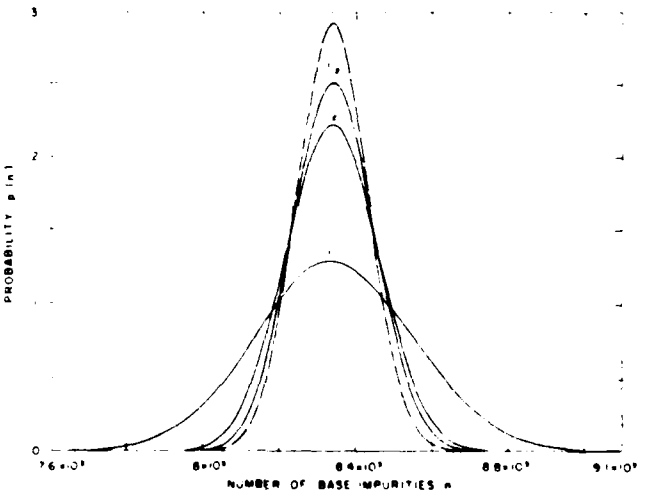

Fig. 2 Dashed curve represents singly-stochastic distribution of base impurities for emitter dimension L = 1. Solid curve represents doubly-stochastic distribution of base impurities corresponding to Gaussian fluctuations in device parameter. Cases r_2, S_1, and S_2 are shown. Three standard deviations of device parameter equals 1% of mean. Here $E\{r_1\} = 0$ μm, $E\{r_2\} = 0.05$ μm, $E\{S_1\} = E\{S_2\} = 0.02$ μm, $A_1 = 10^8/(\mu m)^3$, $A_2 = 10^6/(\mu m)^3$, $A_3 = 10^4/(\mu m)^3$.

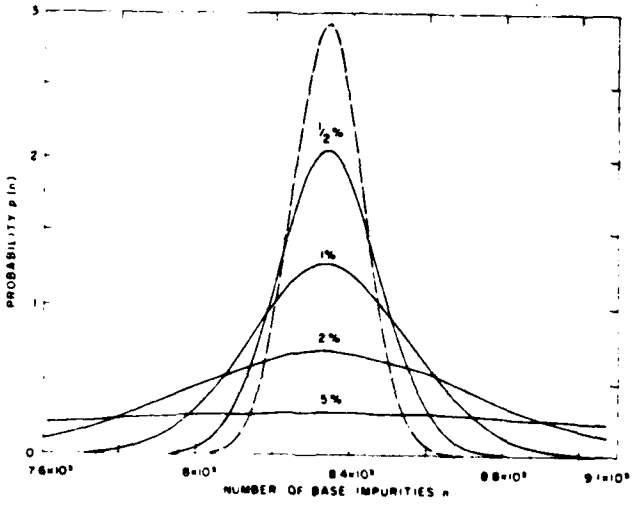

Fig. 3 Same as Fig. 2, except for fluctuations in S_1 only. Three standard deviations of S_1 equals 1/2%, 1%, 2%, 5% of mean.

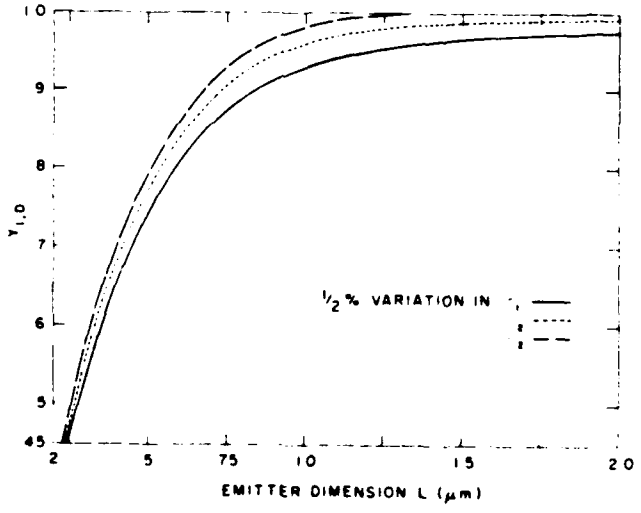

Fig. 4 Device yield versus emitter dimension, where tolerable range of variation of β is $E\{\beta\} \pm 2.4\%$. Here $E\{r_1\} = 0$ μm, $E\{r_2\} = 0.05$ L μm. $E\{S_1\} = E\{S_2\} = 0.2L$ μm, $A_1 = 10^8/[L^2(\mu m)^3]$, $A_2 = 10^6/[L^2(\mu m)^3]$, $A_3 = 10^4/[L^2(\mu m)^3]$. Solid, dotted, and dashed curves correspond to fluctuations in S_1, r_2 and S_2 respectively. Three standard deviations of device parameter equals 1/2% of mean.

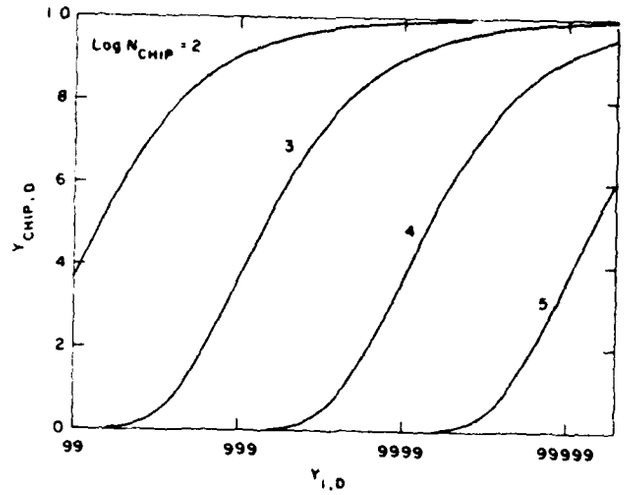

Fig. 5 Chip yield versus device yield for N_{chip} devices and L = 1 μm. Cases $N_{chip} = 10^2, 10^3, 10^4, 10^5$ shown.

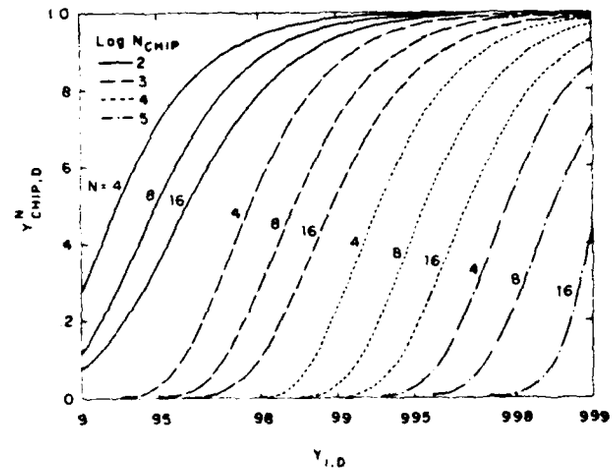

Fig. 6 Same as Fig. 5, except N-bit parity check is introduced. Solid dashed, dotted and dot-dashed curves correspond to $N_{chip} = 10^2, 10^3, 10^4, 10^5$, respectively for N = 4,8,16.

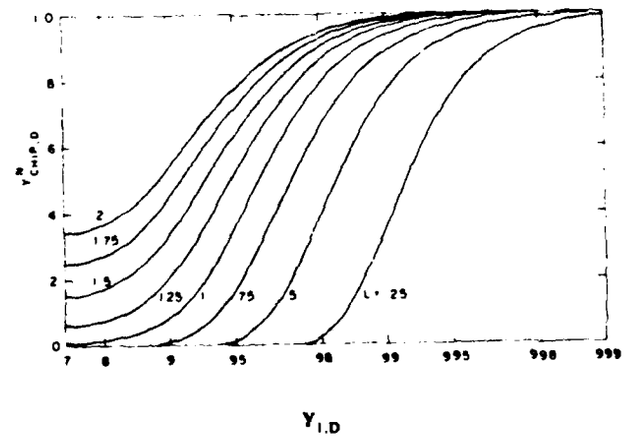

Fig. 7 Chip yield versus device yield for L = 0.25, 0.5, ..., 2. N = 16 and number of devices is $100/L^2$.

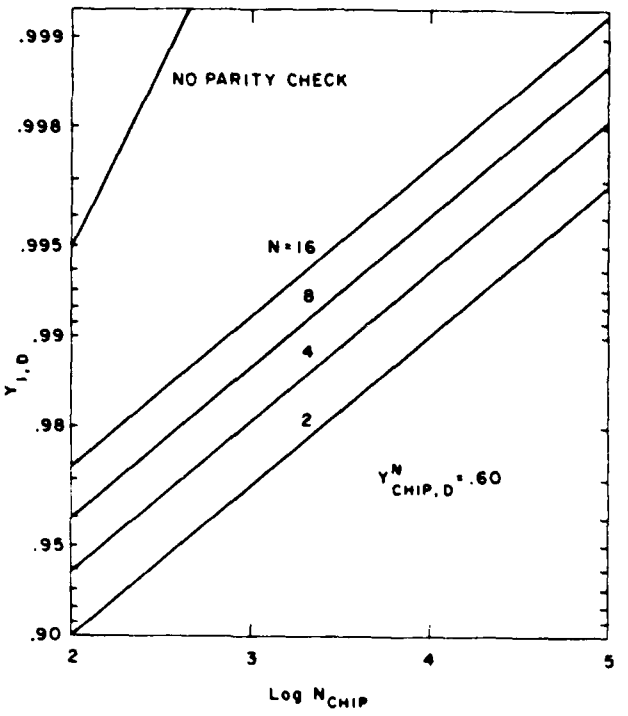

Fig. 8 Minimum device yield necessary for chip yield greater than 0.6 versus log N_{chip}, for L = 1. Cases of no parity check and N = 2,4,8,16.

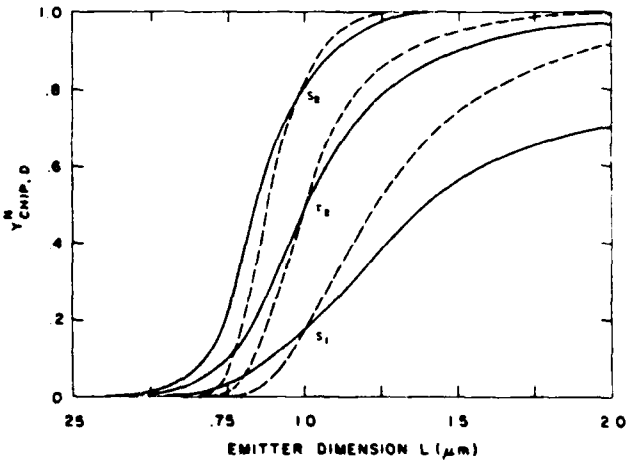

Fig. 9 Chip yield versus emitter dimension for 16-bit parity check. Here $E\{r_1\} = 0$, $E\{r_2\} = 0.5L$ μm, $E\{S_1\} = E\{S_2\} = 0.02L$ μm, $A_1 = 10^8/[L^2(\mu m)^3]$, $A_2 = 10^6/[L^2(\mu m)^3]$, and $A_3 = 10^4/[L^2(\mu m)^3]$. Cases S_1, r_2, and S_2 shown. Three standard deviations of device parameter equals 1/2% of mean. Tolerable range of variation of β is $E\{\beta\} \pm 2.4\%$. Number of devices equals 100 for solid curves and $100/L^2$ for dashed curves.

considered.

3. Device yield decreases rapidly for dimensions less than a well-defined threshold ($\tilde{\sim}$ 0.75 μm for the case considered).

4. Chip yield, without a parity check, exhibits a threshold effect at device yield = $1-1/N_{chip}$. (N_{chip} = number of devices per chip.) The device yield must exceed this threshold to produce large chip yields.

5. The use of a parity check reduces the device yield threshold to $1-10/N_{chip}$. Use of fewer bits per parity check reduces the threshold further.

6. For the example considered, the minimum device dimensions for large chip yields is of the order of 1 to 1.5 μm, using a 16-bit parity check.

The minimum device size for reliable system performance for other cases will depend upon specific device parameters. However, it is apparent that chip yield is extremely sensitive to individual device yield, and that it decreases with increasing uncertainty in device parameters, smaller device dimensions, greater number of devices per chip, larger number of bits per parity check, and with smaller allowed ranges of tolerable device behavior.

2. Signal-dependent noise in frequency-shift keyed fiber communication

An optical fiber communication system was implemented using frequency-shift keying (FSK) and amplitude-shift keying (ASK). The effect of photon noise on performance was studied theoretically and experimentally. The bit-error rates of the FSK and ASK systems were calculated as follows. The mean voltage at the avalanche photodiode receiver output is

$$\langle v_{ij} \rangle = K_1 \langle G \rangle E_r / hf \qquad (1)$$

where v_{ij} is the voltage in channel i given that bit j was transmitted, K_1 is

an irrelevant constant, hf is the photon energy, and E_r is the received pulse energy, taking into account the extinction ratios of the lasers, the cross-talk, and all optical losses. The variance of the voltage is

$$\text{var } v_{ij} = K_1 \langle G \rangle \langle v_{ij} \rangle F + K_1^2 z^2 \tag{2}$$

where

$$F = k\langle G \rangle + (1-k)(2-1/\langle G \rangle) \tag{3}$$

is the APD excess noise factor, and

$$Z = (NEP)B^{1/2}\langle G \rangle T/hf \tag{4}$$

is the preamplifier noise parameter at room temperature, with T the bit interval and B the amplifier bandwidth.

Using a Gaussian approximation for the probability density function of the voltage, the FSK bit-error rate is

$$\begin{aligned} BERFSK = {} & (1/4)\text{erfc}[2^{-1/2}(\langle v_{11} \rangle - \langle v_{01} \rangle)/(\text{var } v_{11} + \text{var } v_{01})^{1/2}] \\ & + (1/4)\text{erfc}[2^{-1/2}(\langle v_{00} \rangle - \langle v_{10} \rangle)/(\text{var } v_{00} + \text{var } v_{10})^{1/2}]. \end{aligned} \tag{5}$$

The ASK bit-error rate is

$$\begin{aligned} BERASK = {} & (1/4)\text{erfc}[2^{-1/2}(\langle v_{11} \rangle - \theta)/(\text{var } v_{11})^{1/2}] \\ & + (1/4)\text{erfc}[2^{-1/2}(\theta - \langle v_{10} \rangle)/(\text{var } v_{10})^{1/2}] \end{aligned} \tag{6}$$

where θ is the threshold.

The bit-error rate for FSK and ASK corresponding to theory (curves) and data (dots) is shown in Fig. 10. Both the theory and the data in Fig. 10 show

approximately a 3 dB improvement of FSK over ASK. The advantage of FSK increases slightly as the optical power increases. This effect can be explained by the performance of FSK relative to ASK, as the contribution of signal-dependent noise increases.

Indeed, the theoretical curves in Fig. 10 reflect the contributions of both shot noise and thermal noise. For the parameters of this system, the shot and thermal noise powers in Eq. (2) are equal when the received optical power is 1.2 nW. Thus, the shot noise is comparable to the thermal noise at the right boundary of Fig. 10 and dominates the thermal noise at the left boundary.

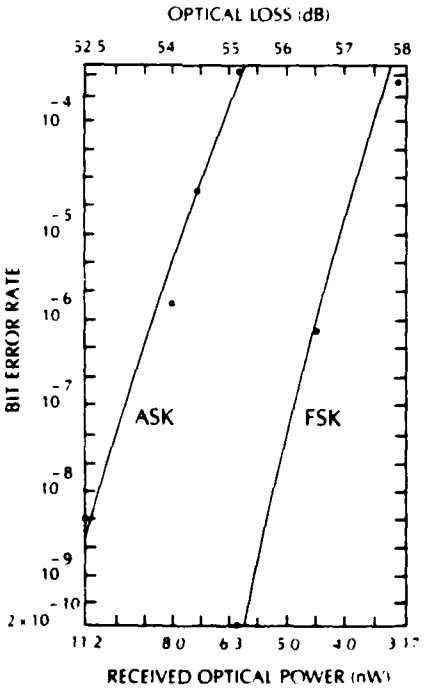

Figure 10

That the advantage of FSK increases as the shot noise increases, is seen as follows. Since the FSK receiver subtracts the output of two detectors, both the signal energy and thermal noise power are doubled, compared to ASK. The advantage of FSK in the thermal noise dominated regime is then 1.5 dB. On the other hand, the shot noise in the FSK receiver is the same as for a transmitted "1" in the ASK receiver. The advantage of FSK in the shot noise dominated regime is then 6 dB, for a transmitted "1". For a transmitted "0", ASK has no shot noise, and FSK may or may not have an advantage, depending on the relative magnitudes of the shot and thermal noise powers. It is pointed out that the SNR-type arguments above are not necessarily sufficient to describe system performance, and are used here only to give an intuitive understanding of the results.

It is apparent from the above considerations that the advantage of FSK may be greater in the shot-noise dominated regime. In fact, other types of noise, with stronger signal dependence than shot noise, could theoretically result in a greater advantage for FSK. This is illustrated by considering a general class of signal-dependent noise in which the variance is related to the mean by the power law

$$\text{var } v = c\langle v\rangle^{2p} \tag{7}$$

where c is a nonnegative constant and $0<p<1$. Equating the SNRs for a transmitted "1" for FSK and ASK and simplifying yields

$$2\langle v_{FSK}\rangle^{1-p} = \langle v_{ASK}\rangle^{1-p}. \tag{8}$$

The decrease in minimum optical power required by FSK for the same performance

The decrease in minimum optical power required by FSK for the same performance as ASK is

$$D = 3/(1-p) \text{ dB}. \tag{9}$$

When $p = 1/2$, the variance is proportional to the mean, as for shot noise, and, $D = 6$ dB, in agreement with the above discussion. As p increases in the region $0<p<1$, D also increases. Therefore, greater signal dependence increases the advantage of FSK. This, and other advantages of FSK, such as immunity to threshold variations, are discussed in reference (2).

*This research was also supported by the National Science Foundation under Grant NSF-ECS80-06881.

(1) P. R. Prucnal, "Wideband FSK fiber-optic communication experiment," J. Opt. Comm., issue #2, in press. (1983).

(2) P. R. Prucnal and H. C. Card, "Effects on VLSI yield of doubly-stochastic impurity distributions," IEEE Trans. Reliability, R-31, 185 (1982).

II. PHYSICAL AND PHOTOCHEMICAL PROPERTIES OF ELECTRONICS MATERIALS

A. CARRIER RECOMBINATION AT GRAIN BOUNDARIES AND THE EFFECTIVE RECOMBINATION VELOCITY*

(W. Hwang, E. Poon, H. C. Card+)
(JSEP work unit 4, 1982-1985)
(Principal Investigators: W. Hwang (212) 280-3115
E. Yang (212) 280-3120)

In problems involving the recombination of excess minority carriers at semiconductor interfaces such as grain boundaries and oxidized surfaces, there often arises a confusion between the actual minority carrier recombination velocity at the interface itself and the effective collection velocity for minority carriers at the edge of the adjacent space charge region. In modelling device behavior it is usually convenient to consider the latter mechanism, since under these conditions, the carrier removal can be considered in terms of an 'effective' recombination velocity at the boundary of a field-free region. One specific example involves the disappearance of the photogenerated minority carriers at the grain boundary in photovoltaic solar cells. A phenomenon of some practical importance in the design and simulation of solar cell devices is the appropriate description of the dependence of the effective recombination velocity upon the photogeneration rate, or optical illumination intensity. It is customary in such cases to associate a constant recombination velocity with the boundary of the field-free region. Recent experimental studies[1,2] indicate, however, that this velocity is not a constant, but rather shows a substantial dependence upon the photogeneration rate, or in other words, on the recombination current density.

A specific example will clarify the distinction between the true interface recombination velocity and the effective recombination velocity, which in many cases is a more convenient variable.[3]

At the grain boundary (GB) interface, the recombination current density is as described in a previous paper.[4] The interface recombination velocity, S, at the GB is defined in terms of the recombination current density, J_R, and the excess minority carrier concentration at the GB (x=0) for n-type silicon as

$$S(0) = J_R/q[p(0)-p_0] \tag{1}$$

where p_0 is the equilibrium concentration of the minority carriers at the GB. For device calculations, the "effective" recombination velocity at the edge of the depletion region, S(w), is given by [5]

$$S(w) = J_R/2q[p(w) - p_{no}] \tag{2}$$

where p_{no} refers to the equilibrium concentration of holes in the neutral region and p(w) is given by [1,6]

$$p(w) = p(0)e^{-qV_d/kT} + bx_r \int_0^{\sqrt{qV_d/kT}} e^{-y^2} dy \tag{3}$$

under assumption $J_R(0) = 2J_R(w)$. (No recombination or generation within the space charge region). V_d is the GB diffusion potential.

$b = \dfrac{J_R}{2D_p q}$ and $x_r = \sqrt{D_p \tau_r} - \sqrt{\dfrac{\epsilon D_p}{q N_d \mu_p}}$.

At the grain boundary plane are localized interface states, which in general are statistically distributed in energy over the energy gap. These states have a distribution determined by the nature of the disorder, by dangling bonds, and by the local electronic potential fluctuations producing

stress fields in the regions of structural irregularities. They may also arise from chemical impurities trapped between adjacent grains. Together dangling bonds and local structural strain can produce an inhomogeneous broadening of the discrete levels in the gap if their effects are sufficiently severe.

As a feasible approximation to the energy spectra for these localized states, Gaussian energy distributions are adopted. These states are classified into two types, "acceptor-like" and "donor-like" interface states $h_{tA}(E)$ and $h_{tD}(E)$, and are expressed by

$$h_{tA}(E) = \frac{H_{tA}}{\sqrt{2\pi}s_A} \exp\left[-\frac{(E-E_{tA})^2}{2\,s_A^2}\right] \tag{3}$$

and

$$h_{tD}(E) = \frac{H_{tD}}{\sqrt{2\pi}\,s_D} \exp\left[-\frac{(E-E_{tD})^2}{2\,s_D^2}\right] \tag{4}$$

where H_{tA} and H_{tD} are the total density of the localized states per unit area, s_A and s_D are distribution parameters and E_{tA} and E_{tD} are the mean value of the acceptor-like and donor-like distributions, respectively. The exact energy and type of traps which are present in polysilicon are not completely understood. It is generally agreed that the trapping levels are near midgap on the basis of the observed activation energies and bias dependence from transport measurements.[7] An important feature of the "deep-level" Gaussian distribution model suggested here is the energy position of the mean value of the "acceptor-like" and "donor-like" distributions. We take these to be, respectively, slightly above and slightly below midgap as in the case of amorphous Si.[8] The density and distribution (broadening) parameters of the

GB trapping states are expected to depend on the conditions of sample preparation, orientational mismatch, passivation and annealing processes. Typical results are presented for the following cases of the GB interface state distribution:

Case(a) : E_{tA} = 0.5 eV, s_A = 10 kT

Case(b) : E_{tA} = 0.56 eV, s_A = 10 kT

Case(c) : E_{tA} = 0.5 eV, s_A = kT

Case(d) : E_{tA} = 0.56 eV, s_A = kT.

In all cases considered here, the donor-like states are assumed to be filled with electrons and therefore neutral. Other values used in the calculations are: $H_{tA} = 10^{11}$ cm^{-2}, doping concentration within the grain $N_d = 2\times10^{15}$ cm^{-3} $\varepsilon_s = 11.8\ \varepsilon_0$, $V_{th} = 10^7$ cm/sec, $\sigma_c = 10^{-14}$ cm^2 and $\sigma_N = 10^{-16}$ cm^2.

The latter two parameters correspond to capture cross-sections associated with coulombic and neutral capture respectively, of carriers by the interface states.[4],[6]

Figures 1 and 2 show the dependence of the interface recombination velocity S(0) and the effective recombination velocity S(w) on the value of ΔE_f, respectively. These results, as reported earlier,[4] show that S(0) exhibits an increase with increasing ΔE_f for small values of ΔE_f, then reaches saturation at high ΔE_f.

The velocity S(w) should not be taken to be constant, but rather increases with increasing ΔE_f, reaches a peak at a critial value of ΔE_f, and then decreases with increasing ΔE_f (with high illumination levels) in all four cases.

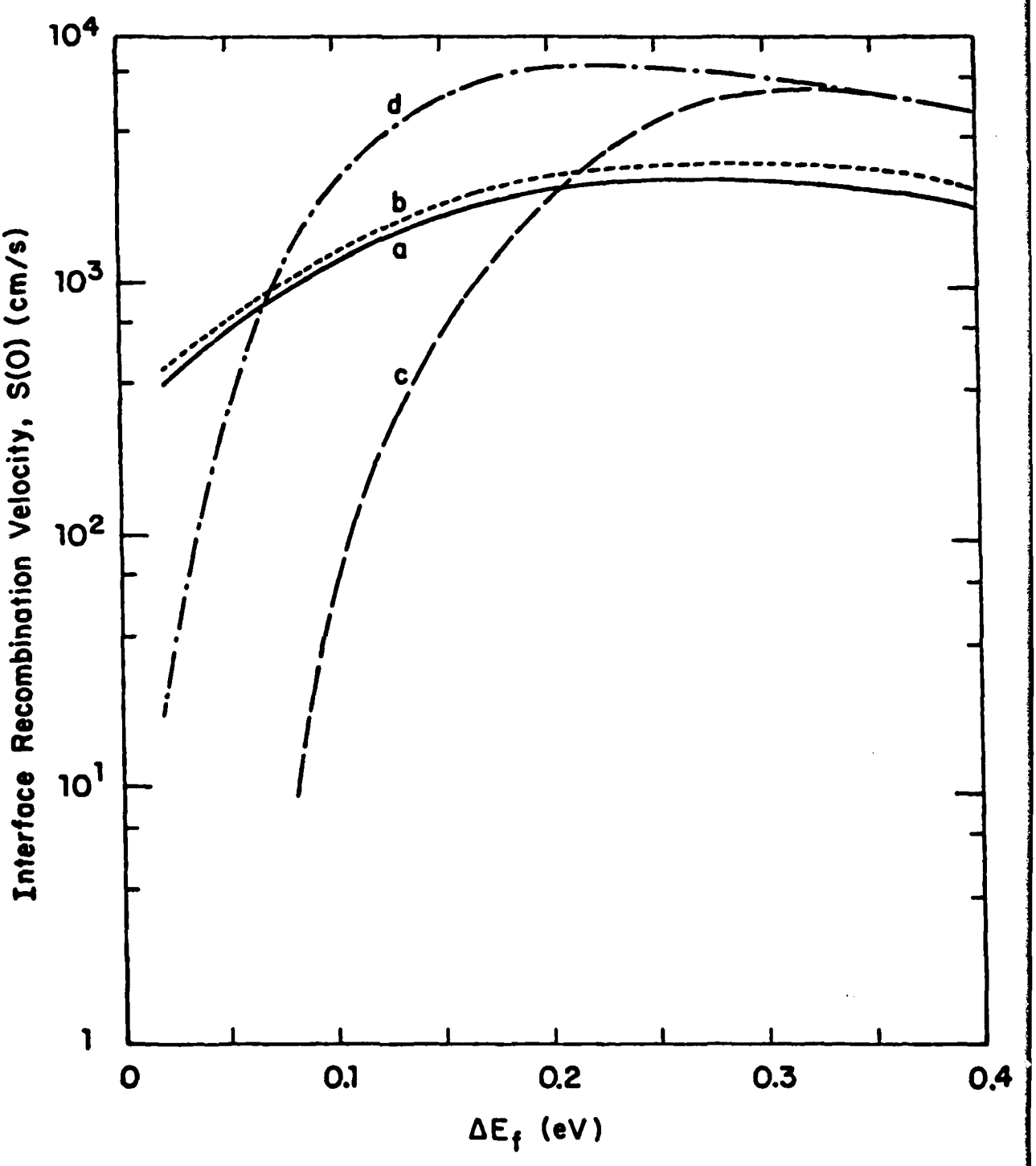

Figure 1. Interface recombination velocity at the GB vs ΔE_f (cases a-d).

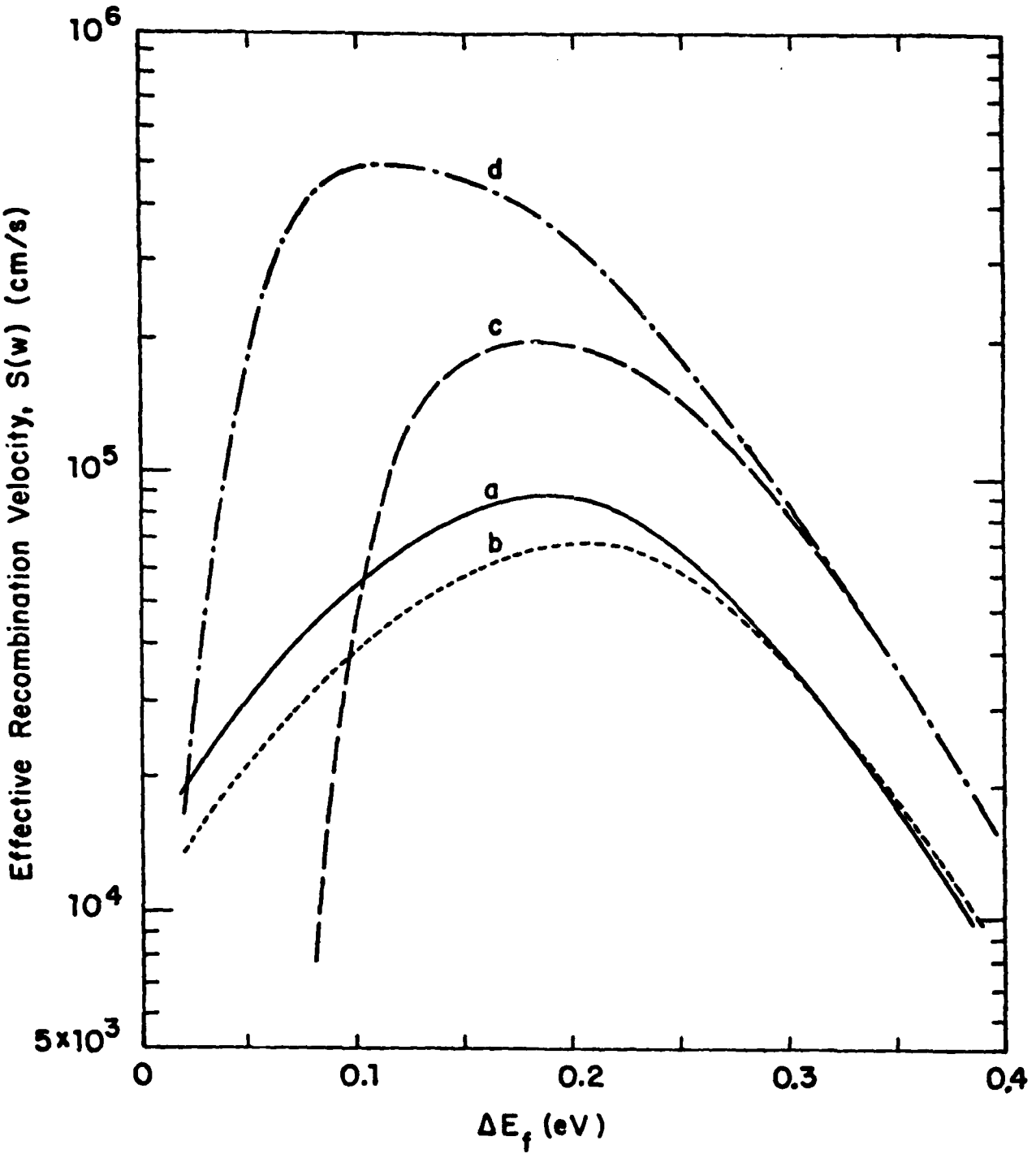

Figure 2. Effective recombination velocity for minority carriers at the edge of the neutral region vs ΔE_f (cases a-d).

In Figs. 3 and 4 we show the interface recombination velocity and the effective velocity as a function of the recombination current J_R. Fig. 5 shows the dependence of the effective velocity S(w) on p(w), the excess minority carrier concentration at the edge of the neutral region. Figs. 4 and 5 are of most utility to device modelers because they simply express a nonlinear boundary condition for effective recombination rate at the edge of a field-free region. The solution to the continuity equation in the quasi-neutral region is obtained with a nonlinear boundary condition, but one which does not contain additional unknowns, such as ΔE_f at the grain boundary.

These results are qualitatively consistent with those of Ref. (9), which considered the effective recombination velocity for grain boundaries with monoenergetic (midgap) recombination centers.

It has been demonstrated in the above example that in grain boundary recombination processes, it is possible for the interface recombination velocities to increase over a range of recombination rates (illumination intensities), while at the same time the effective recombination velocity of the minority carriers decreases with the recombination rate. This has arisen because the diffusion potential created by the interface charge decreases with recombination rate in a way which overcompensates for the increasing recombination velocity.

It is therefore essential that in modelling interface recombination in devices, whether this be at surfaces or at grain boundaries, one distinguishes between the true recombination velocity which depends only upon the recombination process, and the effective velocity at the boundary of the field-free region, which depends also upon the minority carrier transport through the adjacent space-charge region.

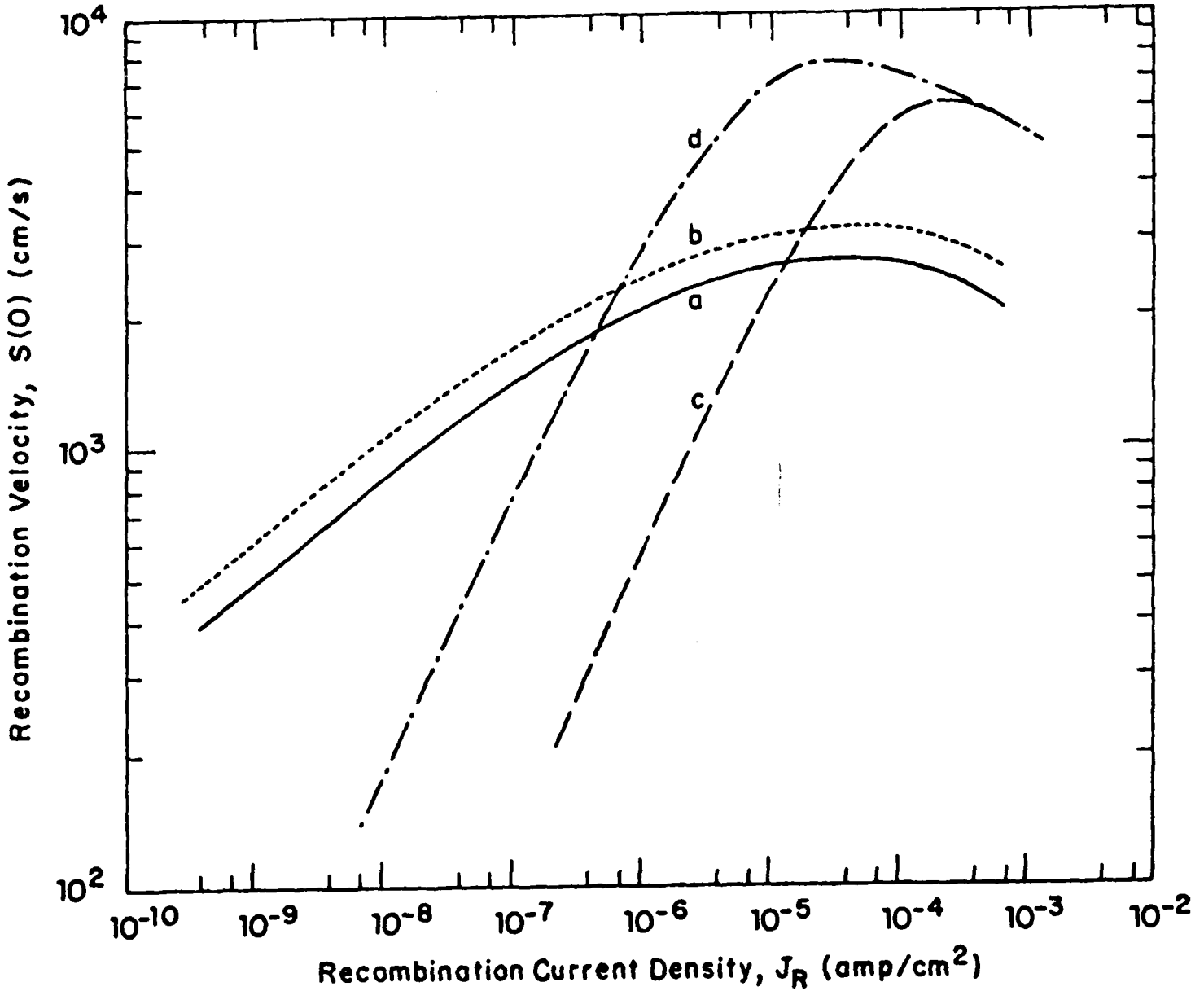

Figure 3. Interface recombination velocity vs recombination rate, or recombination current density (cases a-d).

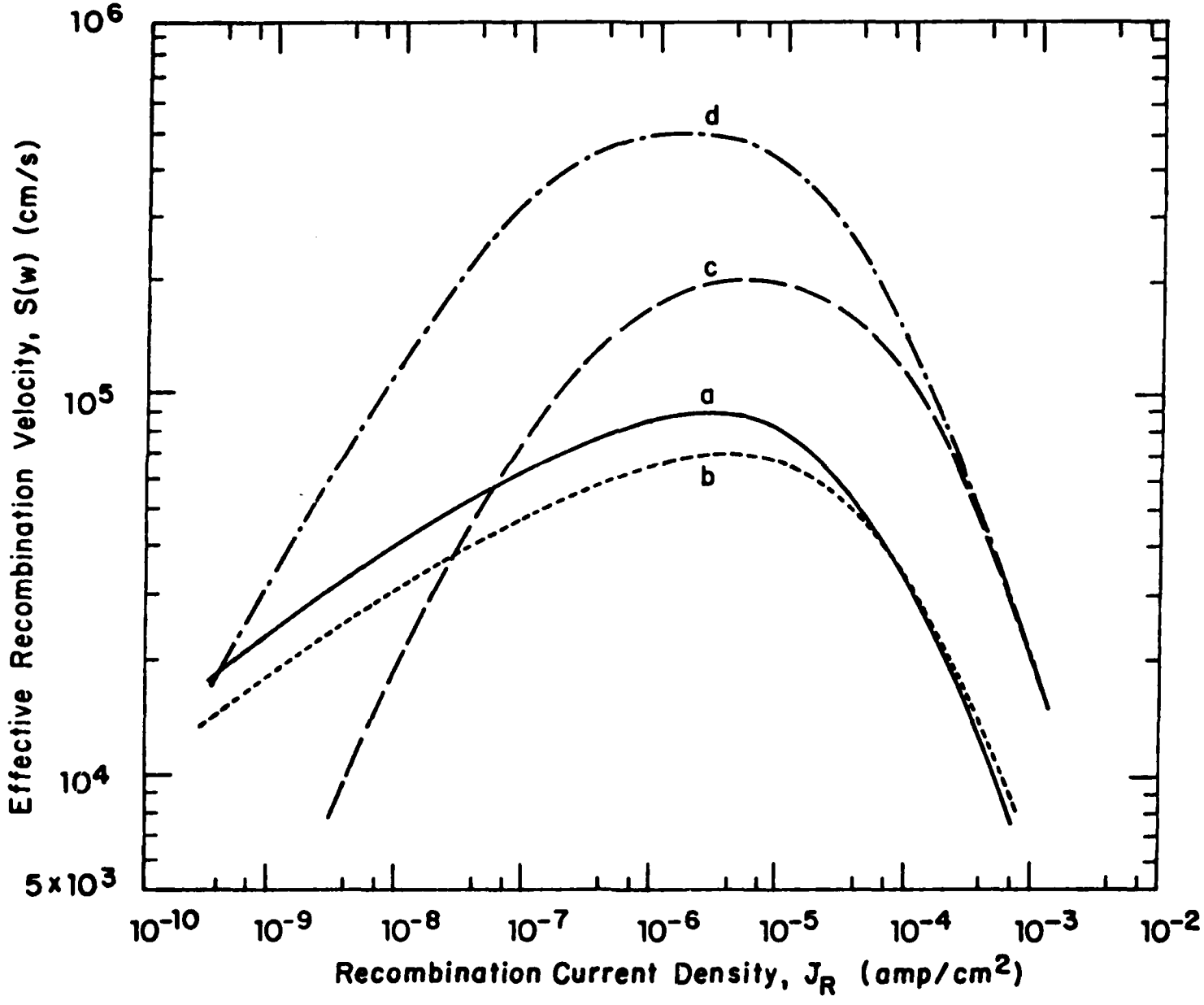

Figure 4. Effective recombination velocity of minority carriers at the edge of the neutral region, as a function of recombination current density (cases a–d).

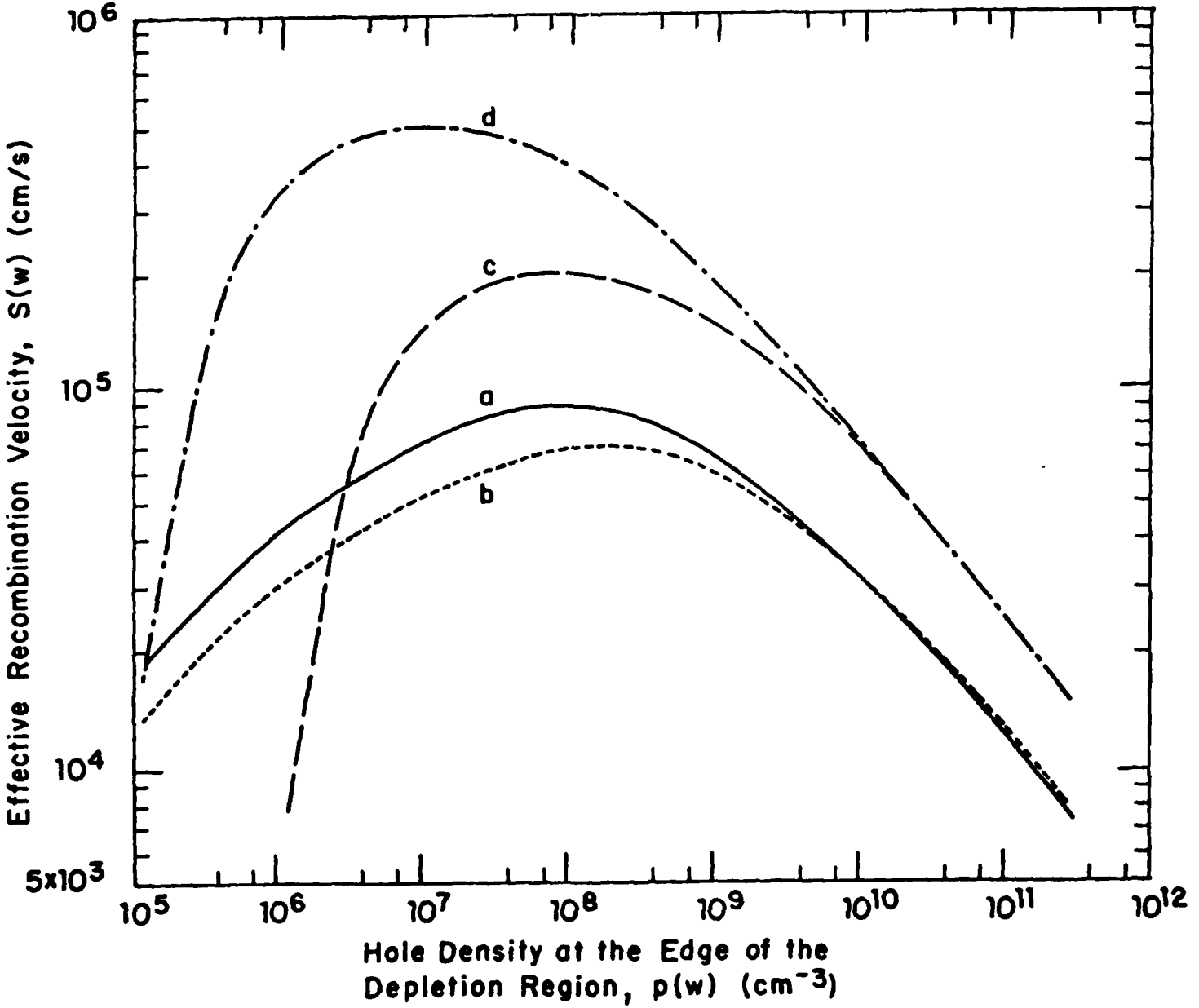

Figure 5. Effective recombination velocity at the edge of the neutral region as a function of excess minority carrier concentrations at this location (cases a-d).

+Department of Electrical Engineering, University of Manitoba, Winnipeg, Canada R3T2N2.

*This research was also supported by the U. S. Department of Energy under contract DOE/SERI xw-1-1272-1.

(1) P. Panayotatos, E. S. Yang, and W. Hwang, Solid State Electron. 25, 417 (1982).

(2) C. H. Seager, J. Appl. Phys. 52, 5960 (1981).

(3) H. C. Card, J. Appl. Phys. 47, 4964 (1976).

(4) E. Poon and W. Hwang, Solid State Electron. 25, 699 (1982).

(5) H. C. Card and E. S. Yang, IEEE Trans. Electron. Dev. ED-24, 397 (1977).

(6) P. Panayotatos and H. C. Card, IEEE Electron. Dev. Lett. EDL-1, 263 (1980).

(7) J. Werner, W. Jantsch, K. H. Froehner, and H. J. Queisser, in Grain Boundaries in Semiconductors, North-Holland, New York, 99-104 (1982).

(8) W. E. Spear, Advan. Phys. 26, 811 (1977).

(9) J. G. Fossum and R. Sundaresan, IEEE Trans. Electron. Dev. ED-29, 1185 (1982).

B. ELECTRICAL CHARACTERISTICS OF LARGE SCALE INTEGRATION (LSI) MOSFETS AT VERY HIGH TEMPERATURES

(F. Shoucair, W. Hwang)
(JSEP work unit 4, 1982-1985)
(Principal Investigators: W. Hwang (212) 280-3115
E. Yang (212) 280-3120)

The main objective of this work has been the study of the effects of high temperature on the electrical behavior of silicon MOS transistors and circuits.[1],[2],[3] The formulation of the theory was based on the physical structure of a commercially available CMOS process with junction isolated N and P channel MOSFETs, but the results obtained are valid for dielectrically isolated transistors (DIMOSFETs) and silicon on insulator (SOI) devices as well, especially with regard to the modelling of leakage currents.

The theoretical approach consisted in examining the MOSFETs' temperature dependent electrical parameters individually. They were found to include the threshold voltage, the channel mobility, and the channel length modulation, the latter parameter being relevant only to devices operated in the saturation region. Necessary and sufficient conditions for the existence of Zero-Temperature-Coefficient (ZTC) gate bias voltages have been developed. The procedure followed for this purpose relied on the mutual cancellation of the threshold voltage and the channel mobility temperature derivatives over a specified temperature range. It has been found that a given transistor has one ZTC gate bias voltage in each one of the nonsaturation and the saturation regions of operation, and that the two gate voltages V_{GS} (ZTC) only depend on the parameters p_0 and q_0 of the threshold voltage temperature dependent function of the device.[1] The small signal parameters of the MOSFET biased at its ZTC points were obtained analytically, and it was shown that small signal capacitances are very weakly dependent on temperature.

Experimental data collected on long N and P channel MOSFETs in the range 25°C to 300°C has revealed that (i) the threshold voltage magnitude $|V_{TH}(T)|$ decreases linearly with increasing temperature, (ii) the channel mobility $\mu(T)$ displays a $T^{-1.5}$ dependence, and (iii) the drain to substrate leakage currents exhibit proportionality to $n_i(T)$, the intrinsic carrier concentration, and to $n_i^2(T)$, in the lower and upper parts of the temperature range under consideration, respectively.

Current voltage characteristics have been obtained in the subthreshold, nonsaturation, and saturation regions of operation. Subthreshold currents have been found to increase exponentially with temperature, thereby severely limiting the range over which MOSFETs can be used in this bias regime. The nonsaturation and saturation region current characteristics were shown to present ZTC bias points to gate voltages $V_{GS}(ZTC)$ in close agreement with the theoretical predictions.[2]

The experimental data has been used to extend the validity of the conventional (room temperature), large and small signal models of the MOSFET up to 300°C. It has been shown that the effects of high temperature on the terminal characteristics of MOSFETs could be adequately modelled by the inclusion of a reverse biased diode between the drain and substrate terminals of these devices. This diode conducts the leakage currents of the drain-substrate junction, which increase exponentially with temperature. The high temperature small signal model was found to be identical to the room temperature one, provided the correct temperature dependences of the various electrical components are used.[3]

The effects of increasing temperature on the dc characteristics of a CMOS inverter were shown to be (i) decreasing noise margins and transition region slope between 25°C and 270°C, and (ii) the triggering of a pnpn latchup

phenomenon near 270°C. At 270°C, the switching speed of such inverters was found to incur a 67% reduction, on average, with respect to that at 25°C.

Resistive load inverters biased near (N channel MOSFETs) or at (P channel MOSFETs) their saturation region ZTC points have been shown to present a decrease in small signal gain with increasing temperature, in close agreement with the predictions of the models developed. Some implications of these models, on the design and analysis of analog MOS circuits have been discussed, whereby it has been shown that the main effect of high temperature is the introduction of a constraint on the choice of MOSFETs' gate widths. This constraint arises because of leakage current considerations, and is necessary in order to avoid the drift of bias quantities.

The results presented in this work have demonstrated that silicon MOSFETs can be used in very high temperature environments for digital and analog applications. In view of the fact that the CMOS process investigated experimentally was designed for room temperature operation, this process shows great promise as a high temperature silicon technology.

(1) F. Shoucair, W. Hwang, and P. Jain, "Electrical Characteristics of Large Scale Integration (LSI) MOSFETs at Very High Temperatures: Part I - Theory," (submitted for publication).

(2) F. Shoucair, W. Hwang, and P. Jain, "Electrical Characteristics of Large Scale Integration (LSI) MOSFETs at Very High Temperatures: Part II - Experiment," (submitted for publication).

(3) F. Shoucair, W. Hwang, and P. Jain, "Electrical Characteristics of Large Scale Integration (LSI) MOSFETs at Very High Temperatues: Part III - Modeling and Circuit Behavior," (submitted for publication).

C. PHONON-ASSISTED CARRIER TRANSPORT ACROSS A GRAIN BOUNDARY*

(C. M. Wu,+ E. S. Yang)
(JSEP work unit 4, 1982-1985)
(Principal Investigators: E. S. Yang (212) 280-3120
W. Hwang (212) 280-3115)

The electrical properties of polycrystalline silicon are extensively studied because of its importance in the development of integrated circuits. The polysilicon prepared by chemical vapor deposition (CVD) usually has a grain size of 1 μm or less. The control of conductivity of the CVD polysilicon is important when it is utilized as an interconnection or a distributed resistor. Seto[1] proposed a model introducing the trapping states to describe the GB electrical properties. Following the same approach, other researchers[2]-[5] have studied samples of both large grain-size wafers and small grain-size polysilicon films. Lu et al. used an attenuation factor in the form of a scattering potential to describe the phonon scattering at the GB. The reported data show that the majority-carrier conduction is significantly less than that predicted by the thermionic emission. This conclusion is reasonable since the transport of carriers from one grain to the other require not only enough energy to overcome the potential barrier, but also an appropriate momentum in the second grain. In other words, the quantum mechanical effect does not allow the incident carrier to exist in the second grain if no suitable state is available. This selection rule causes the reduction of carrier transmission. Since the current conduction due to the emission of carriers trapped by the GB states is limited (5.5 percent of total carriers leaving the GB), we will only discuss the carrier transmission directly from one grain to the other. In addition to phonon scattering, Coulombic interaction with interface charge can be significant, and it has

been reported separately.[6]

Thermionic emission has been discussed in detail for carrier transport across a metal-semiconductor junction.[7] In some cases, the effects of tunneling and quantum mechanical reflection may also influence the current conduction. Since the metal is always degenerated and the electron density is very high, a carrier can be emitted freely from the semiconductor without any limitation on its momentum as long as the kinetic energy is large enough to overcome the potential barrier. But this is not true for a carrier travelling from one semiconductor to another,[8],[9] where the probability of the scattered carrier to occupy an appropriate state in the second semiconductor or grain must be taken into account. We consider the case of electron transport from one conduction-band valley in the first grain (valley a) to one of the valleys in the second grain (valley b). This transition from the wave vector k_a to the other wave vector k_b usually occurs with either absorption or emission of a phonon. Thus the thermionic emission current from the first grain ($z < 0$) to the second grain ($z > 0$) is given by

$$J_{1\to 2} = \sum_i \frac{a}{\hbar} \iiint d\vec{k}_i^3 N(\vec{k}_i) \frac{\partial E}{\partial k_z} T(\vec{k}_i, \vec{K}) \tag{1}$$

where the summation is over the ellipsoids.

Since T is normally less than unity, (1) explains why an attenuation factor is needed to fit the experimental data in the previous work.[1]-[5] Let us compare (1) to the classical form of the thermionic emission current given by

$$J^0_{1\to 2} = \sum_i \frac{a}{\hbar} \iiint d\vec{k}_i^3 N(\vec{k}_i) \frac{\partial E}{\partial k_z} . \tag{2}$$

It is now evident that the average effect of the transmission coefficient T gives rise to the attenuation factor which is defined as

$$\eta = \frac{J_{1\to 2}}{J^{0}_{1\to 2}} \tag{3}$$

It is possible to calculate the current in (1) numerically if $T(\vec{k}_1, \vec{K})$ is given as a function of the kinetic energy E_i and the assisting phonon energy $\hbar\omega$.

If the first grain is located on the Cartesian coordinate system, and the orientations of (100), (010), and (001) are along the x_1-, x_2-, and x_3- axes, respectively, three parameters are needed to specify the orientation of the second grain.

For a cubic crystalline lattice such as silicon, the k-axes have the same directions as the real-space axes. Although the origins of the real space in the two grains may be displaced, the major axes of the two grains in the k-space have the same origin. Thus the carrier at the interface should have zero momentum in the second k-space if it has a zero momentum in the first k-space. Based on this argument, the k-space of the second grain is a system obtained by the three rotations of the k-space of the first grain. Fig. 1(a) shows the three rotations. The system is first rotated along the x_2-axis, then the x_3-axis. Finally, the system is rotated along the x_3'-axis. The rotation angles are θ, ϕ, and ψ, respectively.

As discussed previously, the current is caused by the transition of carriers from one of the energy valleys in the first k-space to the energy valley in the second k-space (Fig. 1(b)). The wave vector of the phonon ranges from 0 to (4/3) (π/a). It could be either an acoustic phonon or an

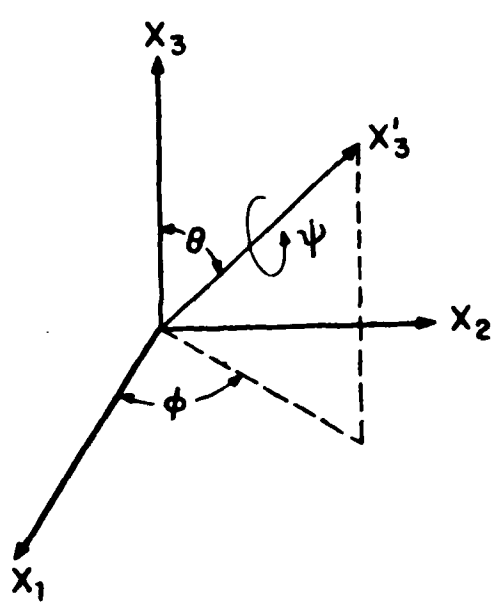

(a)

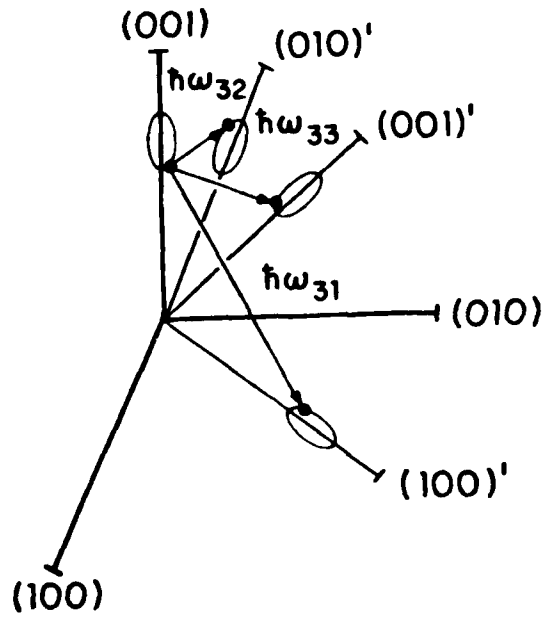

(b)

Fig. 1 (a) The angular relationship between the first grain (unprime system) and the second grain (prime system).

(b) In wave-vector space, the phonon-assisted transition from a valley of the first grain to a valley of the second grain.

optical phonon. The phonon frequency is in the order of 10^{13} Hz and the phonon energy can be as high as 0.06 eV in silicon, which is larger than its thermal energy at room temperature. Therefore, at large angles, the number of phonons available is so limited that the carrier transition is constrained.

By examining the rotated axis in the octant of the original vector space, (Fig. 1(b)), we can always find an original axis which has an angle less than 54.7°. In other words, the carrier in the valley of the second grain can always make a transition with the assistance of less than 0.919 k_0 that corresponds to the phonon energy of 30 meV. The interference integral is approximately 0.75. At room temperature, the average transition probability is estimated to be 30 percent. Once we have a valley with an angle less than 54.70°, the transition probability is greater than 30 percent, and the η-value is higher than 0.3 at room temperature. When we study silicon, a multivalley semiconductor, the overall transition should be taken into account. Thus the numerical method has been employed to calculate the attenuation factor to show the effect of the GB angle.

The GB angle of two neighboring grains is described by three rotation angles θ, ϕ, and ψ. To conserve computer time, we limit the rotation angles with the conditions $0 \leq \theta \leq 45^{\circ}$, $0 \leq \phi \leq 45^{\circ}$, and $\phi = 0$ in the calculation of the attenuation factor η. The results are shown in Fig. 2(a) and (b) for η at 300 and 77 K. The minimum η- value at T = 300 K is 0.8, but the minimum η-value at T = 77 K is 0.05. The transition is influenced strongly by the misorientation of the two grains at low temperatures, but not at room temperature. This is because the phonon-assisted transition depends strongly on the number of phonons even though the phonon energy does not vary with the temperature. This is consistent with Einstein's theory, which specifies the phonon energy as the activation energy of phonon-assisted transition when

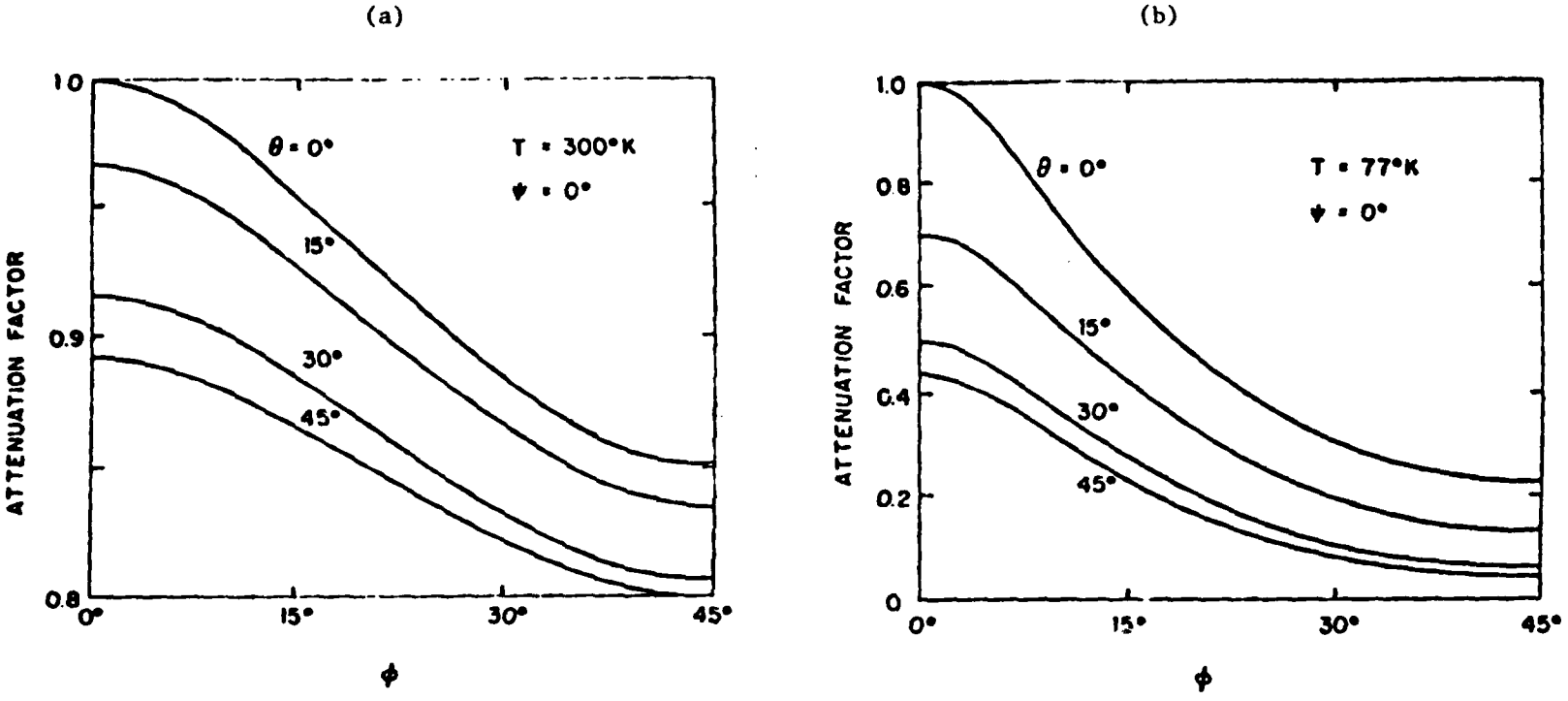

Fig. 2 The attenuation factor for different GB angles, $0<\theta<45^{o}$, $0<\phi<45^{o}$, and $\phi=0$ at (a) $300^{o}K$ and (b) $77^{o}K$. The impurity scattering is neglected in the calculation.

ω_{ij} >> kT. We know that we can at least find a transition from a certain valley requiring a phonon energy less than 300 meV. Thus the activation energy is less than 30 meV. Of course, this condition does not apply when the relaxation time is dominated by other mechanisms such as the impurity scattering. The activation energy due to the number of phonons remains, however, although the transition is scaled down by the low relaxation time. Generally speaking, the scattering potential can be explained by an average phonon energy required for the carrier transition between energy valleys in different grains.

+Xerox Corporation, El Segundo, CA.

*This research was also supported by the Department of Energy under Contract XW-1-1272-1.

(1) J. Y. W. Seto, J. Appl. Phys. 46, 5247 (1975).

(2) G. Baccarani, B. Ricco, and G. Spadini, J. Appl. Phys. 49, 5565 (1978).

(3) G. J. Korsh and R. S. Muller, Solid-State Electron. 21, 1045 (1978).

(4) N. C. -C. Lu, L. Gerzberg, C. -Y. Lu, and J. D. Meindl, IEEE Electron Device Lett. EDL-2, 95 (1981).

(5) E. S. Yang, E. Poon, C. M. Wu, W. Hwang, and H. C. Card, IEEE Trans. Electron Devices, ED-28, 1131 (1981).

(6) C. M. Wu and E. S. Yang, Appl. Phys. Lett. 40, 49 (1982).

(7) S. M. Sze, Physics of Semiconductor Devices. New York:Wiley, (1969).

(8) P. J. Price, "Transmission of Bloch waves through crystal interfaces," in Proc. Int. Conf. on the Physics of Semiconductors, 99-103 (1962).

(9) C. M. Wu and E. S. Yang, Solid State Electron. 22, 241 (1979).

D. DIFFUSIVITY AND GROWTH RATE OF SILICON IN SOLID-PHASE EPITAXY WITH AN ALUMINUM MEDIUM*

(Q. Hua, E. S. Yang)
(JSEP work unit 4, 1982-1985)
(Principal Investigators: E. S. Yang (212) 280-3120
W. Hwang (212) 280-3115)

Solid-phase epitaxy (SPE) is a relatively new crystal-growth process whose importance should not be underestimated. The advantage of this technique is derived from the low temperature at which single crystal layers are grown. For example, when using Al as the transport medium in Si SPE, the growth temperature is between 400-550°C so that an abrupt doping profile at the epitaxial layer-substrate interface can be easily obtained. Moreover, the width of the epitaxial layer depends only on the deposited amorphous (a) Si thickness, which can be controlled during evaporating; thus, submicron thin layers can be readily grown. Tsaur et al.[1] have employed this technique for the formation of p-n junction solar cells which minimize the adverse effects of high temperature, and they have produced devices with high efficiency.

Since the emergence of SPE, a large number of papers have been published on this topic. Most of them describe the growth phenomena by using various techniques such as transmission electron microscopy, Rutherford back-scattering and channeling, and Auger spectroscopy to analyze the structural character of the growth layer. However, the number of experimental studies on the growth mechanisms and related parameters is quite limited. In this work, we attempt to determine the diffusivity and mass transfer coefficient and to estimate the growth rate of SPE.

The classical diffusion equation is used to determine the diffusivity of Al in silicon in the sample structure shown in the insert of Fig. 1. When the sample is heated in a furnace the a-Si will gradually dissolve into the underlying Al layer until the a-Si disappears entirely from the top surface.

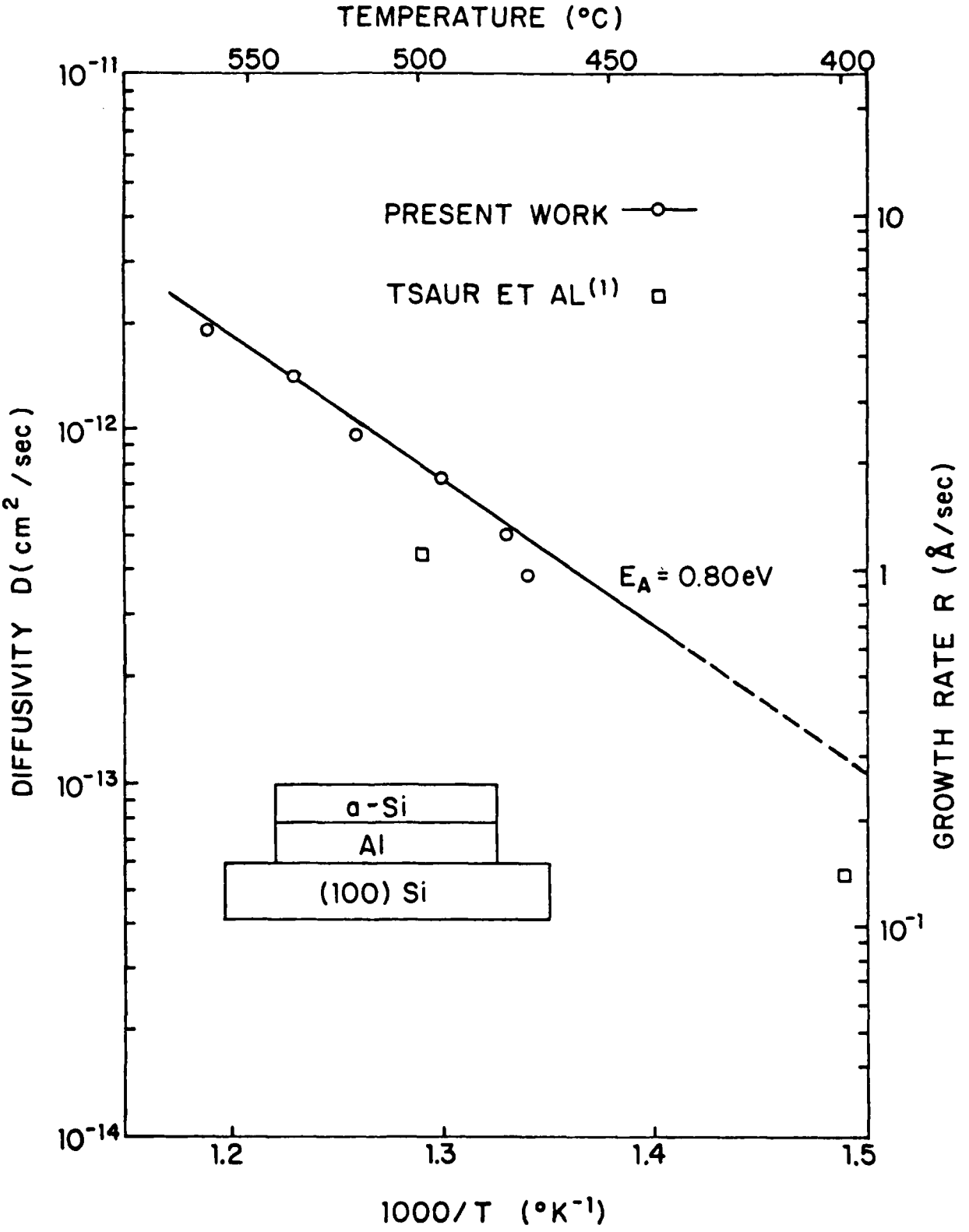

Fig. 1 Diffusivity and growth rate as a function of temperature.

It is implicitly assumed that the transport of Si across the a-Si-Al interface is fast. As it will be explained later this assumption is consistent with the activation energy obtained from our experimental data. If the growth process is interface reaction limited, the activation energy would have to be approximately equal to the bond-breaking energy. In other words, in a structure with a thin a-Si layer and relatively thick Al layer, the transport of Si in Al may be considered as diffusion limited. Since we are studying the initial stage of silicon diffusion up to the point that the surface silicon starts to disappear, we assume that the interface silicon concentration is constant. The solution of the diffusion equation with constant diffusivity at a given temperature is therefore:

$$C(x,t) = C_1 \mathrm{erfc}[x/2(Dt)^{1/2}] \tag{1}$$

where C_1 is the Si molar solubility in Al which specifies the boundary condition at the a-Si and Al interface. D is the diffusivity of Si in Al, x is the distance from the a-Si-Al interface, and t is the diffusion time. Integrating Eq. (1) from x = 0 to ∞, we obtain the relationship between the total amount of deposited a-Si and the diffusivity. A similar study has been done by Immorlica et al.[2] to measure the diffusivity and solubility of Ge and GaAs in Pb in liquid-phase epitaxy, and the resulting equation for D is modified as follows:

$$D = \frac{\pi}{t}\left(\frac{d_{Si}}{2X_{Si}}\ \frac{\rho_{Si}}{\rho_{Al}}\frac{M_{Al}}{M_{Si}}\right)^2 \tag{2}$$

where d_{si} is the thickness of a-Si, X_{Si} is the equilibrium solubility expressed in atomic fraction, which can be obtained from the silicon-aluminum

phase diagram at a given temperature. ρ_{Si} and ρ_{Al} are the densities of Si and Al (ρ_{Si} = 2.33 g/cm^3 and ρ_{Al} = 2.70 g/cm^3). M_{Al} and M_{Si} are the molecular weights of Al and Si. The parameter t is the diffusion time which is specified by the disappearance of the a-Si on the top surface of the sample. Because the color of the thin a-Si film is easily distinguishable from Al under an optical microscope, t can be determined by observing the change of color of the sample.

The samples were prepared by evaporation in a vacuum of 2 x 10^{-6} torr on a (100) n-Si substrate. The thickness of the Al layer was 1 μm, and it was covered by ~100 Å of e-beam evaporated a-Si. The samples were heated in a furnace in a high-purity hydrogen environment. The diffusivity D was calculated from Eq. (2) using the measured t. The experimental results are shown in Fig. 1. Using the equation $D = D_0 \exp(-EA/kT)$, we find D_0 = 1.25 x 10^{-7} cm^2/sec and E_A = 0.8 eV. It is noted that the value of Si diffusivity in Al in this structure is several orders of magnitude less than that in the structures used for Al-Si metallization[3] although it is a factor of two greater than Tsaur's results (Fig. 1). However, the activation energy is almost identical to that of the Al-Si system. We believe that the difference in the values of diffusivity is caused by different experimental conditions. For example, a thin oxide layer at the a-Si-Al interface may reduce the diffusion process significantly.

By using the results of the above measurement, another important growth parameter, the mass transfer coefficient h, can be deduced. The process of SPE may be divided into three steps. In the first step, the a-Si is dissolved into Al and then diffused through the Al layer to reach the Al-Si substrate interface. Subsequently, the migrated Si atom nucleates epitaxially at the Si substrate surface through a surface reaction. It has been established that

the activation energy for surface-reaction-controlled vapor-phase epitaxy is approx. 1.9 eV.[4] Therefore, the surface reaction does not seem to be the dominant mechanism in SPE because of the lower activation energy according to the above measurement and previous experimental values.[3] Therefore, the diffusion flux in the Al layer (J_1) can be expressed as follows:

$$J_1 = -D \frac{dC}{dx} = -D \frac{C_1 - C_2}{d_{Al}} \tag{3}$$

where C_2 is the Si concentration at the Al-Si substrate interface, and d_{Al} is the thickness of the Al layer. The mass transfer process in the epitaxial growth can be expressed as:

$$J_2 = h(C_1 - C_2) \tag{4}$$

where J_2 is the Si mass flux. When the equilibrium growth condition is reached, we have $J_1 = J_2$, so that

$$h = \frac{D}{d_{Al}} \tag{5}$$

The total growth time may be divided into two parts: (1) $t_1 = S_{Al}^2/D$ is the time required to reach the equilibrium growth condition; (2) $t_2 = d_{Si}/h$ is the growth time after the equilibrium condition. In order to compare our results with Tsaur's data on growth rate, we have added the vertical scale on the right of Fig. 1 with the specific conversion parameters of 2000 Å Al and 2000 Å aSi.[1] It is evident that the diffusion-limited mechanism proposed here is consistent with available data. In practice, the growth time usually should be longer to produce higher quality growth layers.

In conclusion, the diffusivity of a-Si in Al in the structure for SPE has been measured between 470-570°C, and the mass transfer coefficient and growth rate have been obtained. These data can be used to explain the results reported by Tsaur et al.[1] The activation energy of this process is found to be 0.80 eV, which is consistent with the literature.[3]

*This research was also supported by the Solar Energy Research Institute contract XW-1-1272-1.

(1) B. Y. Tsaur, G. W. Turner, and J. C. C. Fan, Appl. Phys. Lett. 39, 749 (1981).

(2) A. A. Immorica, Jr. and B. W. Ludington, J. Cryst. Growth 51, 131 (1981).

(3) J. O. McCaldin and H. Sankur, Appl. Phys. Lett. 19, 524 (1971).

(4) H. F. Wolf, Semiconductors, Wiley (1971).

E. THERMAL NITRIDATION OF GERMANIUM*

(Q. Hua, J. Rosenberg, E. S. Yang)
(JSEP work unit 4, 1982-1985)
(Principal Investigators: E. S. Yang (212) 280-3120
W. Hwang (212) 280-3115)

The high mobility of carriers in germanium could make it an important material for realizing high-speed digital or microwave metal-insulator-semiconductor field-effect transistors if a suitable gate insulator could be fabricated. Although germanium nitride powder was prepared by direct reaction of Ge powder with NH_3 as early as 1930,[1] very little information exists in the literature on thin germanium nitride films. Igarashi et al.[2] report the growth of partially crystallized films by direct reaction of germanium wafers with ammonia (NH_3 gas) above 700°C. Several authors[3]-[5] report on chemical vapor deposition of Ge_3N_4 on a variety of substrates (Si, Ge, GaAs, InP) and on the excellent insulating properties of these films.

Since it has been found that thermal nitridation provides a simple and convenient method for fabricating dense, uniform, and pinhole-free silicon oxynitride films,[6],[7] we have investigated the growth of films by a similar technique on germanium substrates.

The system used for film growth is illustrated in Fig. 1. Nearly intrinsic <111> germanium wafers were used as substrates. Wafer preparation consisted of degreasing in organic solvents followed by a chemical etch. Two different etching techniques were studied in order to assess their impact on the resultant film morphology. One etch consisted of a two-minute dip in 30% H_2O_2, followed by a deionized water rinse and immersion in buffered HF until the wafer became hydrophobic. The other etch was a NaOCl (4%): HF:H_2O = 1:1:5 solution. The second etch is much faster than the first, and tends to preferentially attack (and remove) areas of crystal damage or imperfection.

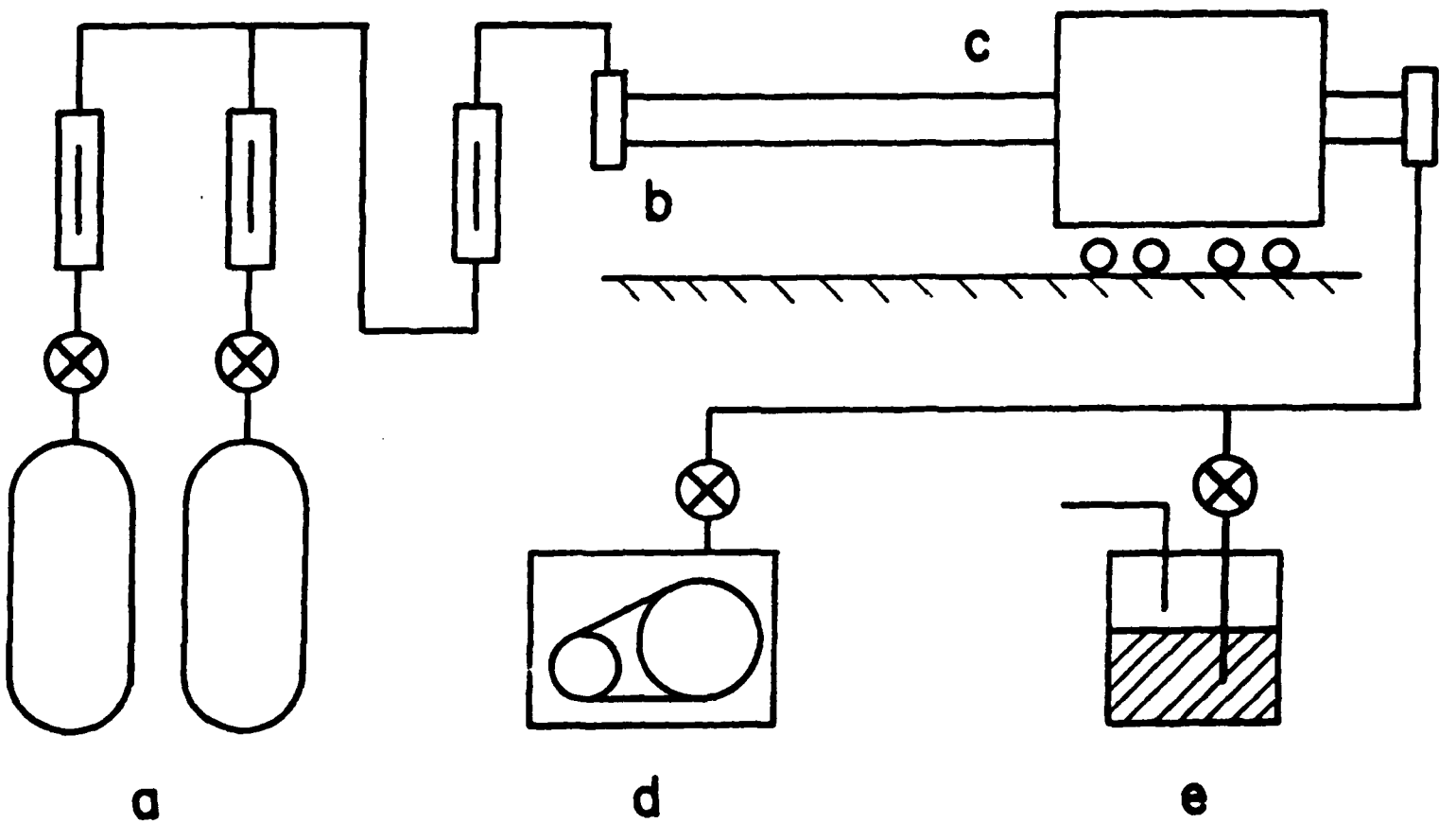

Fig. 1 Schematic diagram of the experimental system. (a) Gas cylinders, (b) quartz tube, (c) rolling movable furnace, (d) rotary pump, and (e) gas trap.

Immediately after etching, the wafers were loaded into the quartz-tube, movable furnace reactor, which was then evacuated to less than 0.1 Torr. The reactor was then purged with high purity nitrogen. After a thirty minute purge, a mixture of NH_3 and N_2 was introduced into the reactor and the preheated furnace was moved into place. After a prescribed growth time, the furnace was removed, and the wafers were allowed to cool for ten minutes before the ammonia flow was stopped. The reactor was purged with nitrogen before the wafers were removed.

Ellipsometry provides a means for determining two of the most fundamental parameters of a thin dielectric film: the thickness and the refractive index.

For our study, we used HeNe laser illumination (λ = 6328 Å), at an angle of incidence of 70°. At the wavelength 6328 Å, the complex index of refraction of germanium is given by 5.2 - 0.8i.[10] The film was assumed to be nonabsorbing (i.e., n_f was assumed to be real).

Following the procedure used by Archer,[8] we present in Fig. 2 a universal chart for determining the thickness and refractive index of any nonabsorbing film on germanium. This chart is applicable for ellipsometry systems utilizing a wavelength of 6328 Å and an angle of incidence of 70°. The different curves each correspond to a different value of n_f. Distance along each curve gives the value of δ, which is indicated by hash marks at intervals of $\pi/9$ (20°) in Fig. 2(a). Film thickness is indicated directly in Fig. 2(b). The chart is used by determining the point on a curve which most closely corresponds to the measured values of ψ and Δ. This determines n_f and δ.[8],[9]

Experience has shown that some oxygen incorporation in silicon nitride is unavoidable when the film is grown thermally. Consequently, we investigated oxygen incorporation in our germanium nitride films utilizing electron beam

(a)

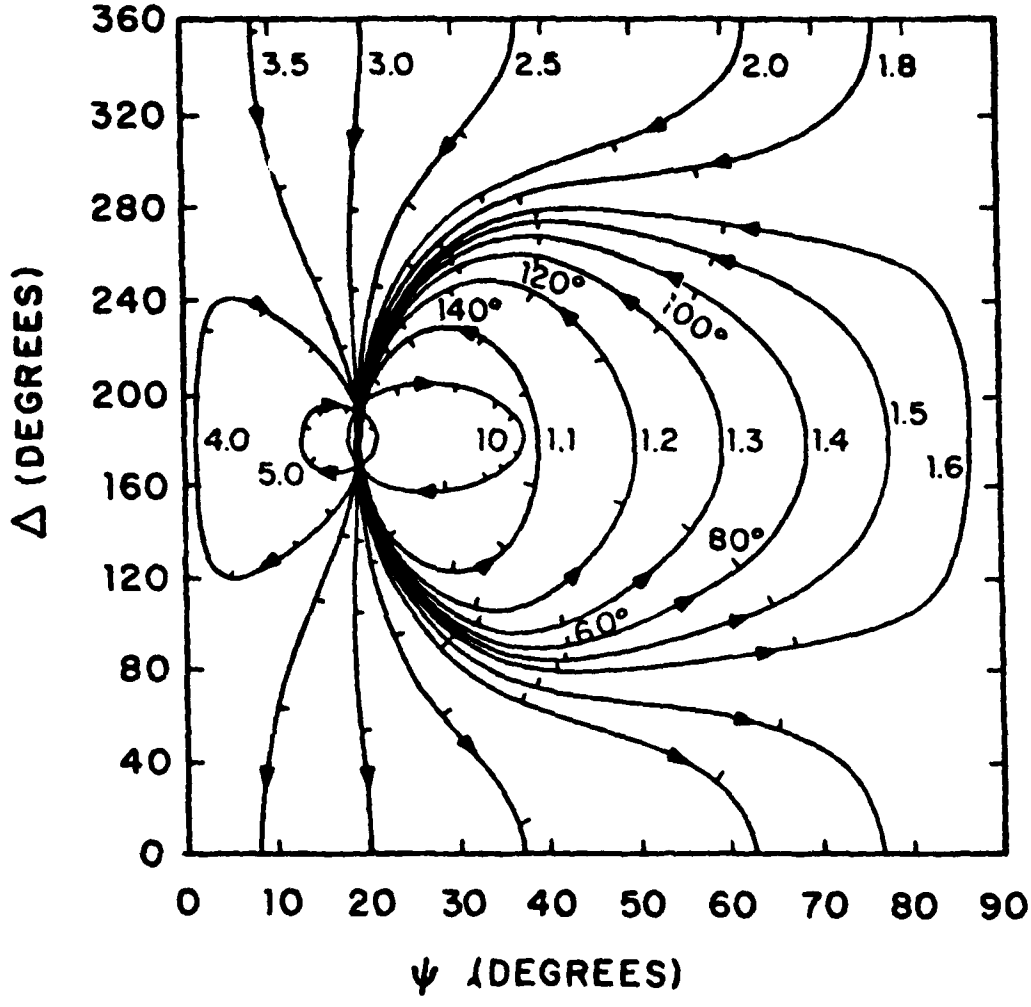

Fig. 2 Universal chart for evaluating thickness and refractive index of non-absorbing films on Ge: (a) full chart

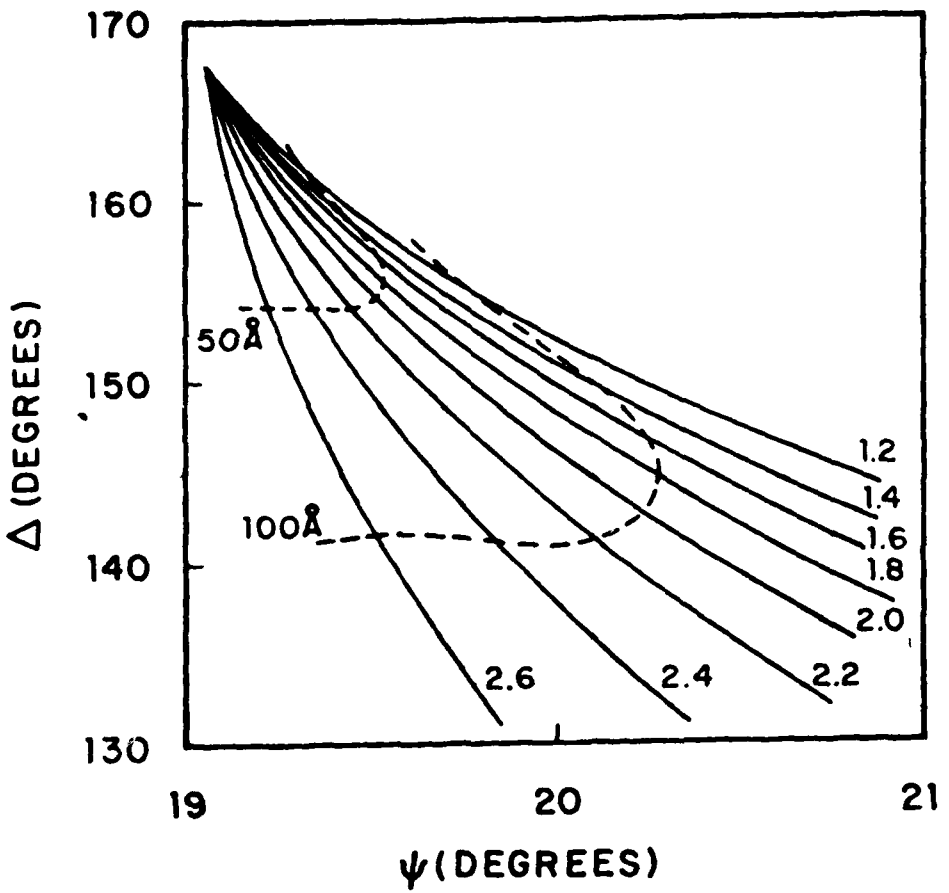

Fig. 2(b) expanded view of thin-film section of the chart.

x-ray coanalysis. This method also provides an estimate of the film thickness which is independent of the optical measurements. In addition, carbon contamination (from sources such as organic solvent residue or pump oil) can be investigated.

Several samples were analyzed by this method. In all cases, carbon contamination was at or below the detection limit (a fraction of monolayer). The nitrogen to oxygen ratios were in the range of 2:1 to 3:1.

The film thickness estimates were made by computing the thickness of a composite film incorporating the nitrogen as Ge_3N_4 and the oxygen as GeO_2 and using the bulk densities for these materials. Despite the crudeness of these estimates, they correspond to the ellipsometry measurements within 10% for films with smooth surface morphology. It would be difficult to make an estimate of the refractive indices of the films from the compositional analysis since the function dependence of the index on composition is unknown.

A wide range of surface morphologies results from different growth conditions. Any leak or contamination in the reactor gives rise to a surface with tetrahedral crystallites and whiskers. Even under clean and leak-free conditions, the film will tend to crystallize if either the growth temperature is too high or the growth time is too long, as observed for silicon nitridation.[11] In our case, the germanium nitride crystallites are triangular and oriented along crystallographic directions. Under appropriate growth conditions (2-4 h at 600-650°C on a substrate which was etched using the H_2O_2 treatment described earlier, and grown in a 1:1 mixture of NH_3 and N_2), very smooth and uniform films can be grown. A preliminary electron diffraction study indicates that the smooth looking films are indeed amorphous.

The results of the ellipsometry measurements are shown in Figs. 3-5.

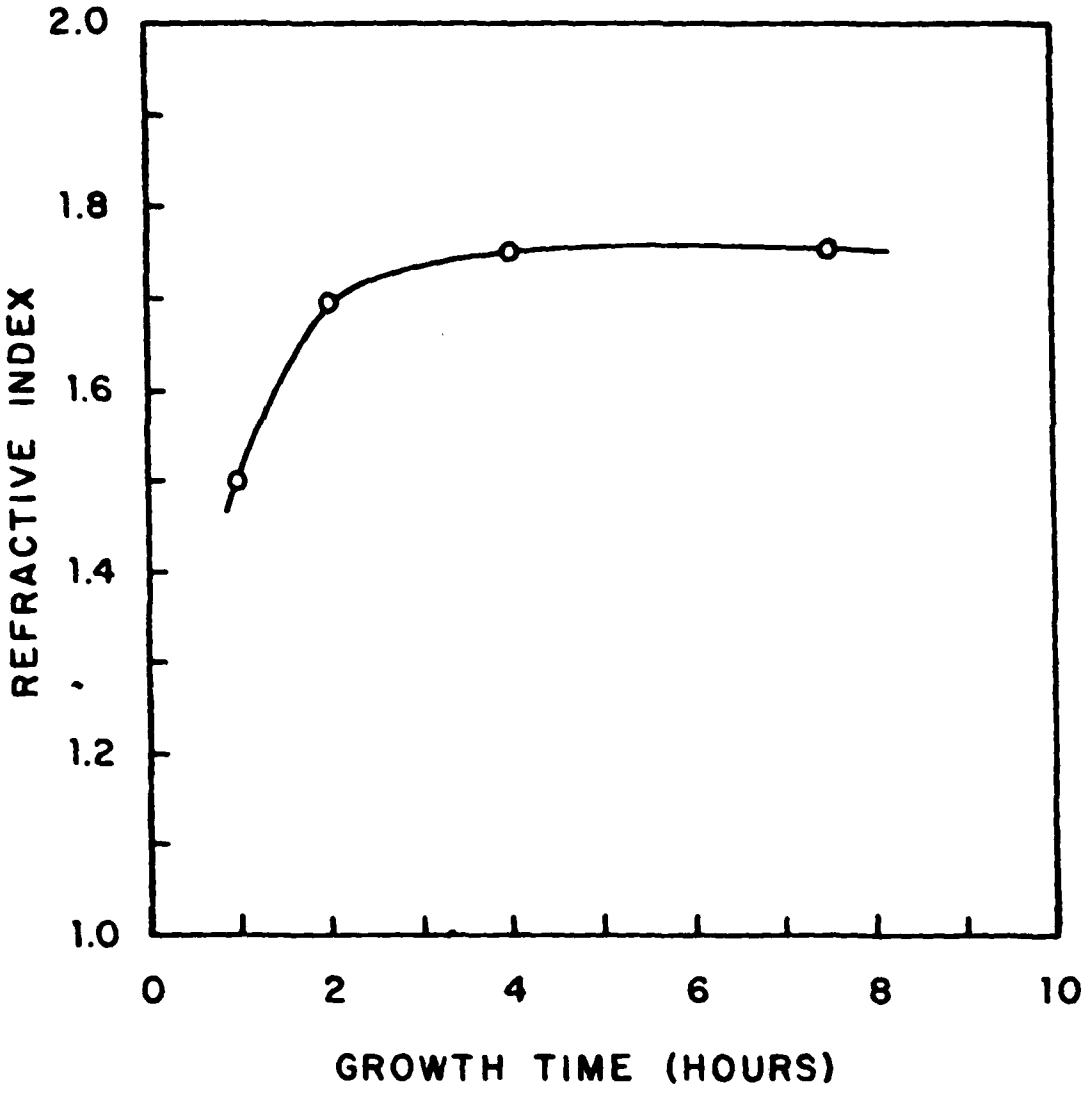

Fig. 3 Refractive index of germanium nitride films vs growth time for films grown in pure NH_3 at 650°C.

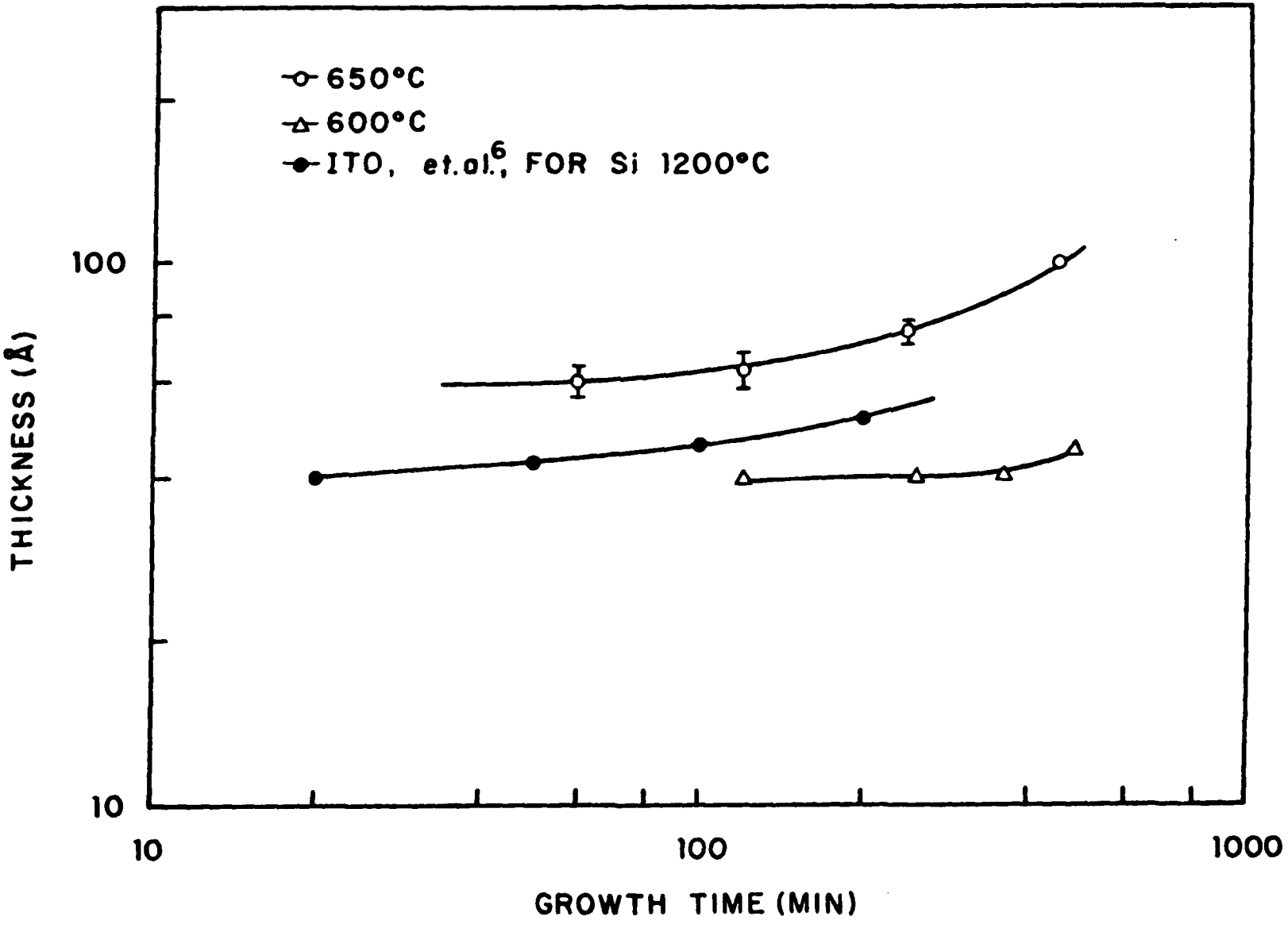

Fig. 4 Film thickness vs growth time for films grown in pure NH_3 on Ge at 600 and 650°C and on Si at 1200°C.

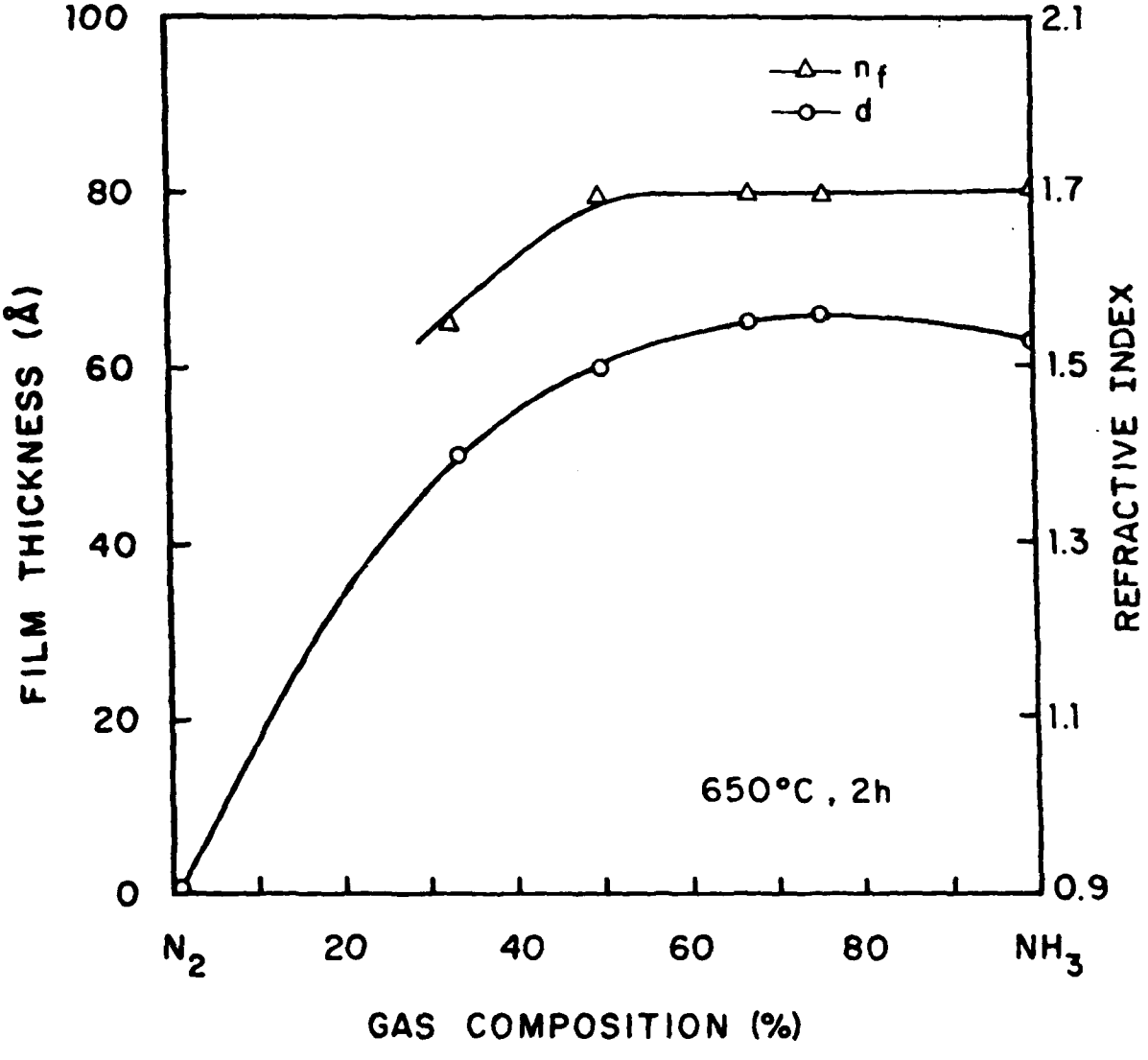

Fig. 5 Film thickness and refractive index vs gas composition for films grown at 650°C for 2h.

Fig. 3 shows the variation of the refractive index of the germanium nitride films with growth time. The average film index increases from 1.5 at one hour to 1.8 at four hours. Thereafter, there is no further increase. It should be pointed out that ellipsometric determination of the refractive index of such thin films is usually not accurate, so the numbers presented here should be regarded primarily in terms of the trend which they indicate. The increase of the refractive index with growth time suggests that an initial oxide layer (which has a lower index than the nitride) is formed on the germanium surface, which is subsequently nitrided during the growth. Some corroboration of this hypothesis is provided by the electron beam microprobe analysis which indicates that films which have a lower refractive index have a lower nitrogen to oxygen ratio. The refractive indices of bulk GeO_2 and Ge_3N_4 are 1.6 and 2.1, respectively.

Fig. 4 shows film thickness as a function of growth time for films grown in pure NH_3 on germanium at 600 and 650°C and on silicon at 1200°C. The data for the silicon growth curve is due to Ito et al.[6] and is included for comparison purposes. In all cases, the films show rapid initial growth, followed by a period of very slow growth. The growth rate increases again for low growth times.

Although the evidence is not conclusive, the fact that the film composition changes as a function of growth time (i.e., the N:O ratio increases) suggests that the growth mechanism involves the diffusion of nitrogen and oxygen into and through the film, which would yield time varying concentrations of nitrogen and oxygen in the film and at the film-substrate interface. If the growth mechanism involved the diffusion of germanium to the surface of the film, the reacting germanium would be exposed to an essentially time invariant environment, and one would expect the film composition to be

essentially independent of growth time. We propose that the initial growth is surface-reaction rate limited. In this regime, there may be significant oxide formation from residual oxygen (as/ both O_2 and water) in the reactor. As the film becomes thicker and the rate of nitrogen and oxygen diffusion through the film becomes the limiting factor in the growth rate, nitride formation will most likely dominate due to the relative concentrations of nitrogen and oxygen. Some replacement of oxygen by nitrogen in the film probably occurs as well. Germanium nitride is substantially denser than germanium oxide, and in the form of a continuous amorphous film, it probably presents a strong barrier against the diffusion of both oxygen and nitrogen (as does silicon nitride). This would account for the regime of very slow growth. The onset of more rapid growth at long growth times corresponds roughly to the onset of crystallization of the films. On the basis of this, we believe that structural changes which accompany crystallization of the films allow increased diffusion of nitrogen through the film (perhaps along grain boundaries), which results in the increase of the growth rates.

Film growth in mixtures of N_2 and NH_3 was also studied. Figure 5 shows film thickness and refractive index as a function of mixture composition for two hours growth at 650°C. Several authors have reported growing nitride films on silicon wafers in pure N_2, but we observed no measurable growth on germanium in pure N_2 at temperatures up to 650°C. This is consistent with Johnson's[1] results on reaction of germanium powder with N_2. The absence of nitride formation on germanium in pure N_2 probably is due to insufficient generation of dissociated nitrogen from N_2 at a growth temperature of 650°C (as contrasted with 1200 to 1300°C used for formation of silicon nitride from pure N_2).

Several nitride films were grown in pure NH_3 for greater than 4 h, which

had thicknesses greater than 100Å and refractive indices greater than 2. Unfortunately, results from these thicker films were not reproducible and are not included in Figs. 3-5.

Several samples were prepared for electrical measurements by evaporating an ohmic contact on the wafer backside (Sn) and 1-mm aluminum dots on the film. The electric field which the films can sustain varies widely with surface morphology. Films with smooth, noncrystallized surfaces show the onset of substantial leakage (10^{-13} A/μm^2) at fields of the order of 10^6 V/cm, and destructive breakdown at fields in excess of 3×10^6 V/cm.

Germanium nitride films with thicknesses less than 150 Å can be grown by thermal reaction with ammonia. The best surface morphology is obtained using NH_3:N_2 mixtures with ratios in the range of 1:1 to 2:1, with growth temperatures between 600 and 650°C. Reactor cleanliness, gas purity, and wafer surface preparation all have significant impact on the resulting film morphology.

*This research was also supported by the National Science Foundation under Grant no. ECS-81-16163.

(1) W. C. Johnson, J. Am. Chem. Soc. 52, 5160 (1930).

(2) Y. Igarashi, K. Kurumada, T. Niimi, Jpn. J. Appl. Phys. 7, 300 (1968).

(3) H. Nagai and T. Niimi, J. Electrochem. Soc. 115, 671 (1978).

(4) G. D. Bageatishuli, R. B. Dzhanelidze, N. I. Kurdiani, Y. I. Pashintsev, O. V. Saksaganski, V. A. Skorikov, Thin Solid Films 56, 209 (1979).

(5) K. P. Pande and S. Pourdavoud, Electron. Dev. Lett. EDL-2, 82 (1981).

(6) T. Ito, I. Kao, T. Nozaki, T. Nakamura, H. Ishikawa, Appl. Phys. Lett. 38, 370 (1981).

(7) T. Ito, T. Nakamura, H. Ishikawa, IEEE Trans. Electron Devices ED-29, 498 (1982).

(8) R. J. Archer, J. Opt. Soc. Am. 52, 970 (1962).

(9) R. M. Azzam and N. M. Bashara, Ellipsometry and Polarized Light (North-Holland, Amsterdam 1977).

(10) H. R. Philippl and E. A. Taft, Phys. Rev. 113, 1002 (1959).

(11) G. V. Samsonov, Oxide Handbook (IFI/Plenum, New York, 1973).

(12) T. Ito, T. Nozaki, H. Arakawa, M. Shinoda, and Y. Fukukawa, J. Electrochem. Soc. 125, 448 (1978).

F. GRAIN BOUNDARY INTERFACE STATES MEASUREMENT BY A LASER BEAM*

(E. Poon, E. S. Yang, H. L. Evans, W. Hwang, R. M. Osgood, Jr.)
(JSEP work unit 4, 1982-1985)
(Principal Investigators: E. S. Yang (212) 280-3120
W. Hwang (212) 280-3115)

Traditionally, polycrystalline materials have been used in integrated circuit interconnections,[1] varistors, and positive temperature coefficient devices.[2] In the last few years, new interest has been centered on recrystallized semiconductors for microelectronics.[3] The earlier applications made use of the unusual electrical properties derived from grain boundaries (GB's) whereas the new research treats the GB as a structural defect giving rise to poor electrical performance. In either case, an understanding of the GB is of fundamental importance for device applications. The GB barrier height is the most important parameter in determining the conductivity. Until now, because of the changing structural properties along the GB between two adjacent grains,[4] accurate measurement of the barrier height has not been possible. For example, large area capacitance and conductance techniques can only yield electrical parameters averaged over an uncertain cross-sectional area. In this report we present a method to overcome these difficulties.

The schematic diagram of the experimental setup is shown in Fig. 1. The chopped He-Ne laser beam is focused on a grain boundary of a p-type polycrystalline silicon sample which rests on the X-Y state. The sample, approximately 2 x 10 x 0.2 mm, contains two electrically active parallel grain boundaries that run across the whole width. The external dc bias V_B is kept constant throughout the experiment. The chopped light beam generates a periodic photoconductance signal which is measured across the load resistor R_L by a boxcar averager. A graph of photoconductance versus temperature is then plotted by an X-Y recorder in real time.

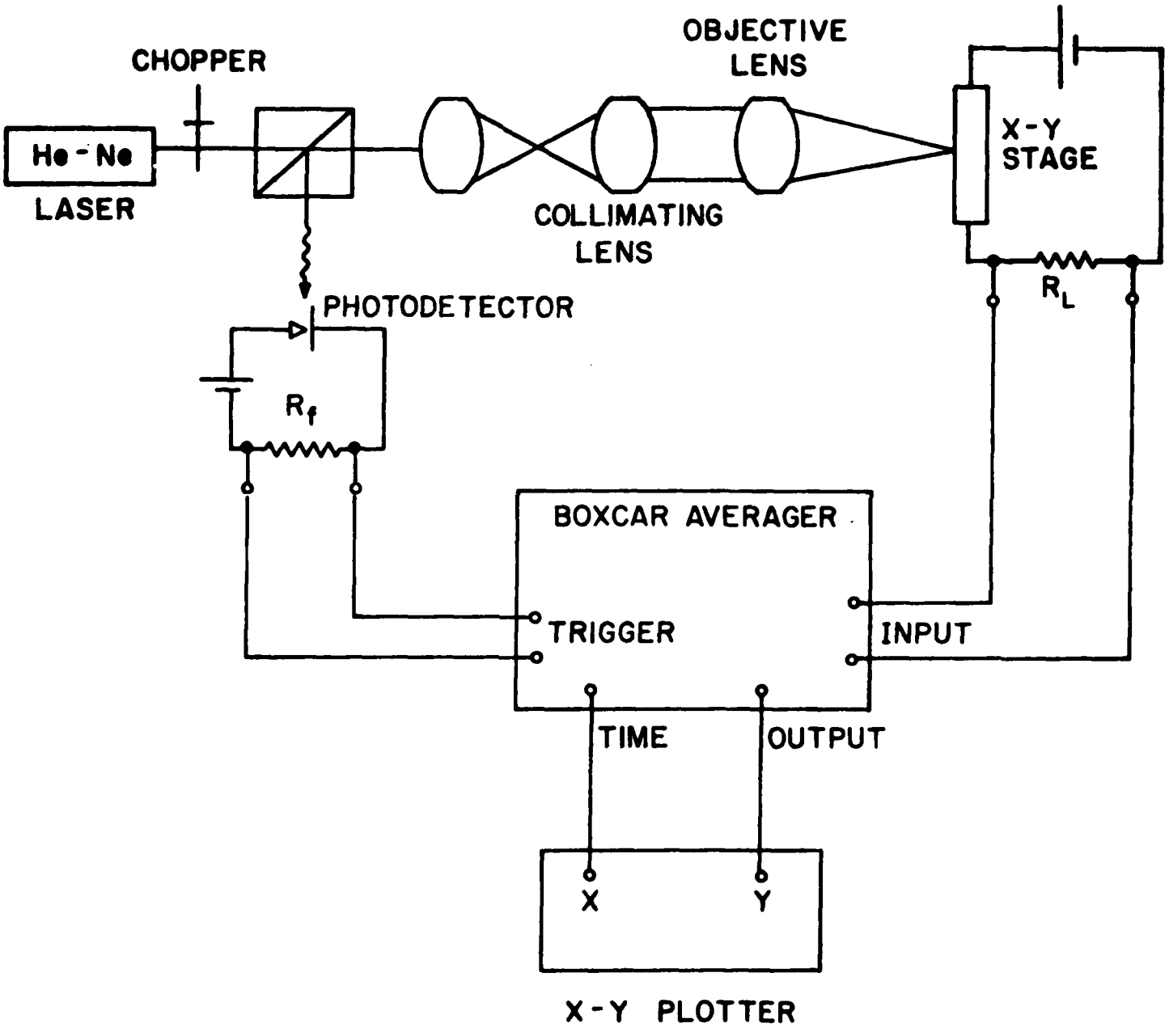

Fig. 1 Schematic diagram of the laser-induced photoconductivity experiment.

The photoconductance signal ΔV_L across the load resistor R_L is given by

$$\Delta V_L = \frac{V_B}{R_L} \frac{k}{AA^*qT} e^{\phi_b/kT} \quad (1)$$

if the intensity of the incident beam is high enough to reach the flatband condition. Since the pre-exponential factor is relatively insensitive to temperature, the slope of the plot of $\ln(\Delta V_L)$ vs 1/T gives the barrier height in the dark ϕ_b.

The laser intensity under typical conditions is estimated to be 12.7×10^2 mW/cm^2 (4×10^{18} photons/cm^2 s). R_L is 150 kΩ and V_B is set at 1.5 V. The sample has a dark resistance of 2 kΩ. From the C-V measurement, the doping concentration is found to be 2×10^{15} cm^{-3}. It is apparent that the flatband condition is established at this intensity since the signal saturates. The signal starts to decrease when the laser intensity is at a value equal to 1/5 of the typical intensity. Figure 2 shows the plot of $\ln(\Delta V_L)$ vs 1000/T at the typical intensity. The barrier height is found to be 0.37 eV.

A typical decay time is shown in Fig. 3 in which two time constants are seen. Our experimental setup limits our ability to measure the fast time constant so that our analysis is based on the slower decay time (5.44 ms) in Fig. 3. The photoconducting decay time (τ_d) is related to the trap emission rate (e_n) by

$$1/\tau_d = e_n = v_{th}\sigma_n N_c \exp[-(E_c-E_t)/kT] \quad (2)$$

where v_{th} is the thermal velocity, σ_n is the thermal capture cross section, N_c is the effective density of states of the conduction band, E_c is the

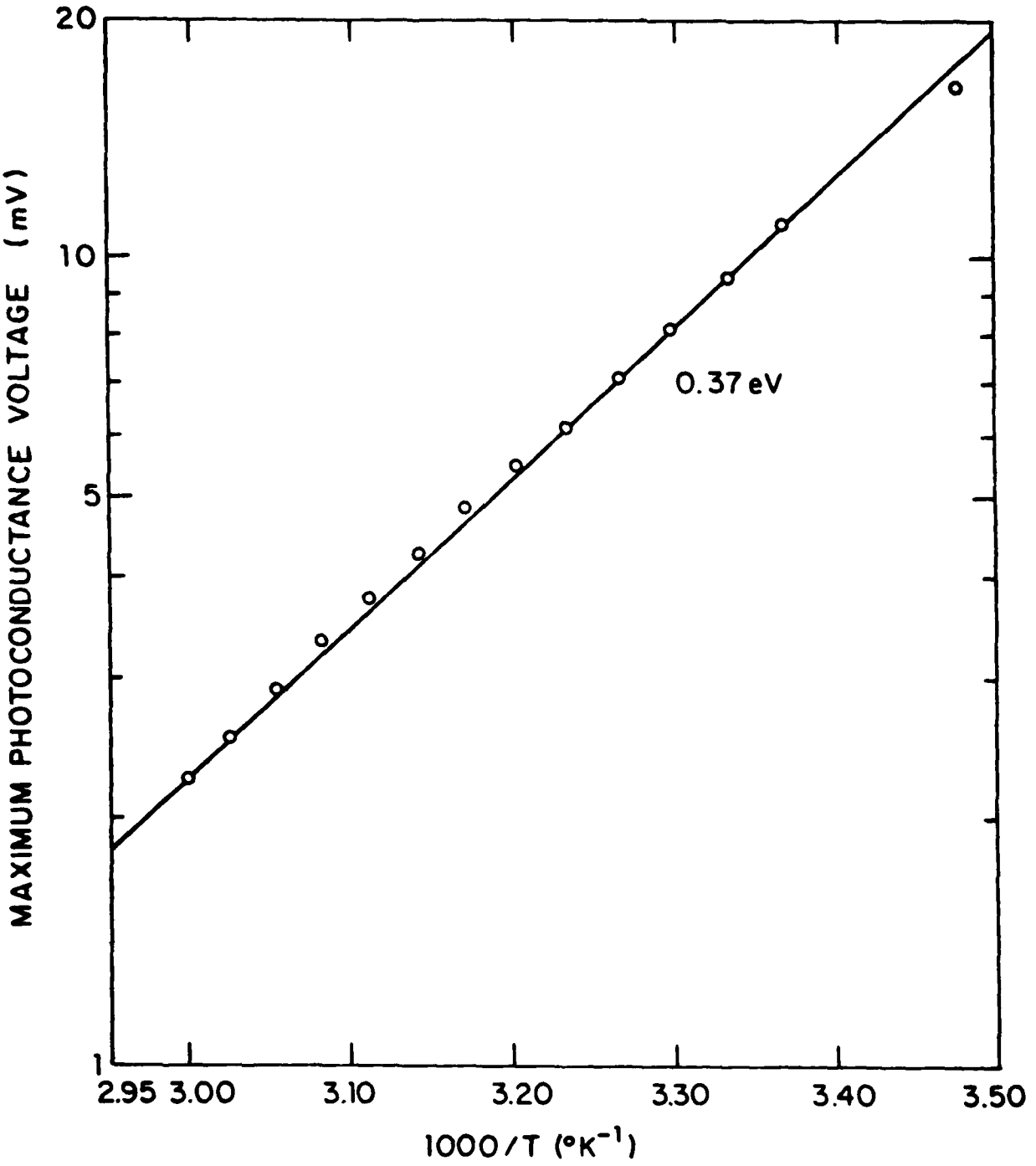

Fig. 2 Maximum photoconductance signals as a function of temperature.

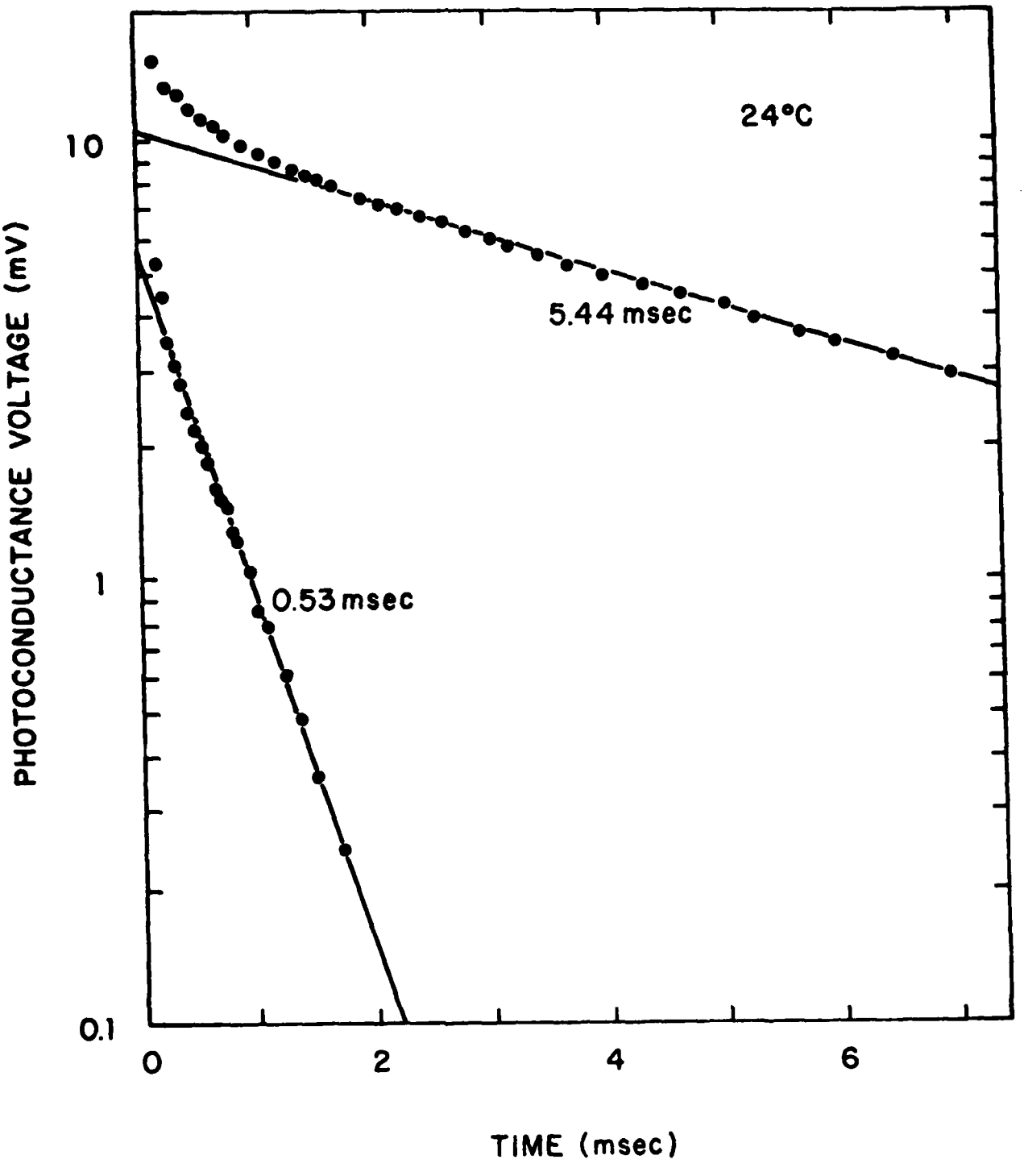

Fig. 3 Transient response of photoconductivity.

conduction-band-edge, E_t is the trap energy, and T is the temperature. Using Eq. (2) and the data in Fig. 4 we obtain an activation energy of 0.5 eV. Since $v_{th} = 10^7$ cm/s and $N_c = 10^{19}$ cm^{-3} at 300°K, we find $\sigma_n = 2 \times 10^{-16}$ cm^2, which is a reasonable value for a deep trap in silicon.

From these experimental data, we have obtained a dominant trap of the donor type at 0.5 V from the conduction-band edge. In a thermal activation experiment performed recently Redfield found that the GB potential barriers increase markedly after annealing at 900 - 1000°C.[5] He concluded that oxygen impurity at the GB's is the only acceptable explanation because oxygen requires low-temperature exposure before segregation at defects occurs.[6] The known energy level of oxygen in silicon is a donor level at 0.51 eV below the conduction-band edge,[7] in remarkable agreement with our measured value. The oxygen segregation at the GB would also explain why the measured GB interface states are not continuous as in the case of SiO_2-Si interface. As for the barrier height, our result is in the range determined from earlier experiments.[8],[9]

An important feature of the present technique is its ability to measure a localized region of defects. In contrast with the capacitance and conductance methods which are capable of measuring materials with a single GB average over a large area, the focused laser beam can probe individual GB in a wafer with many grains and its spatial resolution is limited only by the light beam. In comparison with the electron-beam-induced current (EBIC) technique, the present approach does not require a p-n junction so that materials can be measured without going through a high-temperature process. Thus, influence of device processing can be determined before and after a particular step. Further, the light absorption mechanism is well characterized whereas the electron beam impact on semiconductor remains to be clarified.

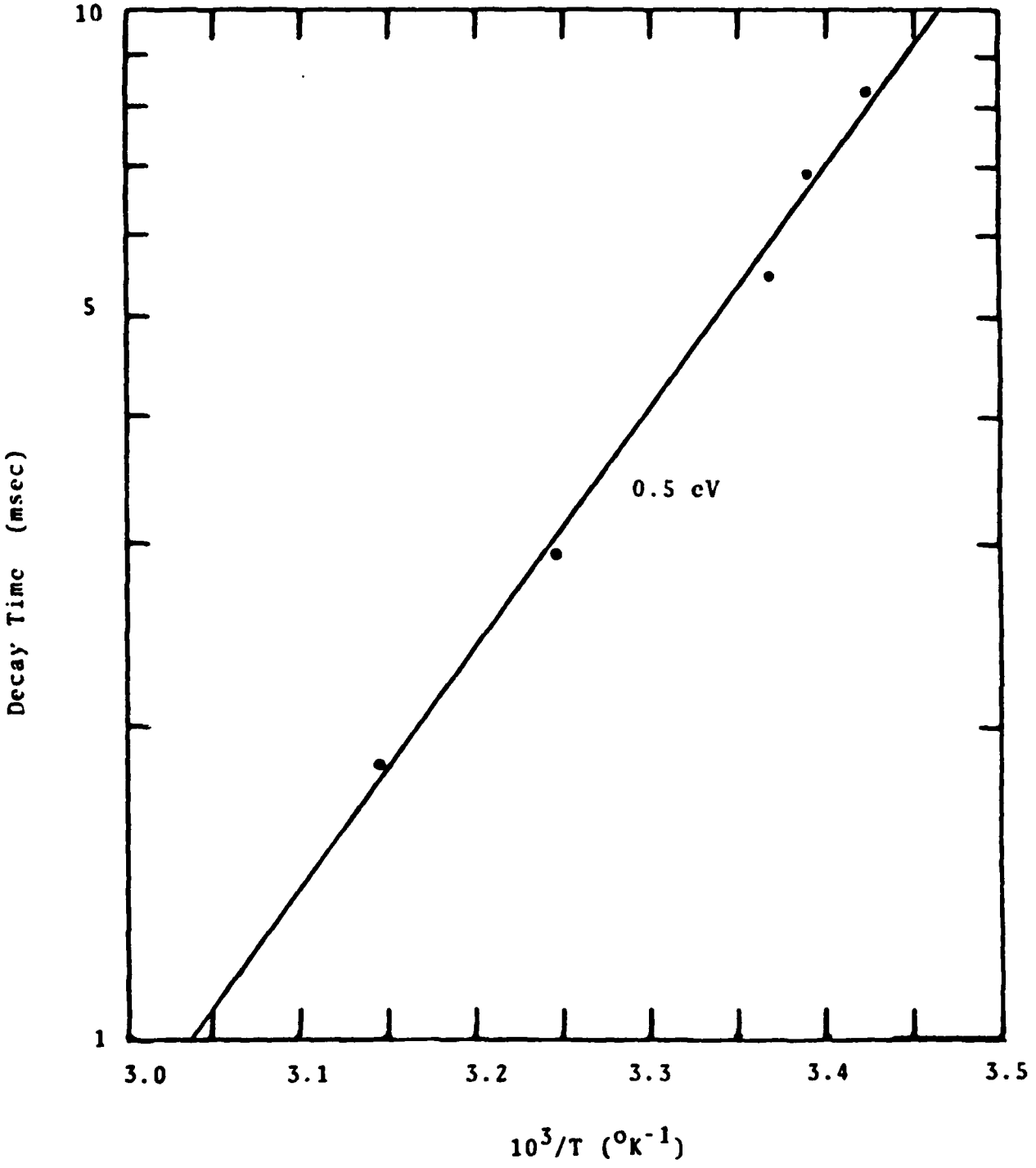

Fig. 4 Photoconductivity decay time as a function of temperature.

In conclusion, the method is simple and has good spatial resolution which is limited by the region activated by the focused laser beam. By observing the steady state transient response, we show for the first time that the photoconductance can be used to calculate the grain boundary trapping states parameters in an unambiguous way.

*This research was also supported by SERI, contract No. XW-1-1272-1 and National Science Foundation grant ECS-81-16163.

(1) C. Mead and L. Conway, Introduction to VLSI Systems (Addison-Wesley, Reading, Mass., 1980).

(2) G. D. Mahan, L. M. Levinson, and H. R. Philipp, Appl. Phys. Lett. 33, 830 (1978); J. Appl. Phys. 50, 2799 (1979).

(3) H. J. Leamy, R. C. Frye, K. K. Ng, G. K. Celler, E. I. Povilonis, and S. M. Sze, Appl. Phys. Lett. 40, 598 (1982).

(4) B. Cunningham and D. G. Ast, in Grain Boundaries in Semiconductors, edited by H. J. Leamy, G. E. Pike, and C. H. Seager (North-Holland, New York, 1982).

(5) D. Redfield, Appl. Phys. Lett. 40, 163 (1982).

(6) K. Nagasawa, Y. Matsushita, and Kishino, Appl. Phys. Lett. 37, 622 (1980).

(7) J. W. Chen and A. G. Milnes, Ann. Rev. Mater. Sci. 10, 157 (1980).

(8) C. H. Seager, G. E. Pike, and D. S. Ginley, Phys. Rev. Lett. 43, 532 (1979).

(9) E. S. Yang, E. K. Poon, C. M. Wu, W. Hwang, and H. C. Card, IEEE Trans. Electron Devices ED-28, 1131 (1981).

G. ETCHING OF SINGLE CRYSTAL GaAs SUBSTRATES BY UV LASER-INITIATED GAS-PHASE PHOTODISSOCIATIONS OF CF_3Br AND CH_3Br

(P. Brewer, S. Halle, R. M. Osgood, Jr.)
(JSEP work unit 5, 1982-1985)
(Principal Investigator: R. M. Osgood, Jr. (212) 280-4462)

The rational behind the use of uv-laser, gas-phase photodissociation in the heterogeneous etching of semiconductor substrates lies in the fact that the initiation of the gas-solid reactions occurs only after the absorption of a uv photon by an inert parent molecule. Various inert-halogen-containing parent molecules have been employed to release reactive halogen atom fragments by uv-photons for etching of amorphous GaAs and InP.[1] In these experiments due to the laser-substrate configuration, the distinction between pure photochemical reactions and laser-surface interactions could not be totally separated. Another approach to gas-phase etching has been in the use of vibrationally excited molecules containing fluorine (F) atoms in etching Si substrates.[2],[3] In the present study bromine atoms ($^2P^o_{1/2}$ and $^2P^o_{3/2}$) are used in the etching of single crystal GaAs by uv laser initiated photodissociation of CF_3Br and CH_3Br.

The nature of the photodissociation of CF_3Br and CH_3Br in the uv region has been summarized.[4] The two primary processes which occur in this region are

$$CX_3Br + h\nu \rightarrow CX_3 + Br(^2P_{1/2}) \qquad X = F \text{ or } H$$
$$CX_3Br + h\nu \rightarrow CX_3 + Br(^2P_{3/2})$$

Leone et al.[5] have found that the quantum yield of the electronically excited $Br(^2P^o_{3/2})$ atoms produced in the photodissociation at 193 nm of CF_3Br to be 0.50. In the case of CR_3Br the increase of the C_2F_6 population as a function of exposure time at 193 nm was measured with an initial pressure of

10 torr of CF_3Br. Shown in Fig. 1 is a plot of the C_2F_6 signal with exposure time indicating a significant portion of the CF_3 radicals are eliminated by bimolecular collisions.

$$CF_3 + CF_3 \rightarrow C_2F_6$$

Early work on gas-phase etching of Si substrates by ir-multiphoton dissociation of CF_3Br indicated that the heterogeneous gas-solid reaction causing etching was the vibrationally excited CF_3 radicals.[2] The evidence from the present experiments indicate that the etching reactions involve the Br atoms with the GaAs substrate. This assumption is based on the similar reactivities of the photodissociate fragments from both CF_3Br and CH_3Br and the likely dissimilar reactivities of CH_3 and CF_3 radicals.

The products of the gas-surface reaction of bromine atoms and the GaAs substrate form liquids on the substrate at room temperature. The effect of the liquid is to coat the surface with a protective film as seen in Fig. 2 where the etch depth as a function of laser power is plotted. In order to eliminate the liquid formation or the GaAs substrates the samples were raised to $T \simeq 100^{\circ}C$.

Two types of experiments were performed with respect to the laser-substrate configuration, positioning in the parallel (indirect) and perpendicular (direct) orientations. The parallel configuration used a focused excimer laser beam positioned between 0.1 mm and 5 mm above the GaAs surface. The etching rate was measured by monitoring the Ga atomic population in the gas phase using a Ga fluorescence line at 417 nm. The detection scheme employed was based on the assumption that the focused excimer laser beam after generating the reactive bromine atoms with one pulse would probe (in the next

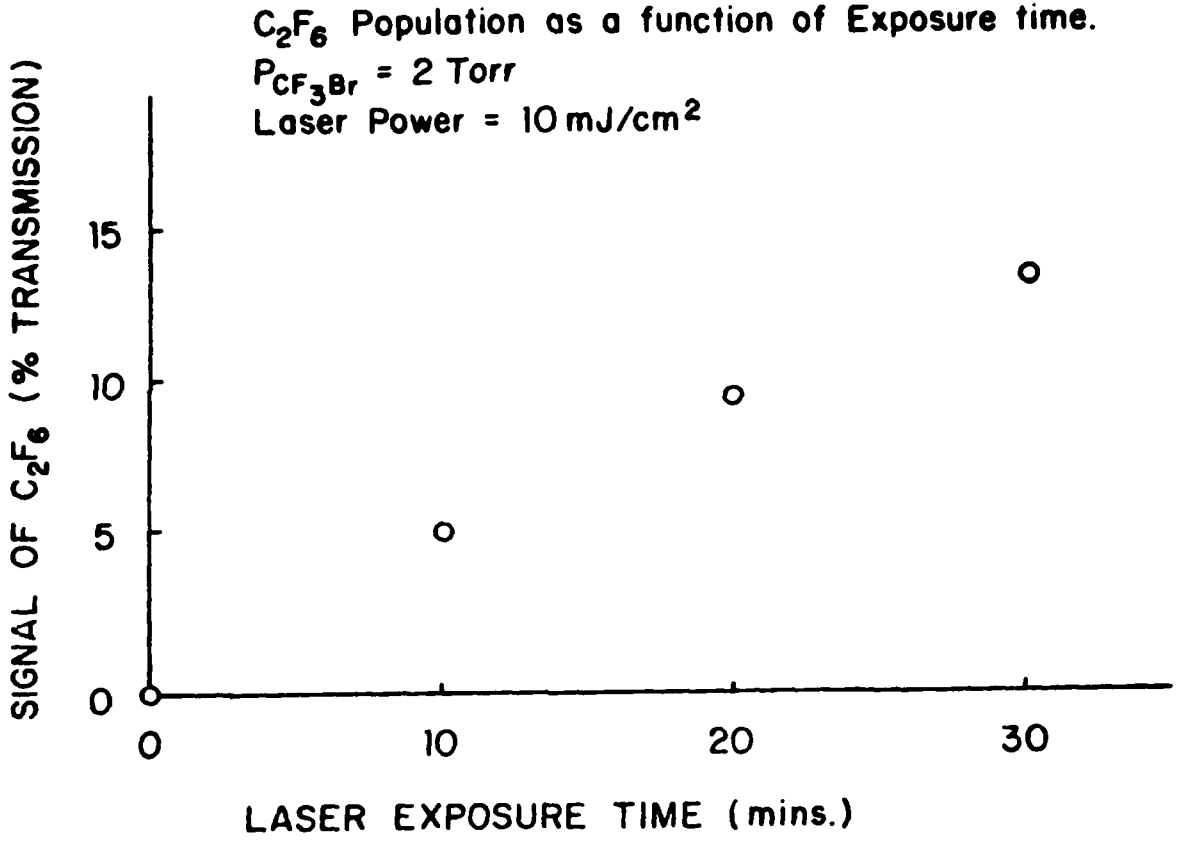

Fig. 1 Shown is the increase in C_2F_6 population as a function of uv-laser exposure time. The exposure time is measured in minutes and the C_2F_6 signal is measured in units of decreased transmission.

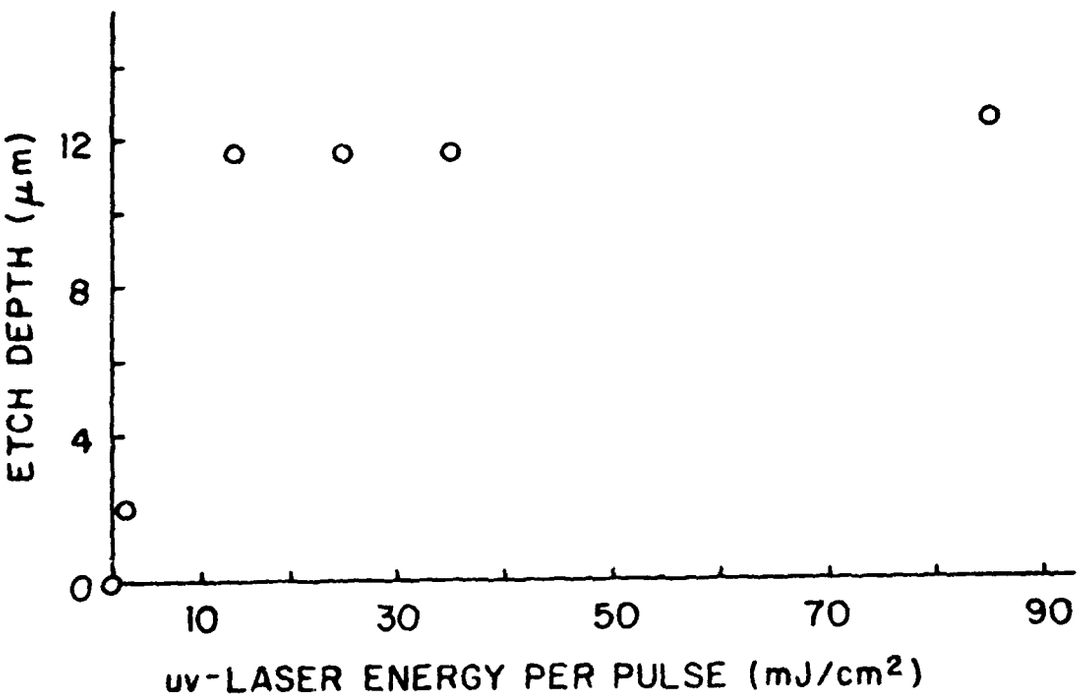

Fig. 2 With the GaAs substrate at room temperature the etch depth was measured as a function of laser power. The direct configuration of the laser-surface geometry was employed in the experiments. The leveling off of the etch depth as a function of laser power is indicative of a "protective covering" forming.

AD-A128 815 RESEARCH INVESTIGATION DIRECTED TOWARD EXTENDING THE USEFUL RANGE OF THE ELECTROMAGNETIC SPECTRUM(U) COLUMBIA RADIATION LAB NEW YORK G W FLYNN 31 MAR 83

2/3

UNCLASSIFIED DAAG29-82-K-0080 F/G 20/3 NL

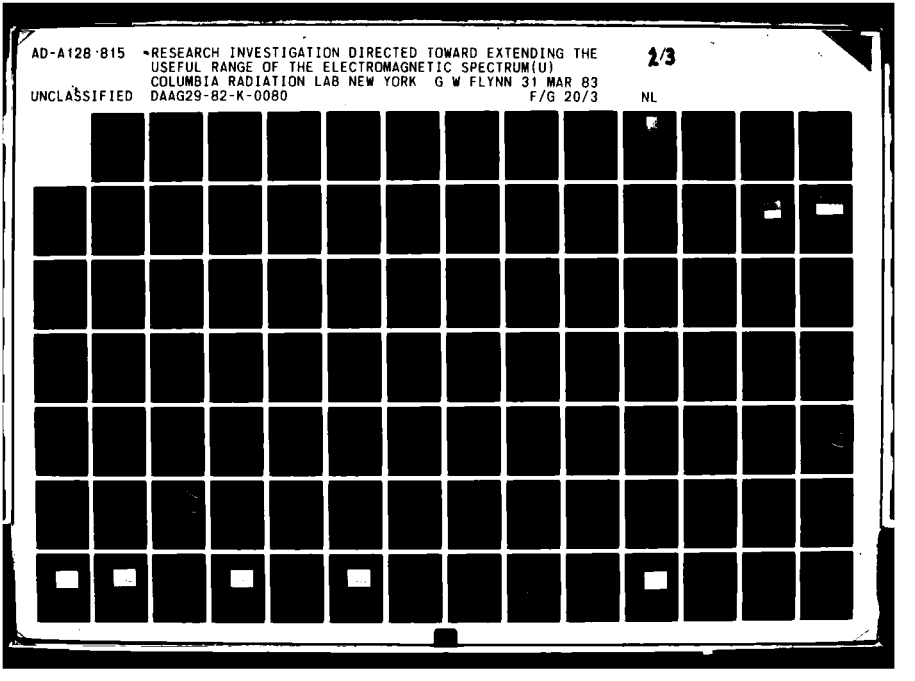

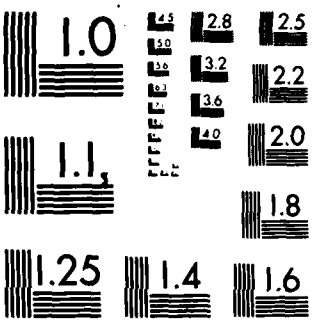

pulse) all Ga and As containing compounds leaving the surface entering the gas phase by multiphoton-dissociating the product compound and exciting the Ga or As atoms produced. Thus by using a static cell, a "steady state" population of Ga or As atoms could be monitored. In Fig. 3 the population of Ga atoms in the gas phase is measured as a function of laser exposure time. Fig. 4 shows the increase of Ga "steady state" population with temperature giving an activation energy of 14.9 Kcal/mole. The etched atom population was insensitive to the position of the laser beam over the GaAs surface. This set of data confirms the "cloud or diffusion" model for the etching reaction. The etch profile of a GaAs (100) surface is characterized by a rough, sawtooth pattern indicative of anisotropic effects. Typical conditions for the indirect (parallel) configuration were: surface temperature ~60°C; laser 20Hz, 350mJ/cm^2 (focused), 15 min exposure; and 7 torr of CF_3Br.

The direct (perpendicular) configuration produced a much more uniform etch with smaller microscopic structures (grain size). The experimental details for a typical direct etch are as follows: surface temperature ~60°C; laser 50Hz, 35mJ/cm^2 (mild focus), 5-10 min exposure; and 7 torr of CF_3Br. The etching of the GaAs was confined mainly to the illuminated area of the sample. Fig. 5 shows a plot of the etch depth as a function of exposure time (laser flux). Strict control of the laser power was required in order to avoid any laser-surface etching by oblation. For long etching times >10 mins the non-illuminated parts of the substrate show etch pits.

This report shows the promise of gas phase etching of single crystal GaAs by uv-laser initiated photochemistry. The method of preference is the direct (perpendicular) configuration due to the small surface microstructure and its applicability to large area etching of GaAs.

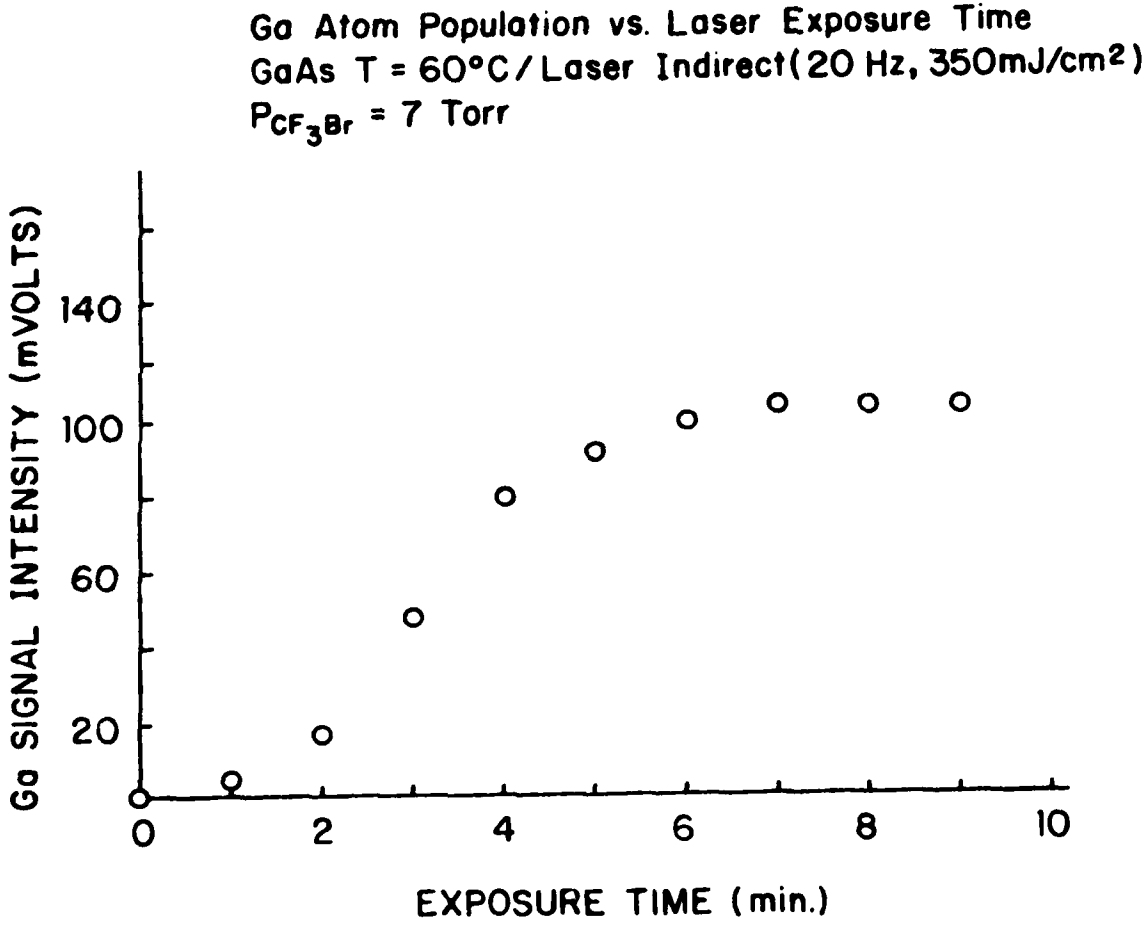

Fig. 3 Ga atom steady state population in gas phase.

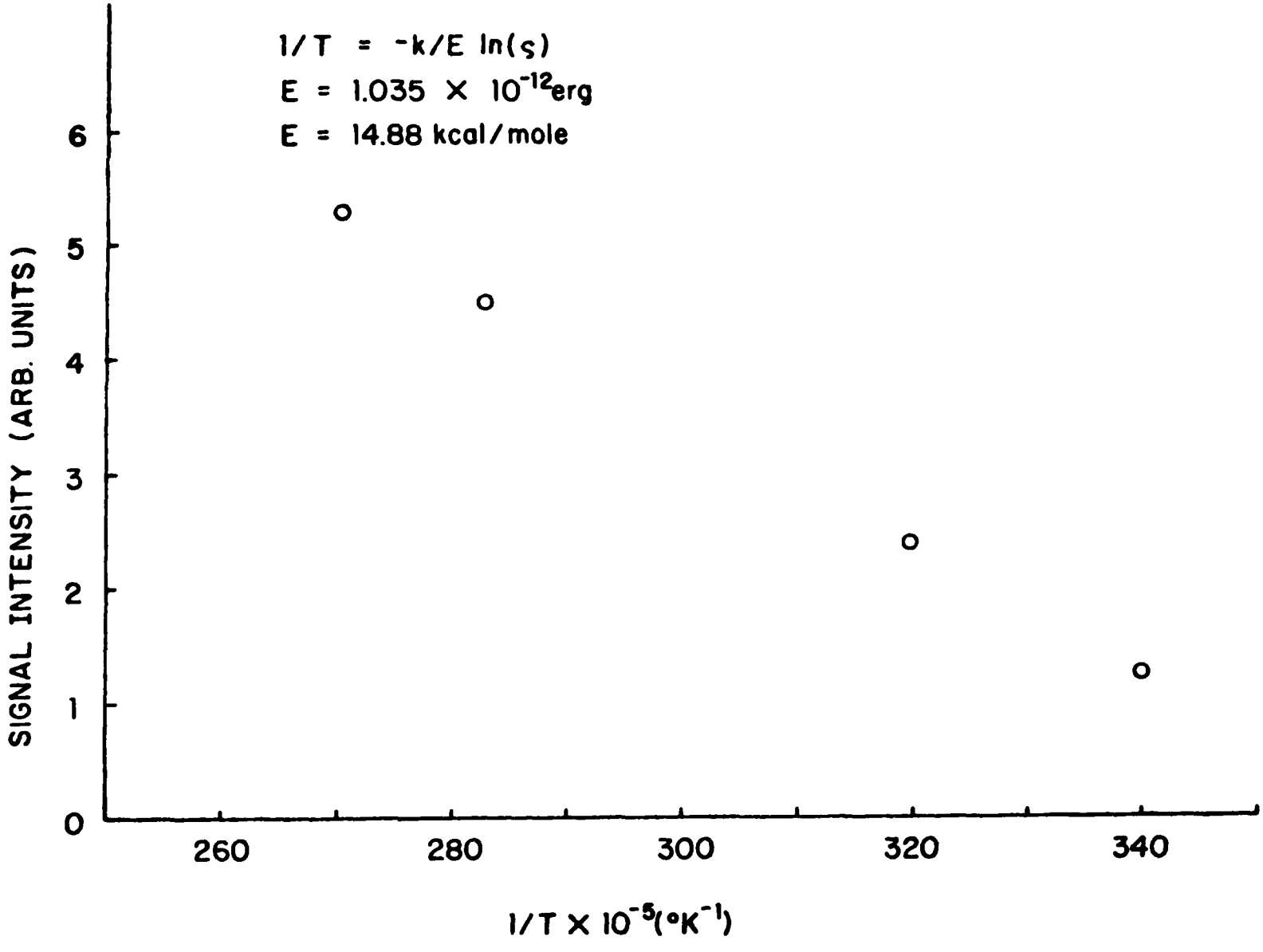
1/T = -k/E ln(s)
E = 1.035 × 10^-12 erg
E = 14.88 kcal/mole
SIGNAL INTENSITY (ARB. UNITS)
0
1
2
3
4
5
6
260
280
300
320
340
1/T × 10^-5 (°K^-1)

Figure 4

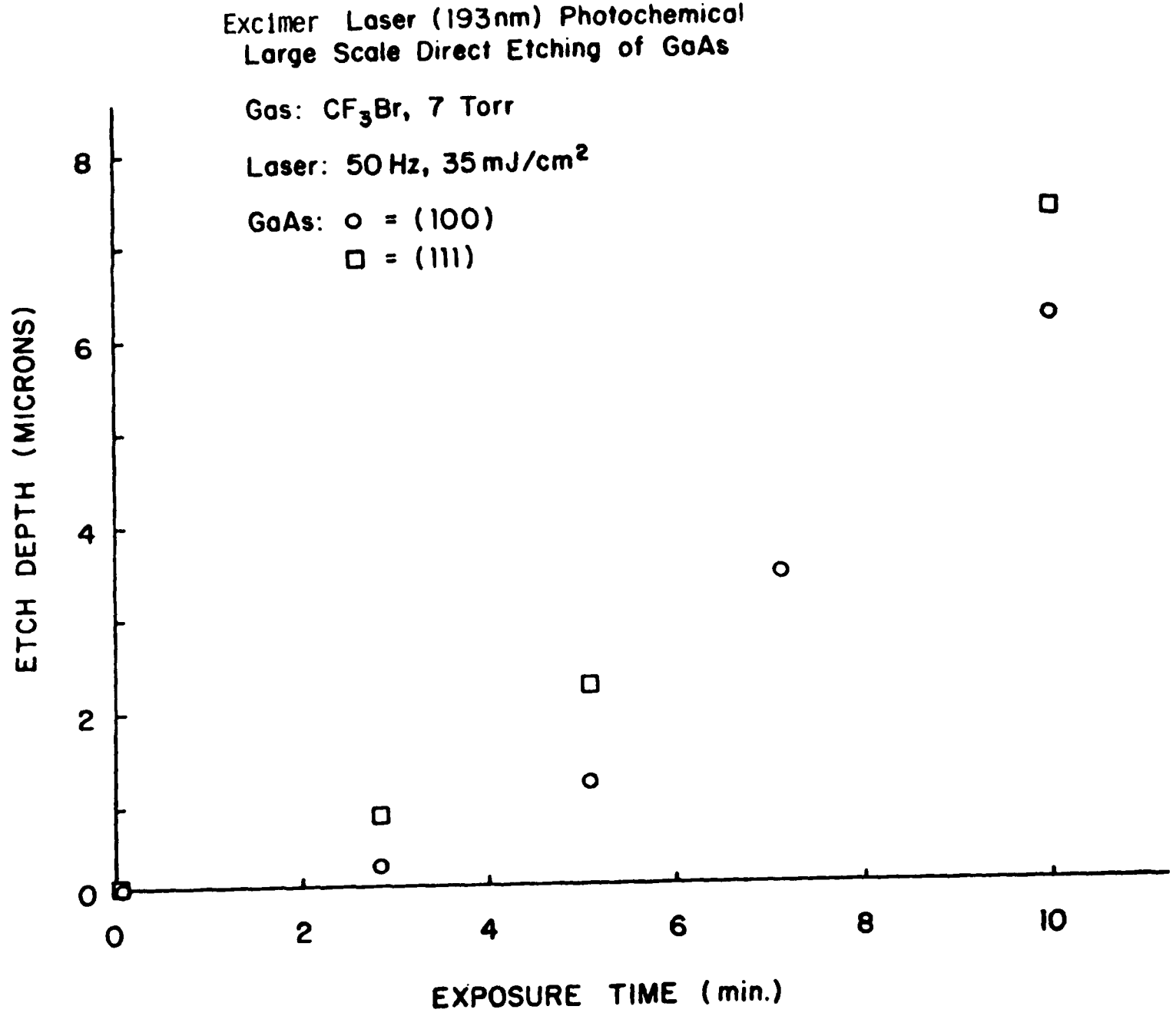
Excimer Laser (193nm) Photochemical
Large Scale Direct Etching of GaAs
Gas: CF_3Br, 7 Torr
Laser: 50 Hz, 35 mJ/cm^2
GaAs: o = (100)
□ = (111)
ETCH DEPTH (MICRONS)
0
2
4
6
8
0
2
4
6
8
10
EXPOSURE TIME (min.)

Figure 5

(1) D. Ehrlich, R. Osgood, and T. Deutsch, Appl. Phys. Lett. 36, 698 (1980).

(2) J. Steinfeld, T. Anderson, C. Reisa, D. Denison, L. Hartsough, and J. Hollahan, J. Electrochem. Soc. 127, 514 (1980).

(3) T. Chaung, J. Chem. Phys. 72, 6303 (1980).

(4) H. Okabe, Photochemistry of Small Molecules, J. Wiley and Sons. NY 1979.

(5) S. Leone, J. Phys. Chem. 85, 3844 (1981).

H. DIRECT OBSERVATION OF A SURFACE-ENHANCED CHEMICAL REACTION*

(C.J. Chen, R. M. Osgood, Jr.)
(JSEP work unit 5, 1982-1985)
(Principal Investigator: R. M. Osgood, Jr. (212) 280-4462)

We have recently published a theoretical study of the optical field near the surface of microscopic, ~200 Å, conducting spheres. The calculations showed that the overall electric field is strongly enhanced if the optical frequency is close to a resonant frequency of the sphere. In addition, the electric field is strongest at the poles of the sphere, where the orientation of the poles is determined by the polarization vector of the light; see Fig. 1. Both the overall and directional enhancements are dependent on the shape, size, and composition of the particle. The growth of the particle by photodeposition is dependent on the electric field at its surface. Thus, there is a coupling between the particles' shape and size and the photo-dissociating electric field. The theoretical study indicates that a spherical particle should grow most rapidly at its poles, transforming itself into an ellipsoid in the process. The final shape of the particle for a relatively short growth period will depend on how close the particle's resonant frequency matches that of the optical field during growth. The final size of the particle is governed not only by the match in frequencies, but also by the optical losses for both very large, 500-1000Å, and very small, 0-50 Å, particles.

In order to observe these effects, we used a collinear observing and illumination microscope, which allowed us to accurately position the sample and observe the deposited film thickness. With this system we observed deposition of Cd from $Cd(CH_3)_2$ molecules adsorbed on Cd spheroids, 10 - 500Å in diameter. These small metal spheres had a resonant frequency close to the

optical frequency of the UV laser at 257 nm.

The metal spheres were made by vacuum depositing the metal in an evaporator filled with a relatively high pressure of argon to encourage gas-phase nucleation. The spheroids were round for small diameters, but incipiently crystalline for large diameter; see Fig. 2. Prior to irradiation with the UV laser light, the spheres, which were mounted on a thin carbon film, were positioned on a fine copper mesh for examination with a TEM. This sample was then placed in a cell chamber and exposed to sufficent $Cd(CH_3)_2$ gas to form an adsorbed film of these molecules on the spheres.

The results of the irradiation are shown in Fig. 3. First, it is apparent that, as predicted, the small Cd spheroids grow into ellipsoids. This growth pattern is in accord with the high electric field at the poles of the particles. Second, although not clearly shown in the figure, the smaller particles do not exhibit rapid growth until after they grow by a much slower process to a critical size of ~50 Å. This latency period is in accord with the optical losses of the small particles. Similarly we find that very large particles, which are lossy because of reradiated light, do not grow rapidly. Fig. 4 shows a recent calculation of this effect based on the theoretical model described above.

In this experiment, we have studied film growth from separately fabricated tiny spheres. However, it is clear that the results obtained are also applicable to the evaluation of small nuclei into macroscopic grains during photodeposition.

*This research was also supported by the Army Research Office under Contract DAAG29-82-K-0009.

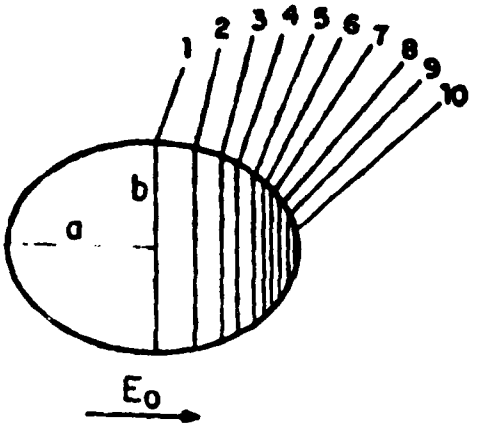

Figure 1

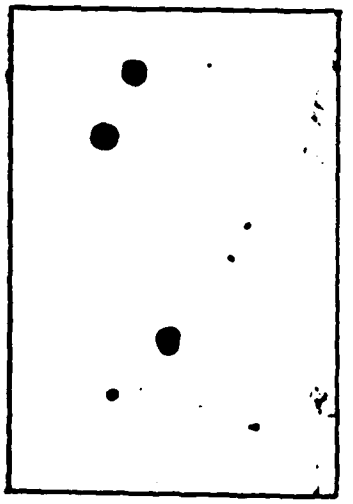

Figure 2

Figure 3

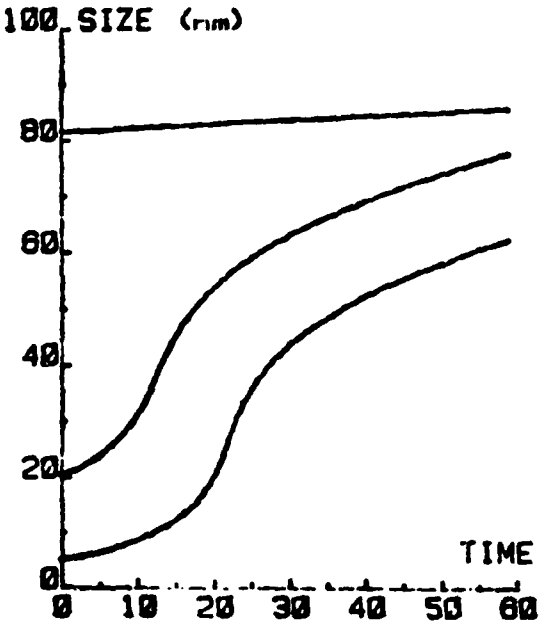

Figure 4

I. LASER-CONTROLLED PLASMA ETCHING*

(G. Reksten, W. Holber, R. M. Osgood, Jr.)
(JSEP work unit 5, 1982-1985)
(Principal Investigator: R. M. Osgood, Jr. (212) 280-4462)

Introduction of light into a semiconductor processing chamber allows one to control the spatial extent and chemical reactions in the chamber. One can envision experiments with laser controlled CVD, MBE, etc. We have recently begun experiments to determine the extent to which visible laser light can be used to control etching of semiconductor wafers in a plasma etching machine. The enhancement can be based on surface or gas-phase heating, a laser-beam generated photovoltage, local ionization, or surface desorption.

A commercial plasma etcher (Technics Model PE II) was used in the experiments described below. The etch rate of n-type phosphorous doped Si in a CF_4 plasma was measured as a function of CF_4 pressure and r.f. power. A 2W argon ion laser (C.W.) was then used in conjunction with the plasma etcher and the effect of the laser beam on the etching process was investigated.

a) Experimental arrangement

A schematic of the plasma etcher and the optical path of the Ar^+ laser beam arrangement is shown in Fig. 1. The r.f. power applied to the electrodes could be varied from 0-300 W and the r.f. frequency of this particular model was 30 kHz. The wavelength of the cw argon ion laser was 514 nm (green) and the maximum power available was 2 W.

In order to find the optimum CF_4 pressure, several Si samples were etched at CF_4 pressures ranging from 50-500 mTorr. The r.f. power was kept constant at 180 W, an arbitrarily chosen value. The resulting curve of etch rate versus pressure is shown in Fig. 2. The maximum etch rate was obtained at a CF_4 partial pressure of 100 mTorr.

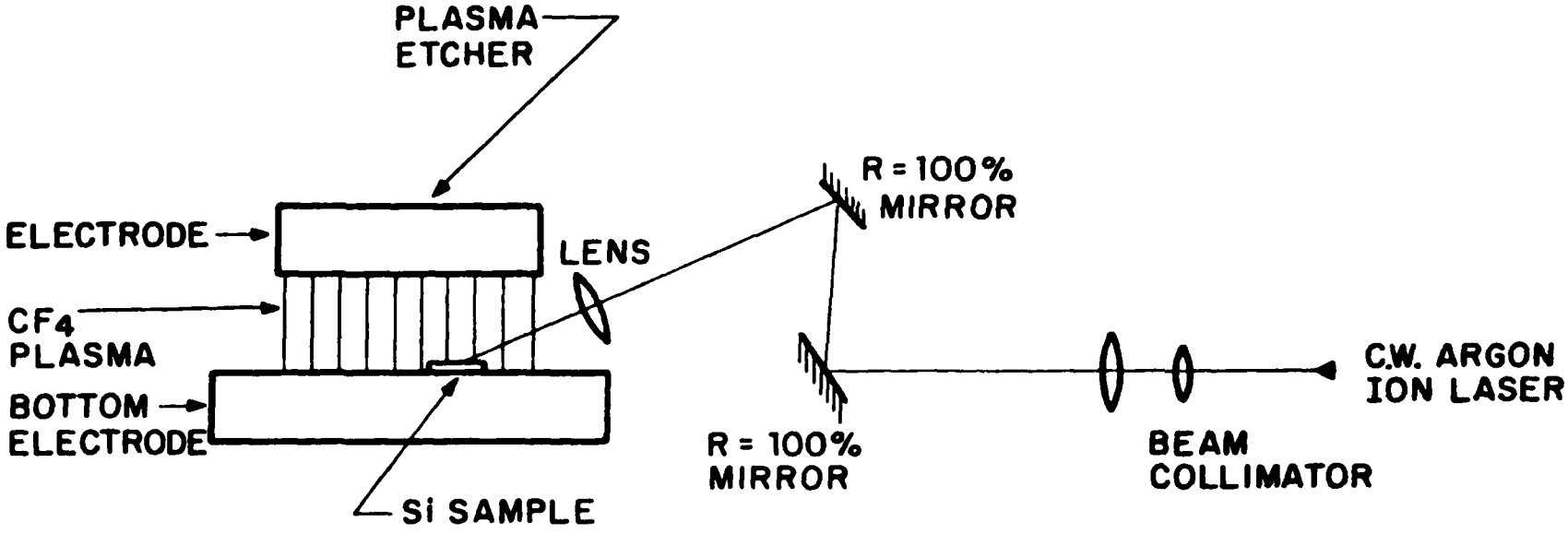
PLASMA
ETCHER
ELECTRODE
LENS
R = 100%
MIRROR
CF4
PLASMA
BOTTOM
ELECTRODE
Si SAMPLE
R = 100%
MIRROR
BEAM
COLLIMATOR
C.W. ARGON
ION LASER

Figure 1

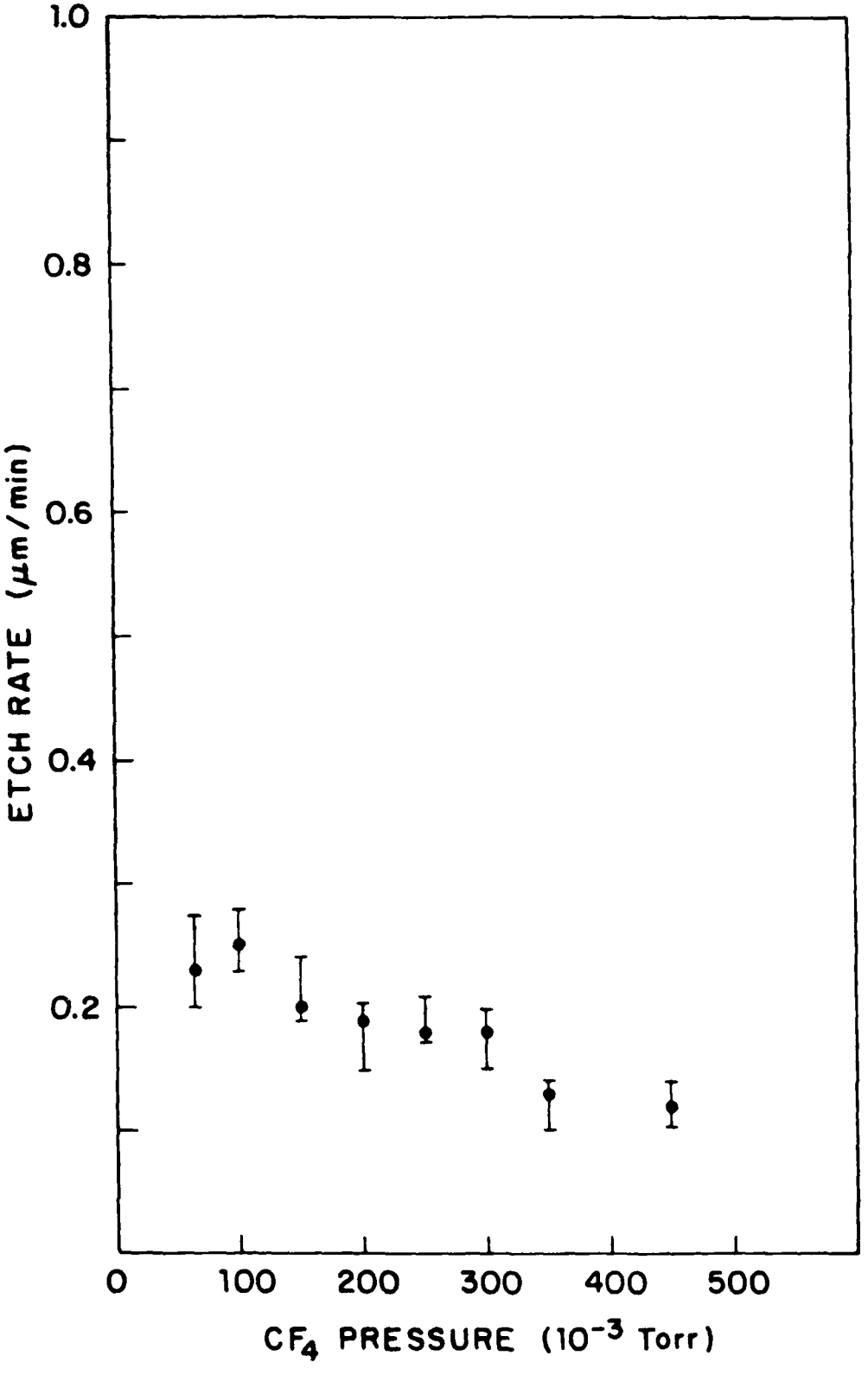
1.0
0.8
0.6
0.4
0.2
ETCH RATE (μm/min)
0
100
200
300
400
500
CF4 PRESSURE (10-3 Torr)

Figure 2

b) Etch rate vs. r.f. power

The above experiment was repeated, this time keeping the CF_4 pressure constant at 100 mTorr and ranging the r.f. power from 50-300 W. The resulting etch rate versus r.f. power curve is shown in Fig. 3. At powers > 100W the etch rate increases linearly with r.f. power.

c) Laser-plasma etching

The effect of the argon ion laser beam on the Si etch rate was investigated using the experimental arrangement shown in Fig. 1. The laser beam was focused onto the Si sample with the aid of a beam collimator and a lens placed inside the etching chamber, but outside the plasma. Ideally the angle of incidence should be closer to 90°, this was however not feasible due to the geometry of the Technics plasma etcher. For every measurement made, a second Si sample was placed near the laser-irradiated sample for comparison purposes. The Si wafers were masked with an aluminum dot pattern (1.5 μm thick.) This pattern stayed intact after the etching process.

Twenty minute runs were then made with the r.f. power constant at 180 W and the CF_4 pressure constant at 100 mTorr - while the laser power was varied from 0.25-2.0 watts. The aluminum mask was then removed and the etch depth measured on both the irradiated and unirradiated sample.

The data resulting from this experiment is plotted in Fig. 4. The plot shows that at high laser powers the etch rate increases dramatically due to the laser. It should be noted that the laser enhances the etch rate over the <u>entire</u> Si sample (7 mm X 7 mm) even though the laser was focused to a spot of 1 mm diameter. Further experiments are needed to explain this and to obtain more data for a more complete etch rate versus laser power curve.

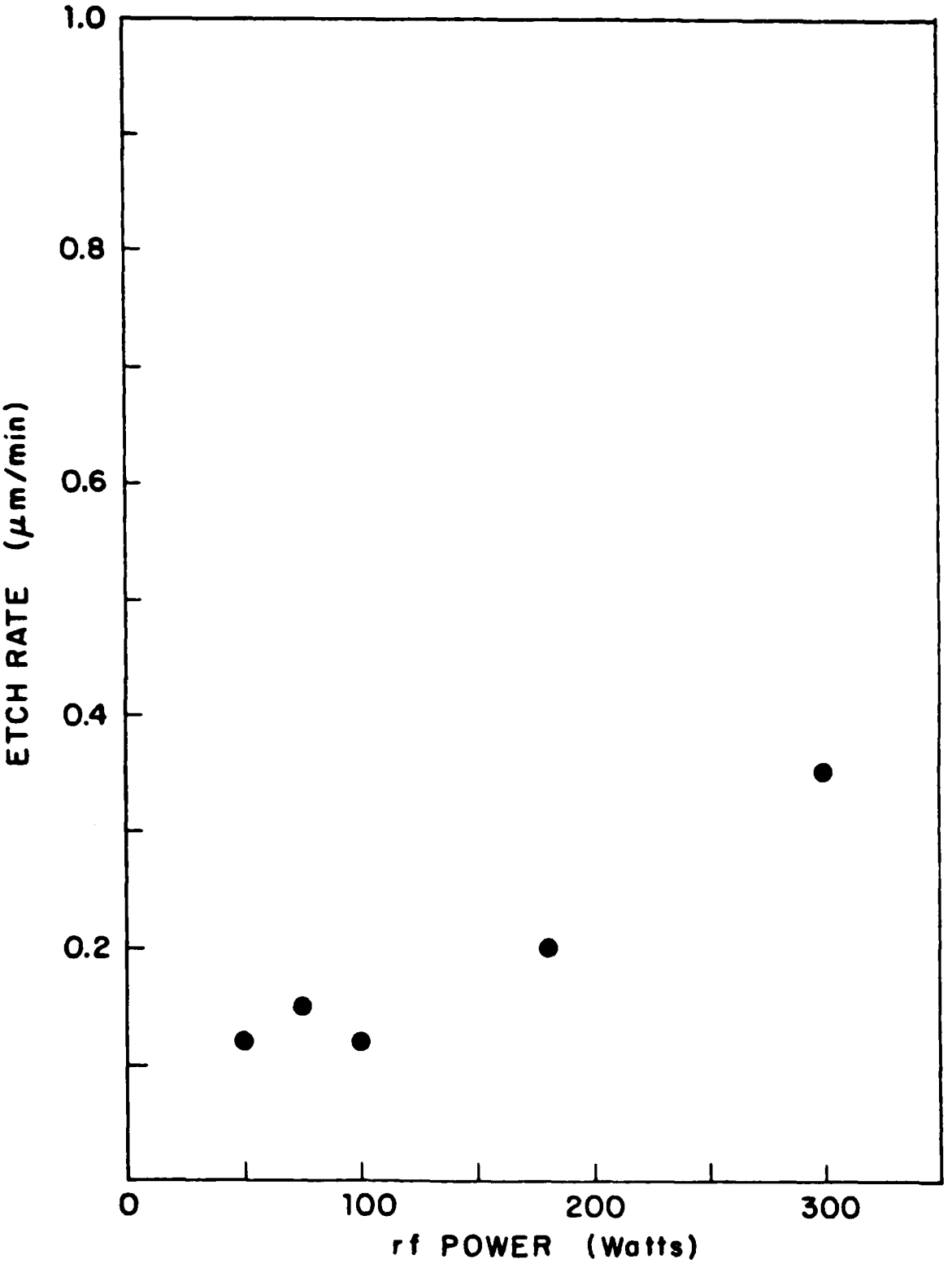

Figure 3

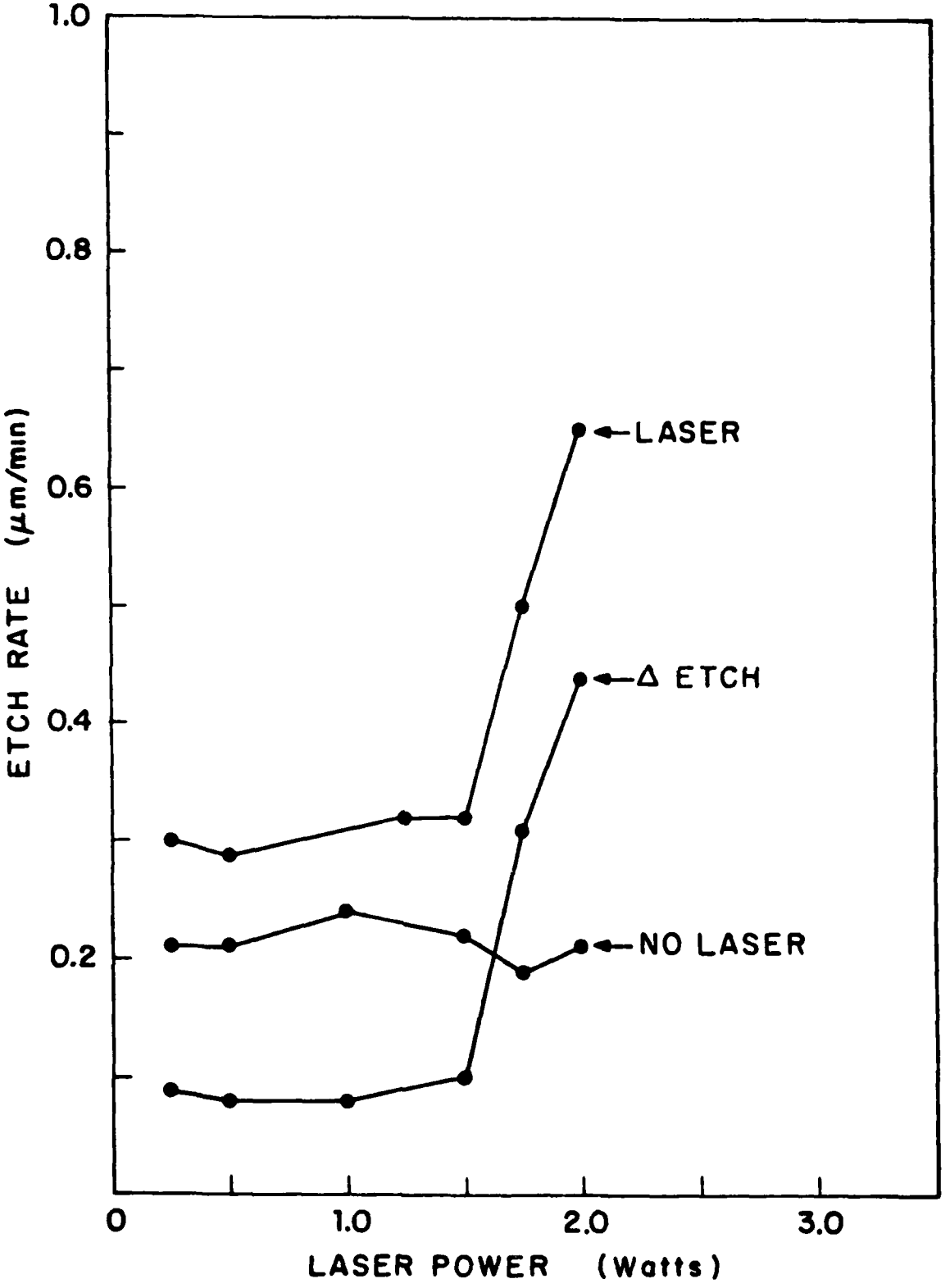
1.0
0.8
0.6
0.4
0.2
ETCH RATE (μm/min)
LASER
Δ ETCH
NO LASER
0
1.0
2.0
3.0
LASER POWER (Watts)

Figure 4

A second "bulk effect" was also observed. At high laser powers (above 1W) the surface roughness over the entire etched Si piece decreased markedly. Surface roughness of Si etched with CF_4 has been reported by other workers when reactive ion etching is employed and from our results we see that laser irradiation may have a positive effect on this problem.

At high laser powers, an etch fit of the focused laser could be seen. The microscope revealed that this mask had a fringe structure which serves to illustrate the potential resolution of this etching method.

*This research was also supported by the Air Force Office of Scientific Research/DARPA under Grant F-49620-82-K-0008.

J. OPTICAL TECHNIQUES FOR INSULATOR FORMATION*

(R. Krchnavek, H. H. Gilgen, R. M. Osgood, Jr.)
(JSEP work unit 5, 1982-1985)
(Principal Investigator: R. M. Osgood, Jr. (212) 280-4462)

Low-temperature oxide formation is a desirable capability in planar processing of microelectronics. The normal high-temperature growth used in standard silicon processing results in the bowing of silicon wafers and prevents the use of photolithographic lift-off techniques for oxide patterning. For direct writing, low-temperature formation is also an important capability because it prevents thermal alteration or damage in a region adjacent to that being processed.

We have recently demonstrated that it is possible to use a pulsed laser to form an SiO_2 structure from a thin layer of silicate which is spun on the wafer. This approach was begun in collaboration with Allied Corporation in Morristown, NJ, which provided the silicate. The technique works by spinning on the silicate which is solvated in an organic liquid; a patterned oxide film is then produced by exposing the film to approximately 0.3 J of UV light at 193 nm.

The writing apparatus used was that described in the previous section. The quality of the oxide line pattern depends sensitively on the laser power and techniques used for removing the untreated spin-on material from the wafer.

Infrared spectroscopy has been used to study the oxide layers produced on single-crystalline silicon using a spin-on silicate subsequently irradiated with an ArF pulsed excimer laser (193 nm). Figure 1 shows the IR spectra of thermally prepared silicates.

Curve A is obtained with the fresh silicate as spun onto an Si wafer; the reference signal is from a bare Si wafer. Curve B shows the coating after a

Thermal SiOG

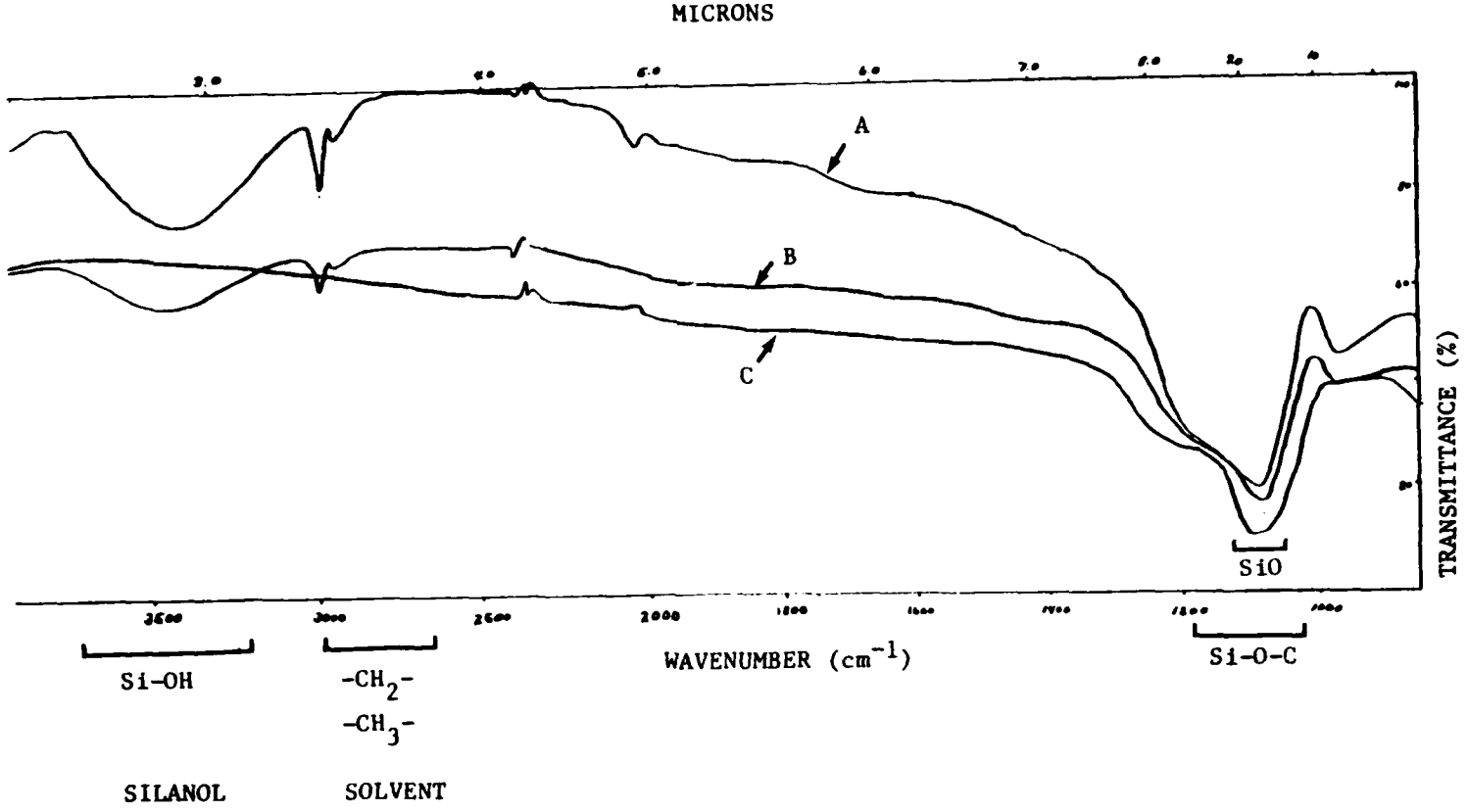

Figure 1

150°C-15 min prebake; it shows a reduction in the CH_2 and CH_3 liganda which is due primarily to volatizing of the solvent. After baking in an oven, Curve C, the CH_2 and CH_3 peaks are completely gone. We also see a decrease in the SiOH (silanol) peak although it is somewhat hidden because of the SiO bonds in curves A+B.

Fig. 2 shows the results after laser irradiation (curve A) and laser irradiation with subsequent baking (curve B). Close examination of these curves shows that the excimer irradiation acts as a low temperature cure. Repeated exposure times did not change the spectrum. Further work will include a measurement of higher UV exposures.

Breakdown voltage tests on irradiated samples show values similar to thermally prepared organosilicate samples (1-2 10^6 V/cm) and slightly less than the published value for thermally grown SiO_2 (10^7 V/cm).

*This research was supported by the Air Force Office of Scientific Research/DARPA under Grant F-49620-82-K-0008.

ArF Laser - SiOG

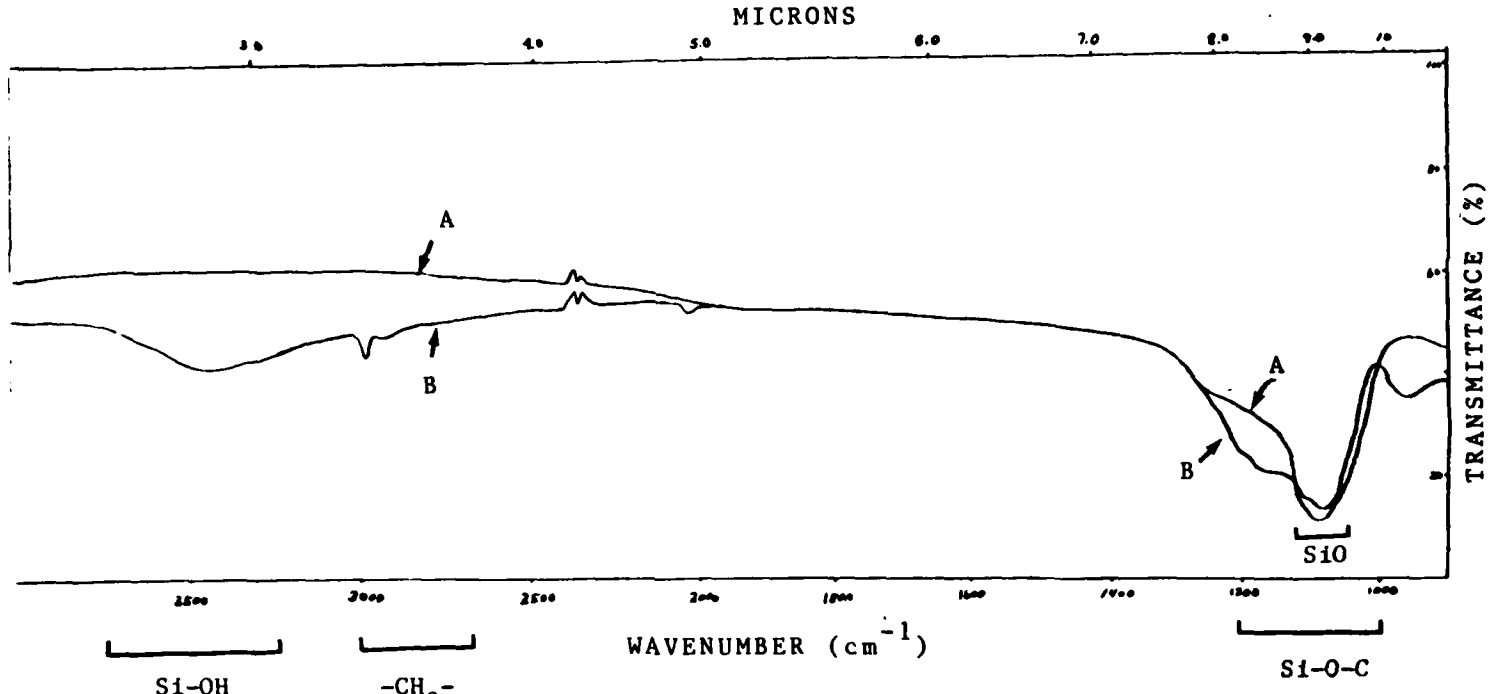

Figure 2

K. MASKLESS FABRICATION OF SUBMICROMETER GRATINGS*

(D. Podlesnik, H. H. Gilgen, and R. M. Osgood, Jr.)
(JSEP work unit 5, 1982-1985)
(Principal Investigator: R. M. Osgood, Jr. (212) 280-4462)

Recent interest in guided-wave optics and distributed feedback lasers has prompted the need for producing gratings with periods on the order of 100 nm on semiconductor materials. Other applications include surface acoustic wave devices and negative-resistance electron devices. Currently, there are two conventional methods for grating fabrication: holographic lithography and electron-beam lithography. With the former method, gratings with spacing as small as 110 nm have been produced; however, this technique is cumbersome, and grating periods are generally restricted to be greater than 180 nm. With the electron-beam technique, gratings with periods less than 100 nm can be produced. But, this method is limited by the difficulties of producing uniform large-area structures and the long exposure times, which, for a 300 nm grating, can be as long as one hour per square millimeter. Both methods involve multiple steps. In addition, for both methods, photoresist residues cause contamination problems, limiting their use in electro-optical applications.

In the present paper we describe a technique for producing submicrometer gratings by a holographic method with direct chemical etching in an oxidizing etch. The resolution of this technique is comparable to those of other methods. Furthermore, this method is a single, one-step process using very low laser intensity. Both uniform large-area gratings and special grating profiles, e.g. blazed, can be easily fabricated.

The anodic dissolution of a semiconductor in an oxidizing etch is generally influenced by the number of carriers present at the surface. Since light incident on the semiconductor surface produces electron-hole pairs,

a pattern of light produces a corresponding pattern of available carriers. The photogenerated carriers, typically holes for n-type GaAs, control the etching rate of the semiconductor, producing an engraved pattern in its surface. The resolution of the etching process may be shown to be a direct consequence of rapid normal electric field, due to the semiconductor band bending at the interface. Our results show that 170 nm gratings are easily obtained and we anticipate that with an appropriate optical arrangement, a resolution below 100 nm is possible.

a) Experiment

The actual experimental arrangement used for the holographic exposure is shown in Fig. 1. A laser beam from an argon-ion laser emitting at 514.5, 488.0, or 457.9 nm passes through a spatial filter. The filtered beam is incident on a right angle corner on which a mirror and a semiconductor sample are mounted. The corner is inside an optical cell containing an etching solution. The interference pattern is produced by the superposition of the direct and the reflected beams inside the solution. The grating period, s, is given by

$$s = \frac{\lambda}{2n \sin\theta_i} \qquad (1)$$

where λ is the free-space wavelength of incident light, n is the index of refraction of the solution and θ_i is the incident angle on the sample surface. The incident light is s-polarized. After passing through the spatial filter, the laser beam goes through the window of the optical cell, and it is, therefore, desirable to match as much as possible the indices of refraction of the solution and the window in order to reduce spurious

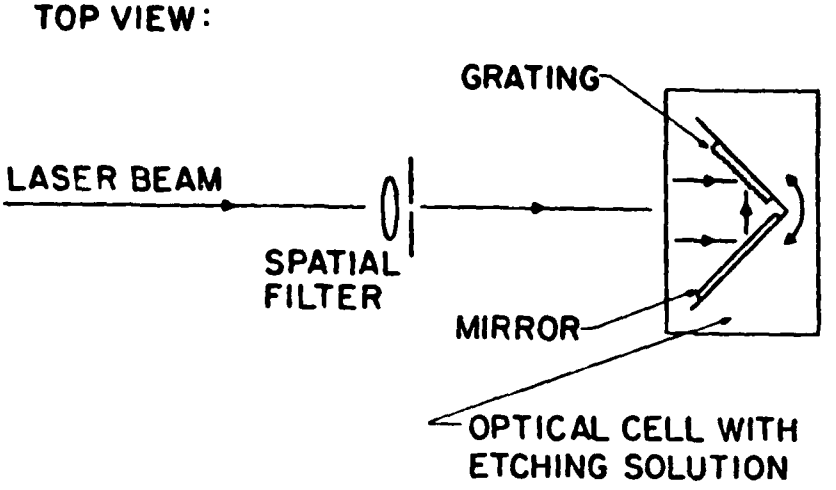

Fig. 1 Experimental arrangement for grating fabrication by direct chemical etching.

interference patterns.

The experiments were done on various GaAs crystals. A comparison was made of etching gratings on n-type (10^{18} cm^{-7}) and semi-insulating GaAs of (100) and (111) orientations. On all samples, good quality and small-period gratings were produced. Figure 2 shows an SEM photograph of 200 nm grating on n-type GaAs. Using the 457.9 nm line we have recently obtained gratings with a 170 nm period. In a separate experiment, we obtained the blazed grating shown in Fig. 3. The approach was to tilt the substrate so that the bisector of the angle of interference was at an angle with respect to the surface normal. This tilting of the interfering beam in conjunction with the continuous dark etching effect, which progresses normal to the surface, produces the clear blazed profile shown in the figure. The profile is triangular or cusped depending on the relative magnitude of the dark and light-enhanced etching rate.

Although several different etching solutions (e.g. NH_4OH, H_2O_2, and H_2O, or KCl, HCl, and H_2O) were used, most of the work was done with the following solution: H_2SO_4, H_2O_2 and H_2O. Since we were primarily concerned with grating periods less than 400 nm, it was necessary to choose an etch composition with a sufficiently slow dark etching rate, so that the products of the etching reaction would not interfere with the development of the grating. Based on an initial measurement of the dark and light-enhanced etching rates for different compositions, we selected the following composition for our experiments: H_2SO_4: H_2O_2: H_2O = 1:1:50.

Finally, in collaboration with a project at Lincoln Laboratory, headed by Dr. Antonio Sanchez, we have explored applying the same etching techniques to CdS. One of the more important findings has been that photochemical grating formation is most effective when etching a crystalline plane parallel to a

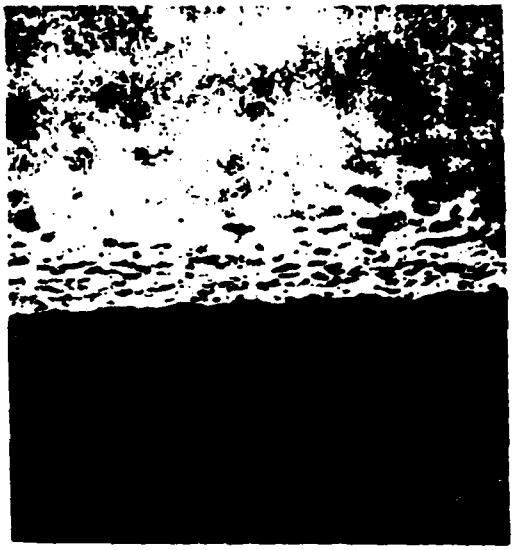

Fig. 2 The SEM photograph of the profile of a 200 nm grating on n-type GaAs.

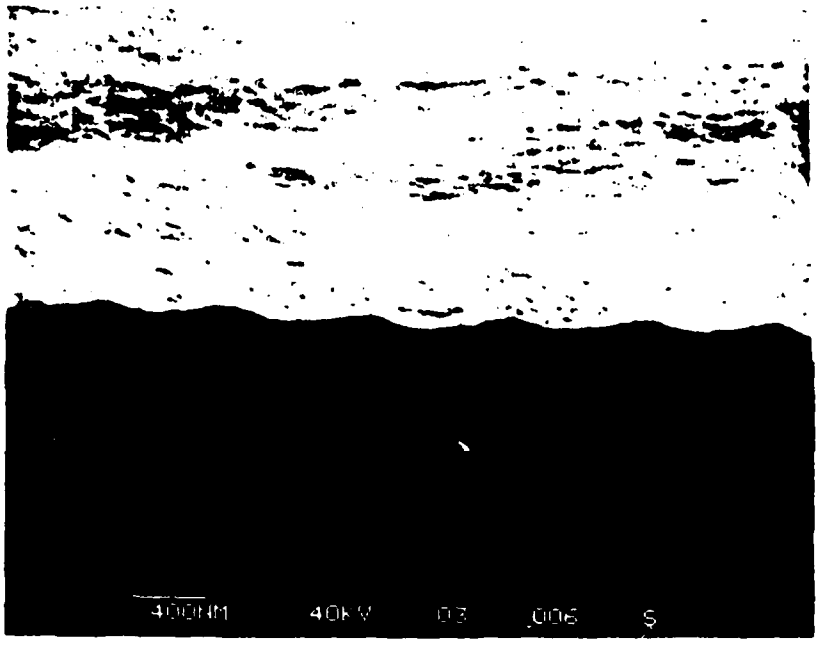

Fig. 3 SEM photograph of 500 nm blared grating on n-type GaAs.

prismatic face of the CdS. In the Lincoln Laboratory project, the grating is necessary to produce distributed feedback to a blue-green, electron-beam-pumped laser. As a result, the requirement for orientation of a specific crystal to form the grating will also determine the crystal orientation of the laser.

b) Metallic Gratings

In addition, we have used the interferometric technique described above in conjunction with the organometallic gas-handling system, built as part of a separate JSEP project, to demonstrate the direct deposition of metallic gratings. Even in the preliminary experiments the resolution of these gratings is comparable to best values obtained by state-of-the-art photolithographic techniques. Experiments to further explore the fabrication of these gratings are currently being planned.

*This research was also supported by the Air Force Office of Scientific Research/DARPA under Grant F-49620-82-K-0008.

L. SPECTROSCOPY OF ORGANOMETALLIC MOLECULES ON SURFACES*

(C. J. Chen, and R. M. Osgood, Jr.)
(JSEP work unit 5, 1982-1985)
(Principal Investigator: R.M. Osgood, Jr. (212) 280-4462)

Since the development of laser photochemical direct writing, there has been an increasing interest in understanding the UV photodissociation mechanism of organometallic molecules. While gas-phase ultraviolet absorption spectra can provide significant information on the dissociation process, the existing spectroscopic data are not complete and an analysis of the excited states has not been made. Although one observation of the chemisorbed monolayer of DMCd (dimethyl cadmium) has been reported the spectrum of the physisorbed molecular layer has not been measured. The difficulty of measuring the spectrum of the physisorbed layer stems from the fact that at high temperatures the physisorbed layers always coexist with a relatively dense ambient gas. As a consequence, the spectrum of the adlayer is obscured by that of the gas.

We have recently begun a study of the UV spectroscopy of adsorbed metal-alkyl molecules. The spectra, which include both the chemisorbed and physisorbed layers, can be interpreted by comparison with our recent measurements of gas-phase metal alkyl molecules as well as by an analysis based on molecular-orbital considerations.

Essentially the apparatus consisted of a carefully designed UV monochromator and a precision multisurface cell. A nitrogen-purged, 0.3-m scanning monochromator with a 1200-groove-per-millimeter grating and a deuterium lamp provides a spectrally-tunable UV probe with 0.6Å resolution. The power supplies for the anode and the filament of the deuterium lamp are both highly stabilized to provide a constant light intensity. A PDP-11 microcomputer controls the scanning of the monochromator, collects and stores

the readings of the photomultiplier, and then performs scheduled computation.

The absorption cell is made of 316 stainless steel with both ends precisely ground. Ten to thirty suprasil (fused silica) discs can be fit in the cell, separated with C-shaped spacers of 25-μm thickness. The cell is enclosed in a copper thermal enclosure with thermal insulation. The temperature of the cell is regulated to within $\pm$ 0.2°C by a dry-ice bath and an electronic thermal controller.

The gas-handling system, with a diffusion pump, is made of stainless steel. It was baked to 200° C in vacuum before use. The cell is directly connected with the gas-handling system. The pressure is read with a digital capacitance manometer to 0.01 torr.

a) Gas Spectra

The gas spectra of DMZn, DMCd and DMHg are shown in Fig. 1. In general, the overall structure of each spectrum is similar; each consists of a weak absorption knee and a strong peak with almost equally spaced bands. However, for DMCd, another weak absorption peak in the short wavelength region is apparent. We will not discuss the detailed assignment of the electronic states here; instead, only our general conclusions will be summarized. Absorption in weak feature at the long wavelength end leads to the immediate formation of a metal atom in the ground state and two methyl radicals. The strong absorption feature, whose cross section is typical for an allowed dipole transition, produces a methyl radical and an excited metal monomethyl which dissociates after radiative emission to the ground state. A third feature is just observable on the blue side of the strong absorption band. In this UV band, the photon energy exceeds the sum of the dissociation energy of the molecule into an excited metal atom and two methyl radicals.

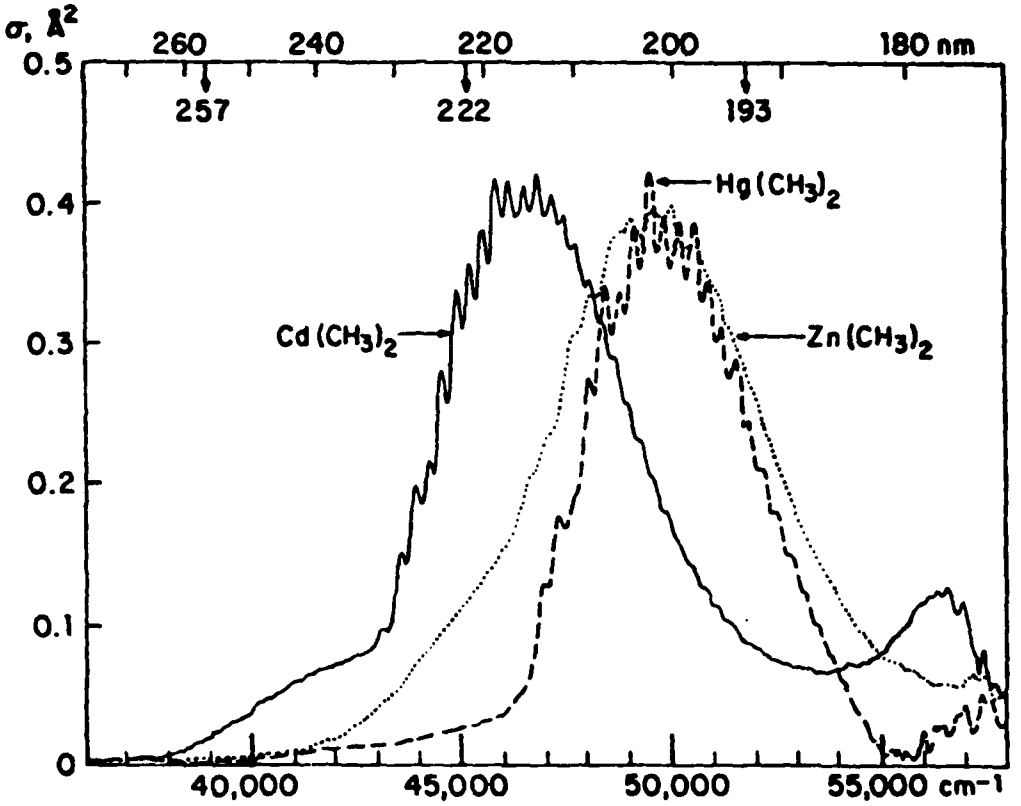
σ, Å²
260
240
220
200
180 nm
257
222
193
0.5
0.4
0.3
0.2
0.1
0
Hg(CH3)2
Cd(CH3)2
Zn(CH3)2
40,000
45,000
50,000
55,000 cm-1

Figure 1

b) Spectra of the Chemisorbed Monolayer

In the case of DMCd, a chemisorbed monolayer forms first on the substrate. Since this layer cannot be removed by pumping, the measurement is simple, requiring no subtraction of the gas spectra (Fig. 2). Note that there is no chemisorbed layer for the related-compound DMHg. This is consistent with the fact that, unlike DMCd, DMHg is air and moisture stable. We believe that the DMCd reacts with the OH radical on the silica surface and produces cadmium monomethyl with its cadmium atom firmly bonded on the surface.

If the monolayer is irradiated with an 193 nm laser beam, the spectrum changes radically, thus indicating that the monolayer is activated or dissociated by ultraviolet light. Exposure to air also changes the spectrum strongly. Note that at 257 nm, the absorption strength of the chemisorbed layer is about 7.8 times greater than for an equivalent quantity of molecules in the gas phase.

c) Spectra of the Physisorbed Layer

The spectra of the physisorbed DMCd layers at 0° C is shown in Fig. 3. Twenty surfaces were used to obtain this spectra in a cell, with a free path of 0.40 nm. Under these conditions the absorbtion due to the gas is only about 30% of the total absorption signal. Thus, even the unprocessed cell spectra are radically different from the gas spectra. The gas portion of the spectra is then subtracted accurately by an on-line computer. Several features of the absorption spectra of the physisorbed layers are notable. First, the strong absorbtion peak is slightly redshifted and its vibrational structure is almost completely washed out. Note, however, that there still appears to be some residual vibronic structure. Second, there is a strong

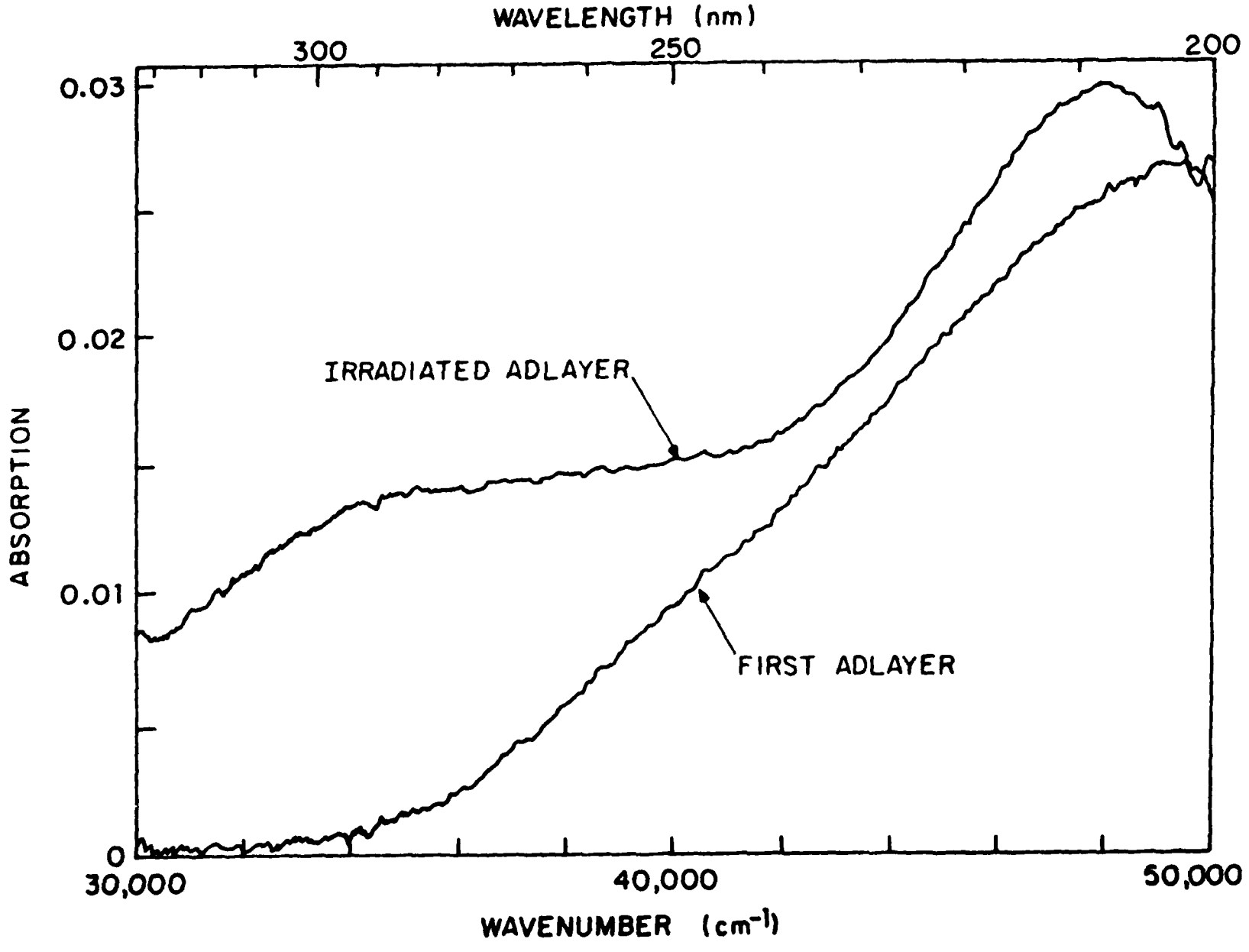
WAVELENGTH (nm)
300
250
200
0.03
0.02
0.01
0
ABSORPTION
IRRADIATED ADLAYER
FIRST ADLAYER
30,000
40,000
50,000
WAVENUMBER (cm⁻¹)

Figure 2

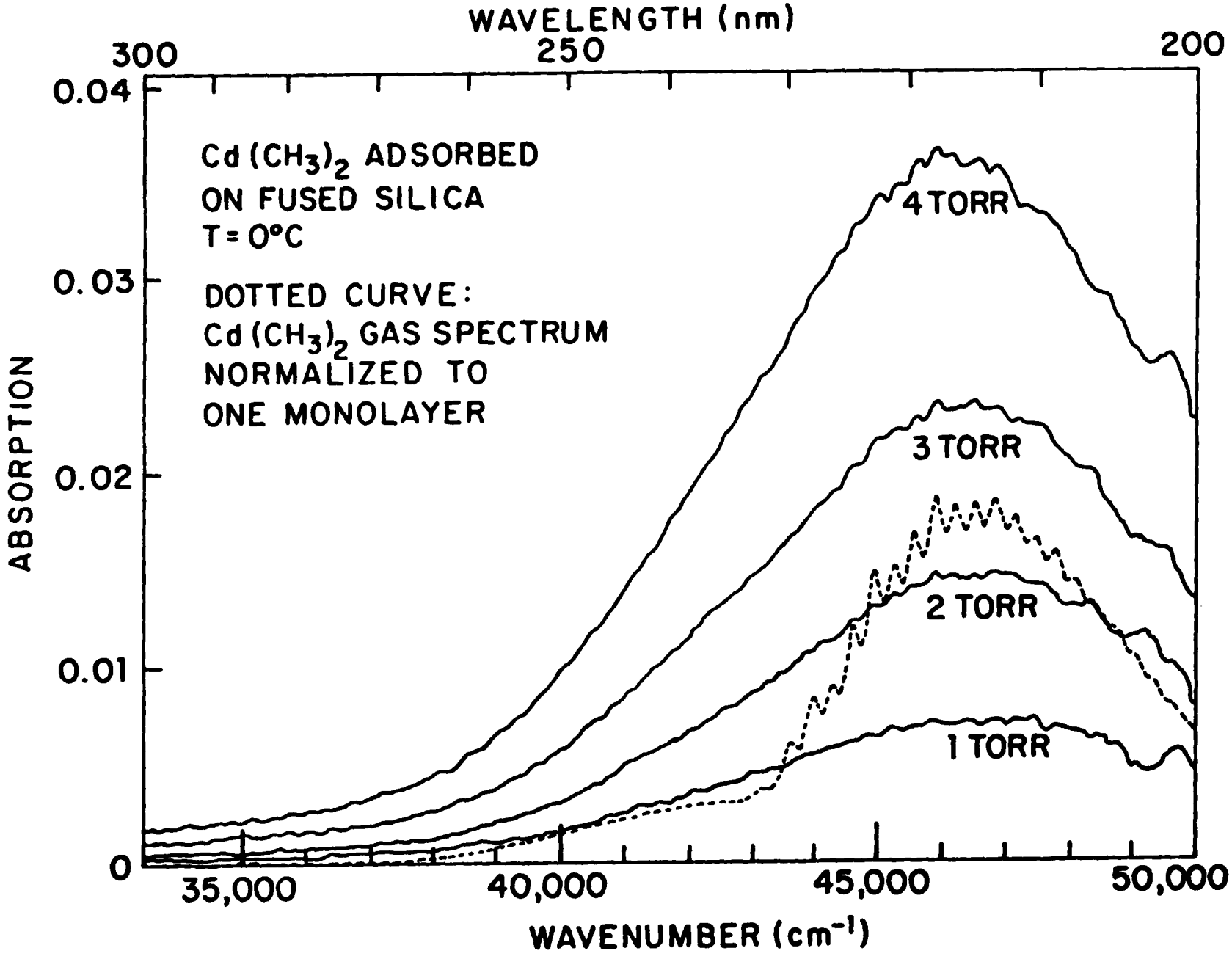
WAVELENGTH (nm)
300
250
200
0.04
0.03
0.02
0.01
0
ABSORPTION
Cd(CH3)2 ADSORBED
ON FUSED SILICA
T = 0°C
DOTTED CURVE:
Cd(CH3)2 GAS SPECTRUM
NORMALIZED TO
ONE MONOLAYER
4 TORR
3 TORR
2 TORR
1 TORR
35,000
40,000
45,000
50,000
WAVENUMBER (cm-1)

Figure 3

pressure and temperature dependence to the adsorption depth of the adlayer. Third, there is a long wavelength tail extending directly to visible wavelengths. The wavelength dependence of this tail is very flat and the pressure dependence of it is radically different from that of the main peak. At low pressures the dependence of this tail is nonlinear; in contrast, the linear dependence of the absorption in the main peak is consistent with measurements of the DMCd isotherm.

The interpretation of the physisorbed layer spectra is as follows. Most of the molecules in the physisorbed layer are in a liquid-like environment, in which the dense molecular environment can broaden spectral features due to shift in the intramolecular potential of the upper and lower energy states. The long-wavelength tail is due to the Rayleigh scattering by the nonuniformity thickness of the adsorbed layer. This nonuniformity increases near the condensation point. Note that the high surface density and the slight spectral redshift of the adsorbed-layers may play an important role in photochemically producing the first metal-atom clusters on the surface.

*This research was supported by the Army Research Office under Grant DAAG29-82-K-0009.

III. CHARACTERISTICS AND PROPERTIES OF ENERGETIC ION AND RADICAL BEAMS

A. THE CAPILLARITRON: A LASERLESS MEANS OF PRODUCING COLD RADICALS*

(B. Brady, T. Allik, G. W. Flynn)
(JSEP work unit 7, 1982-1985)
(Principal Investigator: G. W. Flynn (212) 280-4162)

Ions and radicals are important in varied chemical applications. In the field of microelectronics, ions and radicals of several kinds are important in the etching and implantation of semiconductor surfaces. Ions and radicals are also important in many gas phase reactions and their spectra are often poorly understood. Since ions and radicals are generally created with large amounts of excess energy, there are usually a large number of different states populated. This large variety of states gives rise to congested spectra which are difficult to interpret and also provides for a myriad of competing channels in the reactions of these substances. If one were able to create ions and radicals in just a few of their low energy states, it would simplify the spectroscopy and allow for the preparation of specific states with subsequent study of state-to-state reaction rates. It was with this goal in mind that we first began to look at the capillaritron.

The capillaritron consists of a capillary nozzle held at high positive voltage and an annular ground plate a few millimeters in front of the nozzle. In operation, a gas is fed into the nozzle at a moderate to high pressure and allowed to expand into a chamber at a significantly lower pressure. When voltage is applied to the nozzle, a plasma forms between the nozzle tip and the ground plate and the gas is ionized and sometimes fragmented. In our application, the typical backing pressure is one to five atmospheres with a source chamber pressure of 10^{-3} to 10^{-4} torr. The voltage applied is usually between 500 and 1000 volts and the ion current at the nozzle is a few milliamps.

The experimental setup has two additional differentially pumped chambers

downstream of the source chamber. After a pathlength of about a centimeter in the first chamber, the beam from the nozzle is skimmed and collimated. At the end of the third chamber is a quadrupole mass spectrometer. Pressures in the second and third chambers are generally kept at about 10^{-7} torr.

When no voltage is applied to the capillaritron, the nozzle and chamber arrangement function as a supersonic molecular beam apparatus. As a gas expands into the chamber, it is cooled because the molecules in the beam collide and excess energy is removed by the molecules which travel out of the beam. This process occurs until all the molecules on the beam axis are moving at roughly the same speed at which point the beam becomes collisionless. The velocity distribution along the axis at this point can be described by a Boltzmann equation:

$$f(v) \propto \left(\frac{v}{\alpha_s}\right)^3 \exp\left[(v-v_s)^2/\alpha_s^2\right]$$

where v_s is the stream velocity and is significantly higher than those in bulk samples at room temperature. α_s is the width parameter and is used to determine the effective translational temperature by the equation:

$$\alpha_s = (2kT_s/m)^{1/2}$$

This effective translational temperature, T_s, is very low when the beam becomes collisionless. Other degrees of freedom of the expanding gas are also cooled in this process, but only to the extent that they couple to the translational energy distribution. The ions and radicals from the capillaritron are created early in this expansion, and the primary goal of our characterization of the capillaritron is to determine if these species are influenced enough by the supersonic expansion under normal operating conditions

to cool significantly. Our efforts to determine the energy distribution of the capillaritron output can be divided into two parts: spectroscopic measurements and time-of-flight (TOF) measurements.

The spectroscopic measurements made on the capillaritron to date include observation of visible emission from atoms, molecules and ions excited in the plasma, and measurement of laser induced fluorescence from these species further downstream. The emission at the nozzle tip was initially observed with an optical multichannel analyzer (OMA). This device consists of an array of five hundred detectors directly coupled to the output end of a monochromater. A wide range of wavelengths can be surveyed with the OMA at the same time but since there is no exit slit on the monochromator, the ultimate resolution is fixed by the width of the detector. When a rare gas such as Ar or He is used in the capillaritron, we see only atomic emission lines.[1] The emission from ions is expected to be much weaker; none was observed. When carbon tetrafluoride (CF_4) is used as the fuel gas, we obtain the spectrum shown as the lower trace in Fig. 1. Sharp lines can be seen from both carbon ion (C^+) and neutral fluorine and diffuse bands are observed centered at roughly 570 nm, 500 nm, 300 nm, and 230 nm.

The first task in analyzing these spectra is to determine the emitting species, after which information may be obtained about their energy distributions. The bands at 300 nm and 570 nm have been seen in CF_4 discharges by other workers.[2]-[4] The emission at 570 nm has also been detected recently in the photodissociation of CF_3Br and CF_3Cl and assigned to the CF_3 radical.[5],[6] Unfortunately, since this band is a continuous emission, thought to end on a dissociative state, it indicates nothing about the energy distribution; it does, however, confirm the presence of CF_3 in the discharge.

Fig. 1 Emission from CF_4 discharge.

The ultraviolet emission bands could be from either CF_2 or CF_3. Other investigators have ruled out CF_3 as an emitting species in an RF discharge on the basis of lifetime information;[3] however, we were not able to measure lifetimes. The CF_2 radical also shows sharp band structure when it emits,[5],[7],[8] the absence of this structure either indicates that the emitting species has more atoms or that it is very hot. When CF_4 was seeded in helium and the emission observed with a photomultiplier tube and a monochromator with adjustable slits, some band structure was observed as shown in the upper trace in Fig. 1. The shape of the band and spacing of the peaks is similar to that found for CF_3 in Ref. 5 and 6, but the band is centered at slightly longer wavelengths. The position of this band could be explained if the emission were from higher vibrational states than in Ref. 5, but the assignment remains uncertain.

The emission band centered at 400 nm has not been observed in other discharges. The small peaks on this band do seem to correspond well to a series of lines seen in the source region by Van Sprang, et al. The average spacing in our case is 680 cm^{-1} and in their spectrum it was 718 cm^{-1}. This was said to correspond well to a vibrational progression in CF_4^+ at 730 cm^{-1} and assigned accordingly. This assignment is in doubt, however, because other investigators have found that CF_4^+ decays non-radiatively.[9]

One reason why the emission spectra do not show much cooling is because they sample molecules close to the nozzle and in electronically excited states. One technique which allows us to probe molecules in their ground state at variable locations with very good spatial resolution and sensitivity is laser-induced fluorescence (LIF). Another advantage of LIF is that it allows us to probe one type of molecule at a time instead of collecting fluorescence from every species that might be present (using the OMA). We

used the KrF line of an excimer laser to excite CF_2 radicals in their ground vibrational and electronic states and resolved the resulting fluorescence. The spectrum obtained is shown in Fig. 2 and is characteristic of CF_2.[10],[11] Since only one state was probed, we do not know what the energy distribution is but this does confirm the presence of CF_2 in the beam and provides a basis for future experiments which will determine the internal energy distribution.

The second type of measurement done on the beam was a TOF. A chopper wheel with a small slit was placed in chamber 2. When the wheel was spun a segment of the beam was chopped out and its flight from the chopper wheel to the mass spectrometer was timed. In this manner, the velocity distribution of the various species in the beam was determined. When measuring the TOF of the ions, the ionizer on the mass spectrometer could be turned off and the mass spectrometer used to separate the various fragment ions, CF_3^+, CF_2^+, CF^+, and C^+ to determine their individual time of flights. For the neutral time of flights, the ionizer had to be turned on, and ions from the capillaritron deflected. Unfortunately, CF_4 fragments substantially in the ionizer and fragments created there could not be distinguished from those created in the capillaritron discharge.

When Ar is put in the capillaritron the energy of the Ar^+ ions produced ranges from 0 to 1000 eV. CF_4 produces CF_3^+, CF_2^+, CF^+ and C^+, as mentioned before, and each of these exhibit a narrower distribution than the Ar. Part of the reason for the narrower distributions from CF_4 is that it breaks down at half the voltage required for Ar. The CF^+ ions, however, seem to exhibit a very narrow distribution. We cannot presently determine exactly how narrow this distribution is because the uncertainties in the TOF measurements become very significant when dealing with these fast-moving particles. More accurate

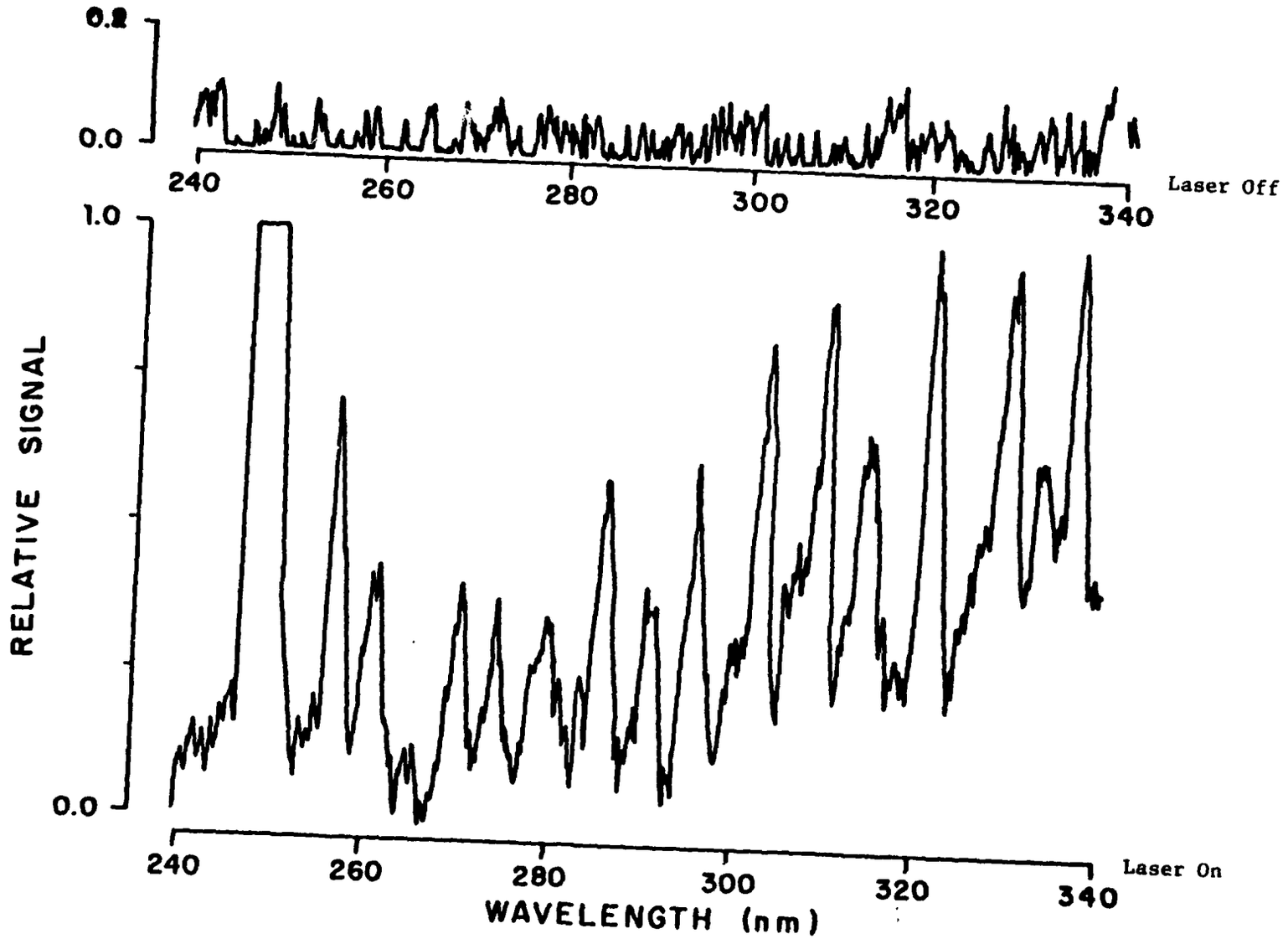

Fig. 2 Laser induced emission from CF_2.

measurement of these velocities is required before anything conclusive can be stated about the distributions.

For neutrals, the TOF measurements are extremely accurate because the particles are traveling at about 1/1000 the speed of the ions. For a neutral Ar beam with no voltage on the capillaritron, the translational temperature is 2.8K. For CF_4, T_s increases to 17K because the internal degrees of freedom of the polyatomic do not cool quite as well. When a discharge is put on the capillaritron, the velocity distribution of the neutral component of the beam does not change significantly. As can be seen in Figs. 3 and 4, the average velocity of the beam speeds up slightly and for Ar, the translational temperature increases by 2K. For CF_4 the temperature does not appear to change at all. We saw no warming upon turning on the discharge. At first this seems surprising since the temperature of the electrons in the capillaritron plasma is several thousand ^{o}K and the ions are hot as observed previously. The electrons are light, however, and cannot transfer much momentum to the other species; the ions are apparently a small enough portion of the beam, 1-2%, that they do not dominate it.

The importance of this discovery is twofold. First, since radicals are neutrals, if their velocity distribution were significantly different from the other neutrals, we would have observed them as an additional peak or as a broadening of the main peak. Secondly, this means the bath in which the radicals are expanding remains cold even if the radicals themselves are formed hot. The OH radical[12] requires 500 to 1000 collisions for the rotational temperature to equilibrate to the temperature of the buffer gas. In our beam, we have more collisions than that between the plasma and the collisionless regime and the buffer gas is at 5K. This means we should be able to cool radicals, at least rotationally, after they have been formed in the plasma.

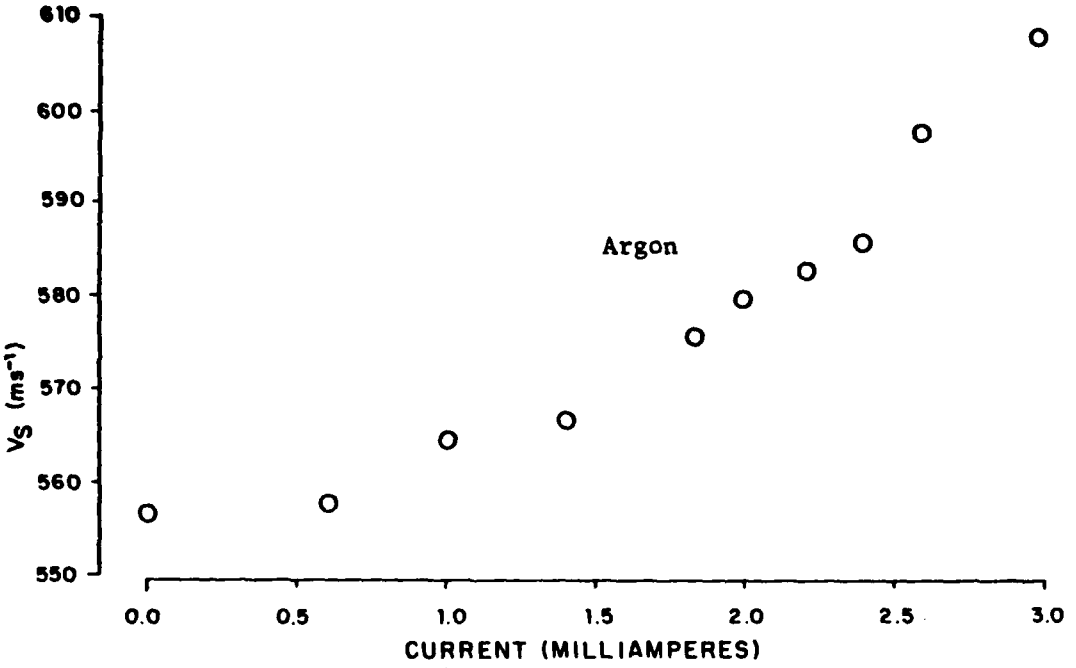
610
600
590
580
570
560
550
V_S (ms^{-1})
Argon
0.0
0.5
1.0
1.5
2.0
2.5
3.0
CURRENT (MILLIAMPERES)

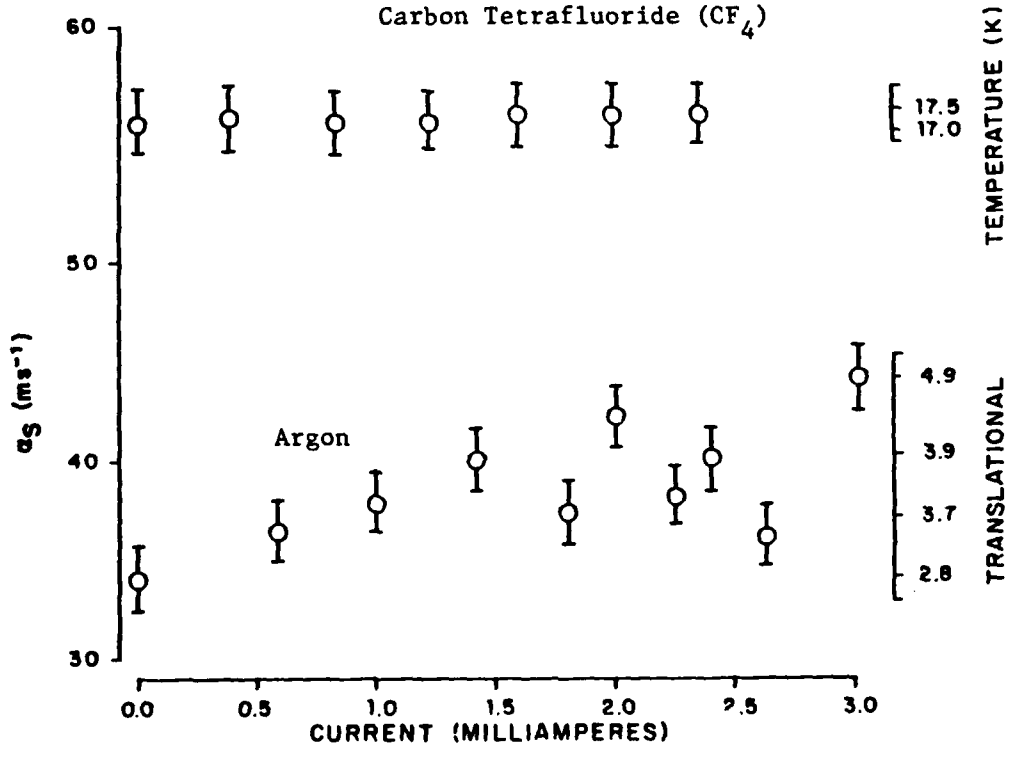
Carbon Tetrafluoride (CF_4)
60
50
40
30
α_S (ms^{-1})
Argon
17.5
17.0
TEMPERATURE (K)
4.9
3.9
3.7
2.8
TRANSLATIONAL
0.0
0.5
1.0
1.5
2.0
2.5
3.0
CURRENT (MILLIAMPERES)

Figure 3

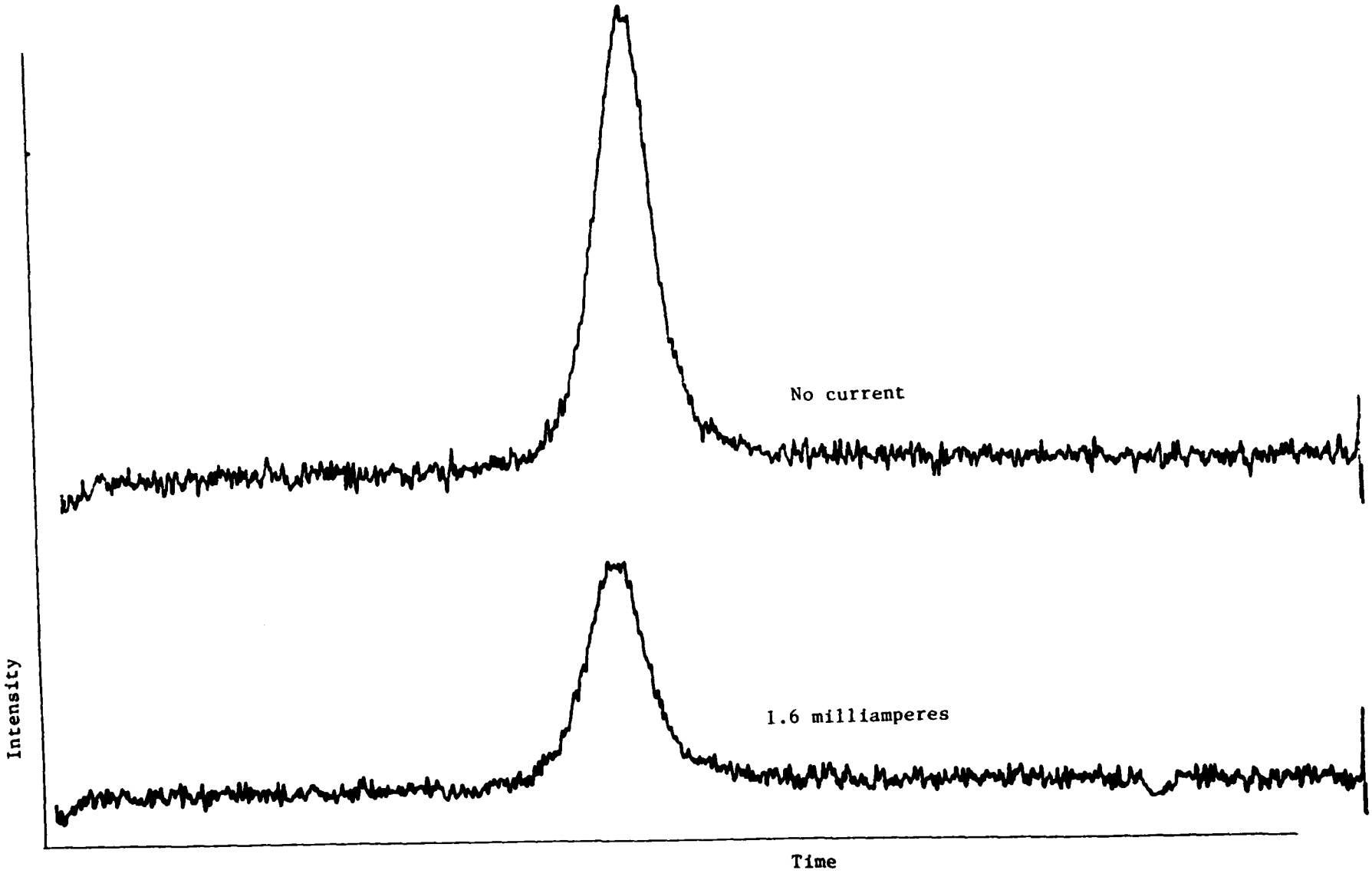

Fig. 4 Time of flight of argon (with and without a discharge)

Future experiments on this project will involve the determination of rotational and vibrational temperatures of the radicals in the beam with laser induced fluorescence (LIF), measuring the TOF of the radicals directly and determining the energy of the ions with an electrostatic energy analyzer. Scanning a dye laser brings various transitions into resonance which will take molecules from various levels in the ground state to some particular excited level. By then monitoring the total fluorescence from the excited state and knowing the Franck-Condon factors for the laser transition, one can determine the population in the various rotational-vibrational levels of the ground state. This population distribution can then be analyzed, assuming it is Boltzmann; to get a rotational and vibrational temperature. The CN radical, produced by a discharge of acetonitrile (CH_3CN) in Ar, has a simple LIF spectrum which can be probed by the fundamental of the BBQ dye at 387nm. This experiment will be done in the near future.

Becuase the ionization potential of CF_3 is about 8 eV lower than that of CF_4, it is possible to ionize only CF_3 by turning down the electron energy on the ionizer of the mass spectrometer. This would eliminate fragmentation of the parent and allow direct observation of CF_3 created by the capillaritron. Another strategy would be to modulate the current on the capillaritron and look for a modulated signal in the time of flight. This method seems more difficult but either method should allow direct determination of the velocity distribution of the radicals from the capillaritron. Determination of the velocity distribution of the ions is simple and involves merely observing their deflection in an electric field.

In conclusion, the creation of cold radicals and possibly cold ions with the capillaritron appears to be possible. Further measurements are needed to confirm this conclusion and these measurements should be done in the near

future. Then if the capillaritron does prove to be a source of cold radicals and ions, it should prove to be an important tool in deciphering spectra and kinetic schemes.

*This research was also supported by the National Science Foundation under Grant CHE 80-23747 and the Department of Energy under Contract DE-AC-02-78ER04940.

(1) A.N. Zaidel', V.K. Prokof'ev, S.M. Raiskii, V.A. Slavnyi, and E.Ya. Shreider, Tables of Spectral Lines IFI/Plenum, New York (1970).

(2) James E. Hesser and Kurt Dressler, J. Chem. Phys. 47, 3443 (1967).

(3) H.A. van Sprang, H.H. Brongersma and F.J. DeHeer, Chem. Phys. 35, 51 (1978).

(4) Daniel L. Flamm, J. Appl. Phys. 51 (11), 5688 (1980).

(5) Masaka Suto and Nobuaki Washida, J. Chem. Phys 78 (3), 1007 (1983).

(6) Masaka Suto and Nobuaki Washida, J. Chem. Phys. 78 (3), 1012 (1983).

(7) P. Venkateswarlu, Phys. Rev. 77, 646 (1950).

(8) Quach-Tat-Trung, G. Durocher, P. Savoageau and C. Sandorfy, Chem, Phys. 47 (3), 404 (1977).

(9) J.P. Maier and F. Thommen, Chem. Phys. Lett, 78 (1), 54 (1981).

(10) A.B. Horwitz, J.M. Preses, R.E. Weston, Jr. and G.W. Flynn, J. Chem. Phys. 74 (9), 5006 (1981).

(11) P.J. Hargis, Jr. and M.J. Kushner, Appl. Phys. Lett. 40 (9), 779 (1982).

(12) C.E. Hamilton, M.A. Duncan, T.S. Zwier, F.C. Weisshauer, G.B. Ellison, V.B. Bierbaum and S.R. Leone, Chem. Phys. Lett., 94 (1), 4 (1983).

IV. ENERGY TRANSFER PROCESSES IN QUANTUM ELECTRONICS

A. PHOTOCHEMICAL AND PHOTOPHYSICAL DYNAMICS OF I_2 IN A RARE GAS MATRIX*

(P. B. Beeken, E. A. Hanson, G. W. Flynn)
(JSEP work unit 7, 1982-1985)
(Principal Investigator: G. W. Flynn (212) 280-4162)

The iodine atom laser is rapidly gaining importance for use in projects such as inertial confinement fusion. One potential drawback to obtaining high power output from this laser is the potential for interference from the low lying electronic states of the byproduct, I_2. Previous work on Br_2 isolated in rare gas matrices has helped characterize the relaxation times and energy transfer pathways among the low lying electronic states of diatomic halogens. Specifically, the emission from the lowest state, $A'\ ^3\pi_{2u}$, was viewed directly. This state and the one slightly higher in energy, $A\ ^3\pi_{2u}$, in I_2 could prove to be efficient quenchers of excited iodine atoms. A complete analysis of the relaxation pathways for I_2 could be of great importance for optimising the I laser.

The following abstract is from a paper to appear in the Journal of Chemical Physics in May of 1983 describing our work on energy transfer in matrix isolated iodine molecules.

The photochemical and photophysical properties of I_2 in Ar, Kr, and Xe matrices have been investigated and are reported here. Following laser excitation high into the $B\ ^3\pi(0_u^+)$ and $^1\pi_{1u}$ dissociative state, prompt emission is observed from the $B\ ^3\pi(0_u^+)$, $A\ ^3\pi_{1u}$, and $A'\ ^3\pi_{2u}$ electronic states depending on the matrix host. In all matrices the emission attributed to the B electronic state lies 200 nm to the red of the excitation wavelength and is generally featureless. The time resolved emission for this state has a detector limited rise and fall. The emission attributed to the $A\ ^3\pi_{1u}$ elec-

tronic state was resolved with a monochromator and the source determined to be the v' = 0 level of the A state. The lifetime for this emission is 260 μsec and was found to be roughly the same in all matrices. Emission from the A' $^3\pi_{2u}$ state was also detected but only in Xe matrices. The measured lifetime for this state was 6.3 msec. Data from a number of previous experiments on matrix isolated halogens in Ar, Kr, and Xe are reviewed and a consistent model for the relaxation pathways for intra-molecular electronic energy transfer is presented. The implications of this model for studies of the solvent cage effect on I_2 photodissociation and the development of the I^* chemical laser are also discussed.

*This research was also supported by the National Science Foundation under Grant CHE-80-23747 and the Department of Energy under Contract DE-AC-02-78ER04900.

B. STUDIES OF IODINE ISOLATED IN LOW TEMPERATURE MATRICES OF CARBON TETRACHLORIDE*

(K. Kasturi, P. Beeken, G. W. Flynn)
(JSEP work unit 7, 1982-1985)
(Principal Investigator: G. W. Flynn (212) 280-4162)

In the past few months we have been involved in studies aimed at exploring the effect of the matrix cage on the photodissociation of iodine in carbon tetrachloride at low temperatures. Iodine is excited by a laser into a superposition of the bound B state and the repulsive $^1\pi$ continuum (Fig. 1). As a result of confinement by the frozen cage, most of the iodine atoms formed upon dissociation are prevented from escaping and recombination is facilitated.

The effect of the cage on the photodissociation of iodine in liquid CCl_4[1] and Xenon[2] has been studied by picosecond techniques. The rate of recombination was studied by probing the recovery of the ground state population of iodine molecules and two rates were reported: 1) a fast rate (timescale: 100 picoseconds) due to the geminate recombination of iodine atoms derived from the same iodine molecule. 2) a slow rate (timescale $>10^{-8}$sec) attributed to the recombination of iodine atoms that have escaped from their cages. Theoretical calculations indicate that only low lying vibrational levels are probed in these experiments, and further suggest that slow relaxation down the vibrational manifold of the ground state makes an important contribution to the recombination dynamics.[3]

Studies of iodine in low temperature matrices performed in our laboratory[4] have shown that upon photodissociation and subsequent recombination the excited state population undergoes relaxation and is partitioned between the different electronic states B, A and A'. (Relaxation to the ground state could not be monitored in these experiments.) The states accessed depend upon the nature of the matrix, the A' state being observed only in Xe matrices.

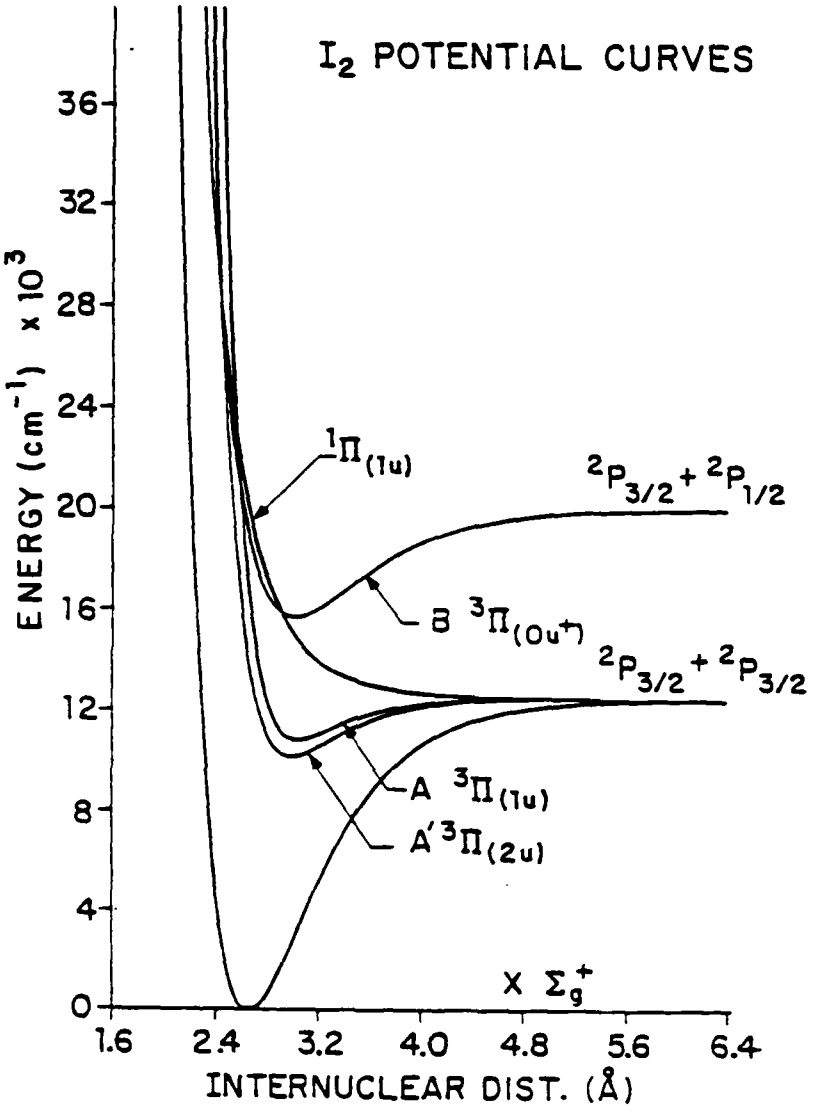

Fig. 1 Potential curve for I_2

It has been suggested[4] that the low lying A' state can be populated by dissociation along the $^1\pi$ state which correlates at long internuclear distances, attainable only in the large Xe cage, to the A' state. The higher energy A state is accessible even in small cages. CCl_4 is expected to form large cages, therefore one may speculate that excited iodine can cross over in a CCl_4 matrix to the A' state, which has a long lifetime. Consequently, a possible explanation for the slow recovery of the ground state population of I_2 in CCl_4 could be slow relaxation from the A' state.

Initially, our goal was to study the channeling of energy into the different electronic states, and to investigate the variation of the relaxation dynamics with temperature. To achieve this end, the emission of I_2 from CCl_4 matrices was subjected to spectral and temporal analysis. Spectral resolution of the emission has yielded intriguing results which are described below.

Summary of results obtained with I_2 in Xe matrices.

For purposes of comparison it is useful to summarize the Xe matrix results.[4] Analysis of the IR fluorescence arising from I_2 in Xe matrices reveals two signals:

1) a fast decay with a lifetime of 240 μsec $\pm$ 20 μsec, which originates from the 1-2 μ spectral region. When resolved the spectrum displayed a progression of 16 peaks due to transitions from the v=0 level of the A state to various vibrational levels of the X state; 2) a slow decay in the 2-3 μ spectral region with lifetime of 6 msec $\pm$ 1 msec. The signal was too weak to be resolved with a monochromator but was presumed to originate from the A' state. A near red signal was observed with a very fast decay (15-40 nsec) and a featureless spectral profile peaking at 740 nm.

Experimental

Matrices were formed by depositing mixtures of Iodine and carbon tetrachloride on a cesium iodine window held at 12°K by an Air Products 202A helium refrigerator. The composition of the samples of iodine in carbon tetrachloride was varied between 1:1000 and 1:2000. The matrices were irradiated with the output of an excimer-pumped dye laser (Lambda Physik EMG 101, FL2002) in the wavelength range 500-540 nm. The fluorescence obtained from the samples was resolved spectrally as well as temporally. The IR signals from 1.0 to 6.0 μ were detected using a cooled InSb (77°K) detector (risetime: 1 μsec). Signals in the near-red up to 900 nm were monitored with an RCA C31034A GaAs photomultiplier tube (risetime: 15 ns). The signals were resolved with either narrow band filters or an Instruments SA 320 monochromator.

The time resolved signals were amplified with a Tektronix AM502 amplifier (bandwidth: 1 Hz-1Mhz) and signal averaged with a Biomation 8100-Nicolet 1170 combination. Spectral scans were taken with a PAR CW-1 boxcar integrator and recorded on a Houston Instruments strip chart recorder.

Liquid phase absorption spectra were taken with a Cary Model 17 Spectrophotometer in the wavelength range 900-1800 nm, using quartz cuvettes of pathlength 1 cm.

Results and Discussion

Upon irradiating matrices of pure CCl_4, no emission was observed. Irradiation of matrices of iodine in CCl_4 yielded emission in the near red and in the infrared. Emission in the near red was monitored with the photomultiplier tube in the region 700 to 900 nm, but no spectrally resolved lines could be obtained upon observation through a monochromator. The signal

decayed very fast but the lifetime could not be measured. This fluorescence probably arises from the B state since it corresponds in wavelength range and fast decay to that obtained from iodine in rare gas matrices.

The total signal in the 1.0-6.0 μ region was characterized by three lifetimes: 1) a very fast decay with a lifetime of 25 μsec which was probably due to formation of an emission from an $(I_2)_2$ dimer, as suggested by studies of the temperature dependence of the emission. 2) a fast decay with a lifetime of 148 μsec. 3) a slow decay with a lifetime of 227 μsec. The risetime of the emission was detector limited in all cases.

The emission was resolved with various narrow band filters, and the time-resolved signals analyzed. From the fitted curves, the relative intensities of the different decays were determined and plotted as a function of the bandpass of the filter (see Fig. 2). The nature of the signals did not change with the concentration of iodine in the matrix, and the emission intensity scaled roughly linearly with laser power.

The emission in the 1-2 μ region was resolved with a monochromator. The emission spectrum so obtained (Fig. 3) exhibited two peaks centered at approximately 1.30 and 1.34 μ against a featureless background which extended beyond 2 μ.

The emission at various wavelengths, resolved with the monochromator, corresponding to different regions of the spectrum, was subjected to temporal analysis. In the vicinity of the 1.30 and 1.34 μ peaks the ratio of the intensity of the slow to the fast lifetimes decreased dramatically (see Fig. 4), as compared to other regions of the spectrum, thereby implicating the fast decay as the source of the spectral peaks. This was confirmed when the same spectrum was obtained with the bandwidth of the amplifer decreased (to 1Khz-100khz), thereby filtering out the slow lifetime. A scan was performed

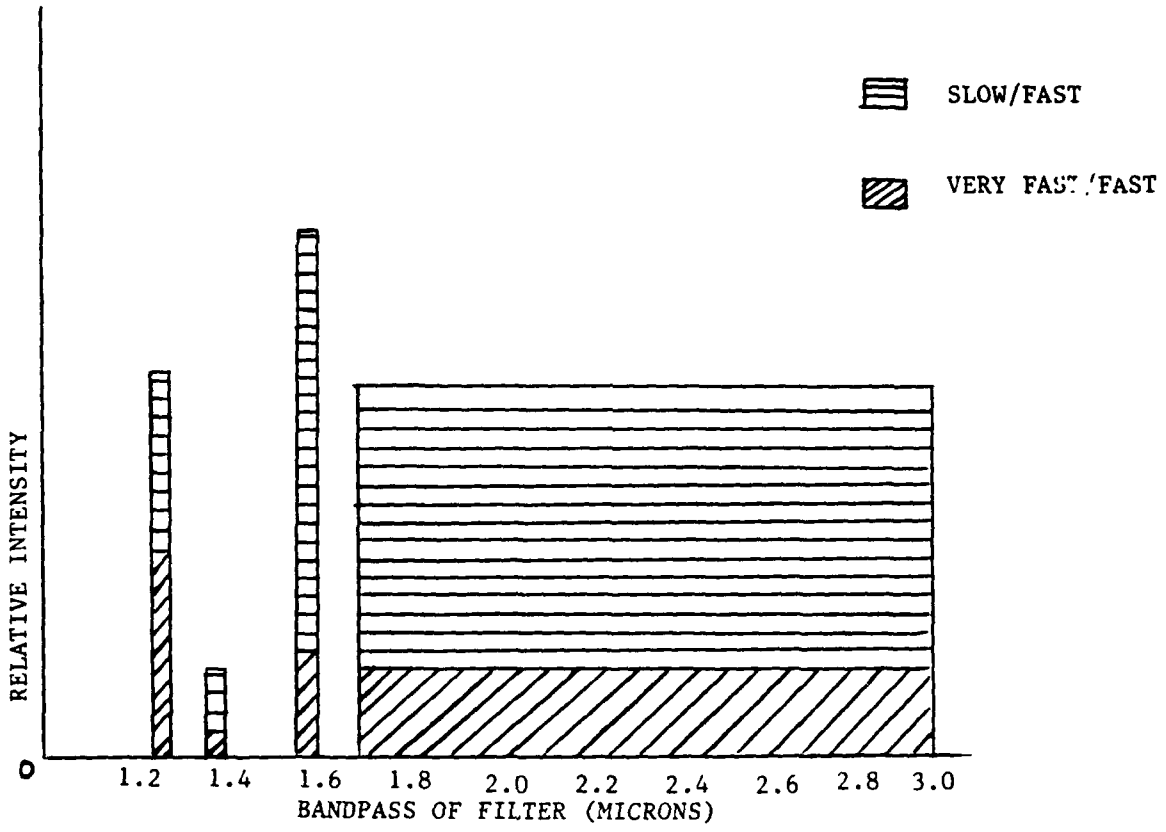

Fig. 2 Ratios of the intensities of the slow/fast and very fast/fast decays plotted against the bandpass of the filter.

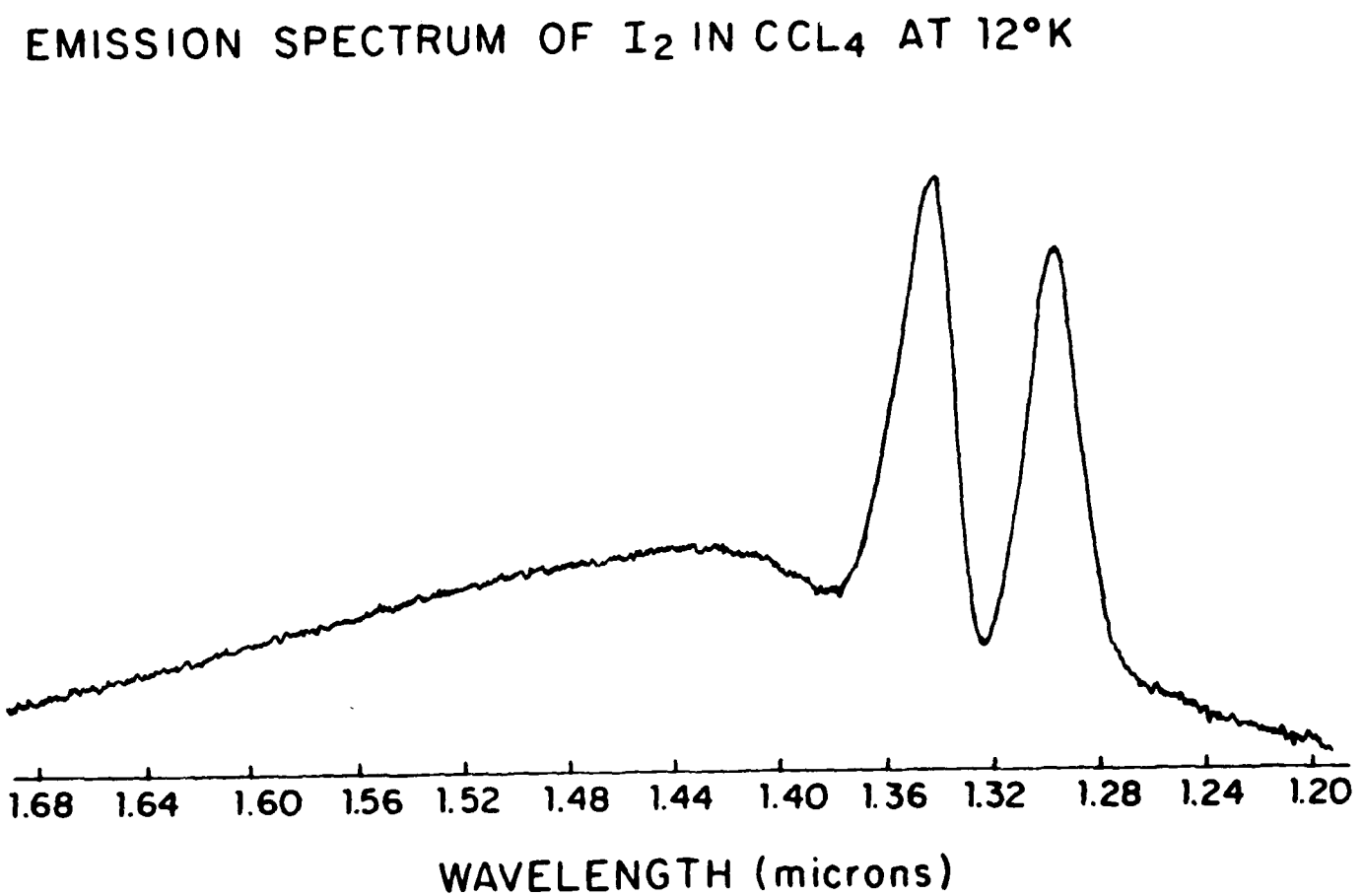

Fig. 3 Emission spectrum of I_2 in a CCl_4 matrix held at $12^{o}K$. The composition of the matrix was 1:1000 I_2:CCl_4.

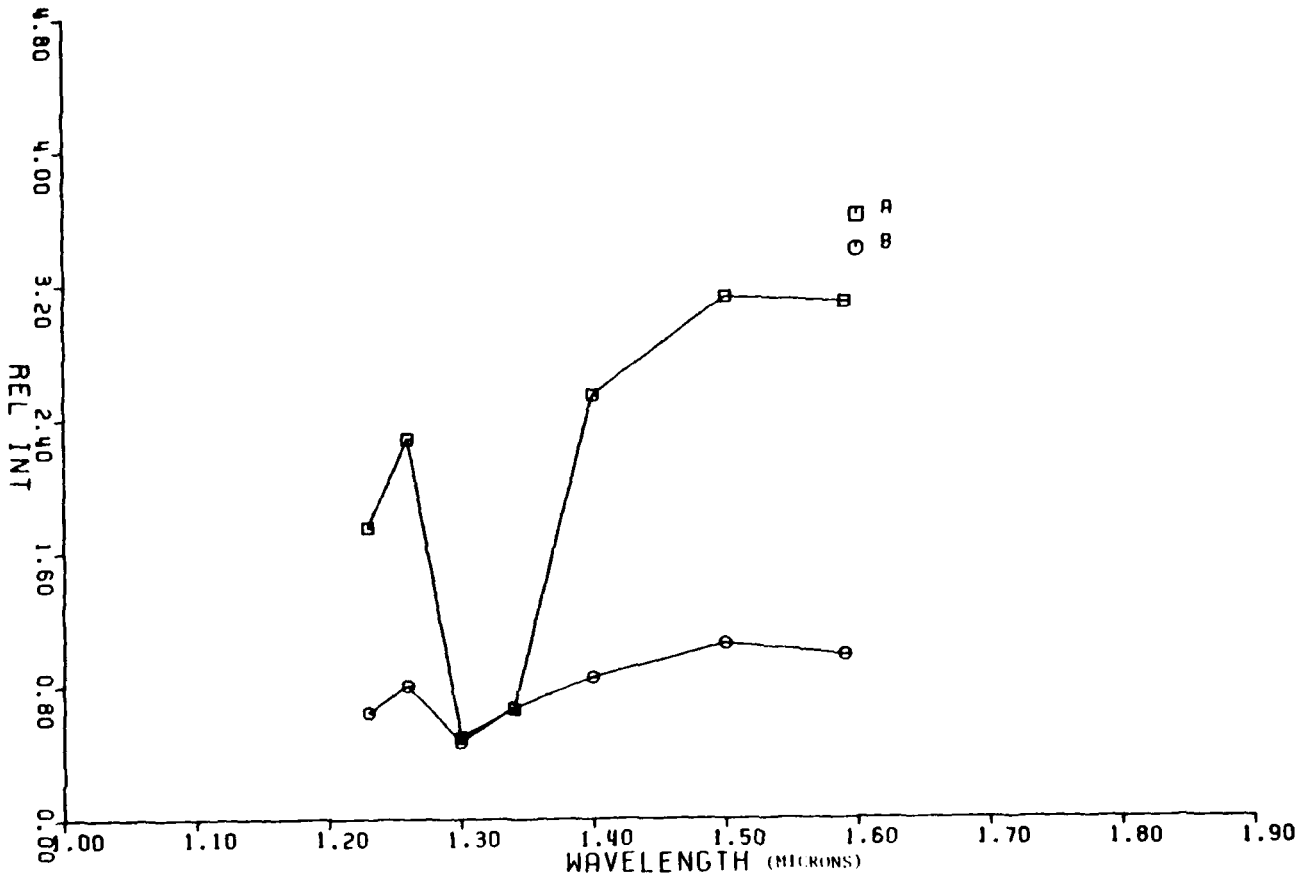

Fig. 4 The ratios of the intensitites of the a) Slow/fast and b) very fast/fast decays measured at various wavelengths. The fluorescence was resolved with a monochromator, signal averaged and analyzed. The ratios of the fitted intensities were then determined.

with the delay on the boxcar integrator increased to 500 μsec, thereby integrating the intensity of the emission in the tail of the fluorescence signal, and discriminating against the fast decay. The profile of the spectrum changed, with the intensity of the peaks decreasing relative to the background. This further suggests that the peaks in the spectrum are due to the fast emission signal.

Comparing these results with those obtained for iodine in rare gas matrices, the fast decay is seen to resemble the emission from the A state of iodine in both wavelength range and lifetime. (Assuming purely radiative decays, the extrapolated gas phase lifetime of the slow decay is 315 μsec while that of the A state emission in the rare gas matrices varies between 426 and 514 μsec; the calculated radiative lifetime in the gas phases is 220 μsec.[5] In the case of rare gas matrices the differences between the extrapolated and calculated lifetimes can be attributed to changes in the Franck-Condon factors induced by the matrix.[4] However, no conclusions can yet be drawn as to the identity of the state giving rise to the fast decay, since the spectrum obtained does not correspond to emission from the A state of iodine, as obtained in rare gas matrices.

An absorption spectrum of a concentrated solution of iodine in liquid CCl_4 was taken, to see whether the solution spectrum displayed features similar to that of the emission spectrum of the matrix sample. Scanning in the .9-1.8 μ range no spectral features could be discerned, except for a very weak absorption at 1.14 μ. Further scans are planned with cuvettes of longer pathlength (up to 10 cm.). If any absorption is discovered in this region a study of the concentration dependence of the absorbance would help to elucidate the nature of the species responsible for the emission. If the same transition is responsible for the absorption as well as the emission spectra,

solution phase studies could help to cast light upon the nature of the emitting species in the matrix sample. However, a survey of the literature has not, as yet, revealed the existence of any such absorption in solutions of iodine in CCl_4.

Temperature dependent studies

A temporal analysis of the total emission intensity in the 1-6 μ region was performed as a function of temperature. The temperature of the matrix was raised in increments of 10°K to 160°K; after annealing the temperature was reduced to 12°K. The matrix was once more heated up to 160°K in the case of 1:1000:I_2:CCl_4 matrices.

At each temperature, the ratios of the initial intensities of the slow/fast (Fig. 5) and the very fast/fast emissions (Fig. 6) were determined. It was found that the ratio of the slow/fast lifetimes increased to a maximum at 60°K, stayed roughly constant till 140°K, and then began to drop sharply. Similar behavior was observed for the ratio of the very fast/fast lifetimes. Thus, with an increase in temperature, the intensities of the slow and fast lifetimes decrease relative to that of the very fast lifetime. In the case of 1:1000 matrices it was seen that after annealing and cooling down the matrix, the relative intensities of the decays at 12°K were nearly the same as those seen at 160°K. For matrices of other composition, the relative intensities at 12°K before and after annealing are not the same, but the very fast lifetime intensity is still large compared to each of the others. Upon a further increase in temperature the relative intensity of the very fast lifetime continues to increase at the expense of the others. Thus annealing causes an irreversible change in the emitting species, suggesting that the iodine dimer might be responsible for the very fast decay. As the temperature increases,

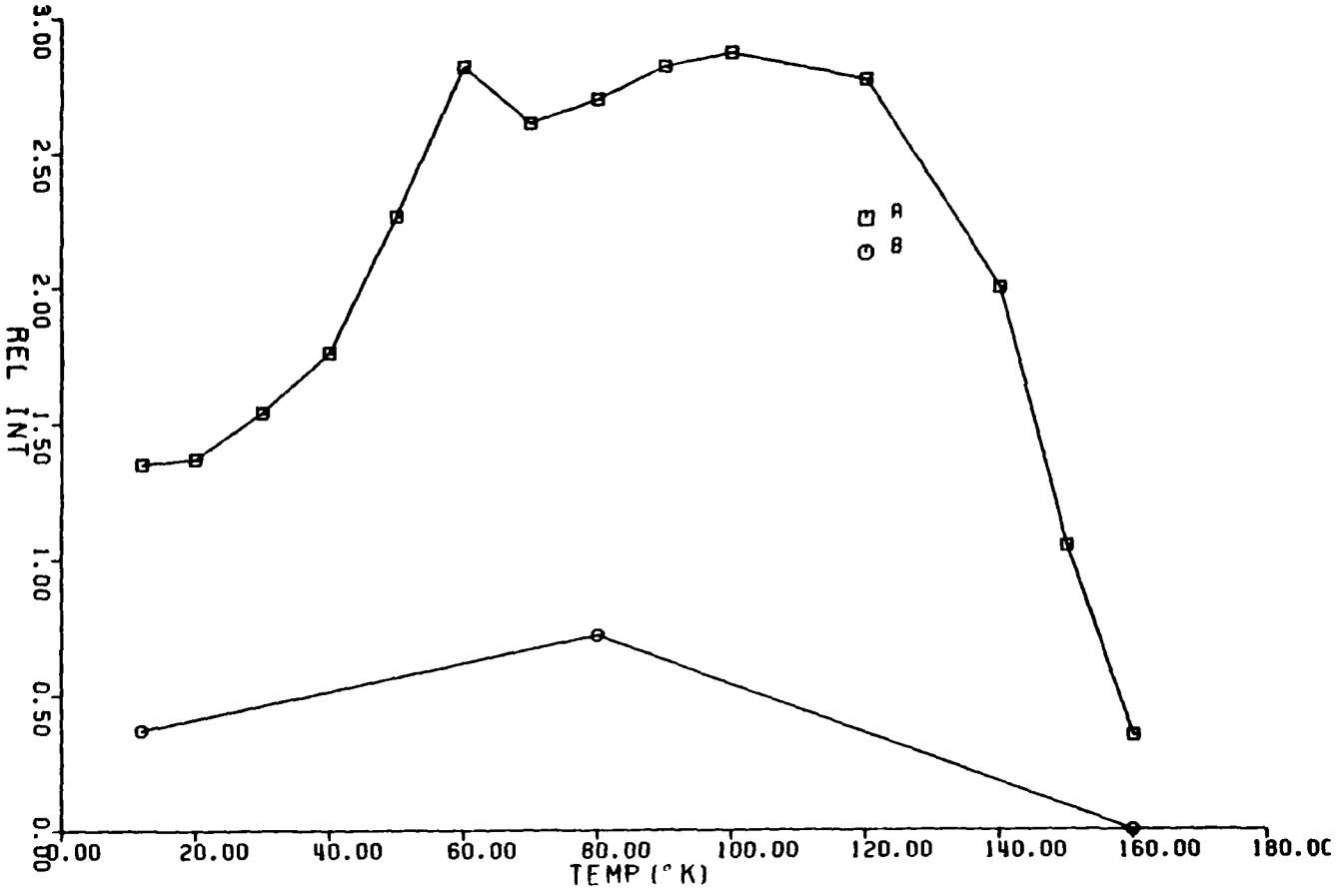

Fig. 5 Ratio of the intensities of the slow/fast decays plotted against temperature a) before annealing b) after annealing a matrix of I_2 in CCl_4 (Composition of matrix: 1:1000 I_2:CCl_4).

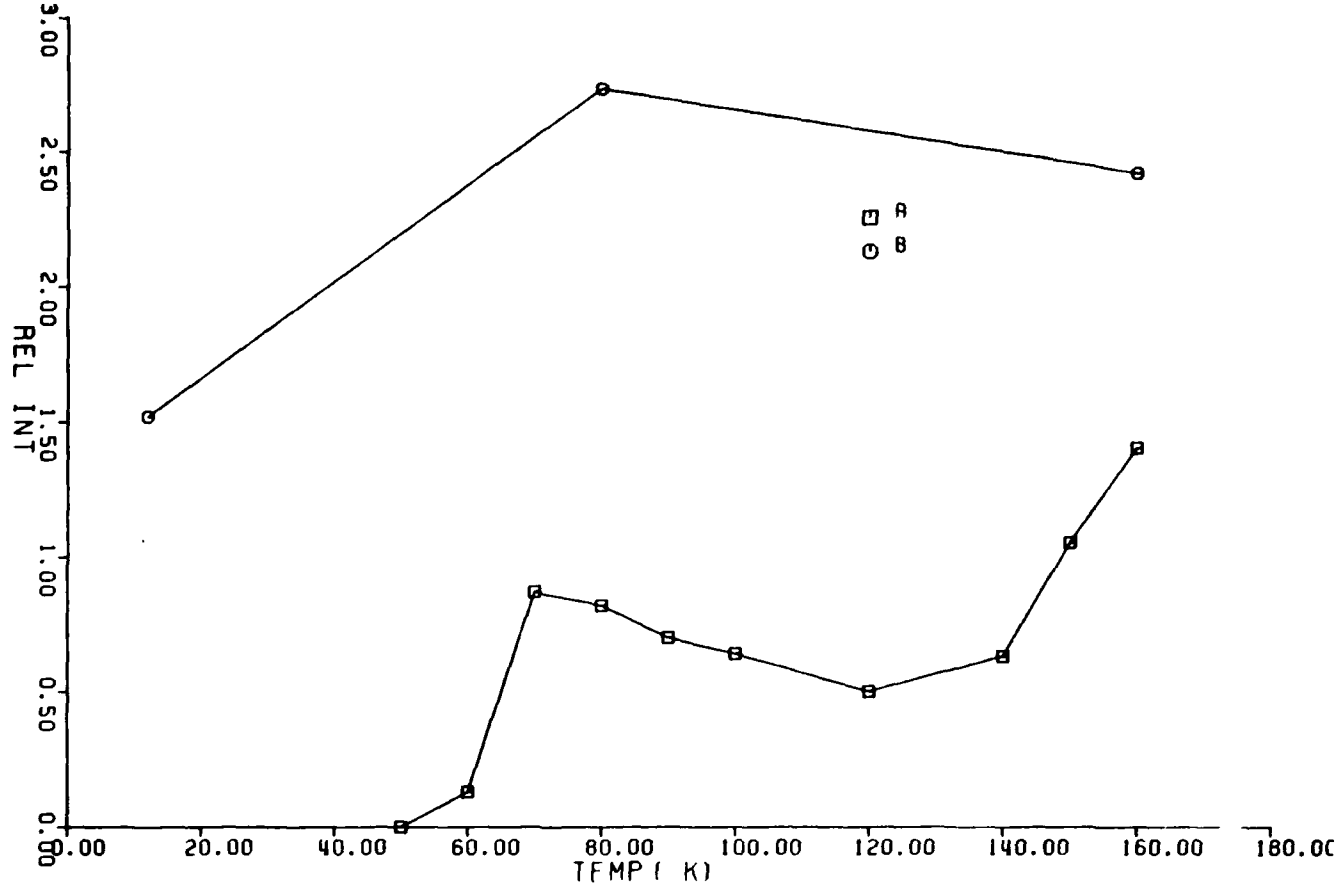

Fig. 6 Ratio of the intensities of the very fast/fast decays plotted against temperature a) before annealing b) after annealing a matrix of I_2 in CCl_4 (Composition of matrix: 1:1000 I_2:CCl_4).

the matrix softens, permitting the diffusion of iodine molecules which can clump together to form dimers. Upon cooling the matrix after annealing, this state of the matrix is frozen out. As the temperature increases, fluctuations in the cage size may be expected to become larger due to increased molecular motion. As a result, the A' state is expected to become more accessible with an increase in temperature. Since the relative intensity of the slow decay increases with temperature this emission might arise from the A' state as in the case of iodine in rare gas matrices.

*This research was also supported by the National Science Foundation under Grant CHE 80-23747 and the Department of Energy under Contract DE-AC-02-78ER04940.

(1) T. S. Chuang, G. W. Hoffman, and K. B. Eisenthal, Chem. Phys. Lett. 25, 201 (1974).

(2) D. F. Kelley and P. M. Rentzepis, Chem. Phys. Lett. 85, 85 (1982).

(3) D. J. Nesbit and J. T. Hynes, J. Chem. Phys. 77, 2130 (1982).

(4) P. B. Beeken, E. A. Hanson, and G. W. Flynn, to be published, J. Chem. Phys. May 15, 1983; See also CRL Progress Report #32, p. 80, 1982.

(5) J. Tellinghuisen, J. Chem. Phys. 58, 2821 (1983).

C. ENERGY TRANSFER AMONG THE SYMMETRIC STRETCH AND THE BENDING MODES OF CO_2: AN INFRARED DOUBLE RESONANCE STUDY*

(C.F. Wood, J.O. Chu, and G.W. Flynn)
(JSEP work unit 7, 1982-1985)
(Principal Investigator: G. W. Flynn (212) 280-4162)

Vibrational energy transfer in CO_2 has been extensively studied and accurate rates for both intermolecular and intramolecular processes have been measured as well as the temperature dependence of these rates.[(1)-(12)] In spite of the vast amount of information obtained on energy transfer rates in CO_2, there is an important question that remains. The fundamental of the bending mode is known to be rapidly coupled to its overtone as well as to the 10^00 level. (See Fig. 1) Furthermore, the ν_2 overtones, and the ν_1 stretch are less than 100 cm^{-1} apart in energy, and the precise coupling among these levels has long been unknown. Huddleston and Weitz measured the "ladder-climbing" rate

$$2CO_2(01^10) \underset{K_D}{\overset{K_u}{\rightleftharpoons}} CO_2(10^00/02^20/02^00)$$

and found it to be 387 $\pm$ 75 $msec^{-1}$ $torr^{-1}$[(12)] in good agreement with the rate measured by Javan, et al.[(5)] However, due to various problems inherent in the fluorescence emission technique that was used, they were unable to perform a complete kinetic analysis. Poor signal to noise ratio of the emission out of these low frequency states, limitations in detector response time, and the low resolution of infrared filters make this type of experiment particularly difficult. Furthermore, the ν_1 symmetric stretch is infrared inactive and cannot be directly observed in emission studies. Whereas exact information could not be obtained, Huddleston and Weitz were able to place a lower limit of about 1100 $msec^{-1}$ $torr^{-1}$ on the rate of energy transfer among the

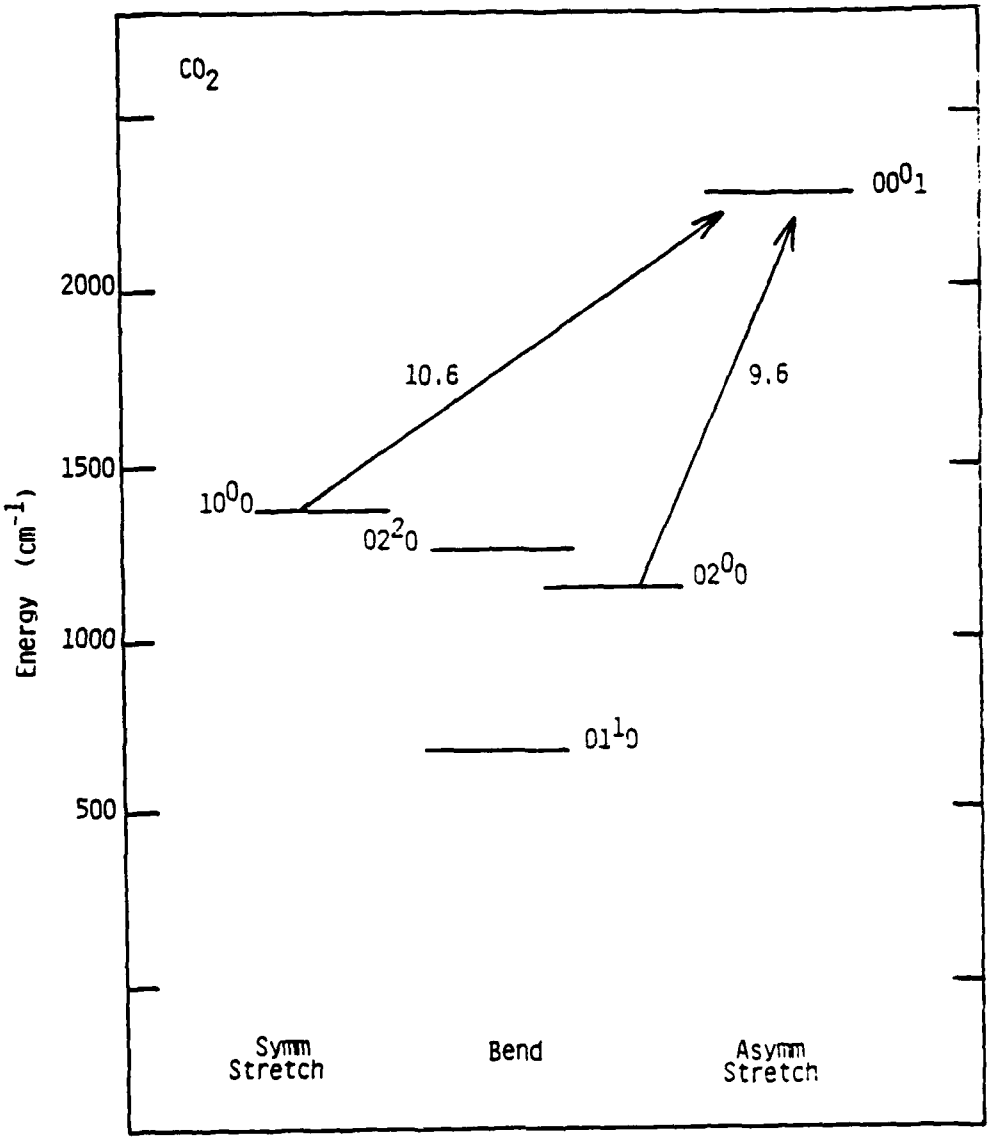
CO_2
00^01
2000
10.6
9.6
1500
10^00
02^20
02^00
Energy (cm^{-1})
1000
01^10
500
Symm Stretch
Bend
Asymm Stretch

Figure 1

$(10^00/02^20/02^00)$ states.

Diode laser infrared double resonance is a perfect technique to obtain the desired information on this system. The high resolution (about .001 cm^{-1}) makes it possible to monitor population in individual rotational/vibrational states of CO_2. By selectively monitoring transitions of the type

$$(10^00) \longrightarrow (10^01)$$
$$(02^20) \longrightarrow (02^21)$$
$$(02^00) \longrightarrow (02^01)$$
$$(01^10) \longrightarrow (01^11)$$

it is possible to observe the time evolution of the population in these states after perturbing the population with a Q-switch CO_2 laser. Not only is there no question as to which state is being observed, but by "riding" the ν_3 transition, the strong oscillator strength of ν_3 can be used to advantage to gain information on the modes with weak oscillator strength and to directly monitor the infrared inactive ν_1 symmetric stretch.

Experimental:

A diagram of the apparatus is shown in Fig. 2. A home built Q-switch laser was used to pump the CO_2 sample, using either the 10.6 micron or the 9.6 micron lines. The laser pulse shape was carefully monitored using a AuGe infrared detector; the pulse width was never more than 1.5 microsec FW at the 10% amplitude points. The CO_2 laser beam was directed through the sample cell and could be easily aligned by means of an NRC optical periscope; the final mirror used to send the beam through the cell consisted of a 2 inch Ge beam splitter, with the front side coated for 80% reflectivity at 10.6 microns and

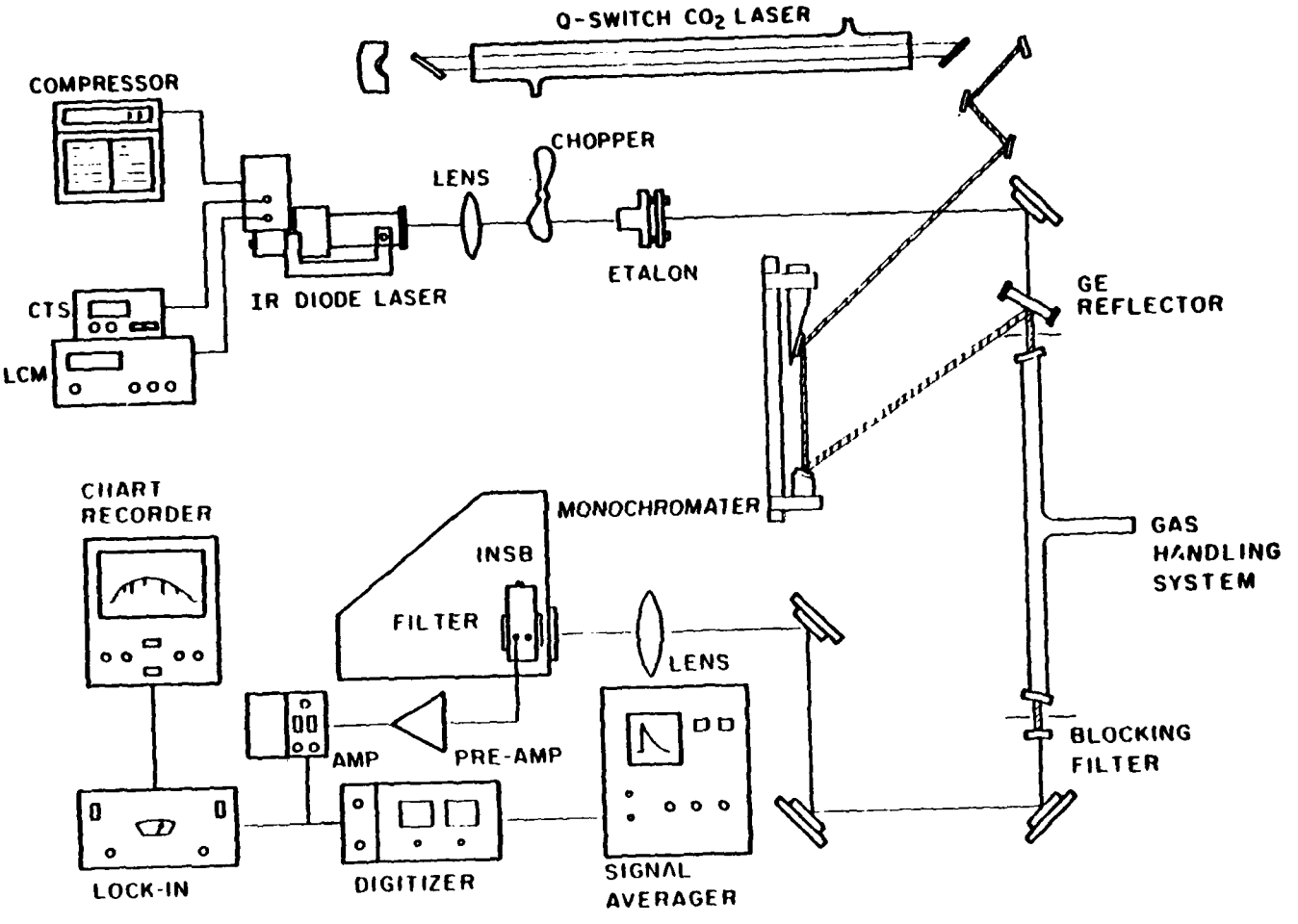
Q-SWITCH CO_2 LASER
COMPRESSOR
CHOPPER
LENS
ETALON
IR DIODE LASER
CTS
LCM
GE
REFLECTOR
CHART
RECORDER
MONOCHROMATER
INSB
FILTER
LENS
GAS
HANDLING
SYSTEM
AMP
PRE-AMP
BLOCKING
FILTER
LOCK-IN
DIGITIZER
SIGNAL
AVERAGER

Figure 2

the back side coated for antireflection at 10.6 microns. Care had to be taken that the samll portion (about 20%) of the 10.6 micron beam which passed through the flat rather than being reflected was not picked up by the probe beam optics and sent back to the diode laser. A 4 to 5 micron bandpass filter was used to block the 10.6 or 9.6 micron laser beam at the output of the sample cell.

The probe beam at 4.3 microns was generated by an infrared diode laser purchased from Laser Analytics. A closed cycle helium compressor maintained the diode at approximately 12K. Current and temperature were controlled by units also supplied by Laser Analytics. The diode laser beam was collimated by means of an F1 CaF_2 lens, and made collinear with the Q-switch CO_2 laser beam by passage through the flat (although the back of the flat was AR coated for 10 microns this coating had little or no effect on the 4.3 micron beam). After passing through the cell, the probe beam was focussed onto the slits of an F4.5 Bausch and Lomb monochromator by means of an F4.5 ZnSe lens. The low power (about 1 mwatt) probe signal was detected by means of an InSb photovoltaic detector with a 3 mm square element. The response time of the detector/amplifier assembly was approximately 1.5 microsec. The signal was preamplified with a Perry Amp, model 730, further amplified by a Tektronix Am502 1 Hz to 1 MHz wideband amplifier, digitized with a Biomation 8100 transient digitizer, and signal averaged with a Nicolet 1170 signal averager. After averaging the signal was sent to a PDP11/34 or a Vax 11/780 computer for further analysis. Spectral scans were taken by chopping the signal at about 400 Hz and using a Keithley Lock-in Amplifier whose output went to a Houston 2000 chart recorder. Relative frequency assignments were aided by use of a 1 inch Ge etalon whose fringe spacings were on the order of .047 cm^{-1} per fringe. Absolute assignment of one point was necessary in order to convert

relative frequency to absolute frequency. This was done by comparison of the relative peak positions and intensities with those reported by the Air Force Cambridge Research Laboratories Atmospheric Absorption Line Parameters Compilations.[13] Additional confirmation was possible by comparing a $^{13}CO_2$ spectrum with the $^{12}CO_2$ spectrum taken over the same current range.

Results:

Transient absorption signals were observed for the transitions

$$(10^00) \longrightarrow (10^01)\ P(20)$$
$$(02^20) \longrightarrow (02^21)\ P(17)$$
$$(02^00) \longrightarrow (02^01)\ P(20)$$
$$(01^10) \longrightarrow (01^11)\ P(31)$$

using both the 9.6 micron and the 10.6 micron CO_2 laser lines as pump sources. In the case of the $(10^00) \rightarrow (10^01)$ P(20) transition with the 10.6 micron pump, as well as the $(02^00) \rightarrow (02^01)$ transition with the 9.6 micron pump, care was taken to ensure that the pump laser was not directly pumping the same rotational/vibrational state that was being probed. In the few instances in which the pump laser was directly pumping the same rotational state, rapid rotational relaxation occurred in the fall of the signal, and the decay curve was more difficult to analyze. Fig. (3A) shows a typical signal observed when pumping with the 10.6 micron line and observing the $(10^00) \rightarrow (10^01)$ P(20) transition. The rise time is detector limited at all pressures, and occurs within the laser pulse, corresponding to rapid depletion of the (10^00) state as population is shifted to the (00^01) level with the Q-switch laser. The fall is rather fast, and corresponds to the adjacent levels, (02^20), (02^00),

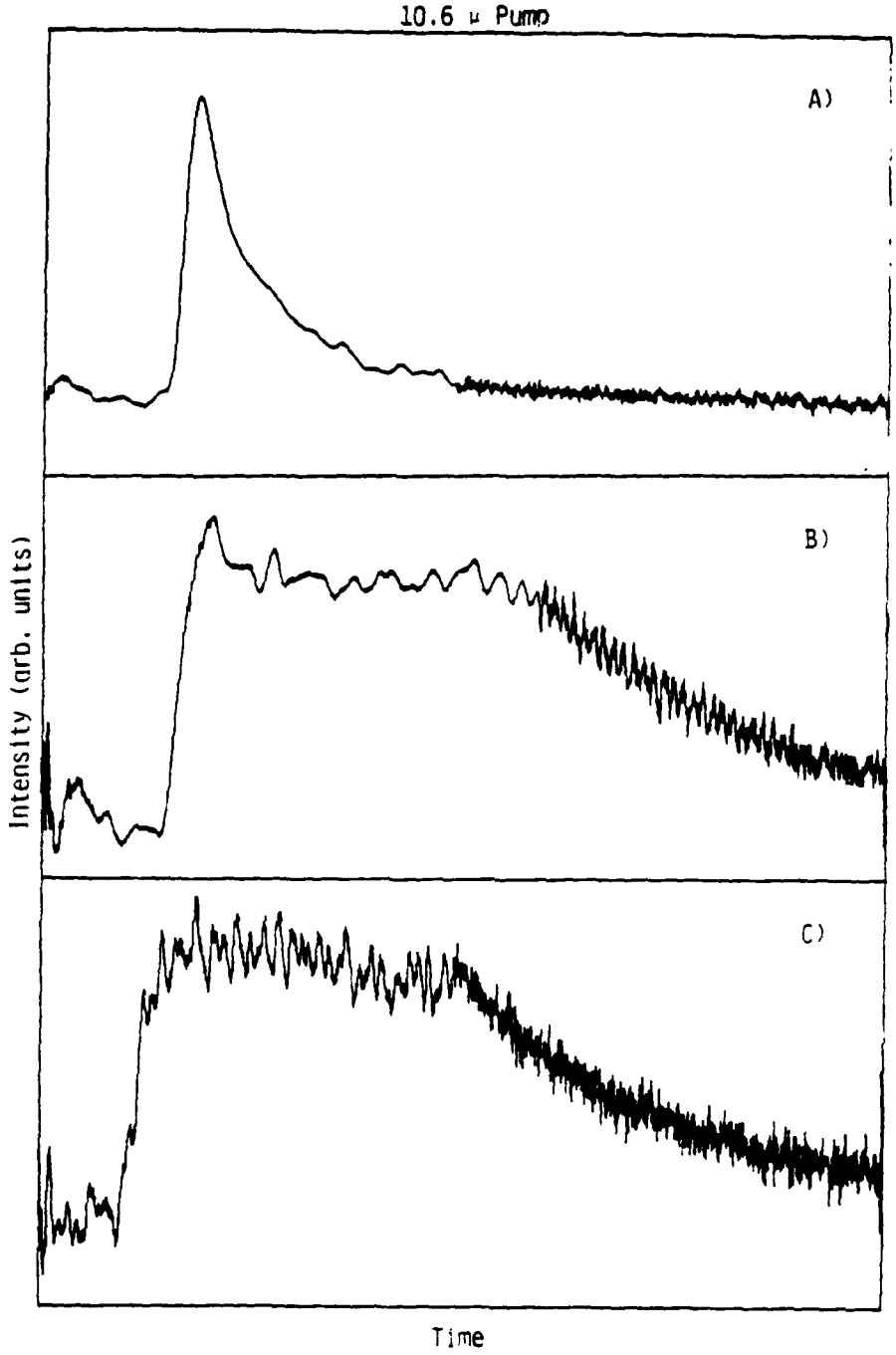

Fig. 3 A) $(10^00) \rightarrow (10^01)$ Probe
.5 torr CO_2
Full scale .52 msec (.02 msec/.05 msec dual time)

B) $(02^20) \rightarrow (02^21)$
.8 torr CO_2
Full scale .824 msec (.024 msec/.08 msec dual time)

C) $(02^20) \rightarrow (02^01)$
.5 torr CO_2
Full scale 1.05 msec (.05 msec/1 msec dual time)

as well as (01^10), sharing their population with the now deficient (10^00) level. Observation of the (02^20) P(20) level with the 9.6 micron pump results in a qualitatively similar signal.

Observation of the $(02^20) \rightarrow (02^21)$, $(02^00) \rightarrow (02^01)$, and $(01^00) \rightarrow (01^11)$ transitions with the 9.6 micron pump can also give information on the coupling among these four states. In this case however, the rise time should not be occuring within the laser pulse, but rather will reflect the time dependent coupling of the states. Depending on the actual coupling among the levels and the level probed, the observed fall may or may not have information on the coupling.

The curves were computer fit using a nonlinear least square fitting routine. The following is a summary of the results:

10.6 micron Pump:

$(10^00) \rightarrow (10^01)$ Probe:

The detector limited rise was followed by a fall which appeared to have three components: 1) an extremely rapid fall, also detector limited, at all but the lowest pressures (less than .1 torr); 2) a second fall was measured to have a rate of about 700 $msec^{-1}$ $torr^{-1}$; 3) a third slow fall was thought to be either the V-T, R rate or the rate of diffusion out of the diode laser beam. All the signals displayed this slow fall. While this rate has no real significance in the population equilibration of the four levels of interest, it had to be subtracted off before the other rates of interest could be analyzed. This rate will be ignored in the description of the other signals.

$(02^20) \rightarrow (02^21)$ Probe:

The signal is shown in Fig. (3B). Studies at low pressures indicate that there is a single fast rise having a rate of 2500 ± 500 msec^{-1} torr^{-1}. The fall has only one relevant component, a small amplitude decay (less than 25% of the total signal), having a rate of about 400 ± 40 msec^{-1} torr^{-1}.

$(02^00) \rightarrow (02^01)$ Probe:

The signal is shown in Fig. (3C). Again, there is only one discernable rise and no fall other than the slow V→T,R rate. The rise was the slowest observed having a rate between 700 and 1000 msec^{-1} torr^{-1}.

9.6 micron Pump:

$(10^00) \rightarrow (10^01)$ Probe:

The signal is shown in Fig. (4A). Pressure studies from .5 torr down to .3 torr place this rate at 1000 ± 300 msec^{-1} torr^{-1}. Again no fall was clearly observed; however at higher pressures an extremely small amplitude "wave" was discernable in the fall. The small amplitude of this portion of the signal, along with the noise made it impossible to fit. This fall is thought to be due to the ladder climbing process.

$(02^20) \rightarrow (02^21)$ Probe:

The signal is shown in Fig. (4B). The single fast rise has a rate of 2300 ± 500 msec^{-1} torr^{-1}. Again no fall was observed other than the slow V→T,R rate.

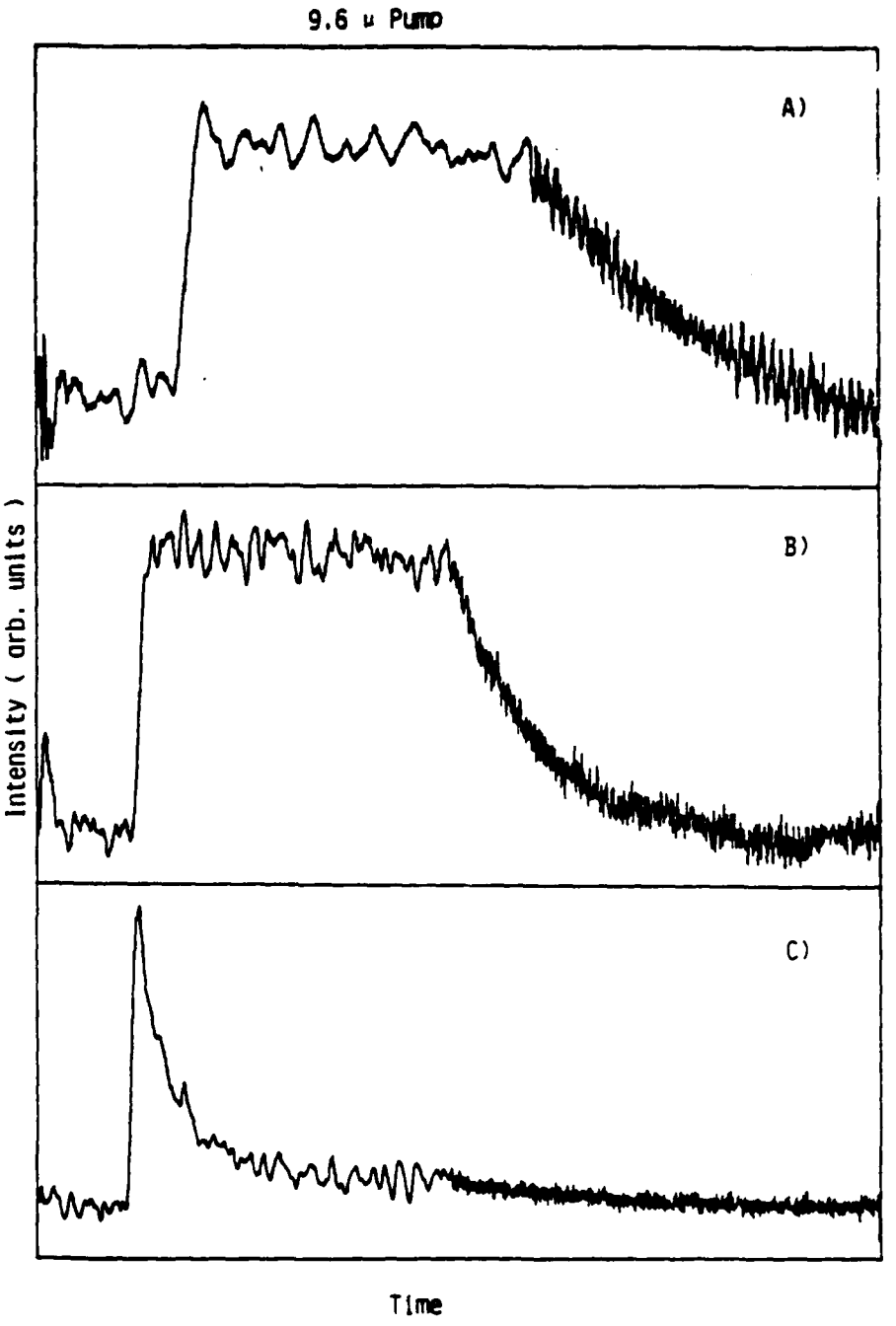

Fig. 4 A) $(10^00) \rightarrow (10^01)$ Probe
1 torr CO_2
Full scale .824 msec (.024 msec/.8 msec dual time)

B) $(02^00) \rightarrow (02^21)$
1 torr CO_2
Full scale 2.05 msec (.05 msec/2 msec dual time)

C) $(02^00) \rightarrow (02^01)$
.5 torr CO_2
Full scale 1.05 msec (.05 msec/1 msec dual time)

$(02^00) \rightarrow (02^01)$ probe:

Here we are observing the state that is being directly pumped by the laser. Thus, all kinetically interesting processes will occur in the fall, the rise being detector limited and within the laser pulse width. The fall clearly has two components: 1) a fast component which is detector limited at all but the lowest pressure studied; 2) a second component with a decay rate of 390 ± 40 $msec^{-1}$ $torr^{-1}$, and a moderate amplitude.

All of these signals should have three components due to the equilibration of four levels (see kinetics section), as well as the $V \rightarrow T,R$ rate. In no case were all three rates clearly discernable. The reason for this seeming reduction of observed number of rates is simply an amplitude problem: one (or more) of the amplitudes may be relatively small in comparison to the other(s). The relatively small amplitude together with the fact that all three rates are rather close in magnitude may make the small amplitude rates difficult to detect. This problem was especially true at the extremely low pressures that were required to ensure that the faster rates were not detector limited. At these low pressures, the noise was on the same order of magnitude as the small amplitude of some signals.

The technique of adding Ar to the sample cell in order to distinguish between resonant versus non-resonant rates was invaluable in helping us to distinguish the ladder climbing rate.[14] The only two states in which extensive Ar pressure studies were done were the (10^00) level with the 10.6 micron pump, and the (02^00) level with the 9.6 micron pump. Qualitative results were obtained for some of the other levels, and the results were quite interesting.

Argon Studies:

10.6 micron pump, (10^00) Probe:

The pure CO_2 signal exhibited only two rates, an extremely fast fall (too fast to measure under the conditions used), and a slower fall which had a rate of at least 700 $msec^{-1}$ $torr^{-1}$. At .125 torr CO_2, addition of up to 10 torr Ar, this intermediate rate of 700 steadily increased. However, addition of 12 to 30 torr Ar caused the observed rate to slow down. (See Fig. (5)). What appears to be occuring is that the Ar causes the rate to speed up and become indistinguishable from the detector limited fast rate, while the small amplitude ladder climbing rate begins to appear. However, at .125 torr CO_2, this slower ladder climbing process has an amplitude too small with respect to the noise to fit well. At .2 torr CO_2 and 30 torr Ar, the ladder climbing rate appeared as 380 $msec^{-1}$ $torr^{-1}$ of CO_2.

9.6 micron pump, (02^00) Probe:

The pure CO_2 signal again exhibited only two rates: an extremely fast one as well as a "slow" one with a rate of 380 ± 40 $msec^{-1}$ $torr^{-1}$. Upon addition of Ar the slower rate remained approximately the same. This fact clearly demonstrated that the rate under study was the resonant ladder climbing process.

9.6 micron pump, (10^00) Probe:

The pure CO_2 signal, which exhibited a rise of about 700 to 1000 $msec^{-1}$ $torr^{-1}$ and no perceptible fall other than the $V \rightarrow T,R$ rate, upon addition of between 10 and 40 torr of Ar exhibited a detector limited rise, followed by a

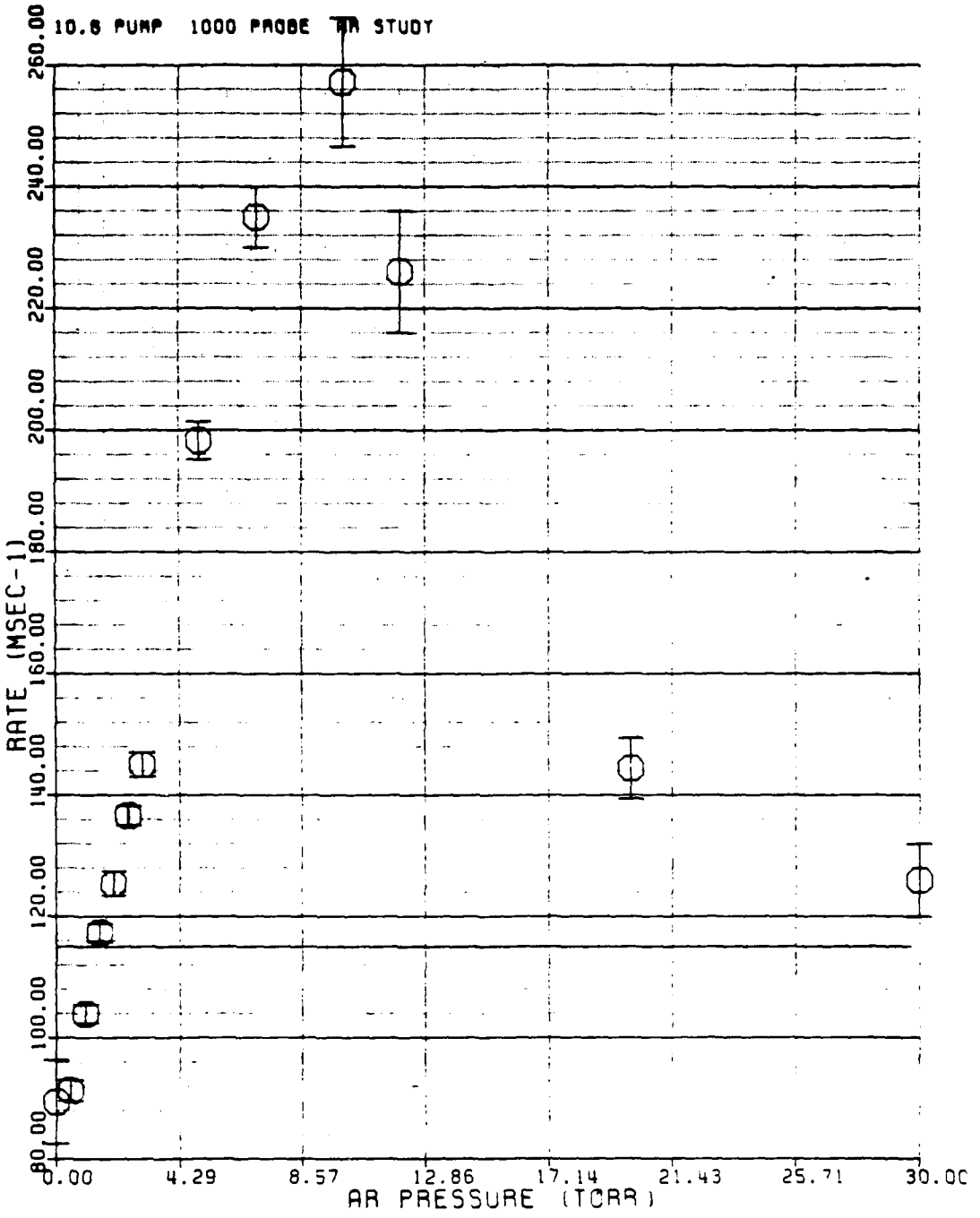
10.6 PUMP 1000 PROBE AR STUDY
RATE (MSEC-1)
260.00
240.00
220.00
200.00
180.00
160.00
140.00
120.00
100.00
80.00
0.00
4.29
8.57
12.86
17.14
21.43
25.71
30.00
AR PRESSURE (TORR)

Figure 5

fast fall whose rate increased with increasing Ar pressure! The source of this Ar pressure dependent rate is a puzzle since the pure CO_2 signal shows no such process at all.

Kinetic Scheme:

Since the four levels in question are fairly well isolated from other levels (see Fig. 1), the system can be treated as a four level system at short times. The validity of this approximation is further assured by the fact that the state to which the population is being pumped, the $(00^0 1)$ ν_3 fundamental, has an exceedingly long lifetime (on the order of 30,000 collisions).[1] Since the slowest rate in the four level system, the ladder climbing rate, is at least 1000 times faster than this, the four level system will have equilibrated with itself before it begins to receive population from the $(00^0 1)$ or other higher energy levels. The ultimate goal, of course, is not only to determine the individual coupling rates of the levels, i.e., the kinetic rate constants, but concomitantly to unambiguously determine the coupling scheme. Since the experiment directly measures the time dependent populations, the rate information that is measured corresponds to convolutions of the kinetic rate constants. In order to deconvolute the measured rates into kinetic rate constants, it is necessary to solve a set of coupled differential equations. To set up the equations a kinetic coupling scheme must be assumed. Two kinetic schemes were tried, and through comparison of both rates and relative amplitudes, one scheme was choosen as the best fit to the data. The two kinetic schemes are shown in Fig. 6. The only difference between the two schemes was as follows. In scheme I, the fundamental of the bend was assumed to couple directly to the $(02^0 0)$ state and only indirectly to the other states through the $(02^0 0)$ state. In scheme II, the $(01^1 0)$ level was assumed to

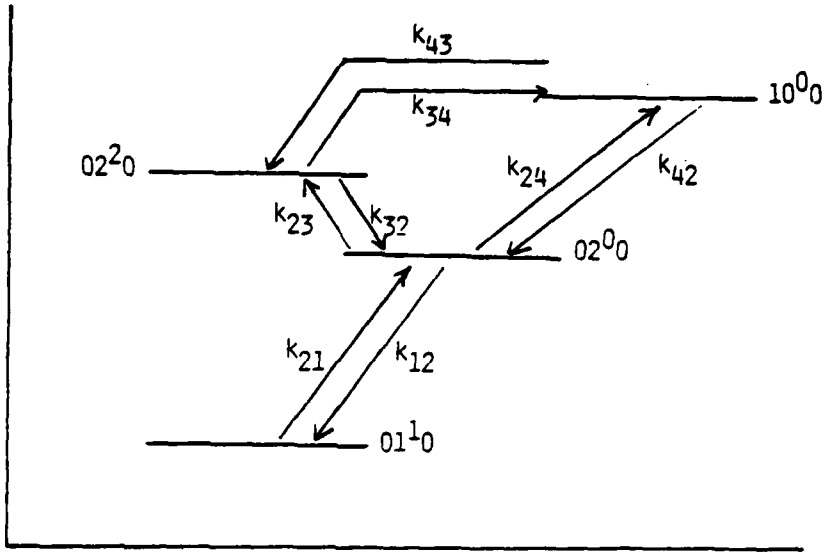

Kinetic Scheme I

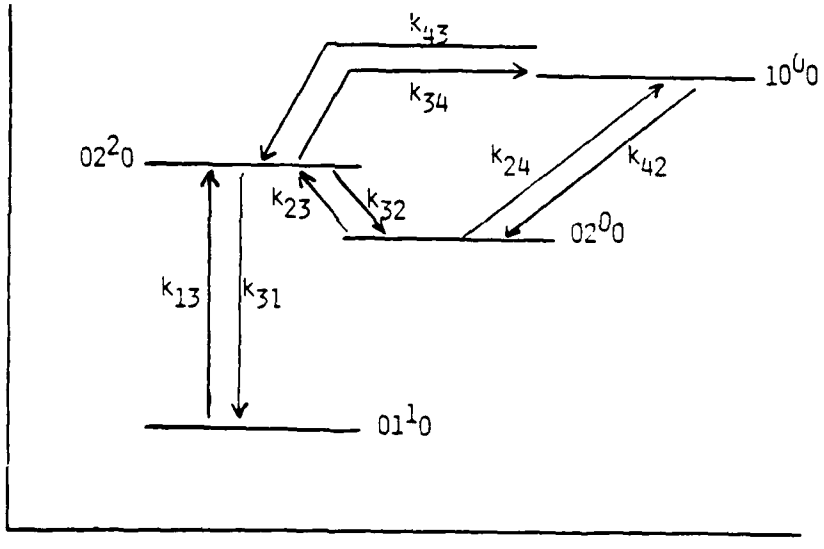

Kinetic Scheme II

Figure 6

couple to the (02^20) level and only indirectly with the other two levels. Of course, if the ladder climbing rate is slow in comparison to the rate of energy transfer among the upper three levels, the two schemes will be virtually indistinguishable.

Since the approach to solving either scheme is exactly the same, only scheme II will be presented in detail as it is the one which best fits the data. The following equations describe the coupling of kinetic scheme II:

$$CO_2(01^10) + CO_2(01^10) \underset{K_{31}}{\overset{K_{13}}{\rightleftharpoons}} CO_2(02^20) + CO_2(00^00)$$

$$CO_2(02^00) + CO_2(00^00) \underset{K_{42}}{\overset{K_{24}}{\rightleftharpoons}} CO_2(10^00) + CO_2(00^00)$$

$$CO_2(02^00) + CO_2(00^00) \underset{K_{32}}{\overset{K_{23}}{\rightleftharpoons}} CO_2(02^20) + CO_2(00^00)$$

$$CO_2(02^20) + CO_2(00^00) \underset{K_{43}}{\overset{K_{34}}{\rightleftharpoons}} CO_2(10^00) + CO_2(00^00)$$

Solution of the coupled differential equations for this kinetic scheme yields 3 eigenvalues which correspond to the three observed rates of the system. The initial conditions are then used to evaluate the eigenvectors of the system which correspond to the observed amplitudes. Since the eignvalues do not depend on the initial conditions, the three observed rates will be the same regardless of which laser line is used to pump the system; however, the amplitudes do depend on the initial conditions, and therefore will be different for the 10.6 pump versus the 9.6 pump.

Discussion/Conclusion:

The three measured rates were:

$$390 \pm 80 \text{ msec}^{-1} \text{ torr}^{-1}$$
$$1000 \pm 300 \text{ msec}^{-1} \text{ torr}^{-1}$$
$$2000 \pm 700 \text{ msec}^{-1} \text{ torr}^{-1}$$

The errors on the two faster rates were set somewhat arbitrarily at approximately 30% of the measured rates. This value was chosen because there are always large systematic errors in measuring rates from fluorescence curves where extensive deconvolution is required. This was particularly apparent in the case of the two faster rates since the pressure range over which they could be measured was limited on the high side by detector response time, and on the low side by poor signal to noise ratios.

The first question to be addressed is whether the two coupling schemes can be distinguished at all. The two schemes were examined and their associated rate constants were evaluated by assuming values for kinetic rate constants and then solving the coupled equations. The resulting rates and amplitude factors were compared to the experimental results and the kinetic rate constants were varied until there was good agreement with the experimental data. Although the data does not absolutely eliminate Kinetic Scheme I, the results do seem to favor Kinetic Scheme II. In scheme II the ν_2 fundamental couples directly to the (02^20) levels with which it is nearly resonant, rather than the Fermi mixed (10^00) and (02^00) levels. The kinetic rate constants which appear to best fit the observed data are:

$$K_{12} \simeq 400 \text{ msec}^{-1} \text{ torr}^{-1}$$
$$K_{23} \simeq 600 \text{ msec}^{-1} \text{ torr}^{-1}$$
$$K_{34} \simeq 600 \text{ msec}^{-1} \text{ torr}^{-1}$$
$$K_{24} \simeq 100 \text{ msec}^{-1} \text{ torr}^{-1}$$

In most fluorescence studies direct comparisons of amplitude ratios is difficult if not impossible because of the large errors associated with their measurement. Fortunately, the 10.6 and the 9.6 micron pump yield different amplitude factors which makes qualitative comparisons possible. The fact that the ladder climbing rate appeared quite clearly in the (02^20) state, but not in the (10^00) state or the (02^20) state when pumped at 10.6 microns is a clue that the ν_2 fundamental appears to preferentially couple to the (02^20) state rather than either the (10^00) or the (02^00).

*This research was also supported by the National Science Foundation under Grant CHE 80-23747 and the Department of Energy under Contract DE-AC-02-78ER04940.

(1) L.O. Hocker, M.A. Kovacs, C.K. Rhodes, G.W. Flynn, A. Javan, Phys. Rev. Letts. 17, 233, (1966).

(2) C.B. Moore, R.E. Wood, Bei-Lok Hu, and J.T. Yardley, J.Chem. Phys. 46, 4222, (1967).

(3) J.T. Yardley, and C.B. Moore, J.Chem. Phys. 46, 4491.

(4) J.C. Stephenson, R.E. Wood, and C.B. Moore, J. Chem. Phys. 48, (1966).

(5) C.K. Rhodes, M.J. Kelley, and A. Javan, J. Chem. Phys. 48, 5730, (1968).

(6) M.A. Kovacs, and A. Javan, J. Chem. Phys. 50, 4111, (1969).

(7) W.A. Rosen, Jr., and E.T. Gerry, J. Chem. Phys. 51, 2286, (1969).

(8) J.C. Stephenson, and C.B. Moore, J. Chem Phys. 52, 2333, (1970).

(9) J.C. Stephenson, R.E. Wood, and C.B. Moore, J. Chem Phys. 54, 3097, (1971).

(10) J.C. Stephenson, and C.B. Moore, J. Chem Phys. 56, 1295, (1972).

(11) I. Burak, Y. Noter, and A. Szoke, IEEE J. Quan. Elec. QE9, 541, (1973).

(12) R.K. Huddleston, and Eric Weitz, Chem Phys. Lett. 83, 174, (1981).

(13) Air Force Combridge Research Laboratories, AFCRL Atmospheric Absorption Line Parameters Compilation, Environmental Research Papers, No. 434, L.G. Hanscom Field, Bedford, Mass. Jan. 26, 1973.

(14) V.A. Apkarian and Eric Weitz, J. Chem Phys., 71, 4349, (1979).

D. COMPETITION BETWEEN INELASTIC AND REACTIVE SCATTERING: A STUDY OF N_2O AND CH_4*

(J. Subbiah, G. W. Flynn)
(JSEP work unit 7, 1982-1985)
(Principal Investigator: G. W. Flynn (212) 280-4162)

Studies of energy transfer dynamics using hot species produced by photofragmentation in the gas phase are valuable because they allow simulation of the chemistry of the upper atmosphere to determine the role of critical species in the oxygen cycle; they contribute to a better understanding of the dynamics of thermalization of hot species, including possible competition among elastic, inelastic and reactive channels on potential energy surfaces; they can be used to measure the dependence of reaction cross section on the relative translational energy; and they provide valuable tests of theories of inelastic scattering and translation-to-vibration (T-V) energy transfer.(1)

We have studied collisions of hot atoms in the gas phase produced by the photolysis of suitable precursors at 193 nm. The first system studied involves the photolysis of N_2O, which is interesting because of its similarity to the linear symmetric polyatomic CO_2, whose excitation by hot atoms has been studied.(2) Although CO_2 is interesting because of its simplicity and huge oscillator strength, its symmetric stretching mode ν_1 is IR inactive and this makes it difficult to compare the relative degree of excitation of the two stretching modes. N_2O, on the other hand, being a linear but unsymmetric triatomic, does not have this problem, and is a good test case to determine the possiblity of mode-selective vibrational excitation by a translationally hot projectile.

The first experiments were performed on the HBr-N_2O system. The relevant processes are:

$h\nu$ (λ=193nm) + HBr ----> H* + Br — Hot Atom Generation

H* + N_2O -----> H + N_2O (ν_i) — T-V Excitation

H + HBr -----> H_2 + Br

H*/H + N_2O ----> OH + N_2 — Reaction (ΔH = -62.4 Kcal/mole) $k = 4 \times 10^{-11}$ ccmol^{-1}s^{-1} at 20,000°K, the temperature of the hot-hydrogen atoms

H/H* + N_2O ----> NH + NO — (ΔH = +30.8 Kcal/mole)

Irradiation of HBr-N_2O mixtures produced strong IR emission from the N-N stretch at 2154 cm^{-1} (see Fig. 1), while the emission from the N-O stretch at 1265 cm^{-1} is very weak. Similar work by Quick et.al.[3] has shown that the high frequency ν_1 mode is significantly more populated than the ν_3 mode. This result is totally unexplainable by the refined impulse approximation approach to T-V transfer which predicts a more favorable excitation of the lower frequency mode.

Irradiation of N_2O alone also gives rise to IR fluorescence from vibrationally excited N_2O, though the signal is much weaker than in the case of HBr-N_2O mixtures (see Fig. 2). The mechanism is postulated to be:

1) $N_2O + h\nu$ (λ = 193 nm) ----> N_2 + O (^{1}D) — Photolysis

2) O(^{1}D) + N_2O ----> O + N_2O (ν_i) — T-V transfer

3) O(^{1}D) + N_2O ----> 2NO (ΔH = -80.95 Kcal/mole) — Reaction
$k_f = 10^{10}$ ccmol^{-1}s^{-1}
----> N_2 + O_2 (ΔH = -124.05 Kcal/mole)
$k_f = 10^{10}$ ccmol^{-1}s^{-1})

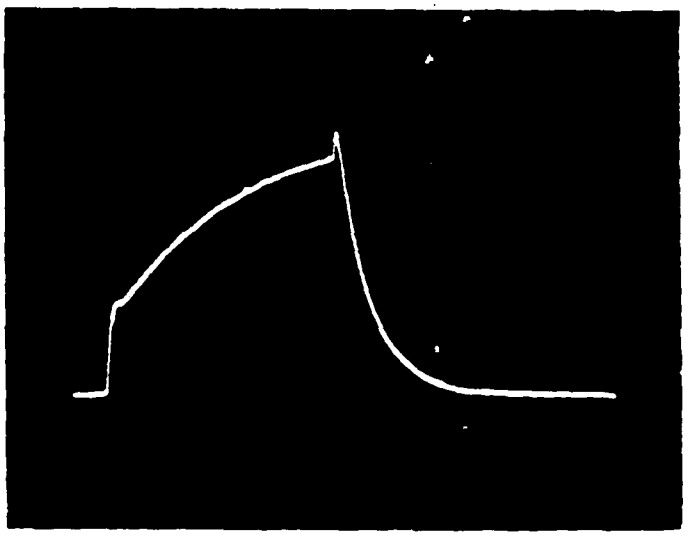

Fig. 1 IR fluorescence emission from N_2O excited by irradiation of 1:1 mixtures of HBr + N_2O at 193 nm

total pressure : 0.5 torr
time base : 100 μs full-scale
detector : InSb
filter : 4 to 5 micron

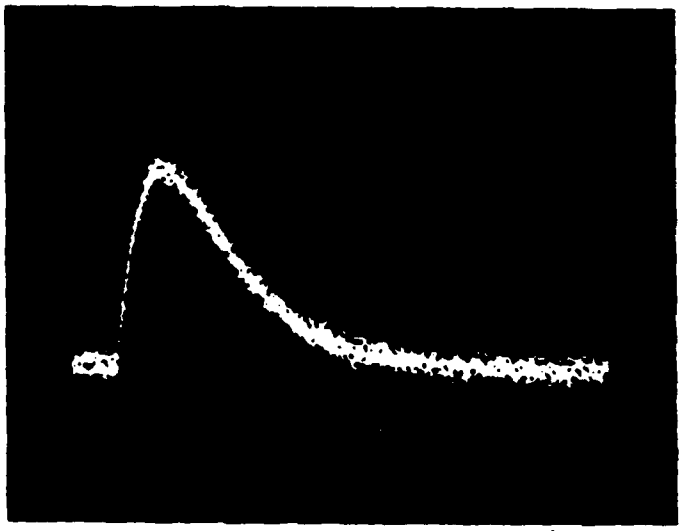

Fig. 2 IR fluorescence emission from N_2O excited by irradiation of neat N_2O at 193 nm

total pressure : 0.5 torr
time base : 10 ms full-scale
detector : InSb
filter : 4 to 5 microns

As in the case of $HBr-N_2O$ mixtures it was again found that the high frequency N-N stretch was much more strongly excited than the lower frequency N-O stretch.

Fig. 2 shows the IR emission of the ν_1 mode of N_2O when the neat gas is irradiated at 193 nm. One of the most obvious differences from the same emission in $HBr-N_2O$ mixtures is that the risetime is not detector-limited, but is rather slow. A pressure-dependent study shows that the rate constant on the rise is about $7(\text{ms torr})^{-1}$ corresponding to about 3900 collisions. It may be that this excitation corresponds to energy transfer from N_2 (vibration-to-vibration energy transfer) or from $O(^1D)$ (electronic-to-vibrational energy transfer). Further work is required to verify this mechanism.

As Eq. 3 shows, one possible excitation channel involves reactive encounters. This was monitored by looking for vibrationally excited NO, which is observed (see Fig. 3). At the photolysis wavelength used, it is energetically impossible for N_2O to dissociate to N + NO, thus the NO is probably formed by the reactive channel (Eq. 3). This reaction is known to occur at gas kinetic rates, accounting for the fast rise, as well as by energy transfer from other species (slow rise). This is one example of a case where reactive scattering actually predominates over inelastic scattering.

Another system studied was Cl_2-CH_4, which can provide information relevant to the possible effects of the presence of chlorine-containing species of natural or anthropogenic origin in the stratosphere, and their role in the ozone balance. The basic features are similar to those for $HBr-N_2O$ and consist of the following steps:

$$Cl_2 + h\nu\ (\lambda = 193\ \text{nm}) \longrightarrow 2Cl^*\ (15000\ \text{cm}^{-1}) \quad \text{Photodissociation}$$

$$Cl^* + CH_4 \longrightarrow Cl + CH_4\ (\nu_1) \quad \text{Inelastic scattering}$$

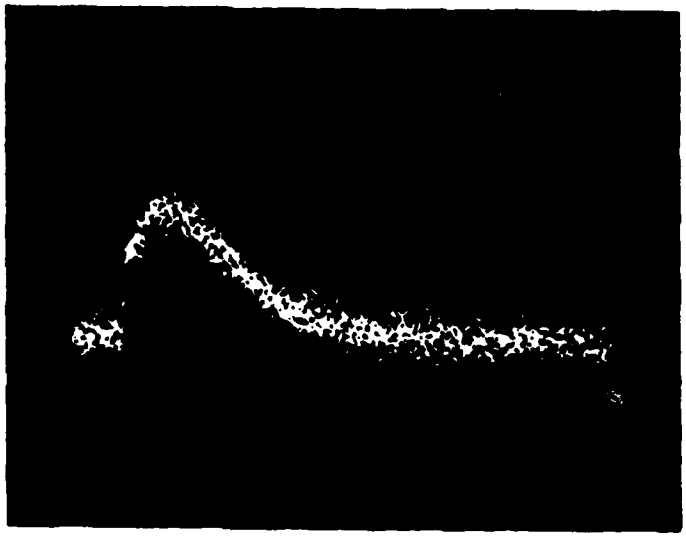

Fig. 3 IR fluorescence of NO following irradiation of neat N_2O at 193 nm

total pressure : 0.5 torr
time base : 20 ms full-scale
detector : InSb
filter : 5.362 micron narrow band

$Cl^* + CH_4 \longrightarrow HCl^\dagger + CH_3$ Reactive channel (ΔH = -1.186 Kcal/mole)

$Cl^* + CH_4 \longrightarrow CH_3Cl^\dagger + H$ Reactive channel (ΔH = +21.4 Kcal/mole)

Both these channels are accessible because of the excess energy of the hot chlorine atom produced in the photolysis. IR fluorescence was monitored from both IR active fundamentals of CH_4 a degenerate stretch at 3019 cm^{-1} and a degenerate deformation at 1306 cm^{-1} to determine the distribution of energy among different modes of CH_4. Some of the more important observations are: (1) Under comparable conditions, the IR emission is much stronger in the Cl_2-CH_4 system than in the HBr-CH_4 system; (2) Strong IR emission was observed in the 3 to 4 micron spectral region when 5:1 mixtures of Cl_2-CH_4 were irradiated at 193 nm (see Fig. 4). This emission could be either from vibrationally excited HCl or from vibrationally excited CH_4. Further work will be done to assign the emission by wavelength resolved detection using either a circular variable filter or a cold gas filter.

Future experimental work will include the use of tunable excitation sources, better wavelength-resolved detection, and precursor variation to obtain a better understanding of the momentum and velocity dependence of T-V energy transfer.

*This research was also supported by the National Science Foundation under Grant CHE 80-23747 and the Department of Energy under Contract DE-AC-02-78ER04940.

(1) D. Rapp and T. Kassal, Chem. Rev. 69, 61 (1969).

(2) J. O. Chu and G. W. Flynn, J. Chem. Phys. 78, 2990 (1983).

(3) C. R. Quick, Jr., R. E. Weston, Jr., and G. W. Flynn, Chem. Phys. Lett. 85, 15 (1981); F. Magnotta, D. J. Nesbitt, and S. R. Leone, Chem. Phys. Lett. 83, 22 (1981).

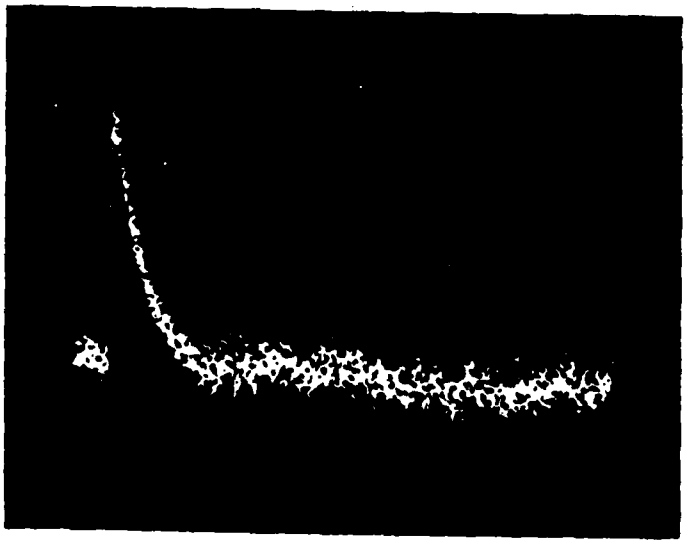

Fig. 4 IR emission following irradiation of 1:5 mixtures of CH_4:Cl_2 at 193 nm

total pressure : 0.8 torr
time base : 2 ms full-scale
detector : Au:Ge
filter : 3 to 4 microns

E. VIBRATIONAL ENERGY RANDOMIZATION IN SO_2 FOLLOWING ELECTRONIC EXCITATION*

(B. Lawrence, P. Beeken, G. W. Flynn)
(JSEP work unit 7, 1982-1985)
(Principal Investigator: G. W. Flynn (212) 280-4162)

Despite much work in recent years, the chemical and physical processes of electronically excited SO_2 are not well understood. The physics is of particular interest because this molecule is an example of an intermediate case in radiationless transition theory. The physics and the chemistry are, of course, interrelated. Spontaneous radiationless transitions occur in large molecules when excited to an electronic state which is coupled in some way to another electronic state with a high density of states at the same energy.[1] In small molecules, the density of states is not large enough to allow for this crossover to occur. Collision-induced radiationless transitions do occur in cases such as SO_2 where, perhaps, collisional broadening of the vibronic levels increases the number of accepting states available so that the probability of curve crossing also increases.[2] If an intermediate-case molecule is electronically excited at a pressure high enough for the molecule to undergo collisions before it radiates, it may cross over to another excited electronic state or to high vibrational levels of the ground state. In any case, the molecule will eventually relax to the ground state - probably with vibrational excitation.

One might ask whether the excess vibrational energy remaining in the molecule when it returns to the ground state will be randomly distributed among the normal modes or whether one mode will be preferentially excited over the others. The answer to this question should give some information about the electronic and vibrational relaxation processes occurring after the initial excitation.

We have been exciting SO_2 electronically and observing time-resolved emission from the ν_3 mode of the ground state. Vibrational relaxation of the ground state of SO_2 has previously been studied in this laboratory[3] by exciting the ν_1 mode and observing emission from the ν_3 mode. Because the rates of intermode vibrational energy transfer are now known, observed emission from one mode will yield information about the initial conditions of vibrational excitation.

SO_2 has three major absorption regions between 200 nm and 400 nm (see Fig. 1). A weak absorption between 390 nm and 340 nm has been assigned to a spin-forbidden transition from the ground state to the $^3B_1$ state. This region is thought to be perturbed by the presence of two other triplet states. A second, somewhat stronger absorption region from 340 nm to 260 nm, called the first-allowed band, has been assigned to two overlapping transitions from the ground state: an electric-dipole-allowed transition to the $^1B_2$ state and an electric-dipole-forbidden but vibronically allowed (with ν_3 excitation) transition to the $^1A_2$ state. These two states are coupled to each other and to the lower triplet states. Therefore, this region is very complex. A third, very strong absorption region, called the second allowed band, starts at 235 nm and is assigned to the allowed transition from the ground state to the $^1B_2$ state.

In these initial studies, we have been electronically exciting SO_2 into the first allowed band using the frequency-doubled output of a Lambda-Physik excimer-pumped dye laser using Rhodamine 6G dye. The SO_2 has been at pressures of 500 mtorr to 8 torr. The time-resolved 7.4μm emission from the ν_3 vibrational mode is detected through a 7-8μm bandpass filter by a AuGe (77K) detector. The signal is collected using a transient digitizer/digital signal averager combination and transferred to a PDP11 computer for later

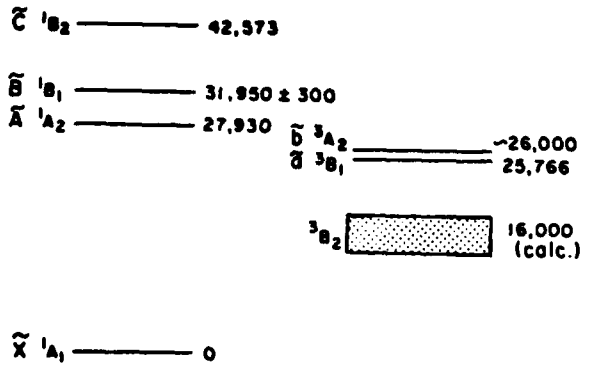

Energy level diagram for low-lying electronic states of SO_2
(EKC Lee and G. Loper in "Radiationless Transitions" (SH Lin, ed.), p.22, Academic Press, New York)

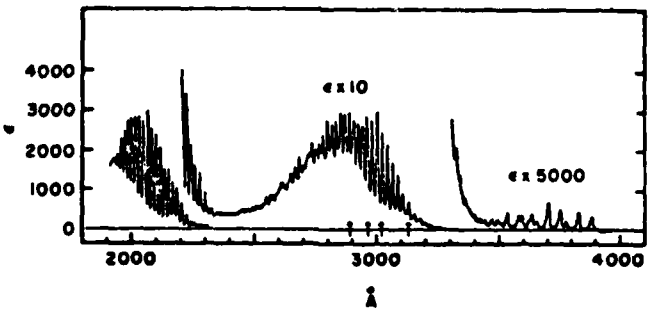

Low resolution absorption spectrum of SO_2
(ε in units of $\ell mol^{-1}cm^{-1}$ to base 10)
From Strickler and Howell, J. Chem. Phys. 49, 1949 (1969).

Figure 1

analysis.

Preliminary results show a fast exponential rise and a slower exponential fall in the ν_3 emission. (see Fig. 2) Data taken at several different pressures was fit to a double-exponential decay curve, after the subtraction of a thermal tail. Using decay curves obtained at an excitation wavelength of 305 nm, Stern-Vollmer plots of rate vs. pressure have rates of 80.7 ($msec^{-1}$ $torr^{-1}$) for the rise and 3.5 ($msec^{-1}$ $torr^{-1}$) for the fall. Comparisons with ground state energy transfer studies from this laboratory[3] show that the rates are roughly comparable to those obtained with direct laser excitation of the ground state ν_1 mode. This suggests that the fast rise corresponds to the population of the ν_3 mode by the rapid equilibration of the ν_1 and ν_3 modes.[3] The slower fall appears to be the result of vibrational relaxation through the bending mode to the translational bath.[3]

In previous experiments,[4] SO_2 was excited at 248 nm. (This is 50 nm higher in energy than the present experiments in a region between the second and third absorption bands.) The resolved emission showed a fast exponential fall followed by a slower exponential fall. The rates were roughly comparable to the rise and fall observed at the longer wavelength. These results seem to indicate that at 305 nm excitation the ν_1 mode is initially, preferentially excited, while at 248 nm excitation the ν_3 mode is initially excited. It should be emphasised that these results and their interpretation are preliminary.

In the immediate future we plan to perform the same experiments using different excitation wavelengths while looking at emission from the ν_1 mode (with a AuGe detector and an 8-9u filter) as well as from the ν_3 mode. Using an excimer laser at 308 nm we would be able to use much lower pressures of SO_2 in order to learn more about the initial rise in population of the

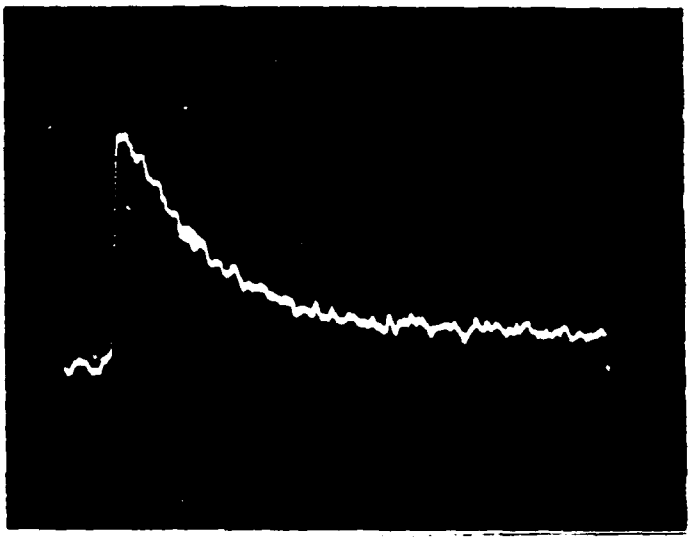

Fig. 2 $SO_2(\nu_3)$ emission
P_{SO_2} = 8.0 torr
Nshots = 400
Time base = 0.2 msec (full scale)
Excitation λ = 305.0 nm

vibrational modes and to rule out other processes such as radiational relaxation or Raman scattering. A careful study of the variation of the decay rates with excitation wavelength for the first allowed band should be done. We would also like to try exciting into the second-allowed and the triplet region. The highest-energy region would be especially interesting because it is much less complicated and the results should therefore be easier to interpret.

*This research was also supported by the National Science Foundation under Grant CHE 80-23747 and the Department of Energy under contract DE-AC-02-78ER04940.

(1) J. Jortner, S. Rice, and R. M. Hochstrasser, Adv. Photochem. 7, 149 (1969).

(2) K. F. Freed, Chem. Phys. Lett. 37, 47 (1976).

(3) J. L. Ahl, Ph.D. Thesis, Columbia University, 1982.

(4) Columbia Radiation Laboratory Report 31, 1980-1981, pp. 104-106.

F. LASER VS. THERMAL EXCITATION OF SF_6 IN A MOLECULAR BEAM AND THE USE OF LASER EXCITED SF_6 IN A CHEMI-IONIZATION REACTION WITH K_2*

(JSEP work unit 7, 1982-1985)
(G. Spector, G. W. Flynn)
(Principal Investigator: G. W. Flynn (212) 280-4162)

During the last year, work was undertaken to complete two projects, the chemi-ionization reaction of K_2 and SF_6 studied in a crossed molecular beam machine and the study of laser- vs. thermal-excitation of SF_6 molecular beams. A manuscript has been prepared[1] for publication which describes the laser heating experiments.

(1) Chemi-ionization

Earlier work in this laboratory had demonstrated that internal energy can be deposited in a supersonic molecular beam of SF_6 with a lower power, cw CO_2 laser [P(16)10.6μm, 6.5W].[2] Later studies showed that laser irradiation inside a transparent nozzle enhanced that internal energy of SF_6 molecules significantly.[3] In early 1982, an application study commenced, using the laser-excited SF_6 beam with effusive beams of K and Na. E.W. Rothe, of Wayne State University, had studied several M + SF_6 systems[3] determining the relative chemi-ionization cross sections of electronically excited M* vs. ground state M. We have studied a similar reaction, but with a vibrationally excited SF_6 beam.

An electron multiplier was employed to detect cations at the scattering center. Unfortunately, the multiplier detects <u>all</u> positive ions, so a definitive prediction of particular product formed is impossible. One can, however, ascertain from Fig. 1 that only the formation of K_2F^+ (M=K) is energetically favored, the positive ion is formed with dimer (K_2). There is no stable ionic product formed with monomer (K). The apparatus used in these

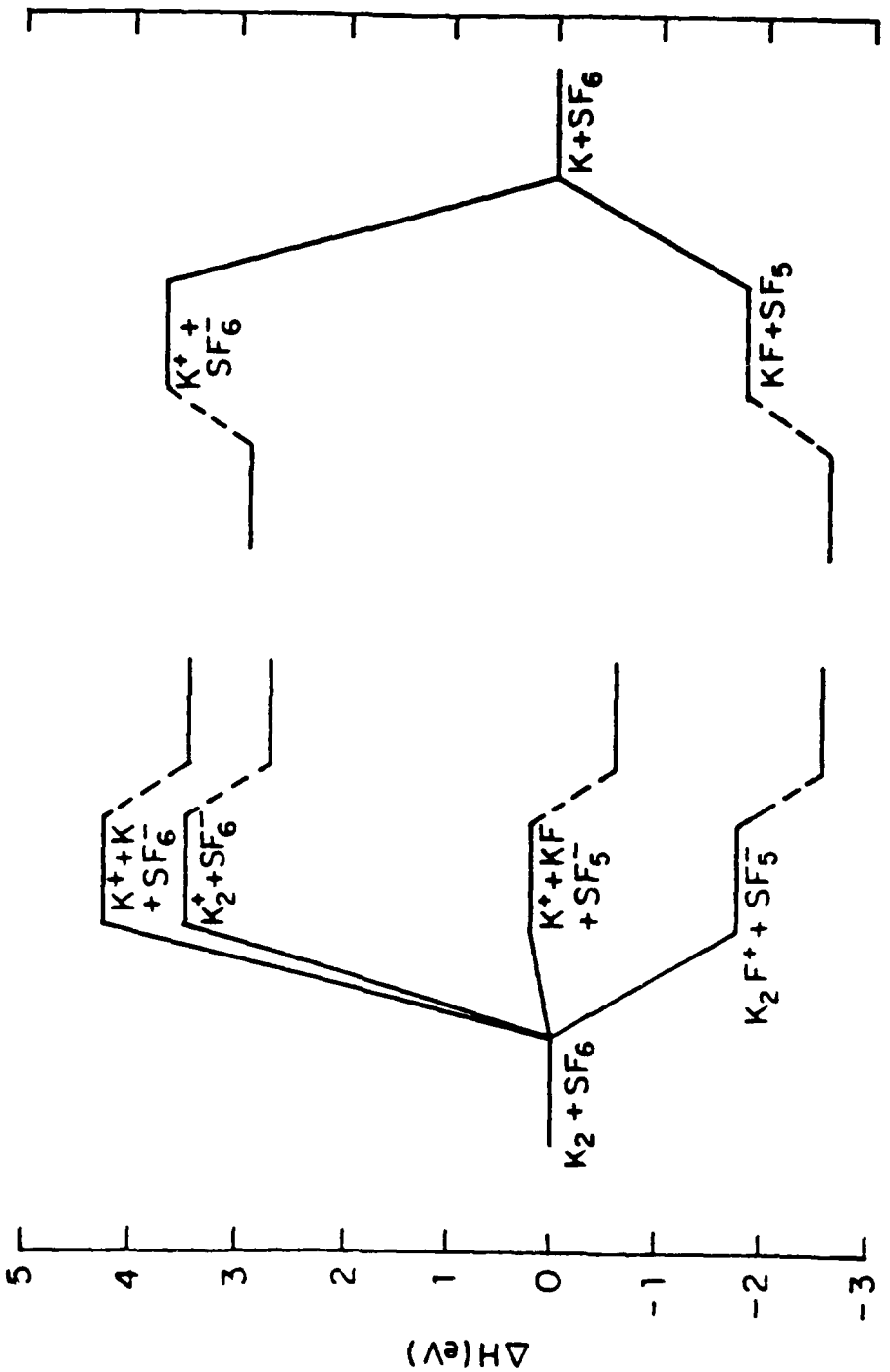
ΔH(eV)
5
4
3
2
1
0
-1
-2
-3
K+SF6
K+ + SF6-
KF+SF5
K2+SF6
K2 + SF6
K+ + K + SF6-
K+ + KF + SF5-
K2F+ + SF5-

Figure 1

AD-A128 815 RESEARCH INVESTIGATION DIRECTED TOWARD EXTENDING THE USEFUL RANGE OF THE ELECTROMAGNETIC SPECTRUM(U) COLUMBIA RADIATION LAB NEW YORK G W FLYNN 31 MAR 83

3/3

UNCLASSIFIED DAAG29-82-K-0080 F/G 20/3 NL

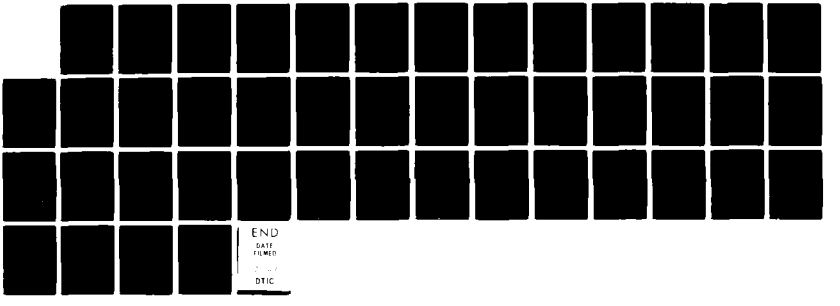

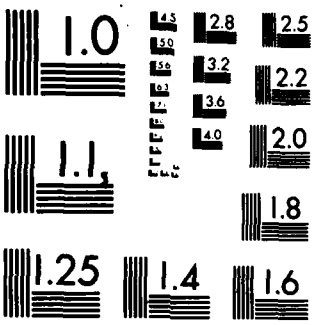

experiments is described elsewhere.[5]

Although the availability of mass selective detection would provide more information, it is the relative (laser excited SF_6 vs. ground state SF_6) reaction cross section, rather than the identity of the products, in which we are most interested. More than thirty scattering experiments were performed with several modifications and adjustments in procedure, including changes in positioning of the electron multiplier, changes in collimation (of the K beam) and the insertion of a repeller plate and a scattering chamber.

Fig. 2 shows the ratio I_L/I_0, the laser on/laser off electron multiplier signal of reaction product as a function of the irradiation position inside the nozzle capillary. From these values, using the equation:[5],[6]

$$\sigma_{rel} = \frac{I^L}{I^0} \frac{\Delta p^0}{\Delta p^L} \frac{\langle v^L \rangle}{\langle v^0 \rangle} \left(\frac{\bar{E}^0_{tr}}{\bar{E}^L_{tr}} \right)^{1/2} \qquad (1)$$

the relative cross section, σ_{rel}, can be determined and is plotted in Fig. 3 as a function of average internal energy, E_{int}.[7] As E_{int} increases (laser on), the chemi-ionization cross section decreases. This is a most interesting result; while there are examples of reactions with energy barriers (endoergic or activation) whose cross sections increase with increasing internal energy[8],[9] and exothermic processes in which σ decreases with kinetic energy,[10],[11] few if any exoergic reactions have been reported with decreasing cross section resulting from internal excitation.

(2) SF_6 thermal heating experiments

In earlier experiments we determined the relative effect of 1) laser excitation and 2) simple thermal heating on the internal energy of an SF_6 molecular beam. Energy fluxes ($W \sim n\langle v \rangle E_{tot} = FE_{tot}$) were measured using a

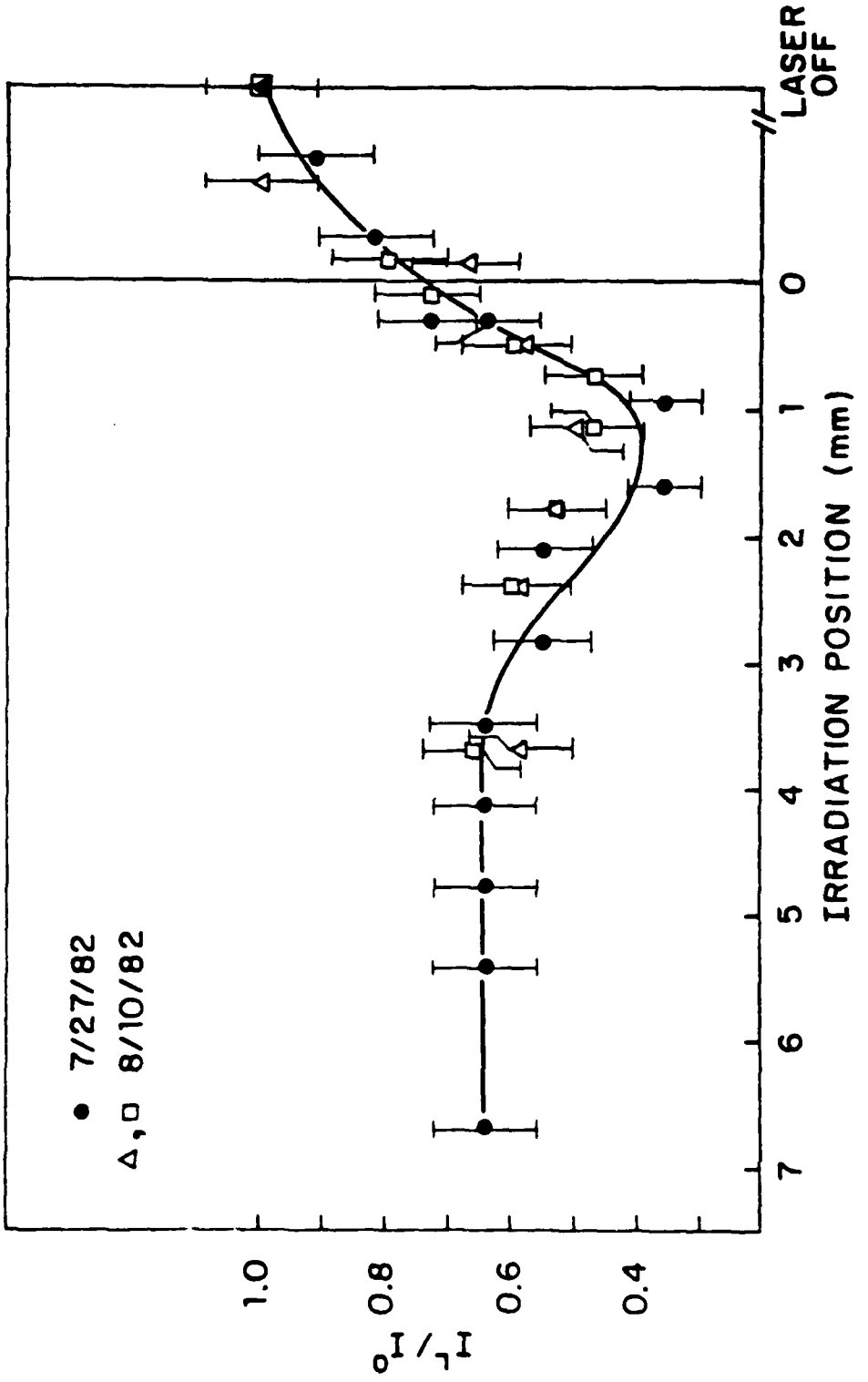
LASER OFF
IRRADIATION POSITION (mm)
I_r / I_o
1.0
0.8
0.6
0.4
0
1
2
3
4
5
6
7
• 7/27/82
Δ, □ 8/10/82

Figure 2

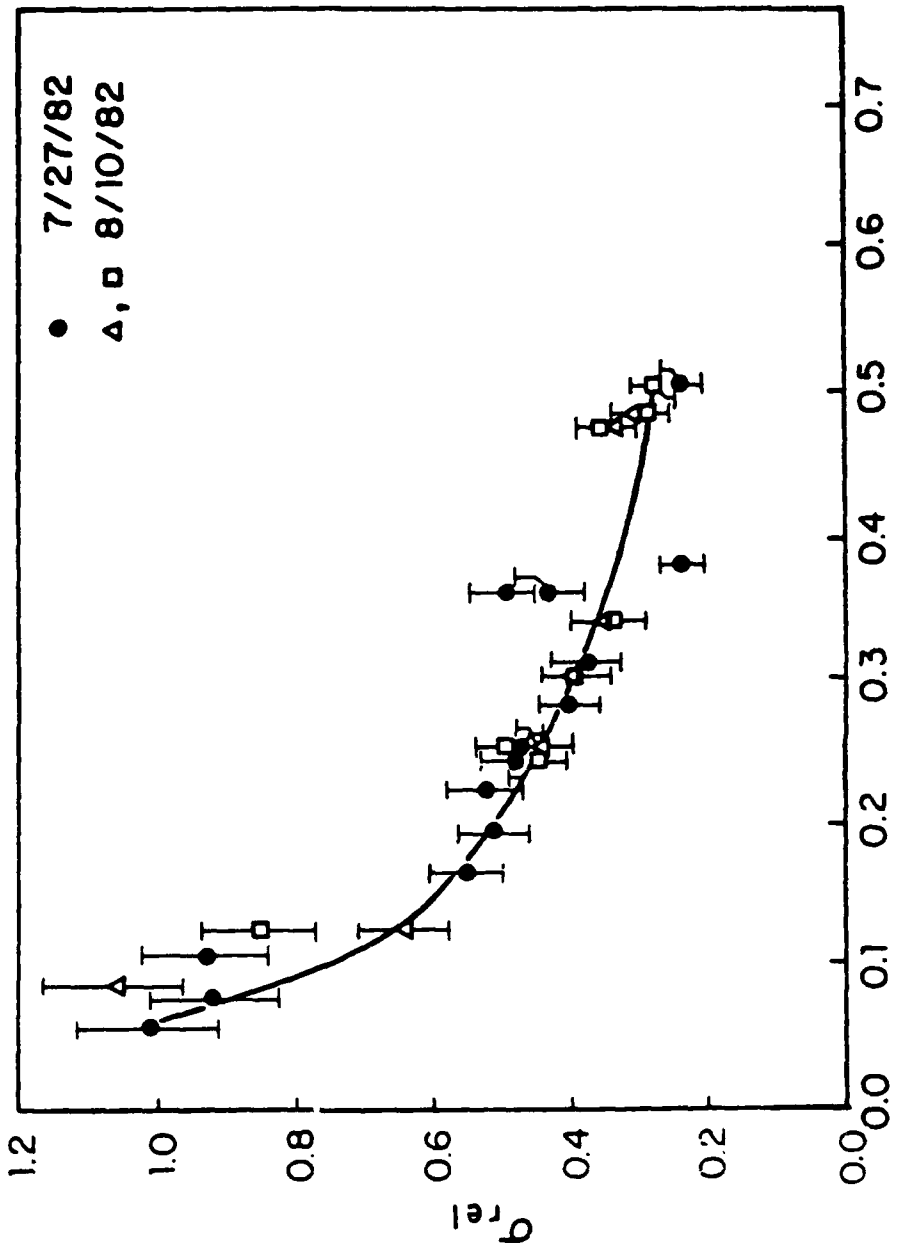
7/27/82
Δ, □ 8/10/82
q_{rel}
$\overline{E}_{int}$ (eV)
0.0
0.2
0.4
0.6
0.8
1.0
1.2
0.1
0.3
0.5
0.7

Figure 3

liquid helium-cooled bolometer; number densities (n) and average beam velocities (<v>) were found using the quadrupole mass filter. An ion gauge flux meter provided an alternate method for determining the beam flux, F.

The internal energy of SF_6 at room temperature, E°_{int}, was determined relative to Ar, a monatomic gas with no internal energy, using bolometer, flux meter and TOF results. Energies at elevated temperatures were then found using the following equation:[1],[12]

$$\frac{W_T/n_T}{W_0/n_0} = \frac{\frac{1}{2} m\langle v_T^3\rangle + (E^T_{int} + E_a)\langle v_T\rangle}{\frac{1}{2} m\langle v_0^3\rangle + (E^0_{int} + E_a)\langle v_0\rangle} \qquad (2)$$

Internal energies of laser-excited SF_6 beams were found in the same manner.

These experiments showed that CO_2 laser excitation of SF_6 beams enhances the internal energy far more than simple heating of the nozzle. There was, however, confusion in that the E_{int} values obtained in simple thermal heating experiments were considerably less than those obtained using an enthalpy balance equation:[13]

$$4\ kT_{nz} + \int_0^{T_{nz}} C_v(vib)dT = \frac{1}{2} m\langle v^2\rangle + \frac{3}{2} kT_s + E_{int} \qquad (3)$$

Experiments were performed to examine this discrepancy. First, TOF measurements of heated Ar beams were studied; they concurred with previous results. Then, SF_6 thermal TOF studies were performed, indicating different velocities at elevated temperatures from those measured earlier. It was discovered that, while other measurements (W,n) were taken while the nozzle was "cooling" in heated experiments, the SF_6 TOF parameters (v_s, α_s) had been measured during "heating" runs. The latter suffer from large uncertainties in temperature because of a rapid change in temperature upon heating. During

"cooling" runs the temperature changes more slowly. The new SF_6 velocities (v_g) are plotted in Fig. 4 as a function of nozzle temperature. Similarly, the width paramter (α_g) is shown. These velocities, considerably slower than those measured earlier, enhanced somewhat the values of internal energy (cf., Eq. 2).

In a related experiment, the entire oven assembly was heated as well as the nozzle to extend the residence time of the SF_6 molecules in a heated chamber. It had been hypothesized that the molecules might not have equilibrated to the nozzle temperature. There was, however, no difference in the TOF parameters with and without the heated oven, indicating that SF_6 molecules had indeed reached T_{nz}.

Once the SF_6 velocities had been measured, energies were calculated. Fig. 5 shows the internal energy E_{int}, the kinetic energy E_{kin} and the total energy E_{tot}, graphed as a function of nozzle temperature. E_{int} remains essentially constant in the range 300-400K, then increases by ~45% in the range 400-544K. These internal energies can be compared to those determined using the enthalpy conservation equation, Eq. 3. The two curves are shown in Fig. 6 as a function of nozzle temperature. There is still a wide discrepancy between them but there is no doubt that laser excitation provides far more internal enhancement than does thermal heating. At the optimum laser irradiation position inside the nozzle capillary, ~0.38 eV $molec^{-1}$ are found in internal degrees of freedom, while at 544K (thermal heated), only ~0.03eV $molec^{-1}$ of internal energy are measured with similar translational energy distributions.

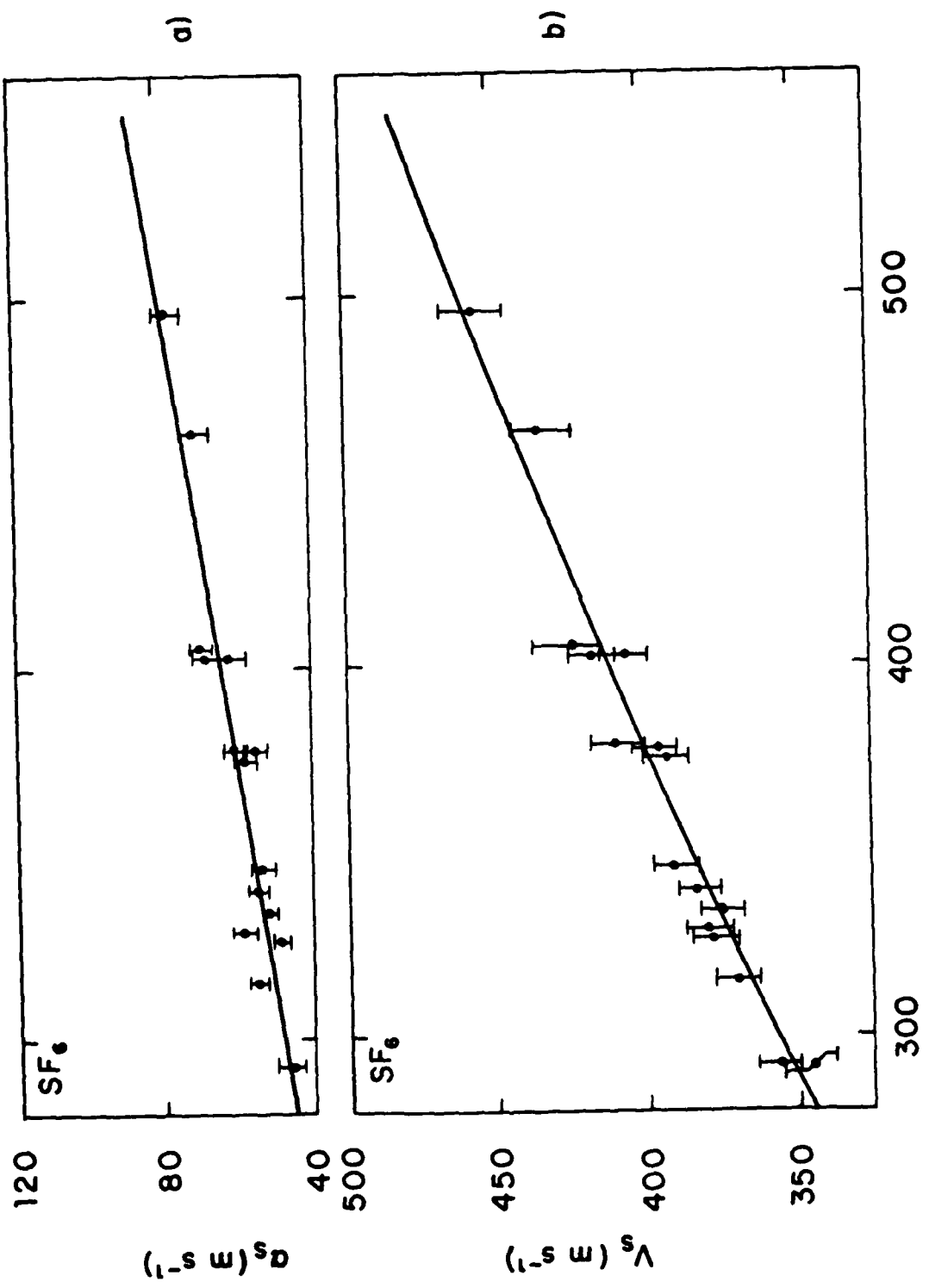
a)
b)
SF6
SF6
120
80
40
500
450
400
350
300
400
500
NOZZLE TEMPERATURE (K)
αs (m s-1)
Vs (m s-1)

Figure 4

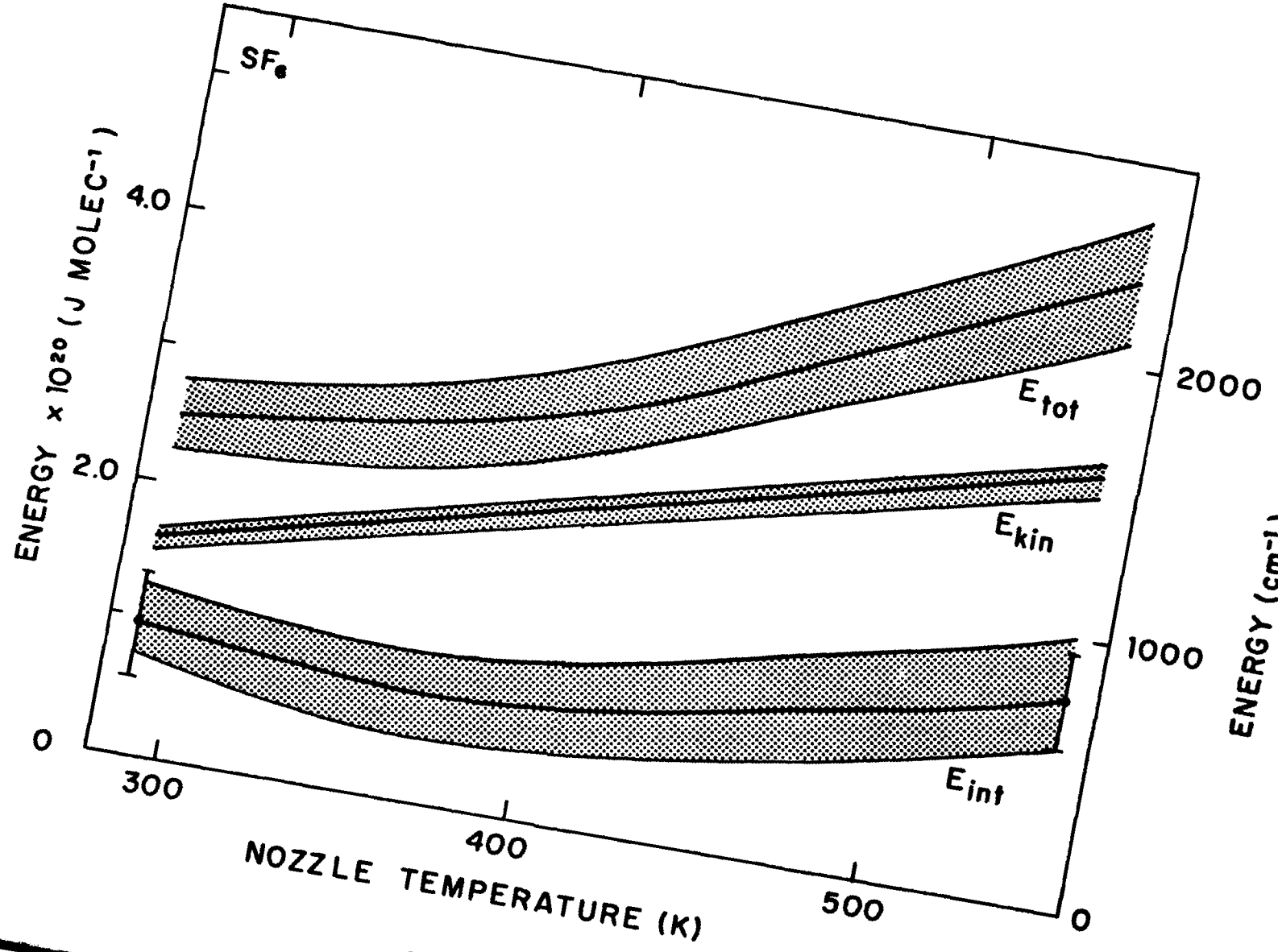
SF6
ENERGY x 10^20 (J MOLEC^-1)
4.0
2.0
0
Etot
Ekin
Eint
2000
1000
0
ENERGY (cm^-1)
300
400
500
NOZZLE TEMPERATURE (K)

Figure 5

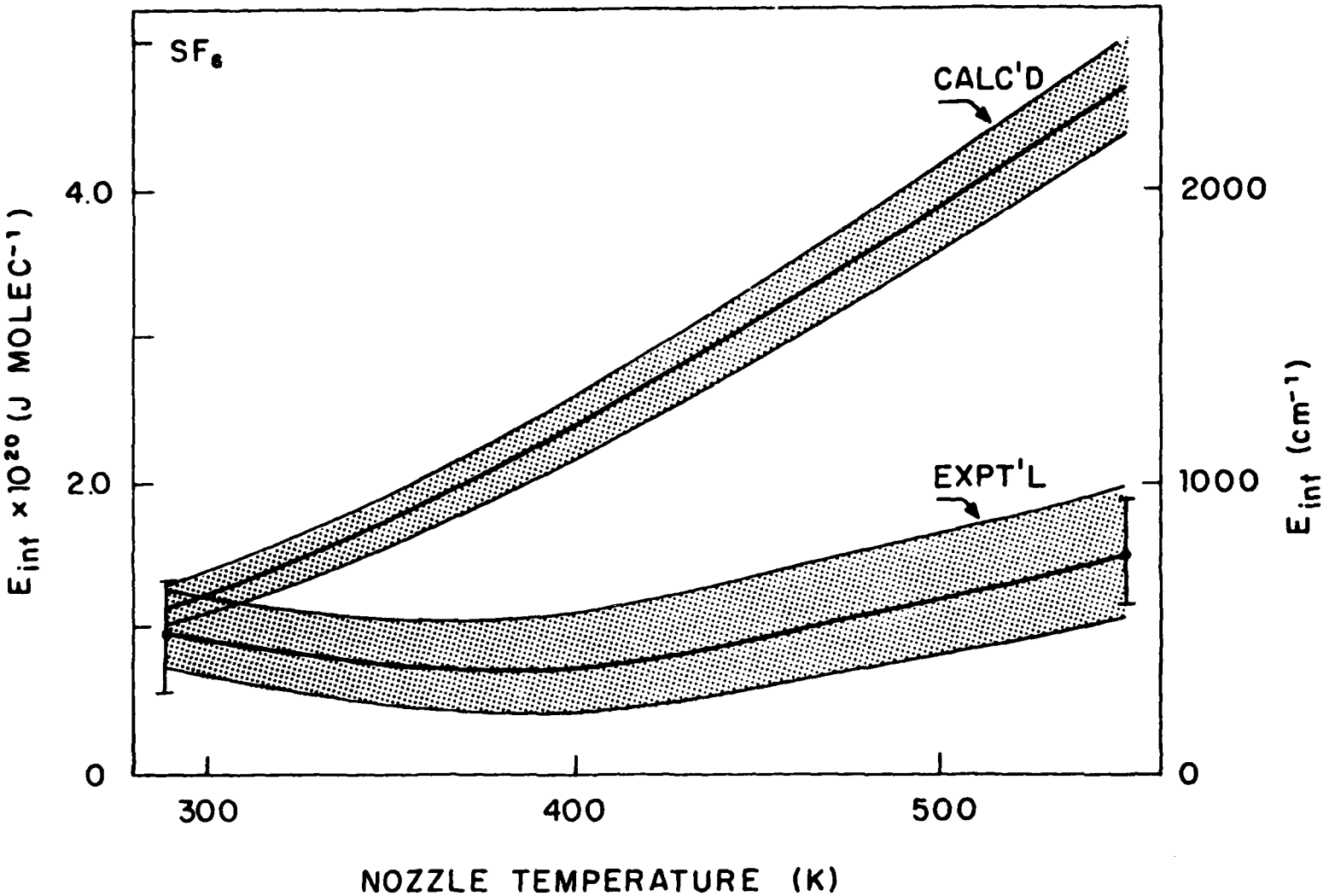
SF6
CALC'D
EXPT'L
4.0
2.0
0
2000
1000
0
300
400
500
Eint ×10²⁰ (J MOLEC⁻¹)
Eint (cm⁻¹)
NOZZLE TEMPERATURE (K)

Figure 6

*This research was also supported by the National Science Foundation under Grant CHE 80-23747 and the Department of Energy under Contract DE-AC-02-78ER04940.

(1) M. I. Lester, L. M. Casson, G. B. Spector, G. W. Flynn, and R. B. Bernstein, "Collisional Effects on the Internal and Translational Energy Distributions of Laser-Excited and Thermally-Heated SF_6 Supersonic Beams," to be submitted.

(2) D. R. Coulter, F. R. Grabiner, L. M. Casson, G. W. Flynn, and R. B. Bernstein, J. Chem. Phys. 73, 281 (1980).

(3) M. I. Lester, D. R. Coulter, L. M. Casson, G. W. Flynn, and R. B. Bernstein, J. Phys. Chem. 85, 751 (1981).

(4) B. P. Mathur, Erhard W. Rothe, and Gene P. Reck, J. Chem. Phys. 67, 377 (1977).

(5) L. M. Casson, Ph.D. thesis, Columbia University, 1982.

(6) ΔP is the flux meter reading, $\langle v \rangle$ is average velocity. E_{tr} is average translational energy. L and 0 superscripts represent laser on and off conditions, respectively.

(7) E_{int} determined from internal energy of SF_6 beam.

(8) J. C. Polanyi and W. H. Wong, J. Chem. Phys. 51, 1439 (1969).

(9) R. D. Levine and R. B. Bernstein, Molecular Reaction Dynamics, Oxford University Press, New York, (1974), p. 121.

(10) ibid, p. 40.

(11) R. D. Levine and R. B. Bernstein, J. Chem. Phys. 56, 2281 (1972).

(12) $\langle v^3 \rangle$ measured from TOF. E_a is heat of adsorption of molecules on bolometer surface (taken to be $-\Delta H_{vap}$).

(13) Adapted from references 1 and 2. T_s is stream temperature, measured from TOF parameter α_s.

V. PICOSECOND ENERGY TRANSFER AND PHOTOFRAGMENTATION SPECTROSCOPY

A. PHOTOCHEMISTRY AND PHOTOPHYSICS OF DIPHENYLCARBENE*

(Y. Wang, F. Novak, E. Sitzmann, J. Langan, K. B. Eisenthal)
(JSEP work unit 8, 1982-1985)
(Principal Investigator: K. B. Eisenthal (212) 280-3175)

In recent years, much theoretical and experimental work has centered on attempting to understand the chemical and physical properties of divalent carbon compounds (carbenes), an important class of short-lived and reactive intermediates.[1] Of particular interest is the presence of an unshared pair of electrons which results in two low-lying electronic spin configurations, singlet and triplet. EPR spectroscopy has been extremely useful in establishing the ground state multiplicity of most aryl and alkyl carbenes to be the triplet.[2] Valuable structural information for these carbenes is also available from EPR and ENDOR experiments,[2] but little is known concerning the energetics and dynamics between the two spin states. An important and controversial aspect of this is the magnitude of the singlet-triplet energy gaps. Numerous calculations of singlet-triplet energy splittings have appeared;[3] however, little quantitative experimental information is available. Recent reports of the experimental determination of the singlet-triplet energy gap in the parent methylene have placed the value at ~8 kcal/mole;[4] however, the corresponding value for other carbenes has not been determined.

In addition to the dearth of experimental information concerning singlet-triplet energy gaps, little is known about the dynamics of the singlet-triplet interconversion. Generation of a ground state carbene, either photochemically or thermally from an appropriate precursor should lead initially to the singlet state because of spin conservation restrictions. The singlet may then

undergo reaction or intersystem cross to the ground state which subsequently reacts. As a result, interpretation of carbene chemistry is often complicated by products originating from both spin states. It is important, therefore, to determine the rate(s) of interconversion of the spin states and in addition the rate constants for reactions of each with various substrates.(5)

We have undertaken an in-depth study of diphenylmethylene (DPM) and wish to report the determination of the absolute rate constants for singlet-triplet interconversion and the energy spacing between these two states for diphenylmethylene by extension of the pioneering work of Closs and Rabinow.(6) Diphenylmethylene is a particularly attractive candidate for study because should be prototypic of arylcarbenes and furthermore, it has been shown to amenable to flash spectroscopic techniques.(6)

We have combined competitive experiments, picosecond and nanosecond flash spectroscopy, and triplet sensitization experiments to evaluate the rates of singlet-triplet interconversion of DPM in acetonitrile at ambient temperature. From these rate constants, K_{eq} and ΔG_{ST} are determined for DPM.(7)

The sequence of energy decay steps following excitation of diphenyldiazomethane with an ultraviolet light pulse, ultimately leading to diphenylcarbene in its triplet ground state, we find can be written as:

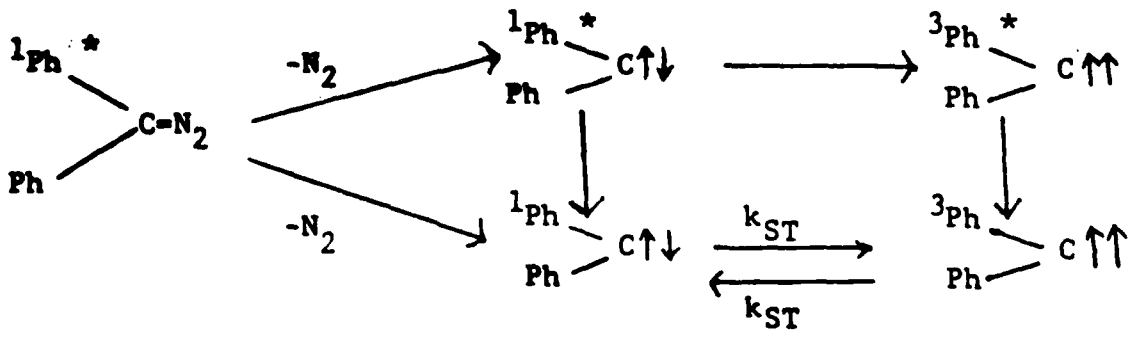

The spin conversion from $^1DPC \rightarrow {}^3DPC$ occurs in 110ps. From measurement of k_{TS} (in collaboration with Professor N.J. Turro and his group) we obtain the equilibrium constant

$$K = \frac{k_{ST}}{k_{TS}} = (2.2 \pm 0.6) \times 10^3.$$

The free energy difference at 25°C is calculated to be 4.6 ± 0.2 kcal/mole. Assuming that the entropy difference between the singlet and triplet states is due chiefly to the multiplicity difference we obtain

$$\Delta H = \Delta G + T\Delta S = 3.9 \pm 0.2 \text{ kcal/mole}.$$

We therefore, have succeeded not only in obtaining the rate of singlet-triplet equilibration, but also an estimate of the energy gap between these states.

*This work is also supported by the Air Force Office of Scientific Research under Grant AFOSR-81-0009-A and the National Science Foundation under Grant NSF-CHE81-21945.

(1) W. Kirmse, "Carbene Chemistry", 2nd Ed., Academic Press, New York, New York 1971; R. A. Moss and M. Jones, Jr., eds. "Carbenes", vol. 1 and 2, Wiley Interscience, New York, New York 1975.

(2) A. M. Trozzolo, E. Wasserman, in R. A. Moss and M. Jones, Jr.'s "Carbenes", vol. 2, Wiley-Interscience, New York, New York 1975.

(3) J. F. Harrison, R. C. Liedtke, and J. F. Liebman, J. Am. Chem. Soc. 101, 7162 (1979) and references therein; J. F. Harrison, Accounts Chem. Res. 7, 378 (1974).

(4) R. K. Lengel and R. N. Zare, J. Am. Chem. Soc. 100, 7495 (1978) and references therein.

(5) (a) Early reports of such studies for fluorenylidene have appeared: J. J. Zupancic and G. B. Schuster, J. Am. Chem. Soc. 102, 5958 (1980); ibid., 103, 944 (1981); A revision of the assignments has been made, however, D. Griller, M. Platz, J. C. Scaiano, personal communications; K. J. Kaufmann, G. B. Schuster, personal communications); (b) For other work on the absolute rate constants for the reactions of carbenes, see P. C. Wong, D. Griller, and J. C. Scaiano, Chem. Phys. Letters 83, 69 (1981); N. J. Turro, J. A. Butcher, Jr., R. A. Moss, W. Guo, E. C. Munjal, and M. Fedorynski, J. Am. Chem. Soc. 102, 7576 (1980).

(6) G. L. Closs and B. E. Rabinow, J. Am Chem. Soc. 98, 8190 (1976).

(7) For a preliminary communication of these results, see: K. B. Eisenthal, N. J. Turro, M. Aikawa, J. A. Butcher, Jr., C. Dupuy, G. Hefferon, W. Hetherington, G. M. Korenowski, and M. J. McAuliffe, J. Am. Chem. Soc. 102, 6563 (1980).

B. CHEMICAL INTERMEDIATES IN THE PHOTOCHEMISTRY OF AROMATIC ENDOPEROXIDES SINGLET OXYGEN*

(C. Dupuy, S. Y. Hou, E. Sitzmann, M. McAuliffe, K. B. Eisenthal)
(JSEP work unit 8, 1982-1985)
(Principal Investigator: K. B. Eisenthal (212) 280-3175)

In our recent studies[1] of the photodissociation of oxygen containing molecules,[2] and in particular anthracene endoperoxide, we discovered a new dissociative pathway which produced not only oxygen in an excited state but also an excited anthracene fragment, A*

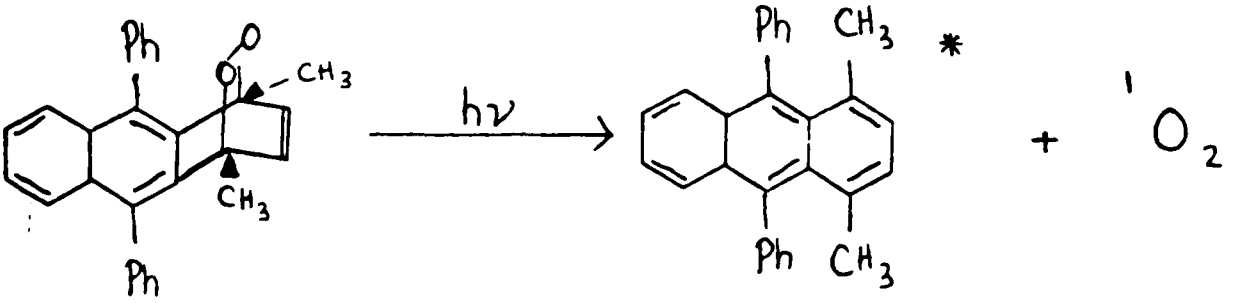

To determine the importance of this pathway for bond breaking, we measured the formation time of the ground state anthracene fragment, A. If the principal route is via the excited state, i.e.,

$$AO_2 \rightarrow {}^1A^* + {}^1O_2$$
$$\downarrow$$
$${}^1A$$

then ^1A would appear as the excited state $^1A^*$ decayed. We found that this was not the case. The ground state appearance time was found to be 45ps, a much longer time than the appearance time of $^1A^*$ which was less than 5ps. This result suggested that a principal path for bond rupture involves not excited anthracene, but a two-step process involving a chemical intermediate. A

sequence showing two possible intermediates is:

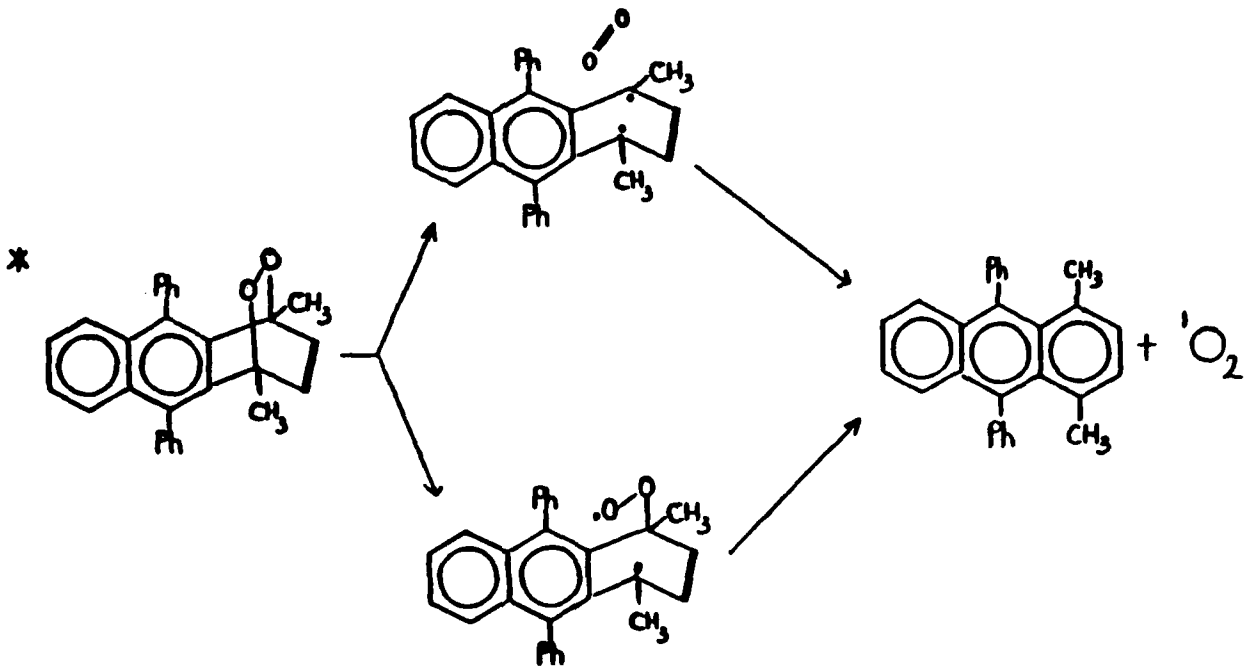

We are presently seeking to trap and identify the chemical intermediate in this adiabatic photodissociation.

*This work is also supported by the Air Force Office of Scientific Research under Grant AFOSR-81-0009-A and the National Science Foundation under Grant NSF-CHE81-21945.

(1) S. Y. Hou, C. G. Dupuy, M. J. McAuliffe, D. A. Hrovat, and K. B. Eisenthal, J. Am. Chem. Soc. 103, 6982 (1981).

(2) For a theoretical and experimental discussion of $^1O_2$, its spectroscopy, and reactions, see: H. H. Wasserman, R. W. Murray, Eds., "Singlet Oxygen", Academic Press: New York, 1979.

C. PICOSECOND DYNAMICS OF TWISTED INTERNAL CHARGE TRANSFER PHENOMENA*

(Y. Wang, M. Crawford, K. B. Eisenthal)
(JSEP work unit 8, 1982-1985)
(Principal Investigator: K. B. Eisenthal (212) 280-3175)

The dual fluorescences phenomena of DMABN and related molecules is a subject that has received intensive studies in the past.[1]-[7] In nonpolar solvents, excitation of the DMABN molecule results in a single fluorescence band centered around 340 nm. However, in polar solvents a new, Stokes-shifted fluorescence appears, which is associated with a large dipole moment of ~16 D.[4] To explain the origin of this new emission band, a number of mechanisms have been proposed. From the results accumulated over the past several years, we conclude that both the bond twisting (between the amino group and the benzene ring) and solvation play important roles in causing the charge redistribution[4]-[7]

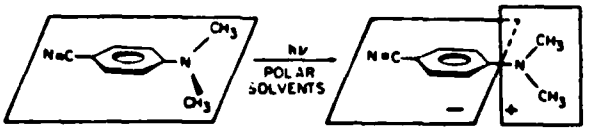

In spite of the numerous studies on the subject, the relationship between the two fluorescence bands was, surprisingly, not fully understood until recently. By using picosecond fluorescence spectroscopy,[7] we have directly demonstrated the parent-daughter relationship between the short wavelength emission band and the long wavelength emission band. We have shown that the two emitting species reach equilibrium very rapidly (~20 ps) with an equilibrium constant $\geq$ 30 in propanol solution.[7]

To study the role of solvent molecules in the intramolecular CT process of excited DMABN molecules and hopefully to gain a better understanding of the

coupling between the twisting motion and solvent relaxation, the dynamics of the CT transfer process in mixed solvents were investigated. The basic idea is to control the local number density of the polar solvent molecules without greatly altering the viscosity of the solution. The effect of the change in local dipole density on the dynamics and yield of the CT process could then yield information on the role of the polar solvent molecules. A convenient way to adjust the local dipole density is by diluting the polar solvent molecules with nonpolar molecules. We have chosen to study the mixed solvent system butanol/hexadecane because of their similar viscosities 3.0 and 3.3 cp at 20°C, respectively.

The evolution of the photoexcited DMABN molecule from the initial planar structure to the final perpendicular structure was followed by monitoring both the singlet fluorescence decay at 350 nm and the CT fluorescence rise at 470 nm as the butanol solution is successively diluted by the nonpolar hexadecane molecules.

The key observations made were: (1) the appearance of a fast and a slow kinetic process upon the dilution of butanol solutions, (2) the dynamics of the fast process is independent of the dilution while the rate of the slow process shows a linear dependence on the butanol concentration, and (3) the relative importance of the two processes is affected by the dilution, the fast process dominates at high butanol concentration.

The origin of the fast process (i.e., the 30 ps rise observed for all butanol concentrations), we believe, is due to the excitation of the complexes already formed in the ground state between DMABN and butanol molecules. This 30ps rise is faster and larger than can be accounted for by a diffusion controlled process for the lower butanol concentrations. The formation of the ground state complexes is really not surprising in light of the large dipole

moment 7D of the ground state DMABN molecule.[4] According to our interpretation, the measured 30 ps risetime for the fast process is then mainly due to the intramolecular bond twisting motion along the C-N bond of the excited DMABN-butanol complex. This intramolecular twisting motion can be impeded by the frictional force of the solvent molecules, thus accounting for the observed viscosity dependence.

As the rapid rise component (30 ps) reflects the population of ground state complexes, the slow component of the rise reflects those excited DMABN molecules which either do not have neighboring butanol molecules or do not have the proper arrangement of butanol molecules for reaction to occur. Even at the higher alcohol concentrations, for which there are several alcohol molecules, on the average, surrounding a ground state DMABN molecule, a slow component is observed. It is not until the appropriate configuration is achieved, as given by the slower time component, that the rapid 30 ps reaction can occur. The key feature in the stabilization of the twisted intramolecular charge transfer structure appears to be the prior formation of a complex between excited DMABN and some butanol molecule or molecules.

Our proposed mechanism can be briefly summarized in the figure shown below, noting that the single butanol entity shown in the figure can be monomeric or part of some higher aggregate.

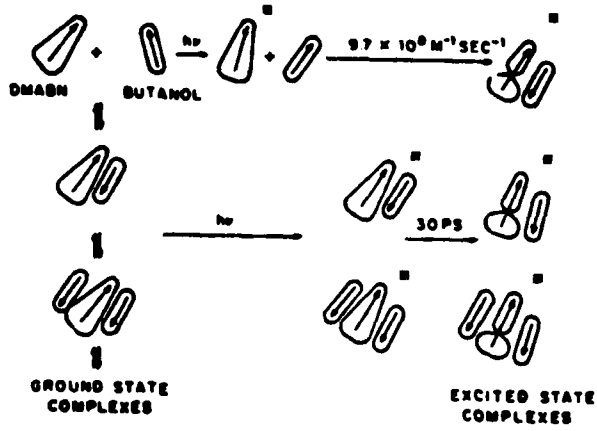

*This work is also supported by the Air Force Office of Scientific Research under Grant AFOSR-81-0009-A and the National Science Foundation under Grant NSF-CHE81-21945.

(1) E. Lippert, W. Lüder, and H. Boos, in Advances in Molecular Spectroscopy, edited by A. Mangini (Pergamon, Oxford, 1962), p. 443.

(2) E. A. Chandross, in The Exciplex, edited by M. Gordon and W. R. Ware (Academic, New York, 1975), p. 187.

(3) K. Rotkiewicz, K. H. Grellmann, and Z. R. Grabowski, Chem. Phys. Lett. 19, 315 (1973).

(4) Z. R. Grabowski, K. Rotkiewicz, A. Siemearczuk, D. J. Cowley, and W. Baumann, Nouv. J. Chim. 3, 443 (1979).

(5) W. Rettig, G. Wermuth, and E. Lippert, Ber. Bunsenges, Phys. Chem. 83, 692 (1979).

(6) W. Rettig and V. Bonavicic-Koutecky, Chem. Phys. Lett. 62, 115 (1979); W. Rettig and M. Zander, ibid. 87, 229 (1982).

(7) Y. Wang, M. McAuliffe, F. Novak, and K. B. Eisenthal, J. Phys. Chem. 85, 3736 (1981).

VI. GENERATION AND CONTROL OF RADIATION

A. OPTICAL COHERENT TRANSIENT SPECTROSCOPY*

(R. Beach, B. Brody, T. J. Chen, D. DeBeer, M. Glick, R. Kinchinski, E. Xu, S. R. Hartmann)
(JSEP work unit 9, 1982-1985)
(Principal Investigator: S. R. Hartmann (212) 280-3272)

The channeling of our two YAG laser/amplifier outputs into four separate laboratories has been completed and we can now pump dye lasers simultaneously at all our experimental stations. A centralized computer facility has been established for control and analysis of all experiments. Each station has its own computer terminal to allow for local interaction. Analysis is performed while data is acquired and the results are displayed in graphical form at the local terminals.

Photon echo signals have been obtained in Li vapor over an unprecedented dynamic range exceeding 10^{10}.(1) Echoes were obtained from atoms which were excited more than 15 natural lifetimes earlier. These results are shown in Fig. 1. It should be noted that our largest echoes were only a factor of 25 weaker than the $\pi/2$ excitation pulse which first excited them. The purpose of this experiment was to study echo degredation due to nonparallel excitation beams. The two sets of data in Fig. 1 correspond to excitation beam angling of 0.70 and 1.40 mrad. The effect of beam angling above is obtained by taking the ratio of these data and is presented in Fig. 2. By taking the ratio we get rid of radiative lifetime and hyperfine structure effects. For beam angling of θ, the echo intensity when the excitation pulses are separated by a time τ is just

$$I_{echo} = I_0 \, e^{-2\left(\frac{\hbar k q_\theta \theta}{m}\right)\tau^2} \, e^{-\frac{2\tau}{T_1}} \, M(\tau)$$

where T_1 is the natural lifetime, k is the wavevector associated with the

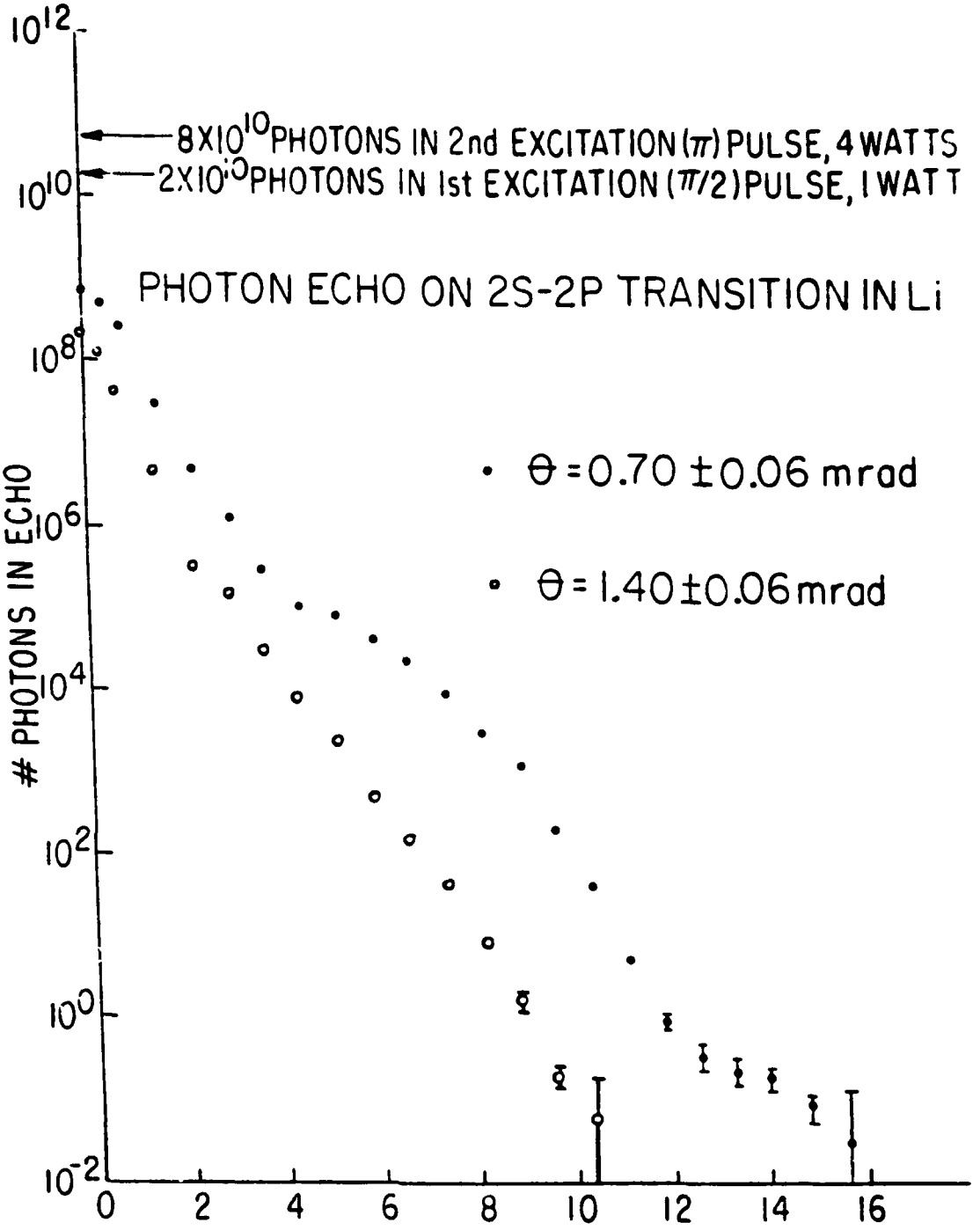

TIME BETWEEN 1st EXCITATION ($\pi/2$) PULSE AND ECHO IN NATURAL LIFETIMES (27 nsec) OF THE $2^2P_{3/2}$ STATE OF Li.

Fig. 1 Photon echo intensity vs time between first excitation pulse and echo for two values of beam angling.

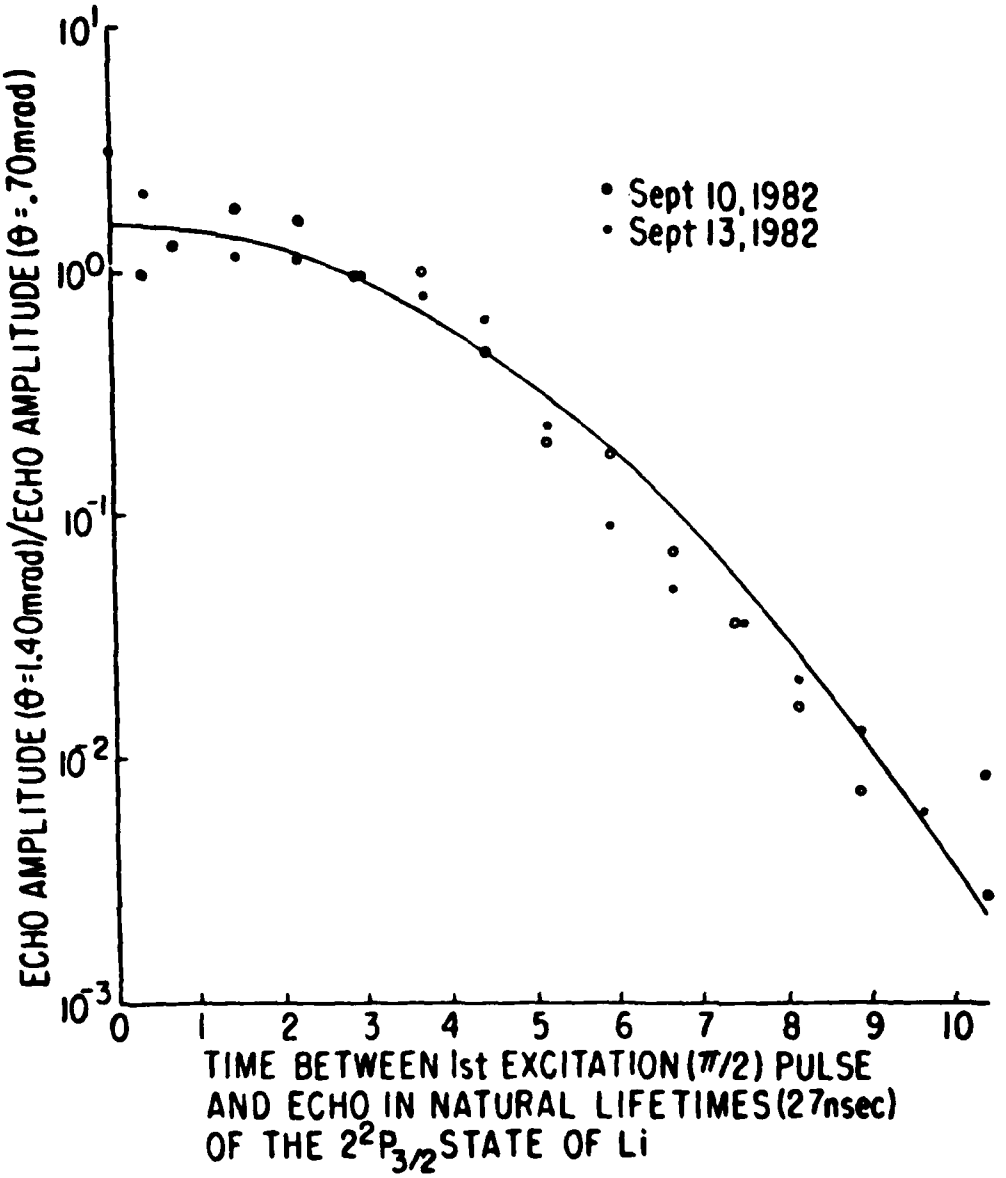

Fig. 2 Photon echo intensity ratio corresponding to $\theta = 14$ and $\theta = .7$ vs time between first excitation pulse and echo.

optical transition, $q_0 = \sqrt{\frac{2mk_BT}{h^2}}$ is the inverse thermal de Broglie wavelength and $M(\tau)$ describes the modulation caused by the hyperfine structure. The ratio

$$R(\tau) = \frac{I_{echo}(\tau,\ 1.4\ \text{mrad})}{I_{echo}(\tau,\ 0.7\ \text{mrad})} = R_0\, e^{-\left(\frac{\tau}{\tau_{eff}}\right)^2}$$

is independent of T_1 and $M(\tau)$. For our experimental conditions $\tau_{eff} = 55$ nsec. The solid line in Fig. 2 uses this value for τ_{eff}.

The initial motivation of this experiment was provided by our extension of the Billiard Ball Echo Theory[2] to include the effects of using sub-Doppler-linewidth lasers in photon echo experiments.[3] Sub-Doppler-linewidth lasers generate nonspherical excited state wave packets, and photon echo experiments such as described above measure the transverse wave packet shape. As explained in the last progress report, the Billiard Ball echo model begins by localizing gaseous atoms with atomic wave packets. When these wave packets are irradiated by a series of light pulses they split into separate parts corresponding to each of the atomic states generated. Each resulting wave packet recoils according to whether it absorbs or emits a photon while it is being formed. Whenever overlap occurs between two daughter wave packets of the same parent, coherent radiation ensues and photon echoes are formed.

The Billiard Ball echo model was developed to obtain a simple analytical tool which would work equally well for the two pulse photon echo and multiple pulse - multiple level echoes. It was specialized to short pulse excitations which uniformly excited all atoms independent of their velocity thus giving rise to spherical wave packets which were called Billiard Balls. Long pulse excitation leads to a more complicated shape; however, just as in the case with the spherical Billiard Balls, wave packet spreading can be ignored. We

have demonstrated that long pulse excitations do not change the essential features of the Billiard Ball echo theory.[3] Even though the shape of the excited state wave packets is no longer spherical, the recoil or billiard ball analysis remains the same.

In the most general case, the excited wave packet shape can be quite complicated. However, in all cases it is characterized by a length to width ratio L/W of

$$L/W = \tau_{1/e}/\tau_D \quad \text{for} \quad \tau_D < \tau_{1/e}$$

where $\tau_{1/e}$ characterizes the width of the excitation pulse electric field amplitude

$$E = E_o \exp\{-1/2(t/\tau_{1/e})^2\}$$

whereas τ_D is a measure of the width of the thermal atomic velocity distribution.

$$\frac{\hbar k}{m} \tau_D = \frac{1}{q_0}$$

It is the time it would take the excited state wave packets, recoiling with velocity $\hbar k/m$, to separate from the ground state wave packet if their spatial extent were given by the thermal de Broglie wavelength.

For short pulse excitation where $\tau_D > \tau_{1/e}$, L/W = 1 and all wave packets are spherical. For $\tau_D < \tau_{1/e}$ but with small area excitation pulses, the excited wave packet shape simplifies and becomes ellipsoidal.

The longitudinal extent of the excited wave packet can be easily measured

as it is equal to the duration of the photon echo. Our echoes have in fact always been as long as our excitation pulses, in agreement with our calculation. The transverse dimension of the wave packet can be measured by angling the excitation beams as then the wave packet collision is glancing rather than head on. This is clear from the recoil diagram of Fig. 3. Our experiments in Li vapor Figs. 1 and 2 show good agreement with theory. Our experimental and theoretical work has recently been summarized.[4]

It should be noted that analysis of photon echoes generated by angled excitation beams allows one to obtain a measure of transient atomic velocity distributions. This may prove valuable in studies involving nonresonant photon assisted collisions which, depending on which side of a resonance a laser is tuned, excited state thermal distributions are produced which are either hotter or colder than that associated with the ground state atoms.[5]

In setting up the experiment to generate photon echoes using angled excitation beams, it was decided to exploit the superradiant character of the photon echo to obtain signals over a large dynamic range. One advantage of using angled excitation beams is that the echo is radiated in the direction $2\vec{k}_2-\vec{k}_1$ where $\vec{k}_1$ and $\vec{k}_2$ are the wave vectors of the first and second excitation pulses respectively. Thus the echo is spatially separated from the excitation beams. At short pulse separation times the echo was several orders of magnitude greater than any leakage from the excitation pulses and optical shutters were unnecessary. At long separation times an AOM was used to eliminate stray leakage so that our photo-tube response was quiet enough to detect .02 photons per echo. The experimental set up is shown in Fig. 4.

The advantage of being able to work with a large dynamic range is that it allows precise studies of relaxation. Spectroscopic measurements are also facilitated as the limitations imposed by the uncertainty principle, although

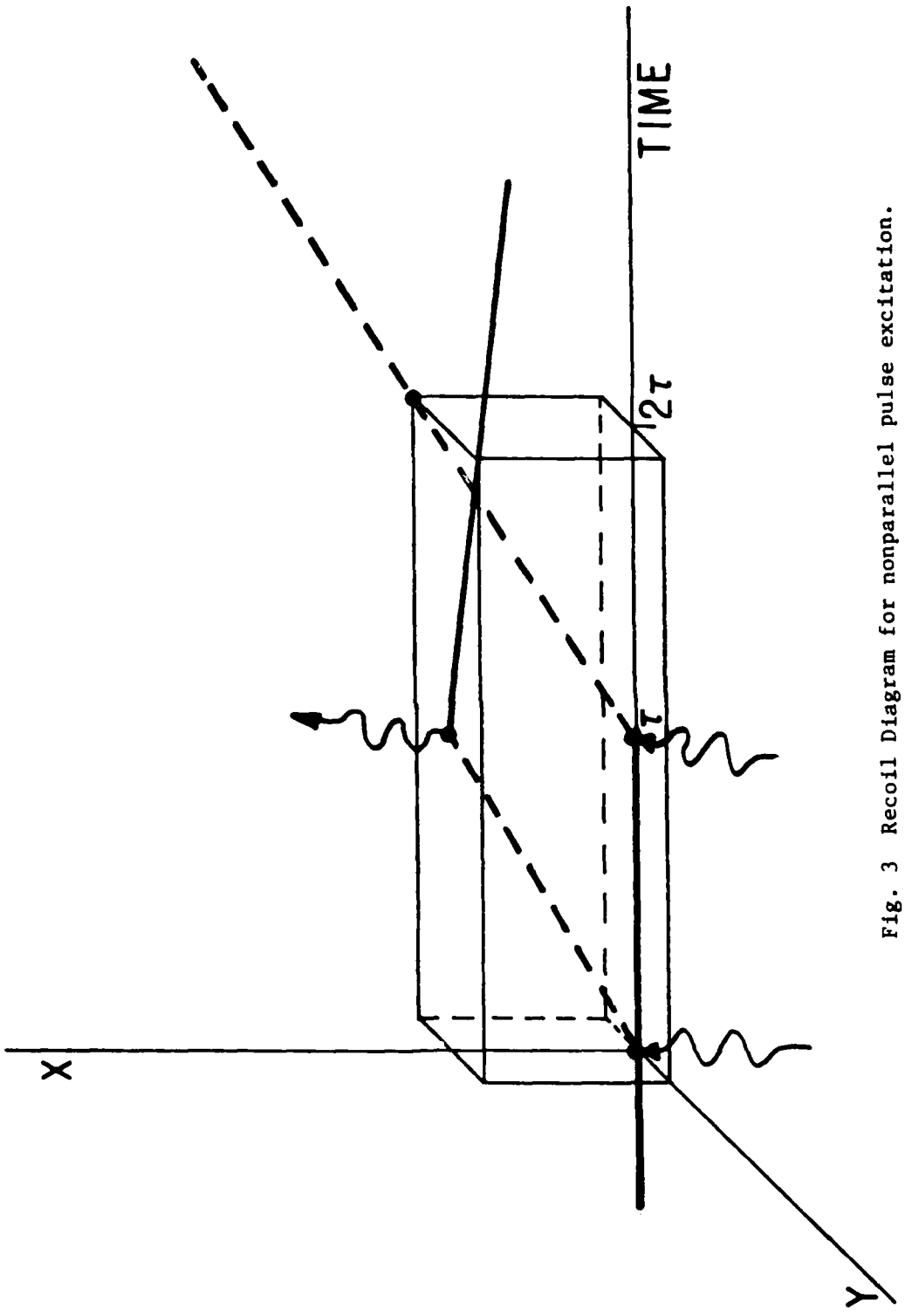

Fig. 3 Recoil Diagram for nonparallel pulse excitation.

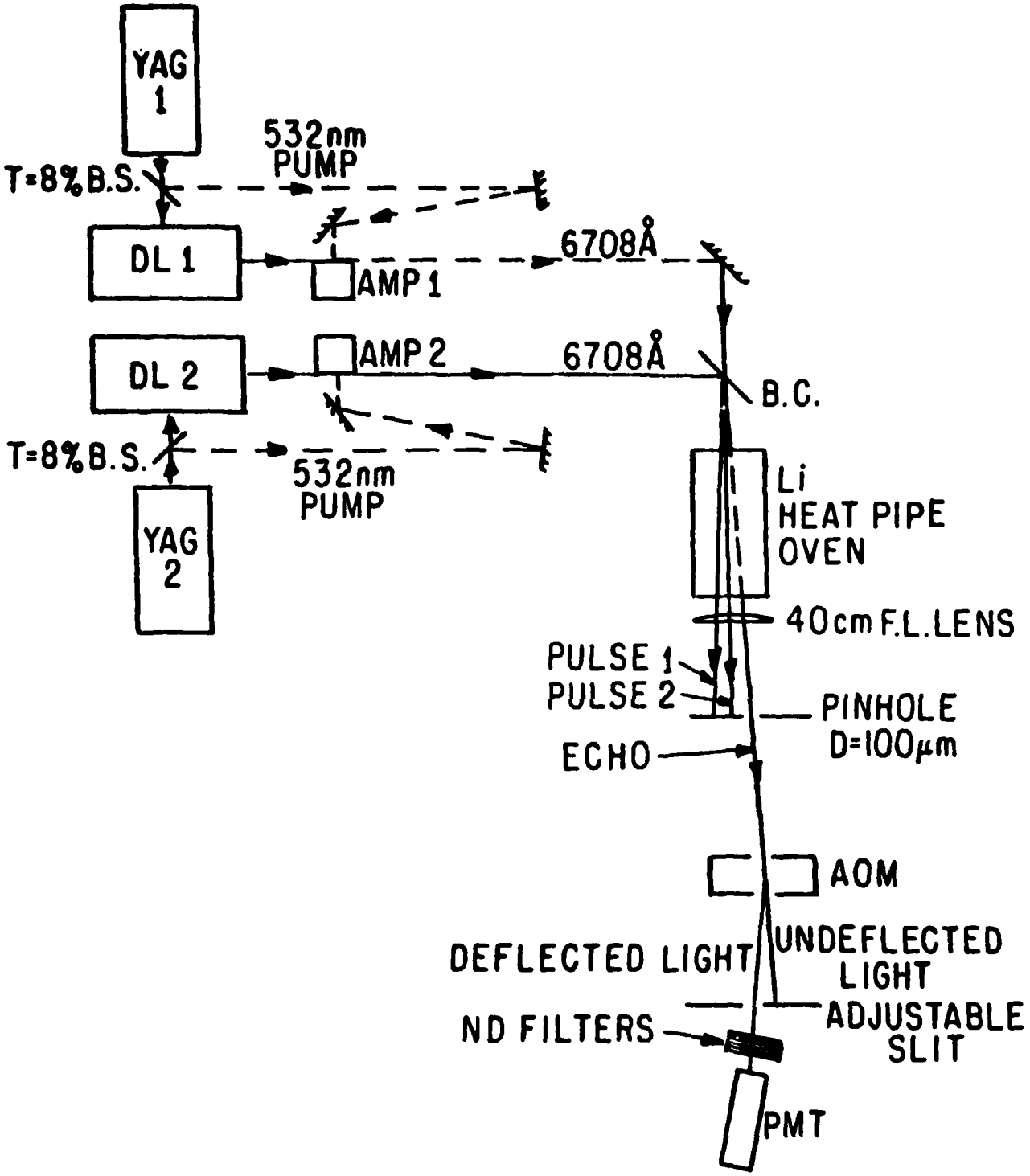

Fig. 4 Schematic diagram of photon echo beam angling apparatus.

still present, are determined by the total time an atom exists in its excited state.

The limiting value of the dynamic range over which echoes can be observed is determined by the competition between the echo signal from atoms excited by the first excitation pulse and the incoherent fluorescence signal from atoms excited by the second excitation pulse applied a time τ after the first. The former decays as $\exp(-2\tau/T_1)$ the latter as $\exp(-\tau/T_1)$, where T_1 is the excited state lifetime. Once these signals become equal, the signal to noise of the echo varies only with the square root of the number of measurements. One can of course continue to average but the payoff is greatly diminished. We estimate this condition as follows.

The number of photons in an echo η_e is given by[6]

$$\eta_e = (\beta/4)^2 \left(\frac{3}{8\pi}\eta\lambda^2 L\right)(\eta AL)\, W\tau_p\, e^{-2\tau/T_1}$$

where n is the number density, L is the sample length, A is the sample area, $W = 1/T_1$, τ_p is the pulse width, and $\beta = (T_2^*/\tau_p)$ if $\tau_p < T_2^*$ otherwise $\beta = 1$. T_2^{*-1} is the inhomogeneous linewidth.

The number of photons incoherently radiated in a solid angle λ^2/A during a time τ_p at the time of the echo is given by

$$\eta_{inc} = \beta\eta AL\, \frac{3}{8\pi}\, \frac{\lambda^2}{A}\, W\tau_p\, e^{-\tau/T_1}$$

Equating η_e with η_{inc} and relating the number density to the absorption coefficient α by the formula

$$\alpha = \frac{3}{8\pi}\eta\lambda^2\, \frac{T_2^*}{T_1}$$

yields the condition

$$\frac{\pi}{6}\,\beta\,\frac{T_1}{T_2^*}\,\frac{A}{\lambda^2}\,\alpha L = e^{\tau/T_1}$$

At this value of τ the number of lifetimes an echo atom has lived is given by

$$N = 2\,\ell n\,\{\frac{\pi}{6}\,\beta\,\frac{T_1}{T_2^*}\,\frac{A}{\lambda^2}\,\alpha L\}$$

If we work with Na vapor using a laser such as ours which puts out 5 nsec pulses then

$$\tau_p = 5 \times 10^{-9} \text{ sec} \qquad A \tilde{\simeq} 3 \text{ cm}^2\,\beta$$
$$T_2^* \tilde{\simeq} 10^{-10} \text{ sec} \qquad \lambda \tilde{\simeq} 6 \times 10^{-5} \text{ Å}$$
$$T_1 = 16 \times 10^{-9} \text{ sec} \qquad \alpha L \tilde{\simeq} 1$$

and we obtain $N \tilde{\simeq} 42$.

Picosecond excitation of long lifetime inhomogeneously broadened lines can increase this estimate considerably. We are now setting up to make a serious measurement in Na vapor. The key to success is good photon counting technique and good echo collection efficiency.

Our application of the tri-level echo technique to relaxation studies in atomic sodium has in the past enabled us to study Noble-gas-induced broadening of transitions to Rydberg S and D states.[7] We are now in the process of performing tri-level echo experiments in Li vapor in order to measure the relaxation of S-S and S-D superposition states due to collisions with various buffer gases. This experiment utilizes three dye lasers. One laser excites the 2S-2P transition at t=0 while a second laser, also at t=0, excites a 2P-nD

or 2P-nS transition. At some delay time later a third laser excites the 2P-nD or 2P-nS transition. These experiments will be able to measure collision cross sections well into the Rydberg regime.

A second kind of two-photon tri level echo is also being investigated, this time in Na vapor. We first resonantly excite the 3S-3P transition and then at a later time we two-photon excite the 3S-4D transition. We observe an echo at the 4D-3P transition. We also observe a coherent burst of radiation at the 4D-3P transition shortly after the 3S-4D transition is excited. This we interpret as delayed superradiance. So far we have only been able to generate echoes at high atomic densities where the absorption length of the 3S-3P radiation is much smaller than the length of the sample. This means that the 4D-3P echo is radiated into a high gain medium. As a consequence it may sometimes be radiated early, before the 3D-3P rephasing is complete. We have evidence of this behavior which we will study further. We are now in the process of replacing our old Hänch type lasers with our newer Thompkin's design 1GHz dye lasers. This will allow us to excite 4D-3P superposition states with much less laser power. We have some evidence of ionization generation which would complicate our analysis. This will be much less important with our new lasers.

Our 4D-3P echoes have been rather weak. Nevertheless they are large enough to enable us to make collisional cross section measurements. We find the cross section for 4D-3P superposition state dephasing is comparable to that for 3S-3P dephasing. By using our improved lasers we will be able to obtain a precise comparison.

In a series of three papers written in 1973 Aihara and Inaba discussed the general problem of multiple pulse excitation of three-level systems.[8] They found that under suitable conditions photon echoes were generated whose

character differed dramatically from those previously observed. It is generally accepted that echoes formed in a two-level system appear at a time after an excitation pulse equal to its separation from a previous excitation pulse or the separation of two previous excitation pulses. This now unremarkable effect is a consequence of the fact that two-level atoms in a static environment have resonance frequencies ω_j whose fractional deviation $\Delta\omega_j/\omega_o = (\omega_o-\omega_j)/\omega_o$ from the central frequency ω_o of the transition being excited after each excitation pulse is a constant.[9] In other words two pulse photon echoes generated by pulses at $t = 0$ and $t = \tau$ form at $t = 2\tau$ because they rephase after the second excitation pulse at exactly the same rate at which they dephased after the first excitation pulse. Echoes do not form at all if $\Delta\omega_j/\omega_o$ changes sign after an excitation pulse, as happens in F spin echo experiments in CaF_2 when the second pulse has area π. On the other hand echoes generated in an electric quadrupole-broadened magnetic resonance experiment can appear at anomolous delays due to the unequal but correlated line broadening of the energy eigenlevels.[10]

The simplest situation in which one obtains high correlation in the inhomogeneous broadening of electronic energy levels is found in a gas. The source of inhomogeneous broadening is the Doppler shift which scales directly with the central frequency of each electronic transition. This essentially perfect correlation has made possible a series of experiments, done in this laboratory, to investigate the collisional relaxation of states of similar parity.[7] The technique is also applicable to studying relaxation of states of opposite parity as we are now doing in Na vapor by observing an echo on the 4D-3P transition generated by two-pulse excitation of the 3S-3P and 3S-4D transitions.

Photon echoes in solids of the same character as those in gases should

also be possible. Phonon induced relaxation however puts a severe limitation on the number of transitions which may be studied. By working at liquid He temperatures some transitions may be frozen in but most remain unavailable to an echo type experiment because they decay too fast by spontaneous emission of a phonon. In Pr^{3+} doped LaF_3 several transitions are available and ordinary two-pulse photon echoes have been observed on both the $^3H_4 - {}^3P_0$ and $^3H_4 - {}^1D_2$ transitions. As we have studied echo behavior on both these transitions it would seem natural for us to extend our work to perform a multiple-level echo experiment in this medium. This could be accomplished by either sequentially exciting the $^3H_4 - {}^1D_2$ and $^3H_4 - {}^3P_0$ transitions and then looking for the echo formed on the $^1D_2 - {}^3P_0$ transition or by performing an ordinary two-pulse echo experiment on the $^3H_4 - {}^1D_2$ transition while performing a single-pulse excitation of the $^3H_4 - {}^3P_0$ transition. This single-pulse excitation of the $^3H_4 - {}^3P_0$ transition will generate an echo since the two-pulse excitation of the $^3H_4 - {}^1D_2$ transition regenerates a $^3H_4$ state component whose state vectors are modulated according to the inhomogeneous broadening associated with the transition. It is best to think of the echo formation process here in terms of a stimulated echo where modulated ground state components are recombined after a single pulse to produce an echo. Ordinarily this pulse would be applied at the same frequency as the pulse pair which produced the modulated ground state components but this is not necessary. The only requirement is that the excitation pulse produce a superposition state which rephases at some rate proportional to the dephasing rate of the primary transition and this will happen according to the degree to which the inhomogeneous broadening is correlated.

Of the two experiments discussed above the first is more difficult for three reasons. (1) The $^1D_2 - {}^3P_0$ transition is in the infrared where

sensitive detectors are lacking. (2) The transition does not appear to be strong enough even to deserve mention in the literature. (3) Phase matching may be a problem as the k vector induced in the $^1D_2 - {}^3P_0$ transition may not correspond to $2\pi/\lambda$ where λ is the wavelength associated with this transition. The single positive feature is that the echo forms at a frequency different from either excitation pulse so that excitation pulse rejection by the detection system would be facilitated. This latter feature together with the fact that only two lasers are required prompted us try this experiment. We failed for some combination of the first three stated objectives.

We plan therefore to work with the second scheme. Phase matching is automatic as we observe the same wavelength at which we excite. Excitation pulse rejection is accomplished, rather, by angling the excitation beams. Calling k_1, k_2, and k_3 the wave vectors associated with the first and second pulses on the $^3H_4 - {}^1D_2$ transition and the pulse on the $^3H_4 - {}^3P_0$ transition, respectively, we make $\not{k}(k_1, k_2) = \not{k}(k_1, k_2) = \not{k}(k_2, k_3)$. The ordinary two-pulse echo at $^3H_4 - {}^1D_2$ will form along $2k_2 - k_1$ while our new tri-level echo at $^3H_4 - {}^3P_0$ will form along $k_3 + k_2 - k_1$. Thus the echoes are separated spatially from each other by the same amount as they are separated spatially from the immediately preceding excitation pulse. Our experience in observing ordinary echoes on both the $^3H_4 - {}^1D_2$ and $^3H_4 - {}^3P_0$ transitions assures us that no problem will be encountered in isolating the echo. This is important for this experiment as we cannot be certain that our Pockels cell shutters will operate quickly enough to separate the echo. Actually, the question of being able to see an echo is moot as in the worst case we still would be able to follow the degradation of the four-wave mixing signal at $k_3 + k_2 - k_1$ formed by the instantaneous application of the three excitation pulses. Echo generation, after all, is no other than a form of delayed four-wave mixing.

The question of whether rephasing occurs does not arise when the pulses are simultaneous.

The degradation of the four-wave-mixed signal with pulse separation should manifest itself in a change of echo amplitude and shape. Echo position is related to echo shape and yields, as in tri-level echo experiments in gases,[7] the scaling factor associated with any correlated inhomogeneous broadening. We also expect that signal modulation will be present which would allow an alternative means of studying nuclear hyperfine structures.

Observation of the position and shape of echoes generated as in the above scheme will provide information regarding atoms whose transitions are broadened in a correlated way.

*This research was also supported by the National Science Foundation under Grant NSF-DMR80-06966 and the U. S. Office of Naval Research under Contract No. N00014-78-C-0517.

(1) R. Beach, B. Brody, and S. R. Hartmann, "Photon Echoes in Lithium Vapor using Angled Excitation Beams," to be published in Phys. Rev. A.

(2) R. Beach, S. R. Hartmann, R. Friedberg, Phys. Rev. A 25, 2658 (1982).

(3) R. Beach, B. Brody, S. R. Hartmann, "Elliptical Billiard-ball Echo Model," Phys. Rev. A 27, 2537 (1983).

(4) R. Beach, B. Brody, S. R. Hartmann, "Photon Echoes Made Simple," Proceedings of International Conf. on Photochemistry and Photobiology, Alexandria, Egypt, Jan. 1983.

(5) P. Berman, Phys. Rev. A 22, 1838 (1980); 22, 1848 (1980).

(6) I. D. Abella, N. A. Kurnit, and S. R. Hartmann, Phys. Rev. 141, 391 (1966).

(7) R. Kachru, T. W. Mossberg, S. R. Hartmann, Phys. Rev. A 21, 1124 (1980).

(8) M. Aihara and H. Inaba, J. Phys. A 6, 1709 (1973); 6, 1725 (1973).

(9) A. Abragam. The Principles of Nuclear Magnetism, Oxford at the Clarendon Press, 1961.

(10) I. Solomon, Phys. Rev. 110, 61 (1958).

SIGNIFICANT ACCOMPLISHMENTS AND TECHNOLOGY TRANSITION REPORT

Significant Accomplishments

I. Quantum Detection and Sensing of Radiation

We have provided a new understanding of the way in which individual atomic photon emissions combine together to generate chaotic light at high average levels. The previous theory was phenomenological.

We have solved an important branching process in statistics, a cascade of Poissons, useful in applications from avalanche photodiodes to cosmic ray noise.

We have defined the role of signal-dependent noise in VLSI system reliability.

II. Physical and Photochemical Properties of Electronic Materials

For the first time high quality germanium nitride insulating films have been grown successfully. It now appears that a germanium insulated gate field-effect transistor can be fabricated using the technology developed in our laboratory.

A new tunneling rectifier has been fabricated using a metal-amorphous silicon-silicon sandwich structure.

For the first time, grain boundary parameters have been measured unambiguously using a laser-spot photoconductivity technique developed in our laboratory. These parameters include barrier height, interface state density, energy level and capture cross section.

Models including both Coulombic scattering and phonon-assisted processes at a semiconductor-semiconductor interface have been completed.

The ultraviolet spectra of physisorbed metallorganics has been measured

for the first time. Metallorganics are a prevalent metal-carrier species in many phases of microelectronics fabrication, including laser direct-writing. Further, physisorbed layers of these molecules are believed to play an important role in many phases of microelectronics processing.

The first observation of laser-enhanced surface chemistry has been made. In these experiments, we have found that submicrometer metal spheres can be used to enhance the surface photochemical decomposition rate of adsorbed molecules. By arranging these spheres in an organized pattern on the surface, it may be possible to further enhance the surface reaction rate. Thus photolithographic fabrication techniques which have been developed for fabrication of semiconductor integrated circuits may prove useful for producing catalytic surfaces for photochemical reactions.

The direct fabrication of submicrometer diffraction gratings has been achieved using laser photochemical interferometry. These results have shown that high quality optical gratings with periodicities as small as 130 nm can be made readily with this laser technique. The "conventional" approach uses electron beam lithography and is thus slower and much more expensive. Five period gratings on compound semiconductors are important as components for electroptical devices and integrated optical circuits.

III. Characteristics and Properties of Energetic Ion and Radical Beams

The energy distribution of both ions and neutrals emanating from a capillaritron ion source have been determined using time of flight mass spectrometry. The neutrals have been found to be extraordinarily cold while the ions are quite hot.

IV. Energy Transfer Processes in Quantum Electronics

Collisional redistribution of electronic energy in sulphur dioxide has been found to preferentially excite the symmetric stretching mode of the ground electronic state. The antisymmetric stretching mode appears to be filled only indirectly by energy transfer from the symmetric stretch and not directly from the electronically excited state.

Photochemically generated hot hydrogen atoms have been found to produce bend-stretch excitation preferentially over pure stretch excitation in CO_2 during H/CO_2 collisions. In H/CO collisions large amounts of rotational excitation are produced in CO along with vibrational excitation of the molecule.

The lifetime of the I_2 $^3\pi_{2u}(A')$ state has been measured for the first time. A matrix isolation technique (10^oK), which takes advantage of the cage effect to produce these triplets following laser excitation, has been used in conjunction with IR fluorescence detection to determine the lifetime of this level. This state may be involved in limiting the maximum power output of the chemical I atom laser.

V. Picosecond Energy Transfer and Photofragmentation Spectroscopy

We have established that the stabilization of intramolecular charge transfer, which is the origin of the anomalous fluorescence in dimethylaminobenzonitrile, is due to formation of an electrostatic ground state complex with a polar solvent molecule or molecules.

We have carried out the first measurement of the equilibration time for spin conversion in a carbene. The value for diphenylcarbene is 110ps. From the kinetic measurements we also obtained an energy splitting of 3.9 kcal/mole between the ground triplet state and the neighboring singlet state.

VI. Generation and Control of Radiation

Photon echoes have been generated in atoms excited more than 15 lifetimes earlier. These experiments were performed in Li vapor where it was possible to observe echo signals over an unprecedented dynamic range exceeding 10^{10}.

Technology Transition Report

1. Bell Laboratories has initiated several programs in laser chemical processing such as those being studied at Columbia. As a result of this interest they have recently awarded a Bell Laboratory Graduate Fellowship to Esaul Sanchez. His work will stress the use of surface spectroscopy in diagnosing surface reactions.

2. Allied Chemical has recently become active in developing new electronic chemicals. They have had a significant interest in finding new applications based on laser processing. With this in mind, they have assisted members of Prof. Osgood's group in developing a new technique for writing micrometer scale oxide patterns and silicon wafers. The technique, which uses a spin-on silicate material, is expected to be useful for directly writing custom rib waveguides.

3. Although too numerous to mention, there are many examples of laser applications to defense, industrial, and research uses. One of the most potentially interesting is the use of lasers in photochemical direct writing of microcircuits. The original research leading to the development of the laser was begun under the JSEP program at Columbia in 1951 when work on the maser started under the direction of Professor Townes.

PERSONNEL

Faculty

K. Eisenthal, Professor of Chemistry

G. W. Flynn, Professor of Chemistry, Director

S. R. Hartmann, Professor of Physics

W. Hwang, Associate Professor of Electrical Engineering

R. Osgood, Professor of Electrical Engineering

P. Prucnal, Assistant Professor of Electrical Engineering

I. I. Rabi, University Professor Emeritus

M. C. Teich, Professor of Engineering Science

E. Yang, Professor of Electrical Engineering

Visiting Faculty

Dr. B. Brody
Dr. J. Peřina
Dr. B. Saleh

Research Associates and Physicists

Dr. P. Brewer
Dr. H. Gilgen
Dr. S. Goates
Dr. W. Hollingsworth
Dr. D. Miller
Dr. G. Reksten
Dr. E. Sitzman
Dr. M. Spencer
Dr. M. Vandersall

Graduate Research Assistants

J. Ahl
T. Allik
R. Beach
P. Beeken
B. Brady
C. Chen
D. Chen
T. Chen
J. Chu
M. Crawford
D. DeBeer
C. Dupuy
H. Evans
M. Glick
B. Grossman
S. Halle
J. Hicks
W. Holber
K. Kastori
R. Kichinski
R. Krchnavek
J. Langan
B. Lawrence
K. Matsuo
D. Podlesnik
E. Poon
L. Pressman
J. Rosenberg
E. Sanchez
M. Santoro
F. Shoucair
P. Siegel
S. So
J. Subbiah
C. Wood
E. Xu

Administration

Ms. I. Moon

Ms. S. Larchuk

Ms. V. Zell

Technician

D. Rivera

JSEP REPORTS DISTRIBUTION LIST

DEPARTMENT OF DEFENSE

Director
National Security Agency
ATTN: Dr. G. Burdge, R-57
Fort George G. Meade, MD 20755

Defense Technical Information Center
ATTN: DDC-DDA
Cameron Station
Alexandria, VA 22314

Defense Advanced Research Proj. Agency
ATTN: Dr. R. Reynolds
1400 Wilson Boulevard
Arlington, BA 22209

Dr. Leo Young
Office of the Deputy Under Secretary
of Defense for Research and
Engineering (R&AT)
Room 3D1067
The Pentagon
Washington, DC 20301

DEPARTMENT OF THE ARMY

Commander
U. S. Army Armament R&D Command
ATTN: DRDAR-TSS # 59
Dover, NJ 07801

Director
U. S. Army Ballistics Research Lab.
ATTN: DRDAR-BL
Aberdeen Proving Ground
Aberdeen, MD 21005

Commander
U. S. Army Communications Command
ATTN: CC-OPS-PM
Fort Huachuca, AZ 85613

Commander
U. S. Army Missile Command
Redstone Scientific Inf. Center
ATTN: DRSMI-RPRD (Documents)
Redstone Arsenal, AL 35809

Commander
U. S. Army Satellite Comm. Agency
Fort Monmouth, NJ 07703

Commander
U. S. Army Atmospheric Sciences Lab.
ATTN: DELAS-AD-DM (Tec Wrtg)
White Sands Missile Range, NM 88002

Director
TRI-TAC
ATTN: TT-AD (K. Lape')
Fort Monmouth, NJ 07703

Executive Secretary, TCC/JSEP
U. S. Army Research Office
P. O. Box 12211
Research Triangle Park, NC 27709

Commander
Harry Diamond Laboratories
ATTN: Technical Inf. Branch
2800 Powder Mill Road
Adelphi, MD 20783

HQDA
Washington, DC 20310

Director
U. S. Army Electronics Technology
and Devices Laboratory
ATTN: DELET-E (Dr. Jack A. Kohn)
Fort Monmouth, NJ 07703

Commander
U. S. Army Comm. R&D Command
ATTN: DRSEL-TES-CR (Mr. David Haratz)
Fort Monmouth, NJ 07703

Director
U. S. Army Electronics Technology
and Devices Laboratory
ATTN: DELET-M (Mr. V. Gelnovatch)
Fort Monmouth, NJ 07703

Commander
U. S. Army Electronics R&D Command
ATTN: DRDEL-SA (Dr. W. S. McAfee)
Fort Monmouth, NJ 07703

U. S. Army Research, Development
and Standardization Group - CA
National Defense Headquarters
Ottawa, Ontario
CANADA K1A OK2

Commander
U. S. Army Comm. Electronics Command
ATTN: DRSEL-COM-RM-4 (Dr. F. Schwering
Fort Monmouth, NJ 07703

Director
U. S. Army Electronics Technology
and Devices Laboratory
ATTN: DELET-I (Mr. Harold Borkan)
Fort Monmouth, NJ 07703

Director
U. S. Army Electronics R&D Command
Night Vision and Electro-Optics Labs
ATTN: Dr. Randy Longshore, DELNV-IT
Fort Belvoir, VA 22060

Commander
U. S. Army Research Office
ATTN: DRXRO-EL (Dr. James Mink)
P. O. Box 12211
Research Triangle Park, NC 27709

Commander
Harry Diamond Laboratories
ATTN: DELHD-RT-A (Mr. J. Salerno)
2800 Powder Mill Road
Adelphi, MD 20783

Director
U. S. Army Electronics R&D Command
Night Vision and Electro-Optics Labs
ATTN: DELNV-IRTD (Dr. John Pollard)
Fort Belvoir, VA 22060

Commander
U. S. Army Research Office
ATTN: DRXRO-EL (Dr. William A. Sander)
P. O. Box 12211
Research Triangle Park, NC 27709

Director
U. S. Army Electronics Technology
and Devices Laboratory
ATTN: DELET-ES (Dr. A. Tauber)
Fort Monmouth, NJ 07703

Director
Division of Neuropsychiatry
Walter Reed Army Inst. of Research
Washington, DC 20012

Commander
USA ARRADCOM
ATTN: DRDAR-SCF-IO (Dr. J. Zavada)
Dover, NJ 07801

Director
U. S. Army Signals Warfare Lab
ATTN: DELSW-D-OS
Vint Hill Farms Station
Warrenton, VA 22186

Director
U. S. Army Electronics Technology
and Devices Laboratory
ATTN: DELET-ED (Dr. E. H. Poindexter)
Fort Monmouth, NJ 07703

Commander
U. S. Army Research & Standardization
Group (Europe)
ATTN: (Dr. F. Rothwarf)
Box 65
FPO NY 09510

U. S. Army Research Office
ATTN: Library
P. O. Box 12211
Research Triangle Park, NC 27709

Commander
U. S. Army Communications Command
ATTN: DRSEL-COM-RF (Dr. T. Klein)
Fort Monmouth, NJ 07703

Mr. Jerry Brookshire
Guidance and Control Directorate
U. S. Army Missile Command
ATTN: DRSMI-RGG, Bldg. 4381
Redstone Arsenal, AL 35898

Dr. Michael Fahey
Advanced Sensors Directorate
U. S. Army Missile Command
ATTN: DRDMI-RER
Redstone Arsenal, AL 35898

Dr. Charles Bowden
U. S. Army Missile Command
Research Directorate
ATTN: DRSMI-RRD
Redstone Arsenal, AL 35898

Dr. Arthur R. Sindoris
Harry Diamond Laboratories
ATTN: DELHD-PO-P
2800 Powder Mill Road
Adelphi, MD 20783

Dr. Horst R. Wittmann
U. S. Army Research Office
P. O. Box 12211
Research Triangle Park, NC 27709

Dr. Jimmie R. Suttle
U. S. Army Research Office
P. O. Box 12211
Research Triangle Park, NC 27709

Mr. Charles Graff
U. S. Army Comm. - Electronics Command
ATTN: DRSEL-COM-RF-Z
Fort Monmouth, NJ 07703

Mr. Edward Herr
U. S. Army Comm. - Electronics Command
ATTN: DRSEL-COM-RX-4
Fort Monmouth, NJ 07703

Mr. Roland Wright
Night Vision & Electro-Optics Labs
Fort Belvoir, VA 22060

Dr. Robert Rohde
Night Vision & Electro-Optics Labs
Fort Belvoir, VA 22060

Dr. Donn V. Campbell
U. S. Army Comm. - Electronics Command
ATTN: DRSEL-COM-RN-4
Fort Monmouth, NJ 07703

Dr. Nick Karayianis
Harry Diamond Laboratories
ATTN: DELHD-RT-CA
2800 Powder Mill Road
Adelphi, MD 20783

Dr. T. N. Chin
U. S. Army ARRADCOM
ATTN: DRDAR-SCF-10
Dover, NJ 07801

Dr. John Malamus
Night Vision & Electro-Optics Labs
Fort Belvoir, VA 22060

Dr. Rudolf G. Buser
Night Vision & Electro-Optics Labs
ATTN: DELNL-L
Fort Belvoir, NJ 22060

Dr. W. Ealy
Night Vision & Electro-Optics Labs
ATTN: DELNV-AC
Fort Monmouth, NJ 22060

Dr. J. Hall
Night Vision & Electro-Optics Labs
ATTN: DELNV-AC
Fort Belvoir, NJ 22060

Dr. J. Burgess
Night Vision & Electro-Optics Labs
ATTN: DELNV-RM-RA
Fort Belvoir, NJ 22060

DEPARMENT OF THE AIR FORCE

Dr. E. Champagne
AFWAL/AADD-I
Wright-Patterson AFB, OH 45433

Mr. W. Edwards, Chief
AFWAL/AAD
Wright-Patterson AFB, OH 45433

Professor R. E. Fontana
Head, Department of Electrical Engineering
AFIT/ENG
Wright-Patterson AFB, OH 45433

Dr. Alan Garscadden
AFWAL/POOC-3
Air Force Aeronautical Labs
Wright-Patterson AFB, OH 45433

Mr. Alan R. Barnum (CO)
Rome Air Development Center
Griffiss AFB, NY 13441

Chief, Electronic Research Branch
AFWAL/AADR
Wright-Patterson AFB, OH 45433

Mr. John Mott-Smith (ESD/ECE)
HQ ESD (AFSC), Stop 36
Hanscom AFB, MA 01731

Dr. J. Ryles
Chief Scientist
AFWAL/AS
Wright-Patterson AFB, OH 45433

Dr. Allan Schell
RADC/EE
Hanscom AFB, MA 01731

Dr. J. Bram
AFOSR/NM
Bolling AFB, DC 20332

Dr. David W. Fox
AFOSR/NM
Bolling AFB, DC 20332

Dr. J. Neff
AFOSR/NE
Bolling AFB, DC 20332

Dr. N. H. DeAngelis
RADC/ESR
Hanscom AFB, MA 01731

Dr. Gerald L. Witt
Program Manager
Electronic & Material Sciences Directorate
Department of the Air Force
AFOSR
Bolling AFB, DC 20332

Dr. Tom Walsh
AFOSR/NE
Bolling AFB, DC 20332

Dr. Edward Altshuler
RADC/EEP
Hanscom AFB, MA 01731

DEPARTMENT OF THE NAVY

Naval Surface Weapons Center
ATTN: Technical Library
Code DX-21
Dahlgren, VA 22448

Dr. Gernot M. R. Winkler
Director, Time Service
U. S. Naval Observatory
Massachusetts Avenue at 34th Street, NW
Washington, DC 20390

G. C. Dilworth, Jr.
Technical Director
Naval Coastal Systems Center
Panama City, FL 32407

Naval Air Development Center
ATTN: Code - 301 A. Witt
Technical Library
Warminster, PA 18974

R. S. Allgaier, R-45
Naval Surface Weapons Center
Silver Spring, MD 20910

Office of Naval Research
800 North Quincy Street
ATTN: Code 250
Arlington, VA 22217

Office of Naval Research
800 North Quincy Street
ATTN: Code 414
Arlington, VA 22217

Office of Naval Research
800 North Quincy Street
ATTN: Code 411MA
(Dr. Stuart L. Brodsky)
Arlington, VA 22217

Commanding Officer
Naval Research Laboratory
ATTN: Dr. S. Teitler, Code 1450
Washington, DC 20375

Commanding Officer
Naval Research Laboratory
ATTN: Mrs. D. Folen, Code 2627
Washington, DC 20375

Commanding Officer
Naval Research Laboratory
ATTN: Mr. A. Brodzinsky, Code 5200
Washington, DC 20375

Commanding Officer
Naval Research Laboratory
ATTN: Mr. J. E. Davey, Code 6810
Washington, DC 20375

Commanding Officer
Naval Research Laboratory
ATTN: Mr. B. D. McCombe, Code 6800
Washington, DC 20375

Commanding Officer
Naval Research Laboratory
ATTN: Mr. W. L. Faust, Code 6504
Washington, DC 20375

Technical Director
Naval Underwater Systems Center
New London, CT 06320

Naval Research Laboratory
Underwater Sound Reference Detachment
Technical Library
P. O. Box 8337
Orlando, FL 32856

Naval Ocean Systems Center
ATTN: Dr. F. C. Fletcher, Code 92
San Diego, CA 92152

Naval Ocean Systems Center
ATTN: Mr. W. J. Dejka, Code 8302
San Diego, CA 92152

Naval Ocean Systems Center
ATTN: Dr. Alfred K. Nedoluha,
Code 922
San Diego, CA 92152

Naval Weapons Center
ATTN: Dr. G. H. Winkler, Code 381
China Lake, CA 93555

Dr. Donald E. Kirk (62)
Professor and Chairman, Electrical
Engineering
SP-304
Naval Postgraduate School
Monterey, CA 93940

Dr. D. F. Dence
Naval Underwater Systems Center
New London Laboratory
ATTN: Code 34
New London, CT 06320

Director, Technology Assessment
Division (OP-987)
Office of the Chief of Naval Oper.
Navy Department
Washington, DC 20350

Mr. J. W. Willis
Naval Air Systems Command
AIR-310
Washington, DC 20361

Naval Electronics Systems Command
NC #1
ATTN: Code 61R
2511 Jefferson Davis Highway
Arlington, VA 20360

Department of the Navy
Naval Sea Systems Command
ATTN: W. W. Blaine (SEA-62R)
Washington, DC 20362

David Taylor Naval Ship Research
and Development Center
ATTN: Mr. G. H. Gleissner, Code 18
Bethesda, MD 20084

Mr. Martin Mandelberg
Coast Guard R&D Center
Avery Point
Groton, CT 06340

Naval Underwater Systems Center
New London Laboratory
ATTN: 101E (Dr. Edward S. Eby)
New London, CT 06320

Mr. Thomas J. Manuccia, Head
Chemistry and Application Section
Code 6543
Naval Research Laboratory
Washington, DC 20375

Dr. Stephen G. Bishop, Head
Semiconductor Branch
Code 6870
Naval Research Laboratory
Washington, DC 20375

Dr. John W. Rockway
Comm. Technology Prog. Off.
Code 8105
Naval Ocean Systems Center
San Diego, CA 92152

Dr. Barry P. Shay
Joint Program Office,
ODUSD(P)
The Pentagon, Rm 4D825
Washington, DC 20301

Dr. Sydney R. Parker
Professor, Electrical Engineering
Code 62PX
Naval Postgraduate School
Monterey, CA 93940

Dr. George B. Wright
Office of Naval Research
Code 427
Arlington, VA 22217

OTHER GOVERNMENT AGENCIES

Dr. Ronald E. Kagarise
Director
Division of Materials Research
National Science Foundation
1800 G Street
Washington, DC 20550

Director
Division of Electrical, Computer
and Systems Engineering
National Science Foundation
Washington, DC 20550

Dr. Dean L. Mitchell
Section Head
Condensed Matter Sciences Section
Division of Materials Research
National Science Foundation
1800 G Street, N. W.
Washington, DC 20550

Judson C. French, Director
Center for Electronics and Electrical
Engineering
B 358 Metrology Building
National Bureau of Standards
Washington, DC 20234

NON-GOVERNMENT AGENCIES

Director
Columbia Radiation Laboratory
Columbia University
538 West 120th Street
New York, NY 10027

Director
Coordinated Science Laboratory
University of Illinois
Urbana, IL 61801

Associate Director of Materials
and Electronics Research
Division of Applied Sciences
McKay Laboratory 107
Harvard University
Cambridge, MA 02138

Director
Electronics Research Center
University of Texas
P. O. Box 7728
Austin, TX 78712

Director
Electronics Research Laboratory
University of California
Berkeley, CA 94720

Director
Electronics Sciences Laboratory
University of Southern California
Los Angeles, CA 90007

Director
Microwave Research Institute
Polytechnic Institute of New York
333 Jay Street
Brooklyn, NY 11201

Director
Research Laboratory of Electronics
Massachusetts Institute of Technology
Cambridge, MA 02139

Director
Stanford Electronics Laboratory
Stanford University
Stanford, CA 94305

Director
Edward L. Ginzton Laboratory
Stanford University
Stanford, CA 94305

Dr. Lester Eastmen
School of Electrical Engineering
Cornell University
316 Phillips Hall
Ithaca, NY 14850

Dr. Carlton Walter
Electro Science Laboratory
The Ohio State University
1320 Kinnear Road
Columbus, OH 43212

Dr. Richard Saeks
Dept. of Electrical Engineering
Texas Tech University
Lubbock, TX 79409

Director
School of Electrical Engineering
Georgia Institute of Technology
Atlanta, GA 30332

Dr. John F. Walkup
Dept. of Electrical Engineering
Texas Tech University
Lubbock, TX 79409

Mrs. Renate D'Arcangelo
Editorial Office
130 Pierce Hall
Division of Applied Sciences
31 Oxford Street
Cambridge, MA 02138